

# **LASER POWDERBED FUSION (LPBF) OF TUNGSTEN AND TUNGSTEN ALLOYS FOR NUCLEAR FUSION APPLICATIONS**

*By*

*Amanda Catherine Field*

A thesis submitted to the  
University of Birmingham  
for the degree of  
DOCTOR OF PHILOSOPHY

School of Metallurgy and Materials  
College of Engineering and Physical Sciences  
University of Birmingham

UNIVERSITY OF  
BIRMINGHAM

**University of Birmingham Research Archive**

**e-theses repository**

This unpublished thesis/dissertation is copyright of the author and/or third parties. The intellectual property rights of the author or third parties in respect of this work are as defined by The Copyright Designs and Patents Act 1988 or as modified by any successor legislation.

Any use made of information contained in this thesis/dissertation must be in accordance with that legislation and must be properly acknowledged. Further distribution or reproduction in any format is prohibited without the permission of the copyright holder.

## ABSTRACT

Tungsten is a candidate material for the plasma facing components (PFCs) within a nuclear fusion reactor as a result of its high melting point (3420 °C), high thermal conductivity (170 Wm<sup>-1</sup> K<sup>-1</sup>), and high density (19.4 gcm<sup>-3</sup>). These allow the components to survive the operating temperatures as well as providing effective radiation shielding and conduction of heat through the components. The comparatively low activation of tungsten means that long-term waste storage does not need to be considered and recycling methods are possible after 75 years. There are difficulties associated with the processing of tungsten, however, as a result of its high melting point and intrinsic brittleness (Ductile–Brittle Transition Temperature (DBTT) ~ 400 °C). Conventionally, powder metallurgy methods including sintering have been used, but as final machining is challenging, the complexity of component geometries has been limited. The simple shape of the current divertor monoblock design is largely dictated by manufacturing issues. Interstitial impurity elements had been shown to significantly worsen the mechanical behaviour of tungsten.

It was considered likely that cracking would be an issue for LPBF tungsten due to the high cooling rate, the residual oxygen content and its sensitivity to thermal shock. Thus, this study was designed as a feasibility study to investigate the potential of LPBF processing of tungsten. While high densities (98 % theoretical density) were achieved, there was a significant issue with cracking. The cracking was found to be hot cracking of the grain boundaries and was caused by segregation of oxygen causing embrittlement. The effect of raw material quality on LPBF processability was also investigated and it was found building with spherical powder resulted in improved part quality with 8.8 % higher densities achieved. This was determined to be due to a higher effective laser absorptivity determined through penetration depth measurements into the build plate.

As it had been shown that LPBF processing of unalloyed tungsten resulted in significant cracking, methods to improve the manufacturability were investigated; the use of bed heating at 400 °C and 600 °C and alloying with 10 w.t.% Ta, through elemental powder blending were trialled. The parts produced with bed heating were found to have a modified cracking structure with a central region which had finer cracking. However, they suffered from extensive oxidation, which resulted in an increase in porosity. The single scan tracks showed significant issues with surface tension which prevented accurate measurement. Alloying with tantalum was found to be more successful with a significant reduction in cracking. It was shown that within the W-Ta alloy oxygen did not segregate to the grain boundaries and instead formed discrete clusters through the material. This was found to have a maximum load three times higher than that of unalloyed tungsten during small punch testing but was still significantly weaker than conventionally produced pure tungsten.

While improvements were made to LPBF processing of tungsten and its alloys, significant improvement would be needed to have a process sufficiently robust for fusion components particularly with regard to oxygen embrittlement. It is likely specialised hardware would need to be designed in order to effectively solve this issue.

## ACKNOWLEDGEMENTS

This work has been carried out within the framework of the EUROfusion Consortium and has received funding from the Euratom research and training programme 2014-2018 under grant agreement No 633053.

The views and opinions expressed herein do not necessarily reflect those of the European Commission. This work has also been part-funded by the RCUK Energy Programme [grant number EP/P012450/1].

I am grateful to the School of Metallurgy and Materials, IOM<sup>3</sup> and the Worshipful Company of Armourers & Braziers for their assistance in attending conferences throughout my studies.

I am extremely grateful to the Engineering & Physical Sciences Research Council (EPSRC) and to Eurofusion and United Kingdom Atomic Energy Authority (UKAEA) for my PhD scholarship and the financial support of this project, without which this research would not have been possible.

My thanks are extended to Dr. Mike Gorley, Dr. David Hancock and Dr. Heather Lewtas and everyone at UKAEA for their support and encouragement throughout my project. Their knowledge of nuclear fusion has proved invaluable and without a doubt their enthusiasm is infectious.

I would like to thank Prof. Moataz Attallah for this opportunity and for being the person to first get me into additive manufacturing, as well as for his academic supervision throughout the project. I would also like to thank him for facilitating me with presenting my work to the international scientific community.

I express my thanks to Dr. Martin Strangwood for his support of my project. His logical and critical approach to research has shaped my thinking, and his guidance and sense of humour has supported me throughout.

A special thank you goes to Dr. Luke Carter for his support, guidance and expert knowledge on Laser Powderbed Fusion. In addition, he as well as Dr. Sam Cruchley, Rachel Jennings and Miles Fan and the other members of AMPLab have given me a helping hand whenever I needed it, and their company has been very much appreciated.

I would finally like to thank my parents for their unwavering support and encouragement as well as the rest of my family and friends for providing me with the encouragement needed to complete my studies.

## **PUBLICATIONS & PRESENTATIONS**

### **PUBLICATIONS**

Field, A.C., Carter, L.N., Adkins, N.J.E. et al. (2020) 'The Effect of Powder Characteristics on Build Quality of High-Purity Tungsten Produced via Laser Powder Bed Fusion (LPBF)' Metall and Mat Trans A. <https://doi.org/10.1007/s11661-019-05601-6>

*Work has been taken from this thesis in accordance with publication copyright transference.*

### **PATENTS**

Patterson, J., Field, A.C., Carter, L.N., & Attallah, M.M. (2016) 'Selective Laser Melting of Refractory Metal Powder' UK Patent Application GB2538874A, filed 30 November 2016.

### **PRESENTATIONS**

Field, A.C., Carter, L.N., Bastin, A.L. & Attallah, M.M. (2015) 'Selective Laser Melting of Pure Tungsten: Process Optimisation and Structural Integrity Development' presented to Industrial Laser Applications Symposium, Warwick, U.K., 17-18 March 2015.

Field, A.C., Carter, L.N., Adkins, N.J.E., Gorley, M.J., & Attallah, M.M. (2016) 'Influence of Powder Characteristics on the Structural Integrity of high purity Tungsten produced via Selective Laser Melting' presented to Materials Science & Technology 2016, Salt Lake City, U.S.A., 23-27 October 2016.

Field, A.C., Carter, L.N., Adkins, N.J.E., Gorley, M.J., & Attallah, M.M. (2017) 'Influence of powder characteristics on the defects and oxidation of high purity tungsten produced via selective laser melting (SLM)' presented to 2017 TMS Annual Meeting & Exhibition, San Diego, U.S.A, 26 February – 2 March 2017.

Megahed, M., Ottow, W., Field, A.C., Carter, L.N., Attallah, M.M., Gorley, M.J., and Porton, M. (2017) 'Process Window Optimization for Powder Bed Additively Manufactured Molybdenum' presented to 2017 TMS Annual Meeting & Exhibition, San Diego, U.S.A, 26 February – 2 March 2017.

Hancock, D., Curtis-Rouse, M., Field, A.C., Homfray, D., Lewtas, H., Porton, M., Surrey, E., Todd, I., Williams, S., and Wynne, B. (2017) 'Additive Manufacturing of High Temperature Materials for Fusion: A Review of Current Capabilities and Future Outlook' presented to EUROMAT 2017, Thessaloniki, Greece, 17-22 September 2017.

# TABLE OF CONTENTS

## CHAPTER 1 – INTRODUCTION

1.1 A Brief Introduction to Nuclear Fusion	1
1.2 Material Requirements for the Divertor Assembly	6
1.2.1 Activation Limits	7
1.2.2 Thermal Property Thresholds	11
1.3 A Brief Introduction to Laser Powderbed Fusion (LPBF)	13
1.4 References	18

## CHAPTER 2 – LITERATURE REVIEW

2.1 – Introduction	20
2.2 – Refractory Metals	20
2.2.1 – Atomic Structure	21
2.2.2 – Thermal & Mechanical Properties	23
2.2.3 – Detrimental Elements	29
2.2.4 – Oxidation	34
2.3 – Welding of Refractory Metals	39
2.4 – Brief Overview of Analytical Techniques	45
2.5 – Laser Powderbed Fusion (LPBF)	52
2.5.1 – Defects in LPBF Processing	53
2.5.2 – Energy Density Relationships	57
2.5.3 – Raw materials in LPBF Processing	62
2.5.4 – Reduction in Residual Stress through Bed Heating in LPBF Processing	66
2.5.5 – LPBF Processing of Tungsten	67
2.6 – Tungsten Alloys	72
2.7 – Concluding Remarks	76
2.8 – Aims & Objectives	77
2.9 – References	79

## CHAPTER 3 – EXPERIMENTAL METHODS

3.1. Introduction	86
3.2. Materials	86
3.3. Powder Characterisation	88
3.3.1. Laser Particle Size Distribution	88
3.3.2. Image analysis of powder particles	89
3.3.3. Shear Ring Testing	90
3.3.4. Apparent and Tap Density Determination	92
3.3.5. Powder Blending	93
3.3. Chemical Composition Analysis	93

3.4. LPBF Sample Production	94
3.5. Metallurgical Sample Preparation	102
3.6. Archimedes' Density Testing	104
3.7. Optical Microscopy (OM)	105
3.8. Scanning Electron Microscopy (SEM)	105
3.9. Image Analysis	109
3.10. Small Punch Testing	110
3.11. Secondary Ion Mass Spectroscopy (SIMS)	112
3.12. X-ray Diffraction	113
3.13. Raman Spectroscopy	114
3.14. References	115

## **CHAPTER 4 – PROCESS OPTIMISATION AND IDENTIFICATION OF CRACK MECHANISM IN LPBF HIGH PURITY TUNGSTEN**

4.1 Introduction	117
4.2 Process Optimisation	119
4.2.1 Parameter Development	119
4.2.2 Validity and limitations of Volumetric Energy Density (VED) model	128
4.3 Determination of Cracking Mechanism	139
4.3.1 Introduction	139
4.3.2 Cracking in Laser Single Scan Tracks	139
4.3.3 Microstructure Investigation of LPBF Deposits	149
4.3.4 Small Punch Testing and Fractography	157
4.3.5 Effect of Interstitial Impurities on Cracking	163
4.4 Effect of Powder Characteristics on Build Quality	166
4.5 References	182

## **CHAPTER 5 – INVESTIGATING METHODS OF IMPROVING THE LPBF PROCESSING OF TUNGSTEN**

5.1 Introduction	185
5.2 Effect of pre-scanning	186
5.2.1 Temperature monitoring results	186
5.2.2 Fusion zone penetration depth measurements	190
5.3 Effect of heated bed module	192
5.3.1 Single Scan Results	194
5.3.2 Build deposits with heated bed	198
5.3.3 Fusion zone penetration depth measurements	208
5.4 Effect of minor tantalum additions	210
5.4.1 Blended powder characterisation	211

5.4.2 Build deposits with tantalum additions	215
5.5 Combined effect of minor alloy addition and heated bed	223
5.5.1 Fusion Zone Penetration Depth Measurements	224
5.5.2 Build deposits produced with alloy additions and heated bed	225
5.6 Small Punch Testing	226
5.7 Demonstration Components	231
5.8 Concluding Remarks	235
5.9 References	236

## **CHAPTER 6 – CONCLUSIONS, EVALUATION AND FUTURE WORK**

6.1. Overall Conclusions	239
6.2. Evaluation of the LPBF Processing Route	243
6.3. Proposed Areas of Future Work	244
6.4. Final Remarks	249
6.5. References	251

## **APPENDIX A – CONCEPT LASER M2 OPERATIONS, MODIFICATIONS AND LASER PROFILING**

A.1 Standard Operation	252
A.2 Build Environment	256
A.3 Laser Profiling	258
A.4 Machine Modifications	261
A.4.1 Laser Preheating	261
A.4.2 Heated Bed Module	262
A.5 References	264



## List of Figures

Page	Caption
3	Figure 1.1 - A schematic showing the variation in potential energy of two nuclei with their relative separation
5	Figure 1.2 - Schematic showing the ITER experimental fusion reactor with divertor assembly labelled
6	Figure 1.3 - Schematic of the divertor cassette and monoblock
9	Figure 1.4 - Time evolution of gamma dose rate for tungsten in three DEMO fusion reactor scenarios: First Wall (red), Blanket (green) and Manifold (blue) along with the corresponding results for iron in the three scenarios (grey)
10	Figure 1.5 - Classification of material activation for fusion
12	Figure 1.6 - Graph showing the transition metals ranked as a function of a merit index, $(T_{m,K})/\alpha$
13	Figure 1.7 - Graph showing fracture strength as a function of maximum service temperature
14	Figure 1.8 - Schematic cross-section of the Concept Laser M2 powder-bed system
21	Figure 2.1 - Representation of refractory metals as defined by various studies
22	Figure 2.2 - Schematic of Body-Centre Cubic (BCC) Crystal Structure
26	Figure 2.3 - Effect of strain rate on yield stress of tungsten
27	Figure 2.4 - Effect of grain size on DBTT in tungsten
28	Figure 2.5 - Graph showing the variation in UTS with test temperature for molybdenum and TZM in stress relieved and recrystallised state
28	Figure 2.6 - Graph to show the variation in 100-hour rupture stress for refractory metals with different fabrication routes.
30	Figure 2.7 - The effect of oxygen and carbon on the DBTT of single crystal and polycrystalline tungsten.
31	Figure 2.8 - Fracture surfaces of tungsten with overlaid maps of oxygen (left) and phosphorous (right)
32	Figure 2.9 - Fracture surface of a molybdenum sample produced by LPBF a) oxide segregations at grain boundaries, b) segregation of the exposed fracture surface, c) Elemental distribution of oxygen at the fracture surface shown in b)
33	Figure 2.10 - Effect of oxygen on yield strength of polycrystalline tungsten
34	Figure 2.11 – Metal-oxide displacement with time of refractory metals in air at around 1000 °C
36	Figure 2.12 - Ellingham diagram showing the formation reactions of the Group IV, V and VI metals with solid circles indicate melting of the base metal, open circles indicating oxide melting and the triangle indicating transition to gaseous oxide.
37	Figure 2.13 - Schematic showing a) Marangoni convection in the melt pool and b) oxide disruption and solidification of the melt pool in aluminium alloys
40	Figure 2.14 - Typical welding microstructures with varying scan speeds (top to bottom, low, intermediate and high travel speeds)
41	Figure 2.15 - Centre-line crack formation in a tungsten weld conducted in an environment with 1800 ppm oxygen
42	Figure 2.16 - Factors affecting hot cracking in welding
44	Figure 2.17 - Graph showing the increase in oxygen in the weld bead with increasing oxygen in the welding atmosphere

- 53 Figure 2.18 - Schematic diagram showing input parameters that will affect build quality
- 54 Figure 2.19 - Micrograph showing LOF defect in LPBF material
- 55 Figure 2.20 - Simulation of keyhole pore formation in Ti-6Al-4V
- 56 Figure 2.21 - Micrograph showing poor bonding defect in LPBF material
- 57 Figure 2.22 - MicroCT data showing the cracks (red) and voids (yellow) in the XY plane with the dashed lines representing the approximate position of the pattern boundaries.
- 59 Figure 2.23 - OM micrographs of Al-12Si LPBF samples with VED of  $55\text{Jmm}^{-3}$  but varying parameters a)  $320\text{ W}$ ,  $1455\text{mms}^{-1}$ , b)  $280\text{ W}$ ,  $1273\text{ mms}^{-1}$ , c)  $240\text{ W}$ ,  $1091\text{mms}^{-1}$ , d)  $200\text{ W}$ ,  $910\text{ mms}^{-1}$ , e)  $160\text{ W}$ ,  $728\text{ mms}^{-1}$ , f)  $120\text{ W}$ ,  $546\text{ mms}^{-1}$ , g)  $80\text{ W}$ ,  $364\text{ mms}^{-1}$  and h)  $40\text{ W}$ ,  $182\text{ mms}^{-1}$ .
- 67 Figure 2.24 - Melting and solidification process of a W-Cu alloy during LPBF processing
- 69 Figure 2.25 - Optical micrograph showing ordered cracking in LPBF tungsten produced with  $400\text{ }^{\circ}\text{C}$  bed heating.
- 70 Figure 2.26 - Microstructure after a thermal shock load of  $0.43\text{ GWm}^{-2}$  at  $200\text{ }^{\circ}\text{C}$
- 73 Figure 2.27 - W-Re phase diagram
- 74 Figure 2.28 - Diagram showing the formation of complete binary solid solutions between refractory metals
- 75 Figure 2.29 - W-Ta phase diagram
- 90 Figure 3.1 - Powder particle morphologies typical of the categories to which they were assigned
- 91 Figure 3.2 - A schematic diagram showing a Schulze Shear Ring Cell
- 98 Figure 3.3 - Schematic representation of the laser scan parameters related to AED
- 99 Figure 3.4 - Schematic of the build set-up for control (left) and pre-scan (right) experiments along with the location of the thermocouples on the tungsten plate (bottom)
- 101 Figure 3.5 Schematic of the heated bed module with (from top) plate loading clips, tungsten build plate (blue), heating plate (grey) with cartridge heaters (red), ceramic insert to limit heat losses (yellow) and attachments to Concept Laser M2 reduced build volume module
- 103 Figure 3.6 - Schematic diagram showing the sections of the LPBF samples
- 104 Figure 3.7 - A Schematic Diagram showing Archimedes' Density Testing equipment
- 110 Figure 3.8 - Schematic representation of the methodology for penetration depth measurements
- 112 Figure 3.8 - Small Punch test set-up; (1) Punch head, (2) Clamping die, (3) Specimen, (4) Receiving die, (5) Extensometer rod. Actual specimen shown top-right
- 121 Figure 4.1 – Optical micrograph of an XY section from parameter A.1, typical of the initial parametric study showing equally spaced lack of fusion defects
- 122 Figure 4.2 – Optical micrograph of an XY section from parameter A.7, showing both equally spaced lack of fusion defects and defects from insufficient energy input and unmelted powder particles (circled in red)
- 123 Figure 4.3 - A photograph showing the build from the second stage of the parameter development with parts showing discontinued parts (red), overmelting (yellow) and well-built parts (green)
- 126 Figure 4.4 - BSE micrograph of an XY section from parameter C.3, showing extensive cracking and limited lack of fusion defects (circled in red)

- 126 Figure 4.5 - BSE micrograph of an XY section from parameter C.3, showing prevalence of cracking on the macroscale
- 127 Figure 4.6 - A graph showing the effect of Linear Energy Density ( $\text{Jmm}^{-1}$ ) on the Archimedes' Density (%) of the samples with varying laser scan spacings (error 1 %)
- 130 Figure 4.7 - A graph showing the effect of Volumetric Energy Density ( $\text{Jmm}^{-3}$ ) on the Archimedes' Density (%) of the samples (unfilled circle corresponded to the low power parameter; error 1 %)
- 132 Figure 4.8 - A graph showing the effect of Linear Energy Density ( $\text{Jmm}^{-1}$ ) on the Archimedes' Density (%) of the samples
- 133 Figure 4.9 - A graph showing the effect of Volumetric Energy Density ( $\text{Jmm}^{-3}$ ) on the Archimedes' Density (%) of the samples with varying laser scan spacings
- 134 Figure 4.10 - A graph showing the effect of specific enthalpy on the Archimedes' Density (%) of the samples
- 137 Figure 4.11 - A graph showing the effect of Normalised Energy Density on the Archimedes' Density (%) of the samples
- 141 Figure 4.12 - A graph showing the effect of Linear Energy Density ( $\text{Jmm}^{-1}$ ) on the melt pool width ( $\mu\text{m}$ ) of the single scan tracks
- 141 Figure 4.13 - A graph showing the effect of the ratio of laser power to the square root of laser scan speed ( $\text{Js}^{-1/2}\text{mm}^{-1/2}$ ) on the melt pool width ( $\mu\text{m}$ ) of the single scan tracks
- 142 Figure 4.14 - SE micrographs of single scan laser tracks at a higher, medium and lower energy input
- 143 Figure 4.15 - SE micrograph showing centreline cracking in single scan track produced with Parameter A
- 144 Figure 4.16 - Schematic illustrating the morphology and possible cause associated with solidification cracking.
- 145 Figure 4.17 - SE micrographs of single scan laser tracks produced at varying powers (400 W (top left), 300 W (top right) and 200 W (bottom)) with a laser scan speed of  $250 \text{ mms}^{-1}$
- 147 Figure 4.18 - SE micrographs of single scan laser tracks produced at varying scan speeds ( $250 \text{ mms}^{-1}$ ,  $675 \text{ mms}^{-1}$ , and  $1500 \text{ mms}^{-1}$ ) with a laser power of 300 W
- 150 Figure 4.19 - Optical micrographs showing the variation in cracking and grain structure through the build height of the deposit
- 151 Figure 4.20 - Typical cracking in tungsten after thermal shock
- 152 Figure 4.21 - BSE micrograph showing cracking pattern found in LPBF tungsten samples
- 153 Figure 4.22 - Band contrast image showing laser scan track and cracking in LPBF tungsten sample
- 153 Figure 4.23 - EDX map of oxygen distribution in LPBF tungsten sample
- 154 Figure 4.24 - Typical welding microstructures with varying scan speeds (low (top), intermediate (middle), high (bottom)).
- 155 Figure 4.25 - EBSD map of LPBF tungsten sample (IPF Z colouring)
- 156 Figure 4.26 - XRD pattern of LPBF W, conventional W and W powder samples
- 157 Figure 4.27 - Low magnification BSE micrograph of LPBF tungsten fracture surface (XZ section)
- 158 Figure 4.28 - XY shift of 'islands' in the chess scan strategy
- 158 Figure 4.29 - Optical micrograph of LPBF tungsten showing the  $1\text{mm}^2$  interference pattern due to 'island' shift
- 159 Figure 4.30 - BSE micrograph of LPBF tungsten fracture surface (XY section)

- 160 Figure 4.31 - Load/ Displacement curves for LPBF tungsten samples tested at RT,  
400 °C and 600 °C
- 161 Figure 4.32 - Load/ Displacement curves for conventional tungsten and LPBF  
tungsten samples tested at 600 °C
- 162 Figure 4.33 - SE micrograph showing the characteristic star cracking pattern of a  
brittle small punch sample (LPBF tungsten tested at RT)
- 162 Figure 4.34 - SE micrographs showing a fractured small punch specimen from  
LPBF tungsten tested at 600 °C
- 163 Figure 4.35 - SE micrograph showing a fractured small punch specimen from  
conventional tungsten tested at 600 °C
- 165 Figure 4.36 - SE micrograph of ion milled craters (left) and a SIMS maps showing  
16O in tungsten showing grain boundary segregation
- 167 Figure 4.37 - Variation of sample density as a function of AED with points for the  
PS-B, CR-B and PS-C and CR-C circled
- 169 Figure 4.38 - Optical micrographs showing i) CR-B and ii) PS-B (optimised build  
parameters for plasma spheroidised powder) and iii) CR-C and iv) PS-C  
(optimised build parameters for chemically reduced powder)
- 170 Figure 4.39 - Micrographs of (a) the plasma spheroidised powder from LPW  
Technology and (b) the chemically reduced powder from H.C. Starck
- 171 Figure 4.40 - Micrograph of section through the substrate plate and deposit  
produced using plasma spheroidised powder and the measured depth of the fusion  
zone at the corresponding position on the sample
- 172 Figure 4.41 - Micrograph of section through the substrate plate and deposit  
produced using chemically reduced powder and the measured depth of the fusion  
zone at the corresponding position on the sample
- 173 Figure 4.42 - Optical micrographs showing variation in penetration depth around  
areas of defects in a) plasma spheroidised powder and b) chemically reduced  
powder
- 174 Figure 4.43 – Schematic diagram of scanning strategy and overlap
- 177 Figure 4.44 - Micrographs of (a) the plasma spheroidised powder from LPW  
Technology and (b) the chemically reduced powder from H.C. Starck
- 178 Figure 4.45 - Comparison of morphologies of the two tungsten powders
- 179 Figure 4.46 - Graph to show the size distribution of the plasma spheroidised and  
chemically reduced powders as determined by LPSD
- 187 Figure 5.1 - A graph showing the base plate temperature with time for the pre-  
scan and control samples
- 187 Figure 5.2 - A graph showing the temperature across the base plate for the control  
sample
- 188 Figure 5.3 - A graph showing the temperature across the base plate for the pre-  
scan sample
- 188 Figure 5.4 – Approximate location of thermocouples on the base plate for control  
and pre-scan samples (plate edge – 30 mm)
- 191 Figure 5.5 - A graph and micrograph showing the penetration depth of the fusion  
zone across the pre-scanned sample
- 191 Figure 5.6 - A graph and micrograph showing the penetration depth of the fusion  
zone across the control sample
- 193 Figure 5.7 - Schematic of the heated bed module with (from top) plate loading  
clips, tungsten build plate (blue), heating plate (grey) with cartridge heaters (red),  
ceramic insert to limit heat losses (yellow) and attachments to Concept Laser M2  
reduced build volume module

- 194 Figure 5.8 - A graph showing the temperature of the heated bed with time for the 600 °C preheat
- 195 Figure 5.9 - Photographs showing a) the oxide formed during temperature stabilisation at 600 °C and b) laser ablation of the oxide
- 197 Figure 5.10 - SE Micrographs showing single scan tracks with room temperature, 400 °C and 600 °C base plates (L to R) with 300 W, 750 mm/s (top) and 300 W, 1000 mm/s (bottom)
- 199 Figure 5.11 - Completed builds produced with bed heating of 400 °C (left) and 600 °C (right)
- 201 Figure 5.12 - Optical micrograph of XY mid-plane section of sample produced with 400 °C bed heating showing inhomogeneous cracking across the surface
- 202 Figure 5.13 - Optical micrograph of XY bottom section of sample produced with 400 °C bed heating showing inhomogeneous cracking across the surface
- 203 Figure 5.14 - Optical micrograph of XY top section of sample produced with 400 °C bed heating showing inhomogeneous cracking across the surface
- 203 Figure 5.15 - Optical micrographs within the region of lower crack density (left) the region of higher crack density (right)
- 205 Figure 5.16 - Schematic showing oxygen contents of various samples across the build plate. All samples were produced with 400 W power
- 207 Figure 5.17 - EBSD map of LPBF tungsten sample produced with bed heating (IPF Z colouring)
- 207 Figure 5.18 - EBSD map of LPBF tungsten sample produced without bed heating (IPF Z colouring)
- 208 Figure 5.19 - A graph and micrograph showing the penetration depth of the fusion zone across the 400 °C heated bed sample
- 209 Figure 5.20 - A graph and micrograph showing the penetration depth of the fusion zone across the 600 °C heated bed sample
- 211 Figure 5.21 - Graph to show the size distribution of the plasma spheroidized tungsten and tantalum elemental powders as determined by LPSD
- 212 Figure 5.22 - BSE Micrograph of the blended elemental tungsten and tantalum powders
- 212 Figure 5.23 - An EDX map of the blended powder with tungsten (red) and tantalum (green)
- 213 Figure 5.24 - BSE micrograph showing tantalum satellite powders in surface depressions in the tungsten powder particle
- 214 Figure 5.25 - XRD Pattern of the elemental tungsten powder and the blended tungsten-tantalum powder
- 215 Figure 5.26 - A graph to show the variation in Archimedes' density with Area Energy Density for LPBF tungsten and tungsten-tantalum alloy samples
- 216 Figure 5.27 - BSE micrographs showing cracking in tungsten (left) and tungsten-tantalum alloy (right)
- 217 Figure 5.28 - BSE Micrograph showing fine cracking around a tungsten-rich region of material
- 219 Figure 5.29 - SE micrograph of an ion milled crater and a SIMS map showing 16O in tungsten (top) and a SE micrograph of an ion milled crater and a SIMS map showing 16O in tungsten-tantalum (bottom)
- 220 Figure 5.30 - XRD pattern of the LPBF W and LPBF W-Ta samples
- 222 Figure 5.31 - Raman spectra of the tungsten sample (blue) and tungsten-tantalum sample (red) along with reference vibrations for tungsten and tantalum oxides

- 224 Figure 5.32 - A graph and micrograph showing the penetration depth of the fusion  
zone across the tungsten-tantalum sample produced with 400 °C bed heating
- 225 Figure 5.33 - Optical micrograph showing the XY section of the tungsten-  
tantalum alloy produced with bed heating of 400 °C
- 226 Figure 5.34 - Load/ Displacement curves for LPBF tungsten samples produced  
without bed pre-heating (RT) and LPBF tungsten-tantalum samples produced with  
(HB) and without (RT) bed heating tested at 600 °C
- 228 Figure 5.35 - SE micrographs showing the fractured small punch specimens from  
LPBF tungsten-tantalum (left) and LPBF tungsten (right) tested at 600 °C
- 229 Figure 5.36 - SE fractograph of LPBF tungsten-tantalum alloy tested at 600 °C
- 230 Figure 5.37 - Load/ Displacement curves for conventional tungsten, LPBF  
tungsten samples produced without bed pre-heating (RT) and LPBF tungsten-  
tantalum samples produced with (HB) and without (RT) bed heating tested at  
600 °C
- 231 Figure 5.38 - SE micrographs showing the fractured small punch specimens from  
conventional tungsten tested at 600 °C
- 232 Figure 5.39 - Brazing cap produced via LPBF using heated bed and the tungsten-  
tantalum alloy
- 233 Figure 5.40 - Conventional divertor monoblock produced with via LPBF with the  
tungsten-tantalum alloy and bed heating after vibro-polishing (left) and shaded  
CAD image of the design (right)
- 234 Figure 5.41 – Wireframe CAD models of the novel rear-fed divertor monoblock  
(top) and the component produced with via LPBF with the tungsten-tantalum  
alloy and bed heating after grit blasting (left).
- 252 Figure A.1 - Photograph of Concept Laser M2 with powder handling chamber  
(left) located in M&M UoB
- 253 Figure A.2 – Schematic diagram of the Concept Laser M2 machine technology  
module with build and powder platforms
- 253 Figure A.3 - Cross sections of the soft (left) and hard (right) recoater blades of the  
Concept Laser M2
- 254 Figure A.4 - Concept Laser M2 recoater assembly
- 255 Figure A.5 – Schematic diagram of the reduced size build plate with tungsten  
plate attached
- 256 Figure A.6 - Schematic diagram showing chess (left) and continuous (right) laser  
scan strategies
- 257 Figure A.7 – Graph showing the oxygen content of the technology module during  
a tungsten build
- 258 Figure A.8 – Laser profiling set up with Spiricon camera (top) and Ophir thermal  
power laser sensor (bottom)
- 259 Figure A.9 – Laser profile of beam at nominal power of 300 W
- 260 Figure A.10 – Laser profile of beam focussed with damaged F-theta lens at  
nominal power of 300 W
- 261 Figure A.11 – Photograph (left) showing thermocouples connected to a data  
logger and a photograph (right) of thermocouples attached to a build plate with  
insulating plate in place.
- 263 Figure A.12 - Schematic of the heated bed module with (from top) plate loading  
clips, tungsten build plate (blue), heating plate (grey) with cartridge heaters (red),  
ceramic insert to limit heat losses (yellow) and attachments to Concept Laser M2  
reduced build volume module.

## List of Tables

<b>Page</b>	<b>Caption</b>
16	Table 1.1 - Table detailing the advantages and disadvantages of LPBF
23	Table 2.1 - Table detailing atomic and electronic structure of the refractory metals
24	Table 2.2 - Table detailing key thermal and mechanical properties of the refractory metals
24	Table 2.3 - Table showing DBTTs for the refractory metals
29	Table 2.4 - Maximum possible concentration (ppm) of interstitials in refractory metals after moderate cooling rate
46	Table 2.5 - Table detailing the advantages and disadvantages of microstructural test techniques
47	Table 2.6 - Table detailing the advantages and disadvantages of the mechanical test techniques
48	Table 2.7 - Table detailing advantages and disadvantages of chemical analysis techniques
58	Table 2.8 - Table showing the papers reviewed utilising each energy density relationship
65	Table 2.9 - Summary of Reported Laser Absorptivity Values
86	Table 3.1 - Powder batch details as supplied by the manufacturer
87	Table 3.2 - Nominal composition of powders as supplied by the manufacturers
88	Table 3.3 - Nominal composition of the plate material as supplied by the manufacturer
92	Table 3.4 - Table showing the thresholds for flowability
95	Table 3.5 - Summary of LPBF process variables in the different studies presented
97	Table 3.6 - Table detailing parameter codes and parameters for the powder morphology study
106	Table 3.7 - Table showing details of the SEMs and the corresponding studies which utilised them
119	Table 4.1 - Nominal composition of powders as supplied by the manufacturers
120	Table 4.2 - Table showing the process parameters from the initial stage of parameter development
124	Table 4.3 - Table showing the process parameters from the second stage of parameter development
125	Table 4.4 - Table showing the process parameters from the final stage of parameter development
129	Table 4.5 - Table showing the process parameters, Volumetric Energy Density and sample density from the energy density model validation study
136	Table 4.6 - Table showing effect of laser power (W) on laser beam diameter ( $\mu\text{m}$ )
140	Table 4.7 - Table showing laser process parameters for single scan tracks
146	Table 4.8 - Table showing effect of laser power (W) on melt pool width ( $\mu\text{m}$ ) of single scan tracks
148	Table 4.9 - Table showing effect of laser power (W) on melt pool width ( $\mu\text{m}$ ) of single scan tracks
170	Table 4.10 - Comparison of tungsten powders following characterisation
200	Table 5.1 - Table showing Archimedes' density with different bed heating temperatures and processing parameters
213	Table 5.2 - Composition of the blended powder as determined by EDX

- 232 Table 5.3 – Table showing the leak testing results for the brazing caps and conventional monoblock designs produced with heated bed LPBF tungsten-tantalum
- 259 Table A.1 – Table showing actual power and laser beam diameter for nominal powers measured on the Concept Laser M2 machine



# CHAPTER 1 – INTRODUCTION

## 1.1 A Brief Introduction to Nuclear Fusion

Nuclear fusion has the potential to be a source of large quantities of sustainable, low carbon energy, providing energy security to countries without reserves of fossil fuels (1). It is estimated that upon industrialisation of the technology as much as 30 % of electricity requirements coming from fusion technologies (2). There are a number of potential advantages to nuclear fusion but there are also significant challenges to overcome in order to realise nuclear fusion as a method for energy production.

The main advantages of nuclear fusion are:

- Safety

Of the two isotopes most commonly required for nuclear fusion, only one, tritium, is radioactive. There are only milligrams of fuel in the reactor at any given time and the difficulties of maintaining the plasma and conditions for fusion to occur, mean that in accidental conditions the plasma would cool, and the reactions would stop unlike in nuclear fission where runaway reactions could occur (3-5).

- Energy Production

The amount of energy released for a given mass of fuel is almost 4,000,000 times greater for the nuclear fusion reaction than the burning of coal and 4 times greater than that of the nuclear fission reaction (3-5).

- Fuel Prevalence

The two isotopes required for nuclear fusion are easily extracted from relatively abundant sources. Tritium can be bred from lithium using the neutrons produced from the fusion reactions. Lithium itself is present in both the earth's crust and seawater.

The earth's crust has reserves sufficient for 1000 years of fusion power, but with around 230 billion tonnes of lithium contained in sea water, supplies are sufficient for millions of years. Deuterium can also be extracted from sea water and supplies are similarly abundant (3-5).

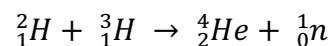
- Environmental Considerations

The products of a fusion reaction are helium and a neutron. The neutrons can be used to breed more tritium fuel and helium is an inert gas which does not contribute to atmospheric pollution or global warming (3-5). While neutron bombardment can cause irradiation of plant material, the utilisation of low activation materials (LAMs) could prevent the need for longer term waste storage (6-8).

- Waste management

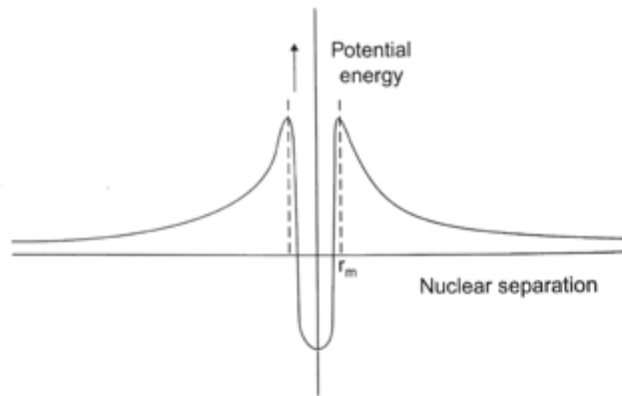
Tritium has a half-life of 12.3 years and is the only radio-active fuel used in nuclear fusion. Using Low Activation Materials in the reactor plant means radioactivity levels would meet the threshold for complex recycling and would not require long term nuclear waste storage (3-5).

The basic principle of fusion involves fusing light elements together. For energy generation, the most researched reaction is the combination of isotopes of hydrogen, deuterium and tritium, to combine to form helium, and a neutron:



This is an exothermic process and the heat produced can be used to produce steam, to run steam turbines in order to convert the heat into electricity (1).

However, the reagents must move close enough to overcome the repulsive force from the two positively charged nuclei. Once close enough, the nuclear attraction draws the nuclei together and allows them to fuse (see Figure 1.1).



*Figure 1.1 - A schematic showing the variation in potential energy of two nuclei with their relative separation. Taken from McCracken and Stott, 2013 (1)*

Herein lies the major challenge to the realisation of fusion, in order to overcome this electrostatic force, the nuclei must have significant energy. This energy generally comes from forming the nuclear fuels in a high temperature plasma (180 – 200 million °C) (1).

The main difficulties associated with nuclear fusion are (9):

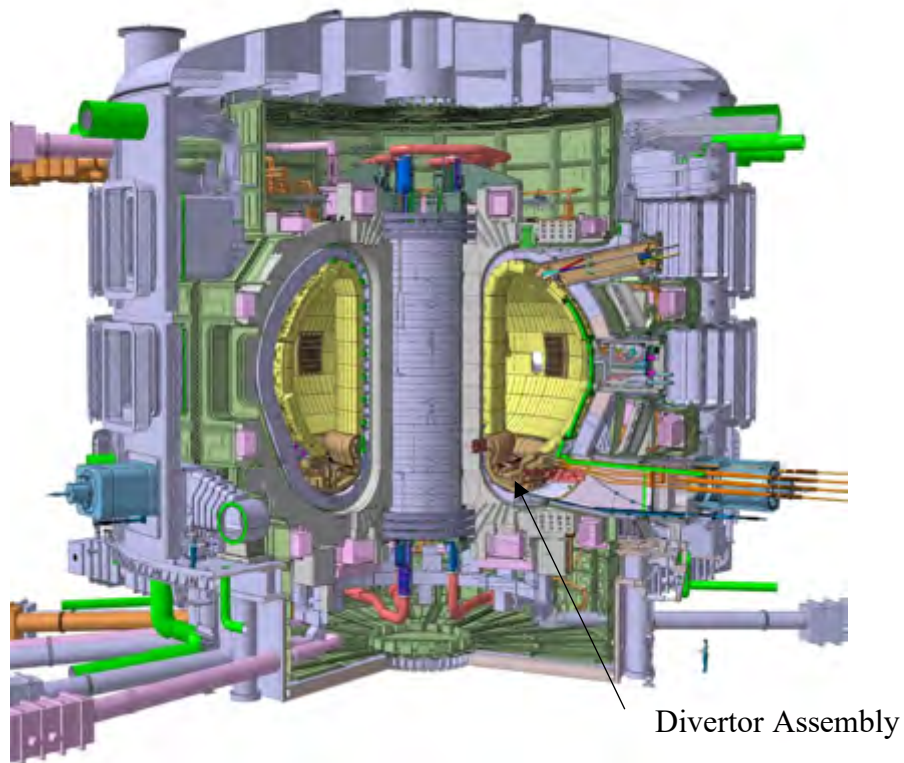
- Maintaining plasma temperatures
- Maintaining plasma confinement
- Plasma facing material environment
- Tritium concerns

As has previously been mentioned, tritium is a radioactive hydrogen isotope. The principle concern is safe handling of radioactive material. There are also concerns with the use of tritium as there is a potential to contaminate water supplies. However, fusion reactors will operate on a closed loop system whereby the tritium will be bred and used in the reactor and

strict limits would be in place on the allowed tritium inventory in order to mitigate this risk. Further information on tritium concerns can be found elsewhere (10).

A significant amount of energy is required to maintain the high temperature plasma. Due to the extreme temperatures no materials can be used to confine the plasmas instead superconducting magnets are most commonly used to generate a strong magnetic field which confines the plasma. These need to be cooled with liquid helium in order to maintain superconductivity, another energy intensive process. Despite the magnetic confinement system, the temperatures at the Plasma Facing Components (PFCs) will still be around 2000 °C with significant radiation damage. Few materials are capable of withstanding this environment, and the lifetime of the components will be limited. Given the potential to produce large quantities of energy (1 g of deuterium has the potential to produce 300 GJ of electricity), there would be a net energy output despite the energy demands of the reactor. The material concerns for PFCs remain one of the bigger challenges associated with nuclear fusion (1, 11).

Recent fusion efforts have focussed on reactors with a Tokamak design, including JET (Joint European Torus) in Oxfordshire, UK and ITER in Caderache, France. A schematic representation of the reactor at ITER can be seen in Figure 1.2. The divertor assembly can be seen at the bottom of the vacuum vessel as indicated (1).



*Figure 1.2 - Schematic showing the ITER experimental fusion reactor with divertor assembly labelled. Taken from McCracken and Stott, 2013 (1)*

The main functions of the divertor are to manage the energy fluxes of the plasma and to minimise the impurity content including particulates from sputtering, and helium ash (a term for the  $\alpha$  particles produced from the fusion reaction and unburnt fuel on the divertor), as these radiate energy causing the plasma to cool. This can be done by altering the magnetic

confinement at the edge of the reactor, allowing the heavier ions which are less well contained than the main plasma, to be removed (1, 12).

The ITER divertor assembly is made up of 54 cassettes which contain a series of monoblocks that form the target plates for the conversion of the kinetic energy of the plasma ions to heat. The current monoblock design is made of tungsten, with a coolant channel running through for energy extraction (around 12 mm in size). Figure 1.3 shows representations of the cassette and monoblock (12-14) . The current divertor monoblock design is limited by the capabilities of manufacturing tungsten. The difficulties associated with its processing are a result of its high melting point and intrinsic brittleness (Ductile-Brittle Transition Temperature (DBTT)  $\sim 400$  °C (15)). Conventionally, powder metallurgy methods including sintering have been used, but as final machining is challenging, the complexity of component geometries has been limited (16). The simple shape of the divertor monoblock is largely dictated by manufacturing issues. As a result, novel manufacturing techniques for tungsten for these components are of interest to increase the potential geometric and design complexity.

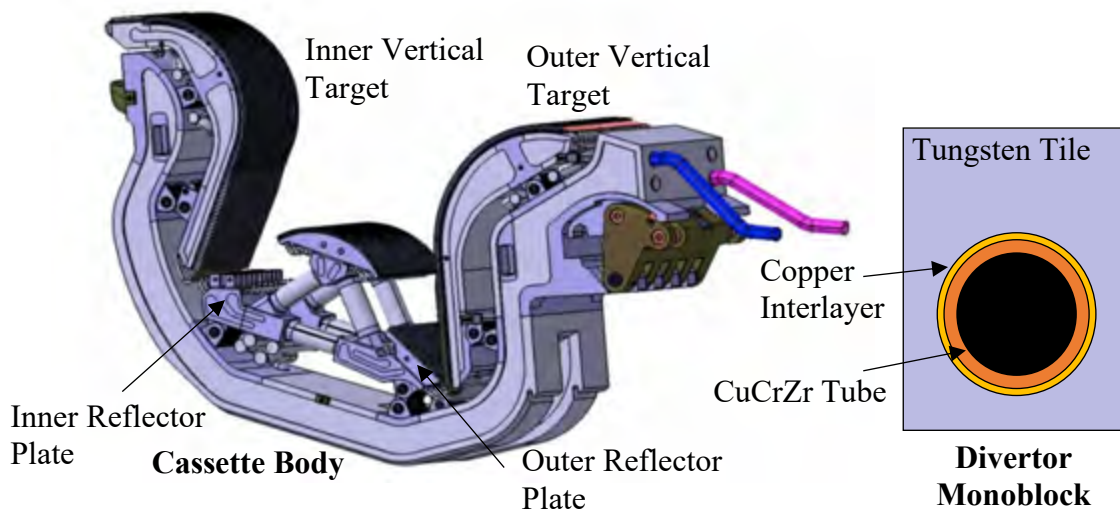


Figure 1.3 - Schematic of the divertor cassette and monoblock. Taken from Hirai et al., 2016 (13)

## 1.2 Material Requirements for the Divertor Assembly

Few environments are as challenging as that of the divertor assembly within a nuclear fusion reactor; it combines temperature and irradiation dose at levels significantly higher than that of a fission reactor. Standard operating temperatures for a commercial fusion reactor would be around 2000 °C in comparison to 300-350 °C for a fission reactor; not only are absolute temperatures higher, heat flux through the materials will also be significantly higher (10 MW/m<sup>2</sup> vs. 1 MW/m<sup>2</sup> for fusion and fission reactors respectively) (13, 17). While the divertor materials in the experimental fusion reactor, ITER, will only experience a damage of 1-2 dpa, a commercial fusion reactor under continuous operation would cause between 150 and 200 dpa damage in the plant materials. Current Gen II fission reactor materials experience damage of up to 50 dpa (17).

In addition, the fuel used which is a mix of deuterium and tritium (both isotopes of hydrogen) can have an embrittling effect on susceptible materials including vanadium alloys and the structural steels used (18). Materials such as tantalum and vanadium with a high solubility of hydrogen would also cause tritium retention making the process less efficient (19). These are less of a problem for tungsten and other Group VI metals as they have very low hydrogen solubility meaning neither retention nor embrittlement will be significant. Indeed, Tietz and Wilson, 1965 and Wilkinson, 1969 showed that there was not a detectible level of solubility of hydrogen in tungsten (20, 21).

Erosion and sputtering of the divertor materials are caused by the impact of 'helium ash'. Other impurity elements present in the plasma including oxygen and carbon ions can also cause sputtering (19, 22).

All candidate materials must pass the basic thresholds of being able to operate in a high temperature, high irradiation environment as well as exhibiting low tritium retention and low sputtering to ensure process efficiency as well as increasing components' lifetime. In addition to this, various more specific requirements are imposed for safety reasons by the regulatory bodies or to ensure process efficiency. For example, materials must have good resistance to sputtering and ideally a low atomic number to prevent excess plasma cooling (23, 24).

### **1.2.1 Activation Limits**

Low activation materials (LAMs) have been an area of research in fusion for several decades (23, 25), as they offer several key benefits; long-term waste storage would not be required, it increases the viability of recycling plant material, increases the viability of robotic maintenance during short periods of reactor shutdown and would prevent long-term site contamination in the event of a serious accident condition. These would effectively combat the main disadvantages of nuclear fission. It is proposed that a time limit would be imposed, typically 50-100 years after which the activity of the material will have fallen to levels which permit complex recycling or shallow burial of the component (6, 7, 23) This is possible because tritium is the only radioactive isotope used as a fuel within a fusion reactor and this has a half-life of 12.3 years, in comparison to the half-life of  $U^{235}$ , the dominant isotope used in fission reactors which has a half-life of 700,000,000 years (8, 26). However, in addition to the fuels, the activation of plant material must also be considered. There are serious challenges associated with LAMs including the activity of transmutation products and impurity elements within the material (22). Figure 1.4 shows the time evolution of  $\gamma$  dose rate ( $Sv.h^{-1}$ ) for tungsten if it were used in various locations within DEMO. DEMO is the next stage of nuclear fusion development after ITER and is designed as a prototype reactor (27).



The  $10\text{mSv}\cdot\text{h}^{-1}$  is the activity level suitable for material recycling after 50 years suggested by the low activation limits (6-8, 22), suggesting the suitability of the tungsten as a PFC material within a fusion reactor.

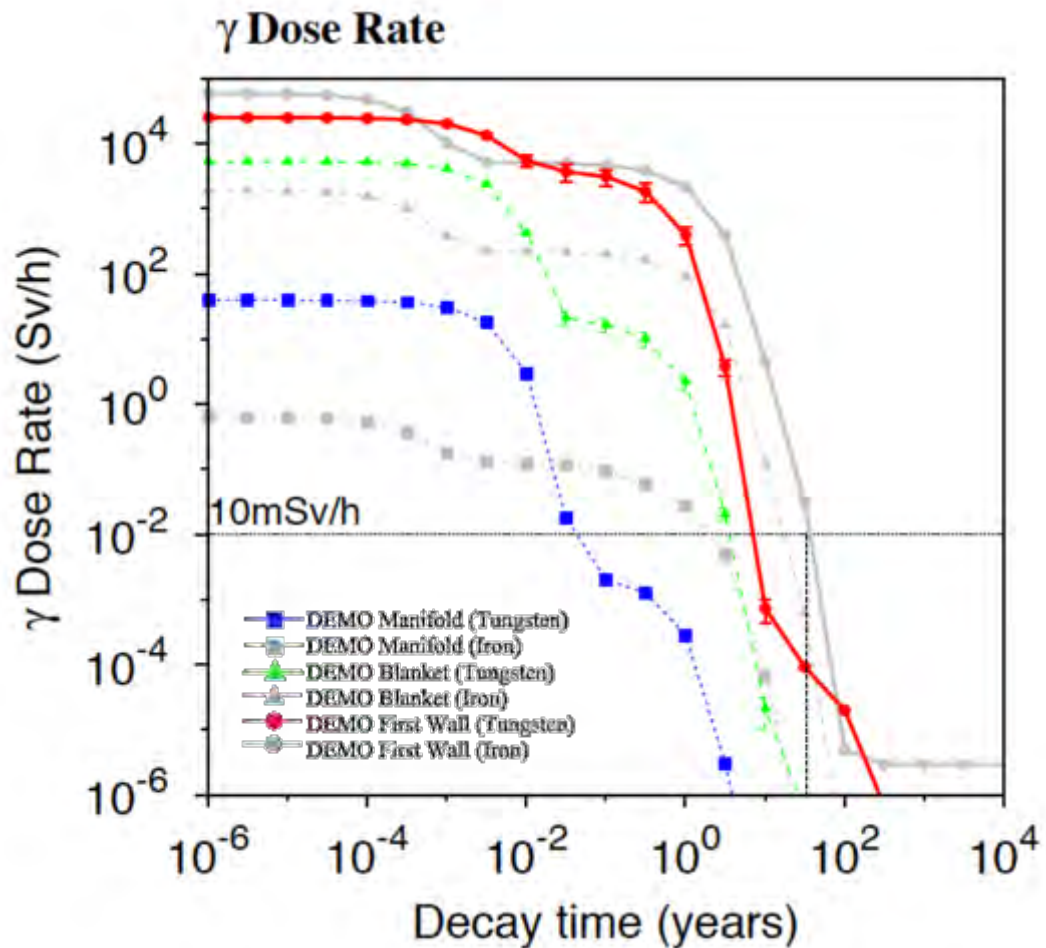


Figure 1.4 - Time evolution of gamma dose rate for tungsten in three DEMO fusion reactor scenarios: First Wall (red), Blanket (green) and Manifold (blue) along with the corresponding results for iron in the three scenarios (grey). Taken from Gilbert et al., 2015 (8)

However, the exact limit and time frame desired varies (6-8, 22, 23); Figure 1.5 is a representation of elements as either high, medium or low activation materials (28). As can be seen, a fairly limited range of materials are considered to be low activation, particularly in the transition metals which are of the most interest for structural and plasma facing components. Vanadium and manganese do not meet the required thermal properties (expanded in section 1.2.2) and neither the thermal nor mechanical properties of chromium make it attractive for

fusion requirements (20). A necessary compromise might therefore have to involve the inclusion of medium activation materials and extend the timeframes discussed, to ensure cost and availability of plant material.

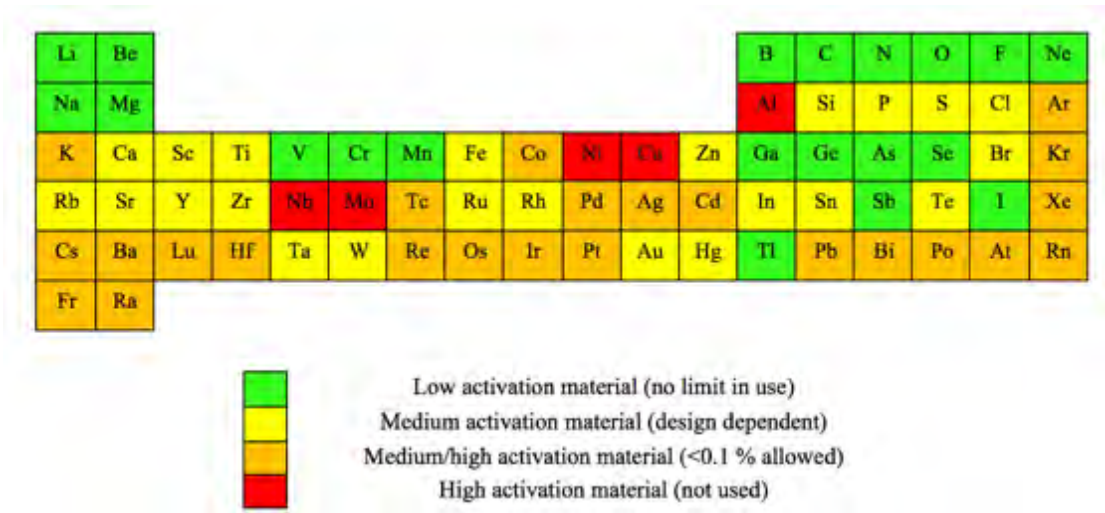


Figure 1.5 - Classification of material activation for fusion. Adapted from SWIP, n.d. (28)

Additionally, materials such as tungsten are borderline to meeting threshold requirements but are currently used extensively as it is one of few materials to meet the other requirements (such as operating temperature) for Plasma Facing Components (PFCs) (6-8, 22). Potential mitigation methods include ensuring extremely low levels of tramp elements and isotopically tailoring material to remove long lived radioisotopes and those which would transmute to those isotopes (6, 7, 23). However, this would significantly increase the cost of the material especially when such large quantities are needed. Smirnov, et al., 2015 (29) estimated that in order to isotopically separate molybdenum, limiting the material to Mo<sup>92</sup>, Mo<sup>98</sup> and Mo<sup>100</sup>, the isotopes with the lowest neutron cross-section, would cost \$1000-8000/kg in comparison to high purity molybdenum from PLANSEE which can be purchased for \$100-200/kg depending on physical form and finish. While these costs may decrease with the economies of

scale required for a power plant, it is unlikely to be feasible for the production large structural components (29, 30).

### 1.2.2 Thermal Property Thresholds

In order for a material to survive the required environment, it must have a sufficiently high service temperature and be able to handle the high heat fluxes associated. Maximum service temperature is associated with the melting point ( $T_m$ ) of a material. In order to efficiently transfer heat away from the plasma facing surface, high thermal conductivity ( $\kappa$ ) is also needed. This, along with the erosion suffered from particulate bombardment, limits the ability to use surface coatings such as a thermal barrier coating. The coefficient of thermal expansion ( $\alpha$ ) should also be minimised in order to prevent adjacent monoblocks expanding and inducing stress or damage into its neighbouring component.

Thus, a merit index was formed, maximising  $T_m$  and  $\kappa$  while minimising  $\alpha$ , in order to assess the relative thermal properties of plasma facing materials in the divertor assembly:

$$\frac{T_m \cdot \kappa}{\alpha} \quad (\text{Equation 1.1})$$

$T_m$  – melting point (K)

$\kappa$  - thermal conductivity ( $\text{Wm}^{-1}\text{K}^{-1}$ )

$\alpha$  - coefficient of thermal expansion ( $\text{K}^{-1}$ )

Using the merit index above, a graph comparing all the transition metals can be seen in Figure 1.6. The refractory metals, which are of particular interest, are highlighted in red. As can be

seen tungsten and molybdenum are the optimal materials from this index. Tungsten particularly, has a merit index value 40 % higher than the next best alternative.

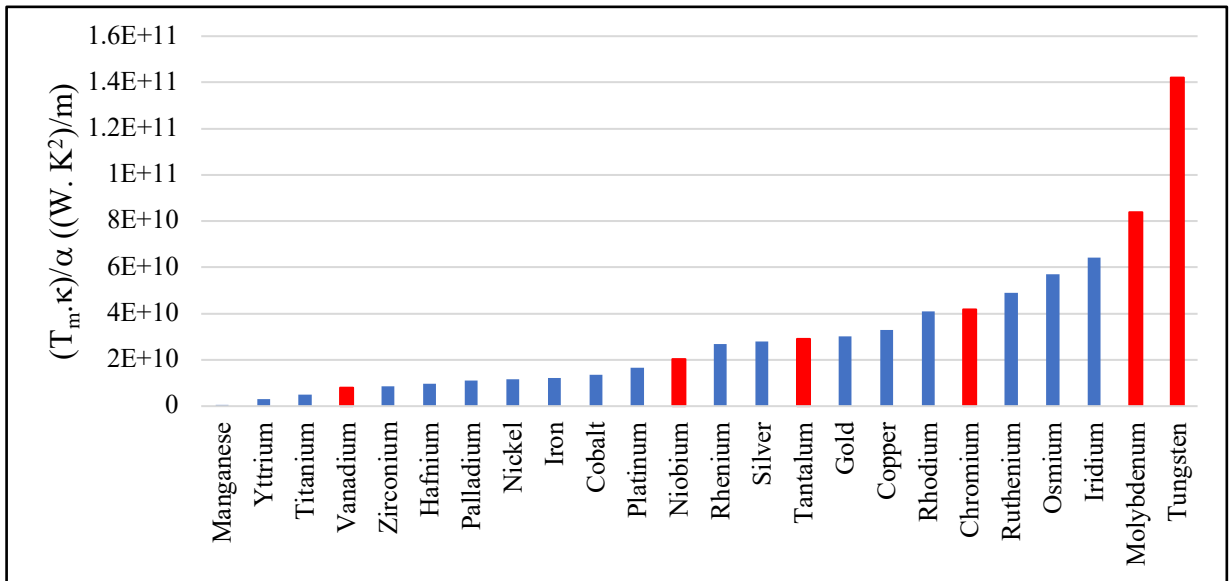


Figure 1.6 - Graph showing the transition metals ranked as a function of a merit index,  $(T_m \cdot \kappa) / \alpha$ . Data taken from Element Data Function, Wolfram Research, 2014 (31)

Additionally, in Figure 1.7 showing materials as a function of strength and service temperature, W-alloys are in the extreme of the graph pertaining to both high fracture strength ( $\sigma_f$ ) and maximum service temperature  $T_{max}$  and only outperformed by ceramic materials which would not be suitable because of their low thermal conductivity.

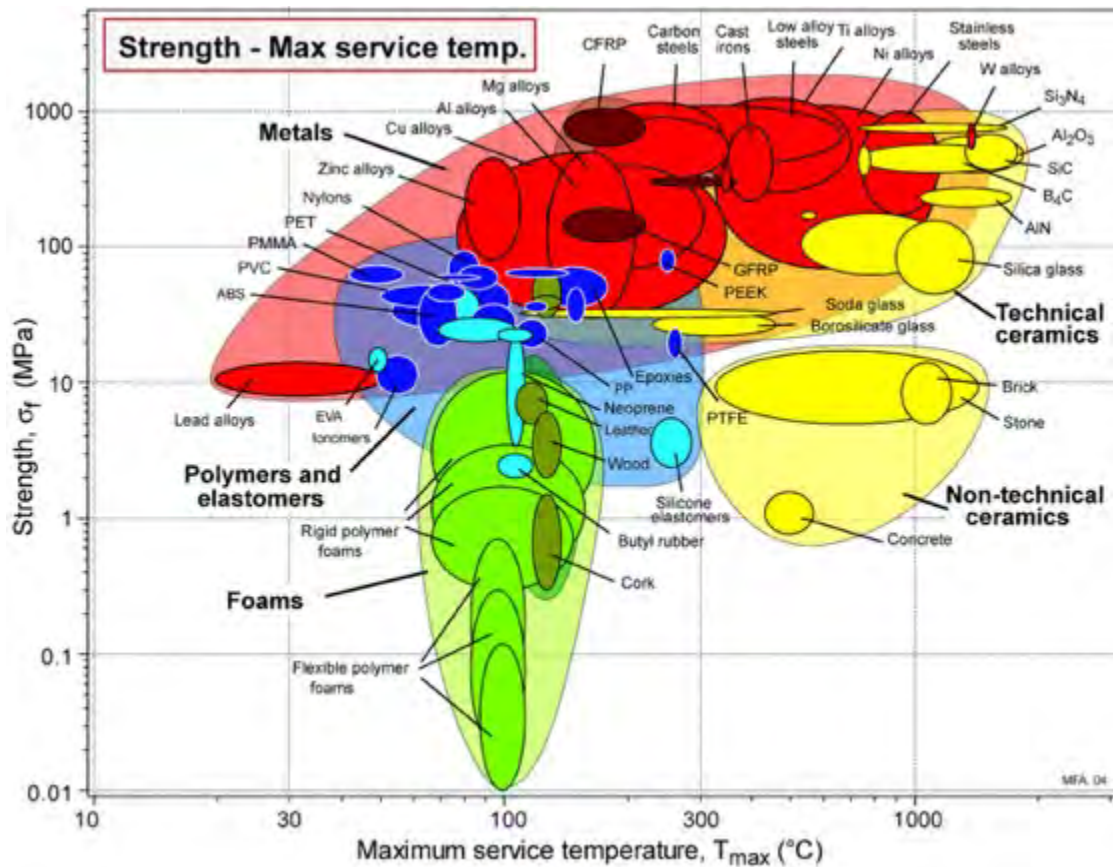


Figure 1.7 - Graph showing fracture strength as a function of maximum service temperature. Taken from Granta Design CES Edupack, 2005 (32)

From the material requirements detailed here along with the material properties discussed, the metallurgical focus of this review will be on refractory metals, particularly tungsten and its alloys, due to their high service temperature and high strength at temperature.

### 1.3 A Brief Introduction to Laser Powderbed Fusion (LPBF)

Laser Powderbed Fusion (LPBF) is a netshape, additive manufacturing (AM) technique capable of producing complex internal geometries in a diverse range of materials from powder based raw materials. In this technique, the use and burnout of a binder is not required.

The basic stages of production via LPBF are:

- A 3D CAD model is produced.
- The CAD file sliced into a series of 2D representations of a given thickness, known as an STL file
- A thin layer of powder is deposited onto the build plate.
- The laser uses the data from the 2D STL layer file to melt the powder material to the build plate.
- The build plate moves down by the known layer thickness.
- Further powder is deposited and melted building the final component in a layer-by-layer construction.

A schematic representation of an LPBF system available at the University of Birmingham is shown in Figure 1.8.

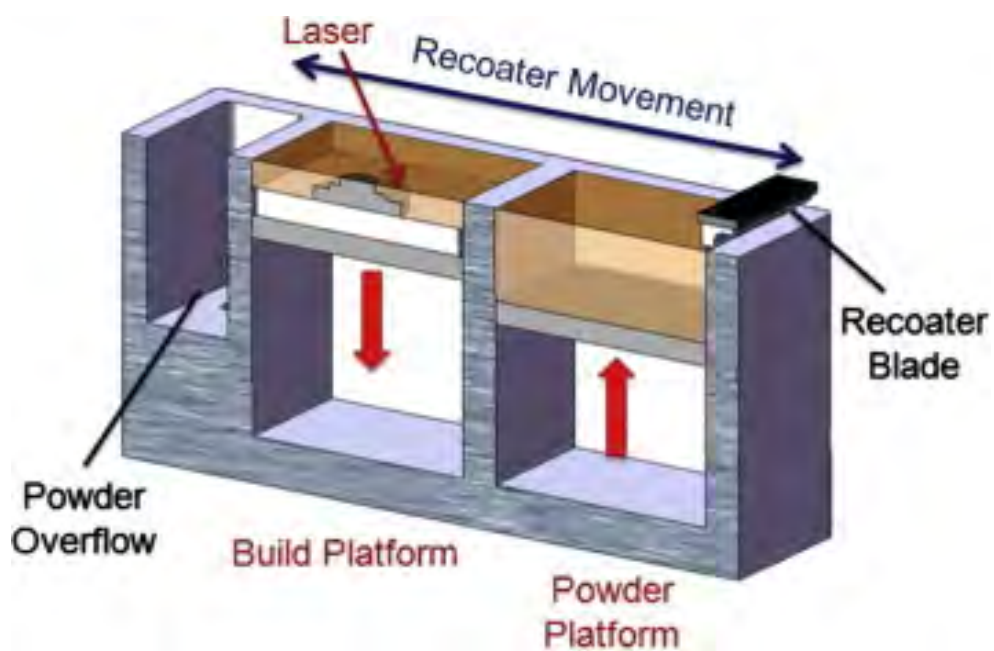


Figure 1.8 - Schematic cross-section of the Concept Laser M2 powder-bed system. Taken from Carter et al., 2014 (33)

There are a number of advantages to LPBF particularly when discussing the production of low volume, high value components, but there are also a number of disadvantages. Some of the disadvantages come from the infancy of the technique and are likely to be improved in subsequent machine iterations. The advantages and disadvantages of LPBF are listed in Table 1.1.

*Table 1.1 - Table detailing the advantages and disadvantages of LPBF*

<b>Advantages</b>	<b>Disadvantages</b>
Ability to produce complex geometries including internal structures	Low deposition rates leading to long processing times and limiting size and batch volume viable
Manufacturing freedom can lead to weight and design optimisation	Machine specific limitations including build volume and environment
The need for tooling is eliminated meaning set-up costs for low volume batches or prototypes are reduced	Technology is in its infancy, so process and supply chain must be optimised for each material and methods to assess build quality and improve part reliability must be developed
Reduction in lead time allowing for greater number of design iterations and prototype testing	Geometries limited by microstructure and properties required in terms of build orientation, support structures and post-processing required
Reduction in material waste as melted material forms part of the netshape component, and unmelted powder can be reused.	High capital investment for machinery (~£1,000,000) with facility costs increasing due to enhancements in capability

LPBF is of interest for plasma facing components as the high-power laser allows for liquid state processing of tungsten and other high melting point materials unlike other conventionally used powder metallurgy techniques e.g. sintering, allowing for in-situ



alloying. LPBF also allowed for greater complexity in part geometry, given the difficulties in tungsten machining, as it is a net-shape manufacturing technique. It also offered the potential for in-situ alloying through powder blending. A feasibility study into LPBF processing of tungsten is therefore of interest to the nuclear fusion community. Greater review of refractory metals including tungsten and its inherent fabrication challenges will be conducted in the literature review of this thesis showing the key difficulties associated with realising the LPBF processing of tungsten.

## 1.4 References

1. McCracken G, Stott P. Fusion: The Energy of the Universe. 2nd ed. Oxford: Elsevier; 2013.
2. Romanelli F, Barabaschi P, Borba D, Federici G, Horton L, Neu R, Stork D, and Zohm H. Fusion Electricity: A roadmap to the realisation of fusion energy. Culham: EFDA; 2012.
3. ITER. Advantages of Fusion Caderache, France2019 [Available from: <https://www.iter.org/sci/Fusion>.
4. CCFE. Fusion - A Clean Future. Abingdon, Oxfordshire: Culham Centre for Fusion Energy; 2016. Contract No.: CPS16.49.
5. EUROfusion. Fusion vs Fission Caderache, France2019 [Available from: <https://www.euro-fusion.org/fusion/fusion-vs-fission/>.
6. Doran DG, Heinisch HL, Mann FM. Reduced activation guidelines in perspective. Journal of Nuclear Materials. 1985;133:892-6.
7. Rocco P, Zucchetti M. Criteria for defining low activation materials in fusion reactor applications. Fusion Engineering and Design. 1991;15(3):235-44.
8. Gilbert MR, Sublet J, R.A. F. Handbook of activation, transmutation, and radiation damage properties of the elements simulated using FISPACT-II & TENDL-2014; Magnetic Fusion Plants. Abingdon: CCFE; 2015. Contract No.: CCFE-R(15)26.
9. Nuttall WJ. Fusion as an Energy Source: Challenges and Opportunities. London, U.K.: Institute of Physics; 2008.
10. Bornschein B, Day C, Demange D, Pinna T. Tritium management and safety issues in ITER and DEMO breeding blankets. Fusion Engineering and Design. 2013;88(6):466-71.
11. Jassby D. Fusion reactors: Not what they're cracked up to be Bulletin of the Atomic Scientists. 2017;April.
12. ITER. The ITER Tokamak Caderache, France2019 [Available from: <https://www.iter.org/mach>.
13. Hirai T, Panayotis S, Barabash V, Amzallag C, Escourbiac F, Durocher A, Merola M, Linke J, Loewenhoff T, Pintsuk G, Wirtz M, and Uytdenhouten I. Use of tungsten material for the ITER divertor. Nuclear Materials and Energy. 2016;9(Supplement C):616-22.
14. Luo GN, Liu GH, Li Q, Qin SG, Wang WJ, Shi YL, Xie CY, Chen ZM, Missirlian M, Guilhem D, Richou M, Hirai T, Escourbiac F, Yao DM, Chen JL, Wang TJ, Bucalossi J, Li JG. Overview of decade-long development of plasma-facing components at ASIPP. Nuclear Fusion. 2017;57(6):065001.
15. Savitskii EM, Tylkina MA, Ipatova SI, Pavlova EI. Properties of tungsten-rhenium alloys. Metal Science and Heat Treatment of Metals. 1960;2(9):483-6.
16. He H, Zeng Y, Qu N. An investigation into wire electrochemical micro machining of pure tungsten. Precision Engineering. 2016;45:285-91.
17. Zinkle SJ, Busby JT. Structural materials for fission & fusion energy. Materials Today. 2009;12(11):12-9.
18. Herschbach K, Maurer W, Vetter JE. Fusion Technology 1994: Elsevier Science; 2012.
19. Andrew PL, Pick MA. Review of tritium retention in first-wall materials. Journal of Nuclear Materials. 1994;212-215:111-7.
20. Tietz TE, Wilson JW. Behaviour and Properties of Refractory Metals. London: Edward Arnold; 1965.

21. Wilkinson WD. Properties of Refractory Metals. New York: Gordon and Breach Science Publishers; 1969.
22. Victoria M, Baluc N, Spätig P. Structural materials for fusion reactors. Nuclear Fusion. 2001;41(8):1047.
23. Bloom EE, Conn RW, Davis JW, Gold RE, Little R, Schultz KR, Smith DL, and Wiffen FW. Low activation materials for fusion applications. Journal of Nuclear Materials. 1984;122(1):17-26.
24. You JH, Visca E, Bachmann C, Barrett T, Crescenzi F, Fursdon M, Greuner H, Guilhem D, Languille P, Li M, McIntosh S, Muller AV, Reiser J, Richou M, and Rieth M. European DEMO divertor target: Operational requirements and material-design interface. Nuclear Materials and Energy. 2016;9:171-6.
25. Butterworth GJ, Giancarli L. Some radiological limitations on the compositions of low-activation materials for power reactors. Journal of Nuclear Materials. 1988;155(Part 2):575-80.
26. British Electricity I. CHAPTER 1 - Nuclear physics and basic technology. In: British Electricity I, editor. Nuclear Power Generation (Third Edition). Oxford: Pergamon; 1992. p. 1-110.
27. Arnoux R. ITER and then what? Caderache, France: ITER Organisation; 2014 [Available from: <https://www.iter.org/mag/3/22>].
28. Gorley M. Activation List for Fusion Reactor Blanket. In: Field A, editor. Chengdu, China: SWIP; 2015.
29. Smirnov AY, Bonarev AK, Sulaberidze GA, Borisevich VD, Kulikov GG, Shmelev AN. Isotopically Modified Molybdenum: Production for Application in Nuclear Energy. Physics Procedia. 2015;72:126-31.
30. PLANSEE. Tungsten. Slough, U.K.; 2017.
31. Wolfram Research. Element Data Source Information Illinois, U.S.2014 [Available from: <https://reference.wolfram.com/language/note/ElementDataSourceInformation.html>].
32. Ashby M. Chart: Fracture toughness - Strength. Granta Design; 2005.
33. Carter LN, Martin C, Withers PJ, Attallah MM. The influence of the laser scan strategy on grain structure and cracking behaviour in SLM powder-bed fabricated nickel superalloy. Journal of Alloys and Compounds. 2014;615:338-47.

## **CHAPTER 2 – LITERATURE REVIEW**

### **2.1 – Introduction**

Chapter 1 provided an overview of the requirements of the application of interest to this study, and this highlighted tungsten as a candidate material. This review will therefore expand on this covering the fundamental metallurgy and behaviour of refractory metals, refractory metal welding, and its associated difficulties, and an overview of Laser Powder Bed Fusion (LPBF). This will include the limited literature on processing of refractory metals but will also encompass the effect of powders and powder production, defect structure and formation, and microstructure and residual stresses. There will also be a brief overview of the analytical techniques that were likely to be utilised in this study.


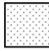



### **2.2 – Refractory Metals**

While there was only limited consensus on which metals are refractory, all definitions of refractory metal refer to the melting points of the materials involved. Some definitions referred to all metals with melting points above that of iron as refractory ( $>1535\text{ }^{\circ}\text{C}$ ) (1) while others referred to those of melting points over  $1855\text{ }^{\circ}\text{C}$  but this rather arbitrarily excluded zirconium which had a melting point of  $1852^{\circ}\text{C}$  (2). The International Journal of Refractory Metals and Hard Materials set the limit at  $1800\text{ }^{\circ}\text{C}$  but excluded many of the platinum group metals (PGM) limiting them to tungsten, molybdenum, chromium, tantalum, niobium, hafnium and rhenium (3) and yet others referred only the materials in Groups V-A and VI-A which included vanadium but precluded rhenium and hafnium (4). Rhenium as a platinum group metal with a Hexagonal Close-Packed (HCP) structure behaves very differently from the remaining metals which were Body-Centre Cubic (BCC) in structure (5). Figure 2.1 is a representation of the different definitions of refractory metals discussed. The legend showed which materials were excluded based on each definition; technetium was not

included as it is both radioactive and not naturally occurring and was therefore considered unsuitable. The Group V-A and VI-A metals highlighted in blue were those which were being defined as refractory metals for this study.

Ti	V	Cr	Mn	Fe	Co	Ni	Cu	Zn
Zr	Nb	Mo	Tc	Ru	Rh	Pd	Ag	Cd
Hf	Ta	W	Re	Os	Ir	Pt	Au	Hg

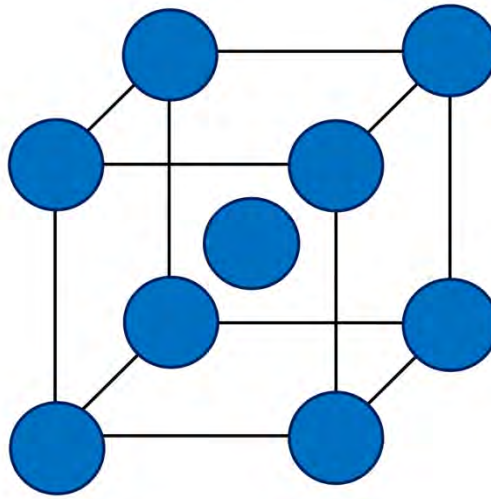
	$T_m < 1535^\circ\text{C}$		$T_m < 1855^\circ\text{C}$
	$T_m < 1800^\circ\text{C}$ or PGM		Not Group V or VI metals
	Refractory Metals as defined by this study		

*Figure 2.1 - Representation of refractory metals as defined by various studies (1-5)*

The Group V and VI metals were defined as refractory metals for this study as there was a greater consistency in both structure and properties which will be elaborated upon in the subsequent sections.

### 2.2.1 – Atomic Structure

The six refractory metals all have a BCC structure to their melting point. The BCC structure can be seen in Figure 2.2.



*Figure 2.2 - Schematic of Body-Centre Cubic (BCC) Crystal Structure*

The BCC structure has a lower density and co-ordination number than FCC and HCP crystal structures with a packing efficiency of 68% and a co-ordination number of 8, in comparison to 74 % and 12 respectively for FCC and HCP crystal structures. This lower packing density of the structure corresponds to a higher entropy of the system which would increase the stability of the phase (6, 7). Increasing the entropy of the system would reduce the Gibbs Free Energy and the phase stability would increase (Equation 2.1).

$$\Delta G = \Delta H - T\Delta S \quad (\text{Equation 2.1})$$

Where  $\Delta G$  was the Gibbs Free Energy (J),  $\Delta H$  was the Enthalpy (J), T was the Temperature (K), and  $\Delta S$  was the Entropy ( $\text{JK}^{-1}$ ) (7).

However, not all BCC metals exhibit such high melting points. Lassner and Schubert, 1999 (7) attributed the high melting point of tungsten to its electronic configuration. Reference values for the atomic structure and electronic configuration of refractory metals can be found in Table 2.1. This gives the electronic configurations according to the Aufbau principle which details the typical order in which electron shells are filled. However, in transition metals it is

known that the half-filled d orbital is stable meaning the electron shell filling follows the  $d^4s^1$  and  $d^5s^1$  patterns for Groups V and VI in the crystalline form. Group V metals have four d electrons and Group VI have five which allows for covalent bonding between adjacent atoms. As Group VI elements have an exactly half-filled d orbital the covalent bonding is stronger contributing to their higher melting point (2, 6-8).

*Table 2.1 - Table detailing atomic and electronic structure of the refractory metals (2, 6-8)*

Element	Atomic Number	Atomic Mass	Lattice Parameter (nm)	Atomic Volume ( $\text{cm}^3.\text{g atom}^{-1}$ )	Group	Electronic Configuration
Vanadium	23	50.942	0.3039	8.35	V	[Ar] $3d^3 4s^2$ *
Chromium	24	51.996	0.2884	7.23	VI	[Ar] $3d^5 4s^1$
Niobium	41	92.906	0.3301	10.8	V	[Kr] $4d^4 5s^1$
Molybdenum	42	95.94	0.3147	9.39	VI	[Kr] $4d^5 5s^1$
Tantalum	73	180.95	0.3303	10.9	V	[Xe] $4f^{14} 5d^3 6s^2$ *
Tungsten	74	183.84	0.3165	9.53	VI	[Xe] $4f^{14} 5d^4 6s^2$ *

\* *Electronic configuration according to the Aufbau Principle; in the crystalline form the electronic configurations were expected to follow the  $d^4s^1$  and  $d^5s^1$  patterns for Groups V and VI respectively.*

### 2.2.2–Thermal & Mechanical Properties

Sources varied significantly on the values for thermal and mechanical properties of refractory metals depending on the purity, fabrication route, thermal history and resultant microstructure; different sources had the thermal conductivity of tungsten between 40 and  $174 \text{ Wm}^{-1}\text{K}^{-1}$  with DBTTs of  $-10^\circ\text{C}$  to in excess of  $600^\circ\text{C}$  as a result, the tables detailing thermal and mechanical properties were taken from a single reference to allow for adequate comparison (1, 2, 4, 5, 7). Table 2.2 showed a summary of key thermal and mechanical properties. This source was selected as the values were comparable to other sources with no values at the extremes indicated above and had all the required properties. If multiple sources were compared normalisation for purity and grain size etc. would be required. Moreover, the trends in the data were consistent between sources, with trends being seen down the Groups or with increasing atomic number.

Table 2.2 - Table detailing key thermal and mechanical properties of the refractory metals (8)

	<b>W</b>	<b>Mo</b>	<b>Cr</b>	<b>Ta</b>	<b>Nb</b>	<b>V</b>
<b>Melting Point (K)</b>	3696	2896	2180	3287	2750	2183
<b>Thermal Conductivity (Wm<sup>-1</sup>K<sup>-1</sup>)</b>	170	139	94	57	54	31
<b>Specific Heat Capacity (Jg<sup>-1</sup>K<sup>-1</sup>)</b>	132	251	448	140	265	489
<b>Coefficient of thermal expansion (10<sup>6</sup>K<sup>-1</sup>)</b>	4.5	4.8	4.9	6.5	7.3	8.5
<b>Density (gcm<sup>-3</sup>)</b>	19.4	10.3	7.2	16.6	8.6	6.1
<b>Young's modulus (GPa)</b>	411	329	279	186	105	128
<b>Hardness (H<sub>v</sub>)</b>	350	156	108	89	135	64

Refractory metals are generally considered to have intrinsic brittleness which was a key cause for concern due to the increased propensity to hot cracking (1, 2, 9). Table 2.3 showed the DBTT for the Six Metals in Groups V-A and VI-A (4). As can be seen from this table, the Group VI-A metals had brittle transitions above room temperature with Group V-A metals having transitions significantly below room temperature.

Table 2.3 - Table showing DBTTs for the refractory metals (4)

<b>Metal</b>	<b>DBTT (°C)</b>
V	<-195
Nb	-120
Ta	<-195
Cr	330
Mo	30
W	340

In Section 1.2.2 a merit index for materials to be used in divertor components was shown (Equation 1.1 shown again here). This allowed materials to be ranked by suitability for use as a divertor material, ensuring a sufficient operating temperature, maximising heat transfer for energy generation and minimising stress within adjacent monoblocks through expansion.



$$\frac{T_m \cdot \kappa}{\alpha} \quad (\text{Equation 1.1})$$

However, in addition to this a metric of fabricability and durability must also be considered; Wilkinson, 1969 (2) found thermal shock to be proportional to Equation 2.2. With fracture stresses associated with tungsten and tantalum of 820 and 140 MPa respectively (10), the thermal shock of tungsten and tantalum was 0.57 and 0.047 gK.10<sup>-9</sup>ms. This showed a significantly higher likelihood of thermal shock occurring in tungsten than in tantalum, largely due to higher stiffness and greater thermal conductivity.

$$\frac{\kappa \cdot \sigma_f}{\alpha \cdot E \cdot C_p} \quad (\text{Equation 2.2})$$

Where  $\kappa$  is the thermal conductivity (Wm<sup>-1</sup>K<sup>-1</sup>),  $\sigma_f$  is the fracture stress (Pa),  $\alpha$  is the coefficient of thermal expansion (K<sup>-1</sup>), E is the Young's Modulus (Pa),  $C_p$  is the specific heat capacity (Jg<sup>-1</sup>K<sup>-1</sup>).

It has been suggested that strain rate sensitivity could worsen the effect of thermal shock; BCC materials were found to be susceptible to thermal shock due to high lattice friction and the high activation energy for dislocation movement given the lack of close packed planes for slip in BCC materials and few slip systems active at low temperatures (11-13). Yih and Wang, 1979 (12) showed a significant increase in yield strength with strain rate (see Figure 2.3), associated with a corresponding reduction in ductility. The rapid cooling associated with welding would induce high strain rates likely increasing the apparent brittleness of the material and the propensity for hot cracking (12).

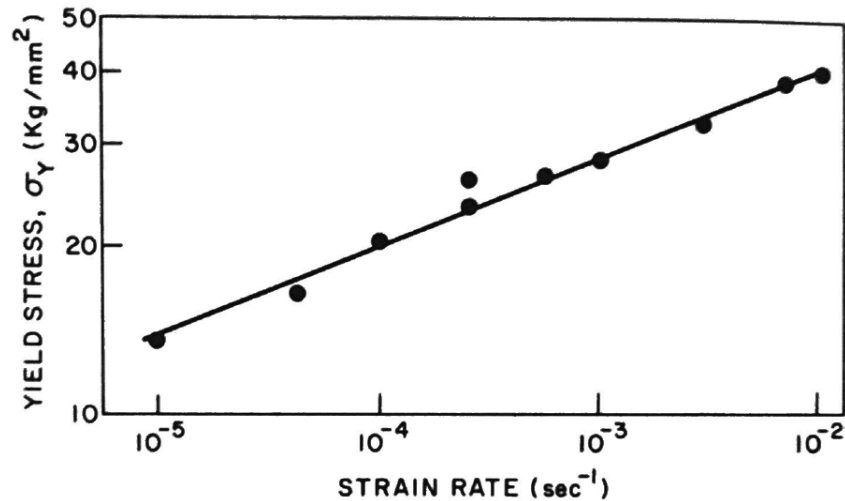


Figure 2.3 - Effect of strain rate on yield stress of tungsten. Taken from Yih and Wang, 1979 (12)

Figure 2.4 showed the variation in DBTT with grain size in tungsten (taken from Lampman, 1997 (9)). The data was compiled from a number of studies. Some clustering of the data could be seen from a single study (indicated by different data point markers and highlighted blue and purple within the figure). Despite this, within grain sizes typical for the microstructures expected in LPBF (<500 μm), the DBTT increased with increasing grain size with the increase from 10 to 100 μm, corresponding to an increase of around 200 °C. The spread in the data was attributed to the differences in purity content and processing history (9).

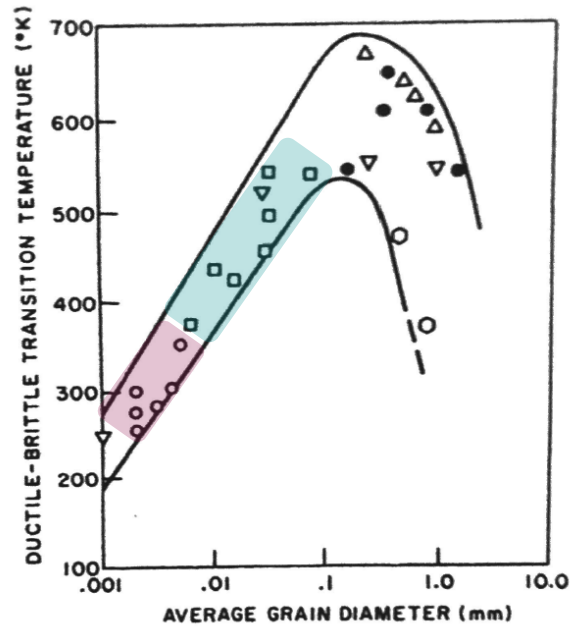


Figure 2.4 - Effect of grain size on DBTT in tungsten. Taken from Lampman, 1997 (9)

The method of fabrication, heat treatment state, end condition (e.g. plate or rod) were also shown to cause significant variation in tensile and creep properties due to their grain size and orientation. Figure 2.5 showed the variation in UTS with heat treatment state for molybdenum and TZM (titanium-zirconium-molybdenum) respectively and Figure 2.6 showed the variation in stress rupture stress with method of fabrication (2, 14). Welding was also shown to have a detrimental effect on mechanical properties due to increased grain size. Powder metallurgy was shown to have residual porosity which could worsen mechanical properties by reducing the effective area of the material (15-17).

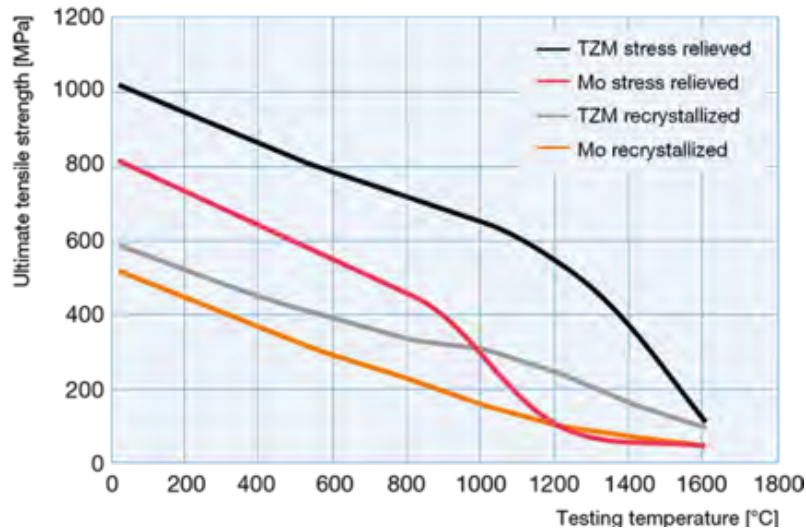


Figure 2.5 - Graph showing the variation in UTS with test temperature for molybdenum and TZM in stress relieved and recrystallised state. Taken from PLANSEE, 2017 (14)

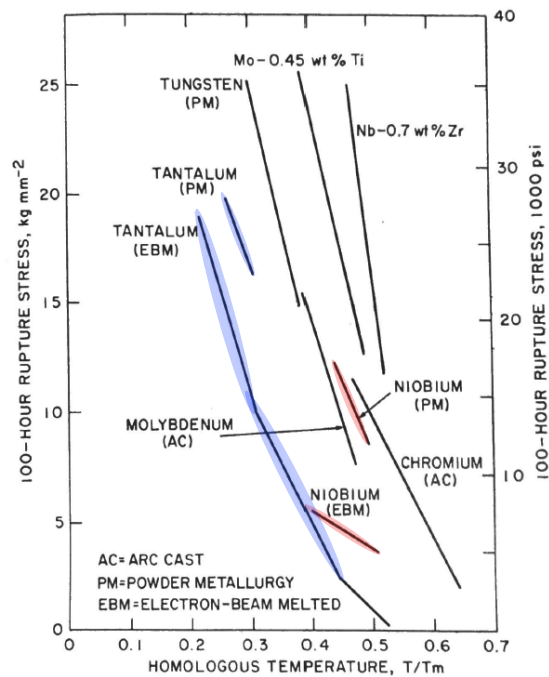


Figure 2.6 - Graph to show the variation in 100-hour rupture stress for refractory metals with different fabrication routes. Taken from Wilkinson, 1969 (2)

While the review has provided some insight into the range of properties expected, it has been shown that both the thermal and mechanical properties of refractory metals depend extensively on processing history and impurity content. There is little understanding on the impact of LPBF processing on the subsequent structure, and the resultant properties. This should therefore be considered as a subject for further research.

### 2.2.3 – Detrimental Elements

It has been widely known that interstitial elements could greatly embrittle refractory metals; the effect varied between metals due to the variation in solubility levels. Group VI metals had particularly low interstitial solubility (<1 ppm in solid solution at room temperature). At elevated temperatures the solubility of interstitial elements in tungsten ranges between 100 and 1000 ppm. During cooling the interstitial elements are rejected to the grain boundaries reducing the cohesive strength of the grain boundaries significantly (2, 4, 7). Table 2.4 detailed the maximum concentration of interstitials which could sit in solid solution in refractory metals.

*Table 2.4 - Maximum possible concentration (ppm) of interstitials in refractory metals after moderate cooling rate. Taken from Tietz and Wilson, 1965 (4)*

Interstitial Element	Group V-A Metals			Group VI-A Metals		
	V	Nb	Ta	Cr	Mo	W
H	10000	9000	4000	0.1-1	0.1	*
C	~1000	100	70	0.1-1	0.1-1	≤0.1
N	5000	300	1000	0.1	1	≤0.1
O	3000	1000	200	0.1	1	1

\*Value not detectable

Group-VA metals were less likely to form brittle secondary phases at low interstitial concentrations, meaning they were less susceptible to cracking during fabrication than the metals in Group VI-A. The presence of second phases such as oxides had been found to be detrimental to the low temperature ductility of Group VI-A metals as cited by Wilkinson, 1969 (2). The detrimental effect of interstitials on grain boundaries of Group VI-A refractory metals could be seen in the change in DBTT caused by the production of a single crystal specimen; for both Cr and W the DBTT reduces from 330 and 340 °C respectively in polycrystalline material to approximately -100 °C in single crystals, well below room temperature (2).

Yih and Wang, 1979 (12) showed the effect of oxygen on the DBTT in single crystal and polycrystalline tungsten (see Figure 2.7) (12). An increase in DBTT of 250 K was seen with an increase in atomic ratio for oxygen of 5 % in polycrystalline tungsten. Additionally, it suggested that oxygen strongly affected grain boundary behaviour; the DBTT of the single crystal material was more than 200 K less for a given oxygen content and was much less strongly affected by the presence of oxygen. The effect of carbon was noticeably weaker and seemed less affected by the presence of grain boundaries (12).

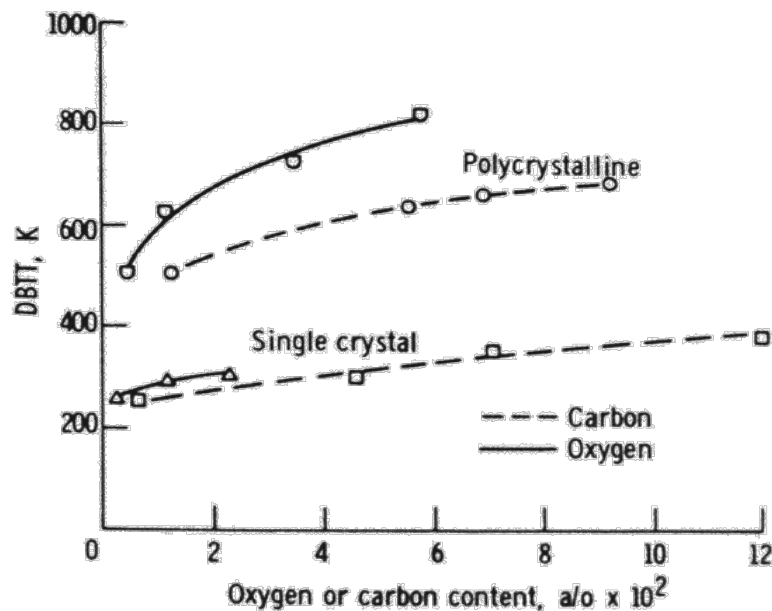


Figure 2.7 - The effect of oxygen and carbon on the DBTT of single crystal and polycrystalline tungsten. Taken from Yih and Wang, 1979 (12)

Most sources agreed on oxygen being the most deleterious element to the mechanical properties of refractory metals (9, 12, 18-21), however, sulphur and phosphorous have also been proffered by various studies (22-25). Moreover, each study had different levels of interstitial impurity and two of the studies were conducted on Tungsten Heavy Alloys (WHA) (2, 22-25).

Scott and Knowlson, 1963 (26) also suggested weldability could be increased through the use of agents to neutralise the effect of interstitial impurities; the most common of which to date have been titanium and carbon. However, most reactive metals have been trialled (Zr, Hf, Al, Nb, Ta). The key factors for success with neutralising agents were that they must have a high affinity for the impurity, have high melting points, and the compounds formed must not form grain boundary films (2, 26).

All suggested segregation of the interstitial element to the grain boundaries as the mechanism of embrittlement. Figure 2.8 showed the grain boundary enrichment of tungsten with oxygen and phosphorous (24). Gludovatz, 2011 (24) suggested impurities had little effect on the nature of fracture seen; indeed, transgranular cleavage is seen in the P-rich fractograph (24). This was in contradiction to the general consensus; for example, Lassner and Schubert, 1999 (7) stated that the DBTT for the grain boundary was 280-330 °C in comparison to 30-40 °C for the grain interior due to the presence of impurities weakening the boundaries (7). Tran-Huu-Loi et al., 1985 (27) showed phosphorous peaks in areas of intergranular fracture and no such peaks were found in areas of transgranular cleavage.

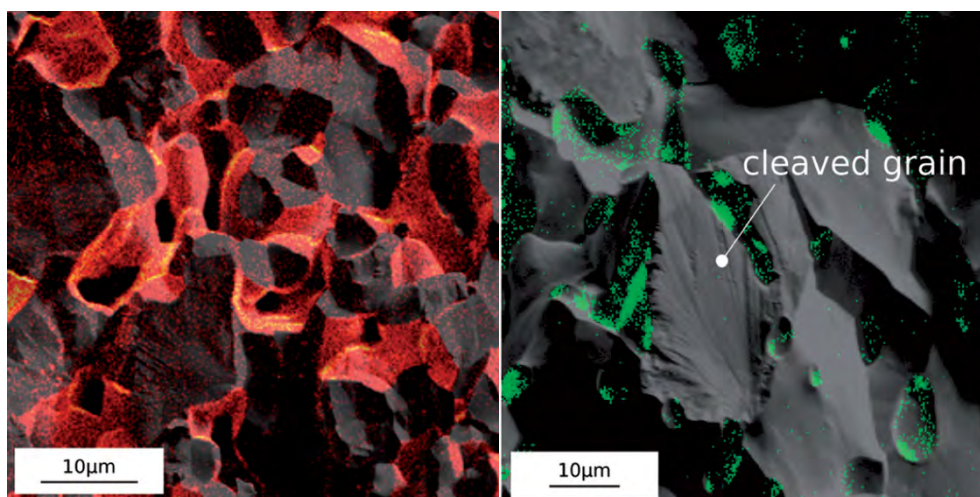


Figure 2.8 - Fracture surfaces of tungsten with overlaid maps of oxygen (left) and phosphorous (right). Taken from Gludovatz et al., 2011 (24)

The literature is unclear whether the deleterious elements sit interstitially at grain boundaries or form secondary phases. Much of the research was conducted in the 1960s and the analytical techniques required were sophisticated, however it was generally considered to be an interstitial phenomenon (1, 2, 4, 7). Braun et al., 2019 (28) suggested the formation of Mo-oxide on the grain boundaries of LPBF molybdenum processed with a chamber oxygen concentration of 800 ppm could be seen in the fracture surface presented (see Figure 2.9). No detail was provided on the preparation of the samples as they do not look typical for a fracture surface. The EDX map did not clearly show oxygen enrichment but this may be due to EDX being less effective at detecting light elements (2, 4, 28). Scott and Knowlson, 1963 (26) also found the formation of grain-boundary films in molybdenum.

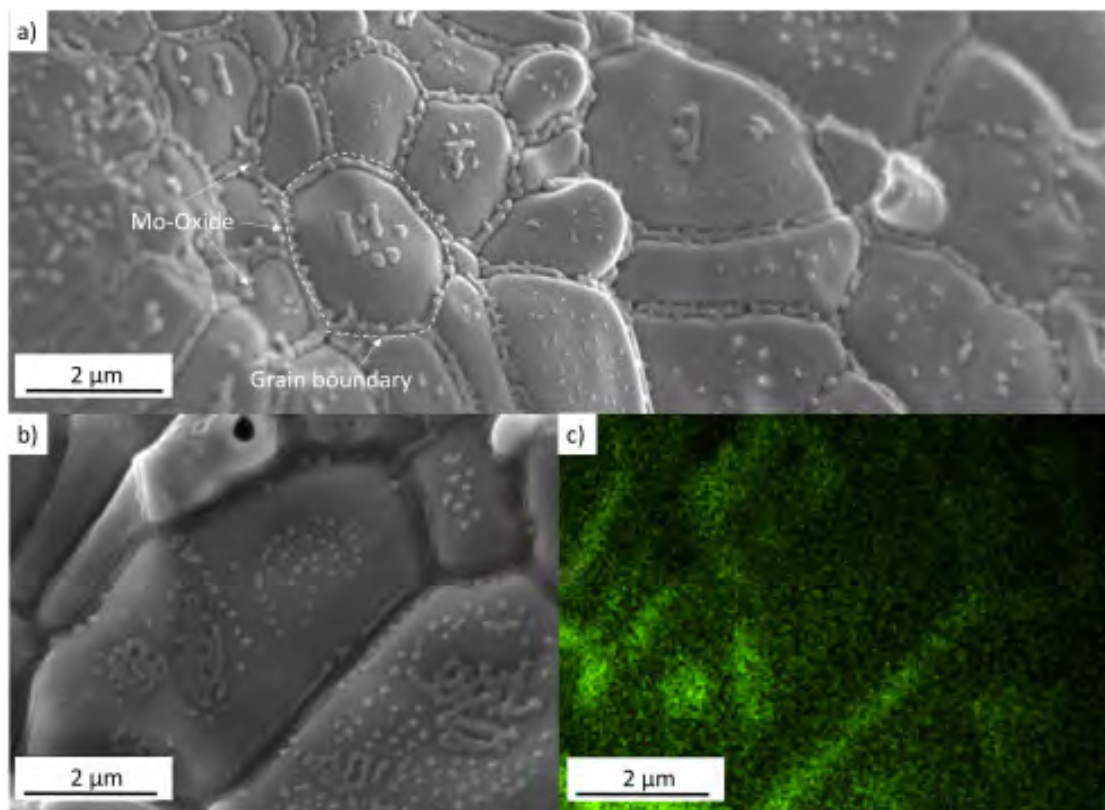


Figure 2.9 - Fracture surface of a molybdenum sample produced by LPBF a) oxide segregations at grain boundaries, b) segregation of the exposed fracture surface, c) Elemental distribution of oxygen at the fracture surface shown in b). Taken from Braun et al., 2019 (28)



Oxygen was shown to have a significant effect on the mechanical properties and ductility of tungsten; at 4 ppm oxygen the yield strength at 370 °C was double that of tungsten containing 50 ppm of oxygen (see Figure 2.10) (20). These oxygen levels were still substantially lower than those typically found in the raw material used for LPBF processing which had oxygen contents of 200 ppm or more (29, 30).

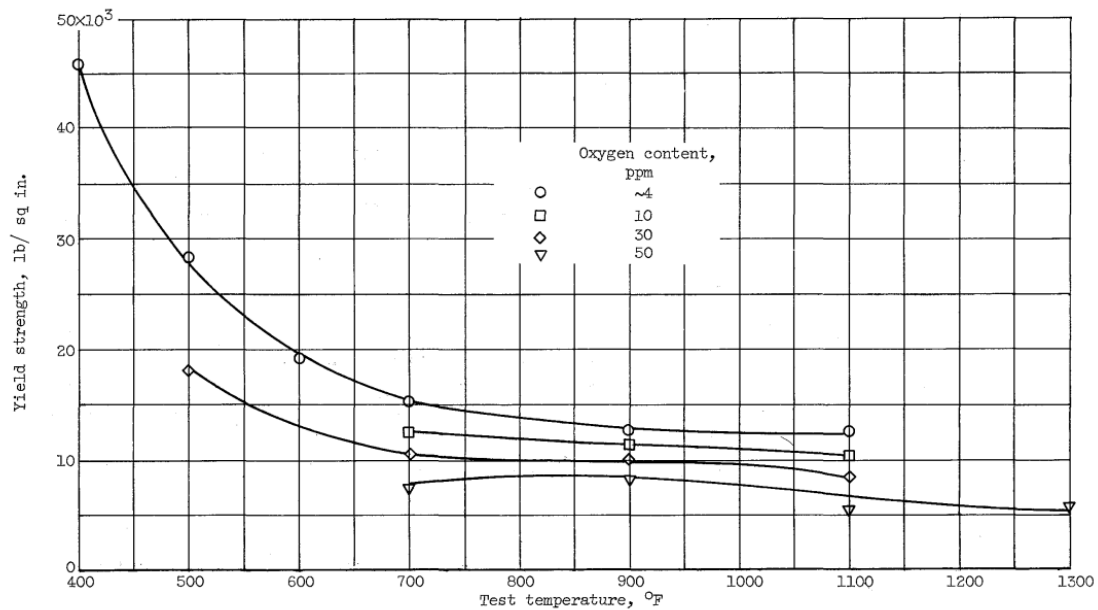


Figure 2.10 - Effect of oxygen on yield strength of polycrystalline tungsten. Taken from Stephens, 1963 (20)

It was possible therefore, that the relative quantities of interstitial content and environment may affect its relative contribution to embrittlement. Additional impurities may have lessened the effect of some interstitials present in the studies. Within LPBF processing, the residual oxygen within the argon atmosphere and surface oxides within the powders are the largest potential for contamination with sources citing oxygen as the deleterious element more consistently within LPBF processing literature (18, 19, 28, 31, 32). Removing or reducing interstitial impurities would seem the obvious method to improve ductility however, given the low concentrations for solid solution at room temperature, the required interstitial content would be extremely low (<10 ppm), significantly lower than the typical oxygen content

within commercial LPBF platforms (~1000 ppm) (19). This is, therefore, a key area for further work with regards to LPBF processability of tungsten.

#### 2.2.4– Oxidation

Refractory metals, with the exception of chromium, were generally found to have poor oxidation resistance and the oxides formed were not adherent and volatilised at temperatures well below the melting point of the metal. The stable tungsten oxide,  $WO_3$ , was found to volatilise above 1000 °C and tantalum oxide,  $Ta_2O_5$  volatilised at 1370 °C. By contrast, chromia ( $Cr_2O_3$ ) was stable to 2440 °C, well above the melting point of the metal (4).

As the oxides were not adherent the rate of oxidation was extremely rapid (see Figure 2.11). Molybdenum in particular was found to oxidise at a rate of 1 mm.hour<sup>-1</sup>. However, absolute oxidation rates were found to vary significantly by study (orders of magnitude) and this was likely due to the surface roughness, purity and test set-up (2, 4, 12).

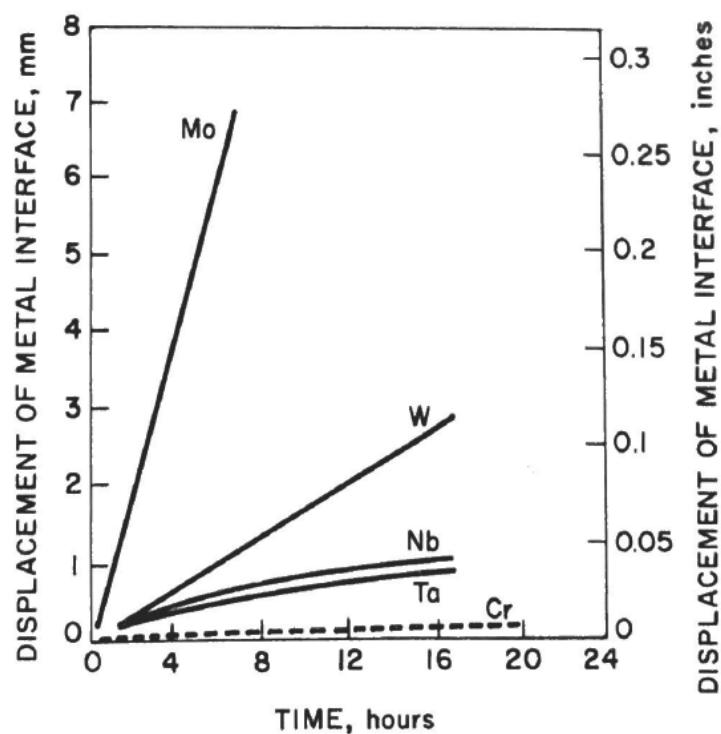


Figure 2.11 – Metal-oxide displacement with time of refractory metals in air at around 1000 °C.  
Taken from Wilkinson, 1969 (2)

Typical welding processing is conducted in atmospheric purities sufficient to prevent extensive oxidation (base metal oxygen content <20 ppm, shielding gas oxygen content ca. 10 ppm (26, 33)); however, given the oxygen concentrations within typical LPBF processing chambers it may still be a cause for concern particularly if attempting fabrication at higher preheating temperatures particularly in the region of 400-1000 °C. Visible blue oxidation has been noted at elevated temperatures and at temperatures as low as 400 °C, rapid tarnishing of the surface could be seen (1, 2, 4).

Figure 2.12 showed an Ellingham diagram of some of the refractory metals. This showed tantalum oxide has a significantly greater stability than tungsten oxide, with the stability of tungsten and molybdenum oxides being very similar. This may suggest Ta<sub>2</sub>O<sub>5</sub> would form in preference to WO<sub>3</sub> in a W-Ta alloy, particularly at lower partial pressures of oxygen (34). However, Ellingham diagrams do not include kinetics and in a non-equilibrium environment such as LPBF, this may be significant. Moreover, sufficient quantity of tantalum alloying addition would be required for the formation of tantalum oxide.

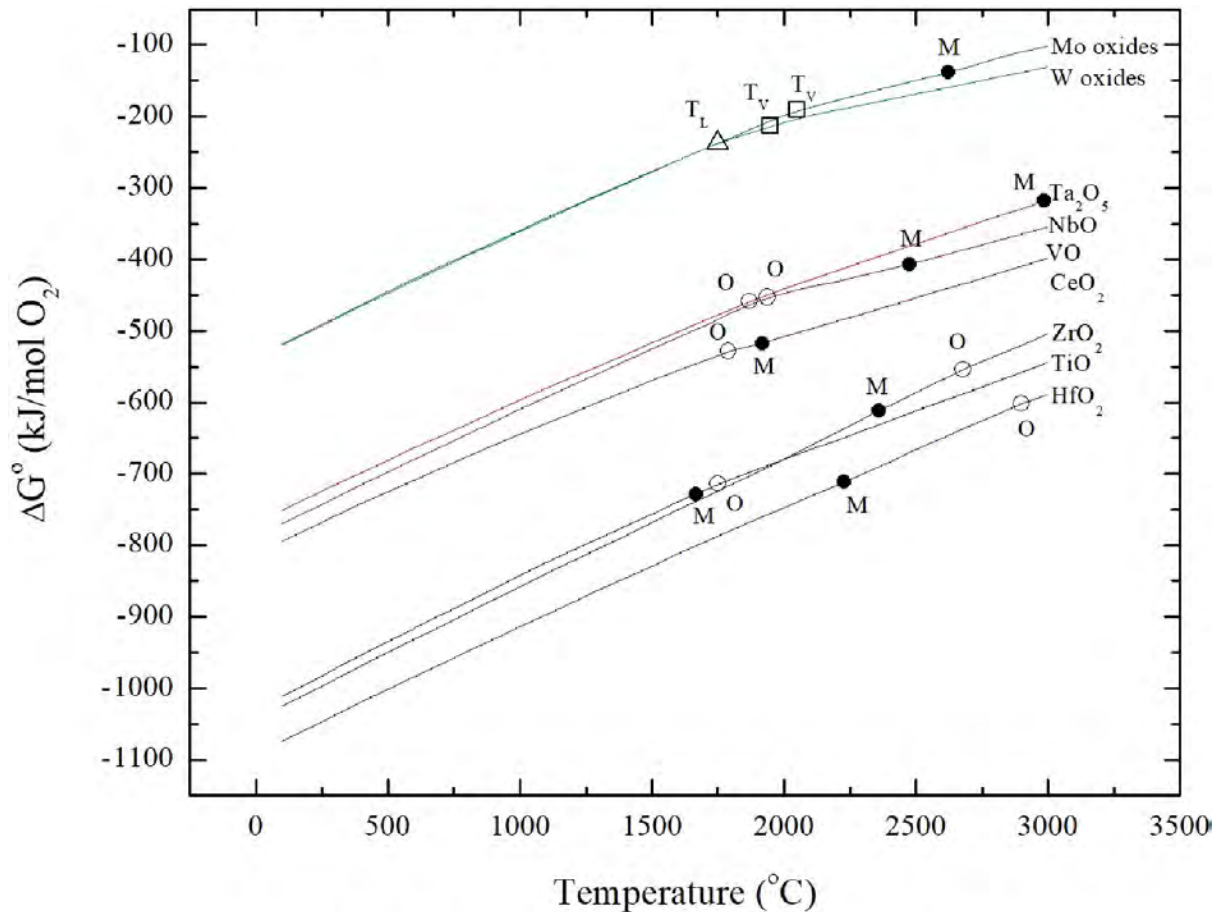


Figure 2.12 - Ellingham diagram showing the formation reactions of the Group IV, V and VI metals with solid circles indicating melting of the base metal, open circles indicating oxide melting and the triangle indicating transition to gaseous oxide. Taken from Backman and Opila, 2019 (34)

In addition, the form the oxide takes was of equal importance to the rate of oxidation.

Tungsten and molybdenum have been shown to form grain boundary films which significantly weaken the strength of the material (7, 28). By contrast, oxygen has been shown to segregate from the bulk to the surface in tantalum and niobium alloys. This would increase the grain boundary strength of the material (35). It has also been shown that spheroidising oxides improved the mechanical properties of the material in comparison to oxide films even if they are still located on the grain boundaries (26).

The circumstances within LPBF processing are known to be very dynamic with rapid heating and cooling. The volatilisation and break up of aluminium oxides during LPBF has been presented; the exhibition of this phenomenon is not clear. Louvis et al., 2011 (36) suggested

that the oxides at the top of the melt pool volatilised with Marangoni convection breaking oxides at the meltpool base. The oxides at the edge of the pool remained intact acting as a point of weakness between adjacent scan tracks (see Figure 2.13). This would likely see porosity formation at the edge of scan tracks with the centre of the track having good integrity (36). By contrast, Tang and Pistorius, 2018 (37) found that volatilised oxide in LPBF processing of Al-alloys was re-deposited in the material as oxide particles. These particles were up to tens of microns in size and were shown to initiate cracking and reduce fatigue life. It was also suggested that the oxides arising from the surface of powder particles were smaller. No regular pattern to oxide location within the deposit was noted by the authors (37). However, consistently it was suggested that the key issue associated with oxides in the material was that it affected wettability and would therefore increase lack of fusion defects. This was also highlighted as an issue in aluminium alloys processed by casting (36-40).

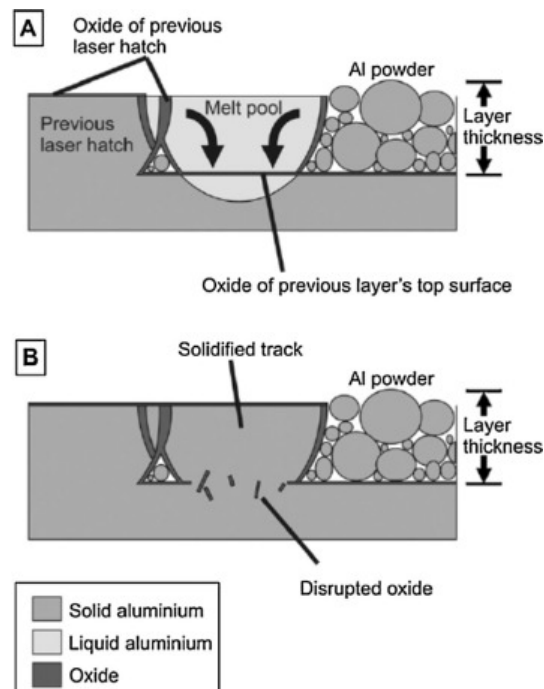


Figure 2.13 – Schematic showing a) Marangoni convection in the melt pool and b) oxide disruption and solidification of the melt pool in aluminium alloys. Taken from Louvis et al., 2011 (36)

Reijonen et al., 2020 (41) presented the effect of shielding gas flow on part quality in stainless steel. It was found at low gas flows ( $<2.5 \text{ ms}^{-1}$ ) the gas was insufficient to move spatter and the vapour plume away from the path of the laser beam reducing melt pool penetration and increasing the levels of lack of fusion, however the study showed no effect on part cracking (41). Anwar and Pham, 2017 (42) found that increasing the speed of argon through the machine from  $1.43 \text{ ms}^{-1}$  to  $2.87 \text{ ms}^{-1}$  increased the ultimate tensile strength of AlSi10Mg parts produced with an SLM Solutions 280HL (42).

From the available literature, it is therefore possible oxide vaporisation and deposition would be a problem within LPBF processing of refractory metals. The melting points of tungsten and tantalum ( $3423 \text{ }^{\circ}\text{C}$  and  $3014 \text{ }^{\circ}\text{C}$  respectively) are significantly higher than the volatilisation points of their oxides (4, 8). During LPBF processing therefore, vaporisation of surface oxides from powders could occur. Some of which would be removed to the filters due to the gas flow.

However, in LPBF processing heat input is very localised so the surface of the deposit can vary significantly in temperature. Arisoy et al., 2019 (43) showed that the surface during LPBF of IN625 could vary between  $600$  and  $1600 \text{ }^{\circ}\text{C}$  on the order of millimetres and the thermal imaging conducted by Hooper, 2018 (44) showed temperatures between  $1000$  and  $4000 \text{ K}$  in Ti-6Al-4V processing (43, 44). Therefore, while some material maybe at a temperature where volatilisation of the oxide could occur other material would be below that threshold and could absorb oxygen which could then diffuse to the grain boundaries.

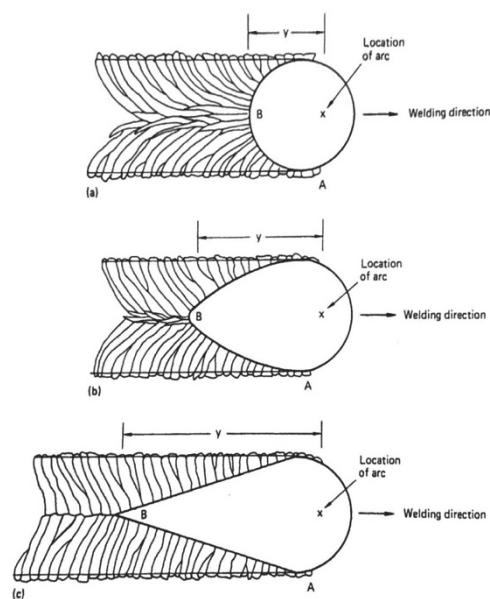
### 2.3 – Welding of Refractory Metals

Due to the limited literature available on LPBF processing of refractory metals, relevant welding literature has been reviewed to increase the understanding of the formation, microstructure and behaviour of welds. It has been well understood that refractory metals, particularly molybdenum and tungsten, are difficult to weld due to their BCC crystal structure, their high melting points, susceptibility to impurity embrittlement, rapid grain growth during welding and strain rate sensitivity. Hot cracking has been well-documented as the dominant defect mechanism in tungsten welding (9, 15, 45, 46). The refractory metals listed with respect to increasing difficulty with welding were Ta, Nb, Mo, W (9).

Refractory metals have been shown to suffer from significant grain growth during fusion welding, which has been shown through the Hall-Petch effect to have a detrimental effect on the strength and toughness of the material (9, 15). Materials with larger grain sizes also have fewer grain boundaries which could increase interstitial content per grain boundary worsening this effect. Tabernig and Reheis, 2009 (46) found that fusion welding had a detrimental effect on mechanical properties of molybdenum and molybdenum alloys. Pure molybdenum had a decrease in Ultimate Tensile Strength (UTS) from 600 MPa to 350 MPa after welding with a corresponding reduction in ductility from around 40 % to only 1 % which was attributed to the grain growth occurring (46). Kolarikova et al., 2012 (17) showed the grains grew from  $\sim 5 \mu\text{m}$  to 40-140  $\mu\text{m}$  following Electron Beam (EB) welding (17). Some alloy development has been designed to prevent grain growth with TZM showing greater grain control than unalloyed molybdenum (9).

The microstructures generated in welding have been shown to be dependent on the welding parameters utilised, with correlations drawn between the melt pool shape and the final

solidified microstructure. Figure 2.14 showed melt pool shapes produced with a variety of travel speeds during welding, with faster welding speeds corresponding to greater elongation in the melt pool (9). Hunziker, et al., 2000 (47) by contrast, found that in fusion welding of IN718 melt pool shape was more strongly dependent on input power than on travel speed. However, there was agreement on the elongation of melt pools resulting in the formation of a centre-line grain boundary (Schematic C) (9, 47). This was found to occur when the growth fronts met the weld centre-line at angles less than  $90^\circ$  (47). Specific input parameters resulting in elongated melt pools may vary with material system. Lower travel speeds were found to increase the aspect ratio of the welds, with narrow deep welds more likely to instigate hot cracking due to stress concentration (48).



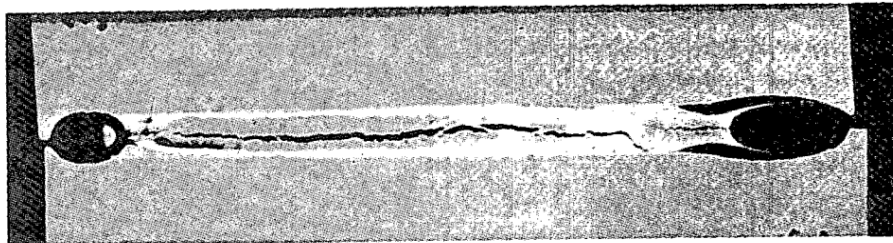
*Figure 2.14 - Typical welding microstructures with varying scan speeds (top to bottom, low, intermediate and high travel speeds). Taken from Lampman, 1997 (9)*

Intergranular crack propagation has been found to result in a tortuous crack path. By contrast, the regular nature of the centre-line grain boundaries could facilitate crack propagation. It would therefore be better to try and avoid the formation of centre-line grain boundaries. However, it has been shown that centre-line grain boundaries occurred at higher energy inputs resulting in higher thermal gradients; it may be possible that in order to completely



melt refractory metals due to their high melting points, high energy inputs, and thus gradients in the absence of bed pre-heating, are needed. This means the formation of elongated melt pools and weld centre-lines are therefore more likely. It has also been shown that as the weld centre-line was the last to solidify the area and would therefore become enriched with impurities or brittle oxide phases which may reduce the strength of the material. Zhou et al., 2015 (19) found that an increase in oxygen in a laser scan track reduced the surface tension of the melt pool, due to the surface active nature of oxygen, and thus reversed the direction of flow, increasing the likelihood of balling and defect formation (9, 19).

Centre-line cracking was found to be common in welds of refractory metals. Figure 2.15 showed a photograph typical of that shown within the literature (15, 33, 48). Cole et al., 1971 also postulated that subsequent re-heating for adjacent weld tracks would significantly worsen cracking present (15).



*Figure 2.15 - Centre-line crack formation in a tungsten weld conducted in an environment with 1800 ppm oxygen. Taken from Lessman and Gold, 1969 (33)*

More generally, hot cracking could be caused by a number of key factors. Figure 2.16 showed a flow diagram of the key factors with ways to alleviate the cracking; the base factors could be grouped under incorrect weld parameters, poor material quality, and high thermal stress.

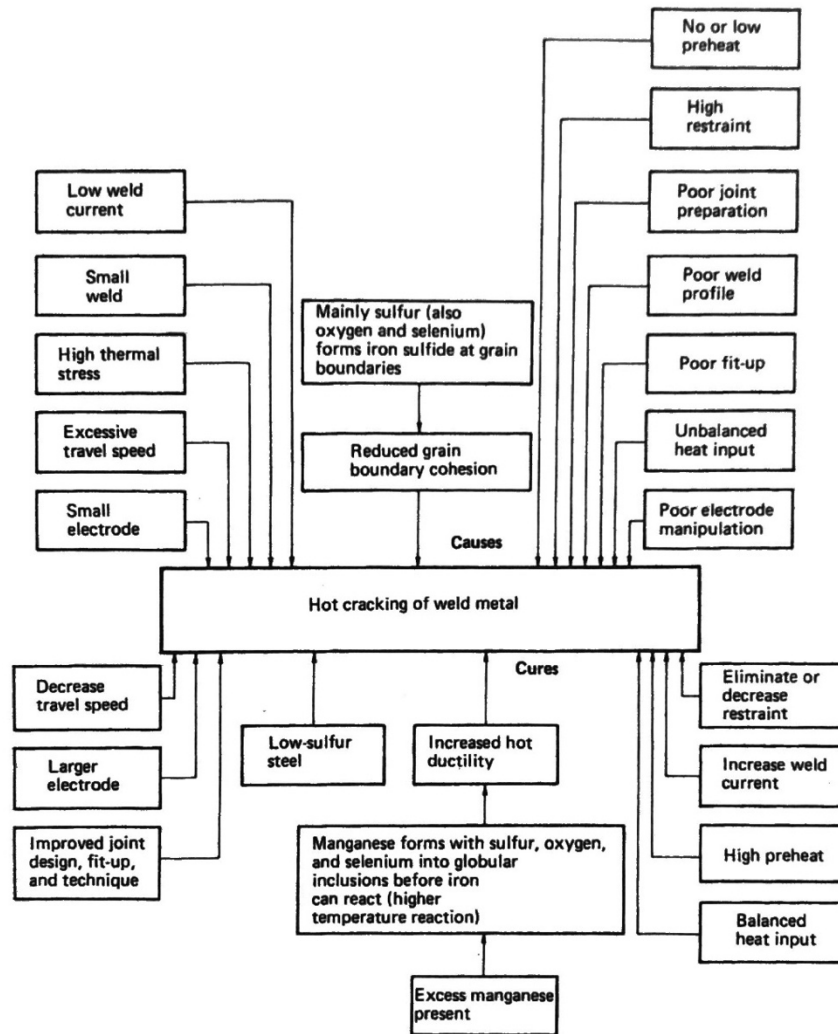


Figure 2.16 - Factors affecting hot cracking in welding. Taken from Lampman, 1997 (9)

Incorrect weld parameters could relate to parameters which precipitate the formation of a centre-line grain boundary or could relate to insufficient optimisation of weld parameters. These were therefore more easily resolved and not therefore the emphasis of this review (9, 47).

As has been previously mentioned refractory metals are particularly susceptible embrittlement from interstitial impurities. The exact mechanism behind the embrittlement was the subject of some contention; there were two main hypotheses behind the mechanism

for this cracking. The first was grain boundary embrittlement through oxide films or interstitial embrittlement which lowered the mechanical properties of the material such that cracking occurred during thermal shock (2, 4, 28, 49). The second was the migration and coalescence of pores to the grain boundaries. It was thought that the pores were gas pores. Farrell et al., 1970 (45) suggested that within CVD tungsten these were tungsten hexafluoride as a by-product of the manufacturing process (15, 16). Scott and Knowlson, 1963 (26) suggested that within other powder metallurgy products, the gas pores occurred due to the volatilisation of grain boundary films that occurred upon reheating of the base metal during welding. However, high purity tungsten failed to show this porosity (26). Leong, 2001 (48) suggested that oxide films could form at the top and base of the weld preventing bonding of the recast material with the base metal (48). The mechanism of cracking within both refractory metal welding and LPBF requires clarification and should therefore be the subject of further study.

The main focus of research into overcoming impurity embrittlement has surrounded the use of improved atmosphere control or alloying to reduce susceptibility. Maintaining the highest possible purity has been noted as being of critical importance to weld quality; interstitial impurities of less than 30 ppm has been suggested for the base material with Lampman, 1997 (9) suggesting oxygen and moisture contents of less than 10 ppm required (9, 26). It was suggested that pre-heating may facilitate the reduction of moisture in the weld area. It was found that oxygen within the weld atmosphere was proportional to that of the oxygen pick-up within molybdenum (see Figure 2.17), with an increase in DBTT from -10 °C to 220 °C when welding in atmosphere with 0.1 ppm of oxygen to 700 ppm of oxygen (9, 15, 26, 45, 46, 48).

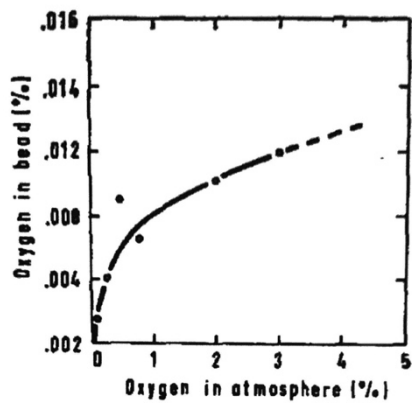


Figure 2.17 - Graph showing the increase in oxygen in the molybdenum weld bead with increasing oxygen in the welding atmosphere. Taken from Scott and Knowlson, 1963 (26)

W-Re alloys showed improved weldability over unalloyed tungsten as it has been shown to improve grain control as was shown with TZM versus unalloyed molybdenum. Mo-Re alloys were shown to maintain a much higher degree of the base material strength in comparison to unalloyed molybdenum. W-Re alloys however, have had the potential to form the brittle sigma phase particularly under some welding conditions which can promote cracking within the material (9, 33, 46).

Weld plate pre-heating and post weld heat treatments (PWHT) have been used to reduce the thermal stresses associated with welding. Only Scott and Knowlson, 1963 (26) found it possible to successfully weld with no work piece preheating in electron beam welding of molybdenum. This was attributed to the smaller weld bead heat affected zone size (45, 46). By contrast, it was generally accepted that heating above the DBTT was required to successfully weld without cracking; the exact temperature however varied significantly, but this was likely due to the variation in DBTT with impurity content; with preheats as low as 150 °C for high purity tungsten to 475 °C for powder metallurgy and EB weld materials (45). PWHT have had some success at reducing cracking which Scott and Knowlson, 1963 (26) attributed to spheroidising the oxide films so they no longer acted as crack propagators. It

has been shown that a 1000 °C heat treatment for two hours could be used to stress relieve molybdenum alloys however, other sources suggested this was only effective if the heat treatment was conducted prior to the work piece completely cooling. There was consistency in PWHT causing significant grain growth and the elevated temperature could cause further issues with oxide precipitation on grain boundaries. PWHT will therefore not be investigated further during this study as increasing the grain size of the material would have a deleterious effect on the mechanical properties (26, 46).

Various properties associated with refractory metals worsen the effect of hot cracking, particularly strain rate sensitivity. The high melting point of refractory metals increased the peak temperature required for melting and the change in temperature experienced by the sample, increasing the thermal contraction experienced over the temperature range. This coupled with the materials' high thermal conductivity meant that thermal gradients were very high; in LPBF it has been estimated that cooling rates are  $10^6 \text{ Ks}^{-1}$  or more (50). Given refractory metals sensitivity to strain rate this increased strain over very short time periods and possibly worsened by impurity embrittlement greatly increased the likelihood of cracking occurring. Increasing the temperature of the build plate through preheating would therefore reduce the change in temperature occurring during welding or LPBF and would likely improve a material's crack resistance by reducing the thermal gradient and will be the subject of further investigation during this study (9).

## **2.4 – Brief Overview of Analytical Techniques**

When reviewing the analytical techniques to be utilized within a study a holistic approach must be undertaken considering the complexity, resolution and limitations of the technique in comparison to the specific requirements of the study. This study for example was likely to

have macroscale cracking where high resolution imaging may provide less value than an understanding of the overall cracking pattern produced. Tungsten has also been shown to be extremely sensitive to oxygen embrittlement meaning analysis techniques which are limited in their ability to detect light elements may be of less use. This will significantly limit the techniques which are suitable.

Table 2.5, 2.6 and 2.7 detailed the advantages and disadvantages of the main possible microstructural, mechanical and chemical test techniques. From this, it was decided to focus on techniques which would have the greatest compromise of sensitivity, cost and availability, and required output; the techniques utilised were highlighted in each table and will form the basis of this review.

*Table 2.5 - Table detailing the advantages and disadvantages of microstructural test techniques (51)*

	<b>OM</b>	<b>SEM</b>	<b>TEM</b>
<b>Advantages</b>	<ul style="list-style-type: none"> <li>• Largest field of view</li> <li>• Fast data acquisition</li> </ul>	<ul style="list-style-type: none"> <li>• Field of view larger than TEM</li> <li>• Mechanical stage and stitching increased field of view</li> <li>• Can yield chemical information</li> </ul>	<ul style="list-style-type: none"> <li>• High resolution</li> <li>• Can yield chemical information</li> <li>• Sensitive to light elements</li> </ul>
<b>Disadvantages</b>	<ul style="list-style-type: none"> <li>• Lowest resolution</li> <li>• No chemical information possible</li> </ul>	<ul style="list-style-type: none"> <li>• Conductive samples or coating required</li> </ul>	<ul style="list-style-type: none"> <li>• Difficult to be representative due to small field of view</li> <li>• Small samples size</li> <li>• Time consuming sample preparation</li> </ul>

Table 2.6 - Table detailing the advantages and disadvantages of the mechanical test techniques (29, 52-55)

	<b>Small Punch Tensile Testing</b>	<b>Tensile Testing</b>	<b>Compression Testing</b>	<b>Hardness Testing</b>
<b>Advantages</b>	<ul style="list-style-type: none"> <li>• Small sample size required</li> <li>• More effective than conventional tensile testing with brittle materials</li> <li>• Suitable for irradiated materials and so greater body of data for fusion relevant materials</li> </ul>	<ul style="list-style-type: none"> <li>• Well understood</li> <li>• Easy to conduct</li> </ul>	<ul style="list-style-type: none"> <li>• Samples easy to produce</li> <li>• Compressive properties less affected by lack of ductility</li> </ul>	<ul style="list-style-type: none"> <li>• Samples easy to produce</li> <li>• Rapid data acquisition</li> <li>• Hardness properties less affected by lack of ductility</li> </ul>
<b>Disadvantages</b>	<ul style="list-style-type: none"> <li>• Surface layer not representative of bulk</li> <li>• Stress varies through test</li> <li>• Difficult to compare to conventional tensile tests</li> </ul>	<ul style="list-style-type: none"> <li>• Brittle materials likely to fail during test piece clamping</li> </ul>	<ul style="list-style-type: none"> <li>• Not affected by presence of cracking therefore limited use to compare build quality</li> </ul>	<ul style="list-style-type: none"> <li>• Low loads possible for brittle materials</li> <li>• Vickers hardness not suitable near sample edge</li> </ul>

As certain techniques (Optical Microscopy (OM), Scanning Electron Microscopy (SEM) and Electron Dispersive X-ray Spectroscopy (EDX)) are commonly used no further discussion will be conducted. Good reference material can be found elsewhere (51).

Table 2.7 - Table detailing advantages and disadvantages of chemical analysis techniques (51, 56-59)

	EDX	WDX	Auger	Raman	XRF	ICP	IGF	XRD	SIMS
<b>Advantages</b>	<ul style="list-style-type: none"> <li>• Rapid data acquisition</li> <li>• Large elemental spectrum given</li> </ul>	<ul style="list-style-type: none"> <li>• Can differentiate between elements where peaks overlap in EDX</li> <li>• Lower detection limits than EDX (10-100 ppm)</li> <li>• Suitable for light elements</li> </ul>	<ul style="list-style-type: none"> <li>• High spatial and elemental resolution</li> <li>• Suitable for light elements</li> </ul>	<ul style="list-style-type: none"> <li>• Non-destructive technique</li> <li>• Simple sample preparation</li> <li>• Rapid data acquisition</li> <li>• Sensitive to oxide bonds</li> </ul>	<ul style="list-style-type: none"> <li>• Non-destructive technique</li> <li>• Simple sample preparation</li> <li>• Rapid data acquisition</li> </ul>	<ul style="list-style-type: none"> <li>• Fast acquisition rate</li> <li>• More accurate than XRF</li> <li>• Suitable for most elements commonly used in alloys</li> </ul>	<ul style="list-style-type: none"> <li>• Accurate for determining light elements</li> <li>• Sample needed in specific dimensions or powder/granule form</li> </ul>	<ul style="list-style-type: none"> <li>• Non-destructive technique</li> <li>• Molecular, microstructural and residual stress information possible</li> </ul>	<ul style="list-style-type: none"> <li>• Simple sample preparation</li> <li>• Versatility in material and sample state</li> <li>• High spatial resolution in image area of interest (~100 nm)</li> <li>• Detection threshold (~ppb/ppi)</li> </ul>
<b>Disadvantages</b>	<ul style="list-style-type: none"> <li>• Lower resolution that alternative techniques (micron size interaction volume)</li> <li>• Large sampling area</li> <li>• Problems with overlap in element peaks</li> <li>• Problems with detection of light atomic elements</li> </ul>	<ul style="list-style-type: none"> <li>• Narrow detection range in usage</li> <li>• Lower spatial resolution than Auger/SIMS</li> <li>• Time consuming</li> <li>• Standards needed for quantification</li> </ul>	<ul style="list-style-type: none"> <li>• Hydrogen and helium not detectable</li> <li>• Surface technique</li> <li>• Quantification difficult</li> </ul>	<ul style="list-style-type: none"> <li>• Raman effect weak</li> <li>• Not suitable for metallic bonds</li> </ul>	<ul style="list-style-type: none"> <li>• Poorer chemical resolution</li> <li>• No spatial resolution</li> </ul>	<ul style="list-style-type: none"> <li>• Requires acid dissolution for certain elements</li> <li>• Problems arise with spectral interference</li> <li>• No spatial or molecular information</li> </ul>	<ul style="list-style-type: none"> <li>• Destructive technique</li> <li>• Only suitable for interstitial impurities (C, O, N, H)</li> <li>• No spatial or molecular information</li> </ul>	<ul style="list-style-type: none"> <li>• Can have high concentration thresholds for detection</li> <li>• Derived from crystal structures so subsequent pattern analysis needed</li> <li>• Can be affected by sample preparation</li> </ul>	<ul style="list-style-type: none"> <li>• Quantification difficult</li> <li>• Sputtering destroys molecular information</li> </ul>



## **Raman Spectroscopy**

Raman scattering occurs when coherent light interacts with molecular vibrations resulting in a shift in the scattered light; The Raman effect is weak with 0.00001% of light experiencing a shift. Raman spectroscopy can be used to identify the vibrations and rotations of specific bonds. The Raman effect only occurs when the bonds can be polarised. The Raman shift corresponds to the strength and weight of the bonds with strong, light bonds experiencing a greater shift than heavy, weak bonds. Raman is particularly ineffective with metal-metal bonds as they are not easily polarised. Some bond vibrations are Raman active but inactive in infrared spectroscopy; Raman typically requires an overall change in bond length but does not require a change in dipole. Symmetric stretching of carbon dioxide, for example, would only be detected by Raman spectroscopy whereas the bending would only be detected by Infrared spectroscopy. Raman spectroscopy was utilised in this study due to its sensitivity to metal-oxide vibrations (57, 60-62).

## **Secondary Ion Mass Spectrometry (SIMS)**

SIMS analysis is a compositional analysis technique whereby an ion beam is used to sputter away material causing secondary ions to be ejected from the sample. These ions are measured by a mass spectrometer and the mass/charge ratios detected are used to identify chemical compositions. Due to the rastering of the beam across the imaging area a map can be developed. SIMS has high resolution in both elemental and spatial detection across the imaging area. Due to the ionisation process undertaken during the sputtering, the chemical information is destroyed so this cannot identify molecular information. Quantification of the material is difficult due to the similarity needed between the known standard and test

specimen in terms of alloy and impurity composition etc. and as such should be considered a semi-quantitative technique (58).

### **Inert Gas Fusion (IGF)**

Inert gas fusion (IGF) is a chemical analytical technique to determine the quantity of oxygen, nitrogen and hydrogen within a material. For this study, the primary element of interest was oxygen. IGF involves the material being added to a graphite crucible which is then heated to extremely high temperatures. This allows the energy intensive process of oxide reduction using carbon to be realised. Oxygen within the samples to be tested, then reacts with the carbon in the crucible reducing the oxides to form carbon monoxide or carbon dioxide. IR detection was then used to evaluate oxygen quantity in the material. Sources on the use of IGF for refractory metals can be found elsewhere and is considered accurate for oxygen contents in excess of 50 ppm in refractory metals (63, 64). The material is often broken down prior to testing which increases the likelihood of impurity pick up during preparation. It also provides an average value with no spatial distribution through the material. However, it is a relatively simple technique which could be used to provide threshold values of impurity elements. This would be of particular interest given the susceptibility of tungsten to interstitial embrittlement (65).

### **X-ray Diffraction (XRD)**

Lab based X-ray Diffraction (XRD) is a popular analytical technique, due to the relative simplicity of sample preparation, speed of data acquisition and variety of data (phase balance, crystallite size, residual stress, texture etc.) which can be found (29, 56). Both variation in grain size and residual stress can result in peak broadening; these effects can be separated

using the Williamson-Hall methodology, details of which can be found elsewhere (66). Composition in solid solutions can be estimated using Vegard's law where the lattice parameter of the solution varies linearly with the composition of its constituent parts (67). The technique can also be used on a wide variety of sample types with limited preparation; this allows for the comparison of powder and solid samples in LPBF. The results could be affected by sample preparation (excessive force in surface grinding of solid samples or irregular surfaces) with increasing sample roughness resulting in a slight peak shift to the left (68). Typically the peaks are normalised against the maximum intensity to correct for different signal intensities and to remove the effects of the background and allow for better comparison (29, 56).

### **Small Punch Testing**

Small Punch was a micro-mechanical test technique capable of producing load/displacement graphs from small discs (0.5 mm thick, 6 mm  $\varnothing$ ). The key advantage to the technique was the small amount of material required making it particularly desirable for irradiated material or as a pseudo-non-destructive testing technique. As the end use application for this study was nuclear fusion, techniques which were suitable for irradiated samples were of interest and as a result there was a greater body of data for relevant materials available for comparison. For LPBF processing this is also an advantage particularly within crack susceptible materials as the residual stress could increase with build height. It was difficult to compare the data produced in small punch testing to conventional tensile due to the variation in stress throughout the test. On initial contact of the sample by the die, the stress level was extremely high. It can be difficult for brittle materials to survive this initial contact. They are less likely to fail during pre-loading than more conventional tensile testing for example and are more applicable to determining part build quality than compression testing where cracks

within the sample will close during testing. The other key difficulty is that the surface of a material is different from that of the bulk and with such a thin sample there would be a higher proportion of surface material than that of a dog-bone tensile; however, this could be mitigated through careful sectioning and sample preparation from a larger blank using EDM cutting and surface finishing (52-54).

## **2.5 – Laser Powderbed Fusion (LPBF)**

LPBF is a layerwise manufacturing technique which had been found to result in anisotropic mechanical properties, microstructure and defects which were different from those common in conventional manufacturing. This review will detail the defects, potential limitations associated with common energy density relationships, the raw materials used in LPBF, residual stress development in LPBF and the current literature available on LPBF processing of tungsten and other refractory metals.

A key difficulty associated with the review of literature associated LPBF processing is the number of variables in effect. Figure 2.18 showed the input parameters that affecting build quality. In addition, the spacing between adjacent laser scan tracks and material substrate could also cause variation. Rarely are all these parameters clearly detailed; thus, when comparing studies, additional factors may have been at play that were not considered. An example of which, Ivekovic et al., 2018 (31) compared two machine platforms and found one to have improved build quality; it was concluded that the improvement was due to the lower oxygen content but there were other platform variables including a smaller laser spot size (31, 69).

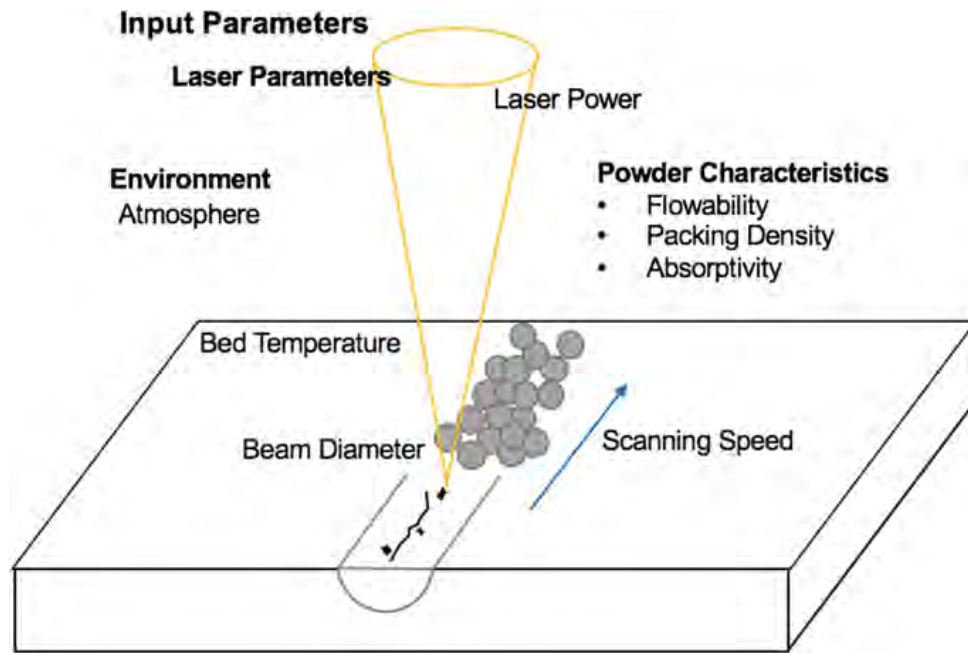


Figure 2.18 - Schematic diagram showing input parameters that will affect build quality. Taken from Field et al., 2020 (69)

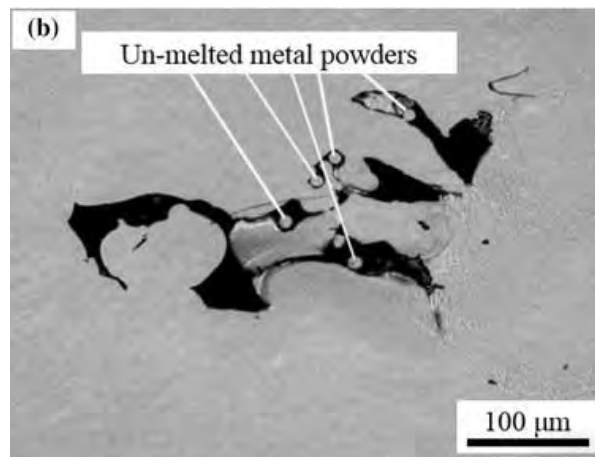
### 2.5.1– Defects in LPBF Processing

Defects in LPBF processing could be broken down into three key categories; porosity, cracking and lack of fusion defects due to insufficient energy input. Some defects, particularly within cracking, were more likely to occur within specific materials or alloy systems including Strain Age Cracking, Liquation cracking, Ductility Dip Cracking (DDC). This review will focus on hot cracking as it was the most likely mechanism to occur within a pure material system (70, 71).

The mechanisms behind defect formation were found to be complex; Galy et al., 2018 (72) mapped possible causes of defects formation in LPBF aluminium, however, it could be simplified to incorrect input energy (either insufficient or excessive) or impurities from the raw material or build environment (71, 72).

Very fine spherical gas porosities were also found to be possible, if gas atomised powders were used in the LPBF process due to the introduction of the shielding gas used in the powder manufacture. In aluminium alloys, this may also result from fine hydrogen pores due to moisture in the powder particles, but is not readily seen in other material systems (73). Due to the high melting points of refractory metals, the powders are more typically produced through chemical reduction or mechanical grinding. Plasma spheroidisation is used to form spherical powders without the introduction of gas porosity (30, 71).

With insufficient energy input, lack of fusion defects (LOF) were found to be the most common. Unmelted powder particles can often be seen around sights of LOF defects where there was insufficient melting or insufficient spreading or wetting of the molten material to form defect free material (see Figure 2.19) (19, 71, 72). These defects were characterised by their irregular shape. Increasing the laser power, thus expanding the penetration depth typically reduced the quantity of defects.



*Figure 2.19 - Micrograph showing LOF defect in LPBF material. Taken from Zhang et al., 2017 (71)*

Excessive energy input was also found to be detrimental to LPBF build quality. Spherical keyhole pores were shown to form upon material vaporisation. Trapp et al., 2017 (74) found the modelled boiling power in tungsten to be 446 W; it was therefore unlikely that in pure tungsten keyholing would occur. Alloys were more likely to suffer keyhole porosity due to

the vaporisation of lower melting point additions (71, 74). Defects such as keyholing, Figure 2.20, were shown to be more likely in lower melting point systems or alloys which had constituents with significantly different vaporisation temperatures. A W-Cr alloy would suffer from this; chromium had boiling point of 2671 °C versus the melting point of tungsten of 3420 °C (8).

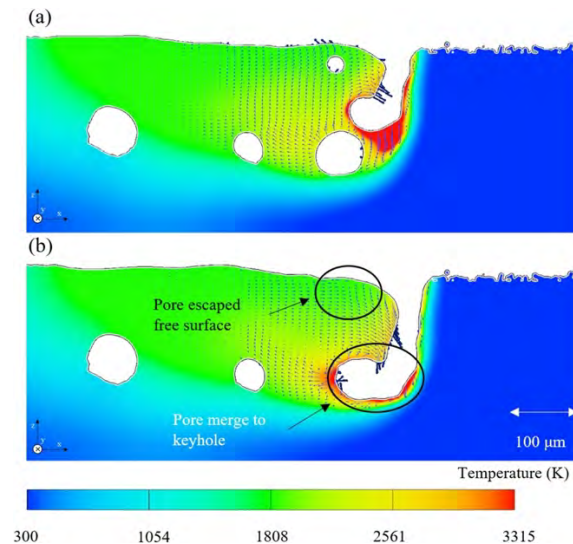
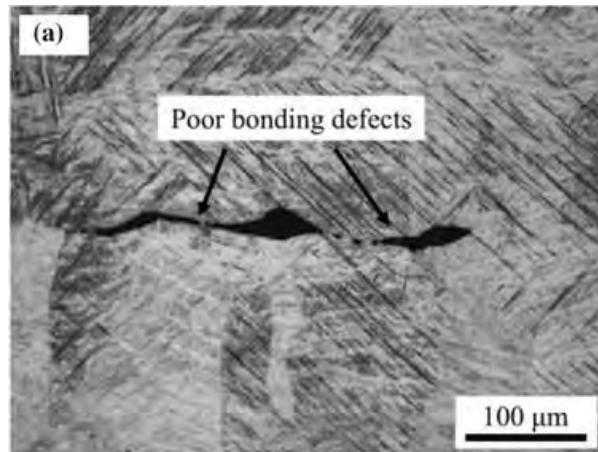


Figure 2.20 - Simulation of keyhole pore formation in Ti-6Al-4V. Taken from Bayat et al., 2019 (75)

Impurities such as the surface oxide of the powder, or the residual oxygen content within the chamber has been shown to affect the oxygen content within the final part (9). The presence of oxides, such as alumina, has been shown to affect the surface tension altering the wettability of the tracks and increasing the likelihood of lack of fusion defects (19, 71, 72). This was covered in greater detail in Section 2.2.4. Figure 2.21 showed an example of a poor bonding defect (76). Such defects are common in other manufacturing techniques such as casting where double oxide film defects have been found to prevent bonding (77).



*Figure 2.21 - Micrograph showing poor bonding defect in LPBF material. Taken from Zhang et al., 2017 (71)*

Laser scan strategy was shown to have a significant effect on cracking. Figure 2.22 showed the distribution of cracking within a CM247LC alloy along with the laser scan islands highlighted in blue. This showed the importance of laser input variables in materials prone to cracking such as tungsten (78). Hot cracking principally occurred due to the effects of shrinkage during cooling. The presence of impurities or other defects could weaken the material and the low melting point phases act as an initiation site for hot cracking. It was shown that tungsten typically had a highly ordered scan pattern in high density LPBF tungsten whereas in lower densities the cracking was more irregular initiating from sites of porosity (30, 31). Reviews of the cracking in welding and in the LPBF of tungsten could be found in Sections 2.3 and 2.5.5 respectively.



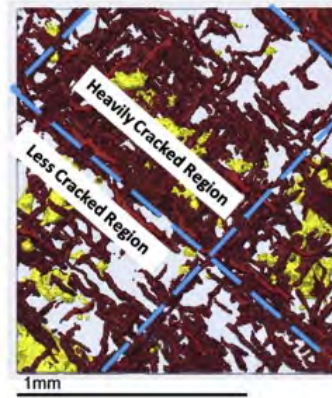


Figure 2.22 - MicroCT data showing the cracks (red) and voids (yellow) in the XY plane with the dashed lines representing the approximate position of the pattern boundaries. Taken from Carter et al., 2014 (78)

Defects within LPBF processing have been shown to be affected by the presence of impurities, and the input parameters used; it has also been shown that certain material systems have a greater likelihood of certain defect types forming such as DDC in nickel superalloys (70). It was shown that laser scan pattern as well as input parameters affected the defect density and distribution within LPBF material, highlighting the need to tailor laser scan parameters to optimise build quality (78). When investigating a new material system, a comprehensive parametric study should be undertaken to minimise defects within the samples.

### 2.5.2– Energy Density Relationships

There are a significant number of processing variables to consider with Laser Powderbed Fusion (LPBF) processing. In order to simplify the situation, the additive manufacturing community has used a number of ‘energy density’ parameters to group the key variables into a single value (Equations 2.3-2.6).

The most common of these energy density relationships are listed below:

Volumetric Energy Density, VED ( $\text{Jmm}^{-3}$ ):

$$VED = \frac{P}{v \cdot h \cdot t} \quad (\text{Equation 2.3})$$

Areal Energy Density AED (Jmm<sup>-2</sup>):

$$AED = \frac{P}{v \cdot h} \quad (\text{Equation 2.4})$$

Linear Energy Density, LED (Jmm<sup>-1</sup>):

$$LED = \frac{P}{v} \quad (\text{Equation 2.5})$$

Global Energy Density, GED (Jmm<sup>-2</sup>):

$$GED = \frac{P}{v \cdot d} \quad (\text{Equation 2.6})$$

Where P is power (W), v is the laser scanning speed (mms<sup>-1</sup>), h is the scan spacing (mm), t is the layer thickness (mm), and d is the laser beam diameter (mm)

These arose from the welding community that has also utilised energy density relationships (see Equation 2.7):

$$ED_{weld} = \frac{I \cdot V}{v} \quad (\text{Equation 2.7})$$

Where ED<sub>weld</sub> is the energy density of the weld (Jmm<sup>-1</sup>), I is the welding current (A), V is the welding voltage (V) and v is the welding speed (mms<sup>-1</sup>)

As part of this review, 20 papers with above average citations which utilised the energy density relationships were discussed here. Table 2.8 showed the number of papers utilising each of these density relationships (29, 31, 32, 55, 71, 72, 79-92).

*Table 2.8 - Table showing the papers reviewed utilising each energy density relationship*

	VED	AED	LED	GED
No. of studies	12	3	4	1

From this it could be seen that in the sample selected, the VED is by far, the most commonly used energy density relationships, and will be the focus of this review.

Some studies have suggested limitations to the suitability of these relationships, particularly Prashanth et al, 2017, (79) which investigated the efficacy of the volumetric energy density relationship in an Al-Si alloy. Figure 2.23 showed micrographs of the alloy produced with consistent VED of  $55 \text{ Jmm}^{-3}$  which corresponded to parameters of 40 W power input with a  $182 \text{ mms}^{-1}$  scan speed (h) as well as the optimised input of 320 W and  $1455 \text{ mms}^{-1}$  (a). As could be seen, significant variation in density was noted, with a maximum density in excess of 90 % and minimum density around 40 % theoretical density (79).

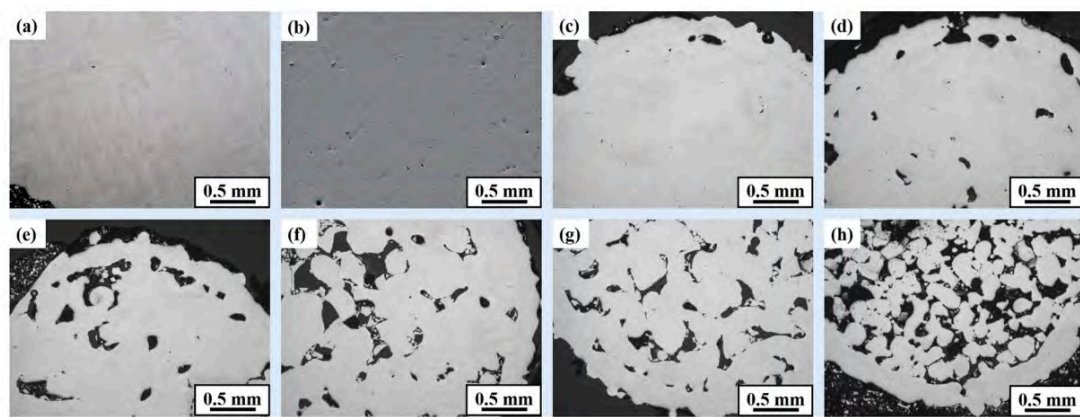


Figure 2.23 - OM micrographs of Al-12Si LPBF samples with VED of  $55 \text{ Jmm}^{-3}$  but varying parameters a) 320 W,  $1455 \text{ mms}^{-1}$ , b) 280 W,  $1273 \text{ mms}^{-1}$ , c) 240 W  $1091 \text{ mms}^{-1}$ , d) 200 W,  $910 \text{ mms}^{-1}$ , e) 160 W  $728 \text{ mms}^{-1}$ , f) 120 W  $546 \text{ mms}^{-1}$ , g) 80 W  $364 \text{ mms}^{-1}$  and h) 40 W  $182 \text{ mms}^{-1}$ . Taken from Prashanth et al., 2017 (79)

It has been noted that a constant VED could be achieved with significantly different input parameters (82); Carter, 2013 highlighted the variation in thermal energy input between two parameters with the same VED by utilising the  $n_3$  value (proportional to the product of power and laser scanning speed) from welding literature. It was shown that parameters 200 W,  $200 \text{ mms}^{-1}$  had the same VED as 100 W,  $100 \text{ mms}^{-1}$  but would have significantly different  $n_3$  values (70).

Trapp et al., 2017 (74) modelled minimum power required for melting and boiling to occur. For tungsten, these were determined to be 286 W and 446 W respectively. However, it has been shown experimentally melting can occur at lower powers. This is possibly due to

variations in absorptivity with metal-oxides having higher absorptivity than the base metal as well as varying absorptivity occurring with oxide volatilisation (32, 74). However, if the laser power was within the modelled range for a given VED, this should be optimum for minimising build defects although it may be possible to lower power inputs slightly. Numerous studies used VED to determine parameters required to maximise density of samples produced. Greater problems were found when attempting to correlate VED to microstructure or cracking density as these were more strongly related to thermal input (79, 81, 82).

The other key weakness to the VED relationship is the assumption that all parameters have equal weighting on the required outcome (typically density). However, Eagar and Tsai, 1983 (93) showed that for a laser with Gaussian distribution the peak temperature reached was proportional to the ratio of power to the square root of the travel speed, suggesting hatch spacing and layer thickness would have less impact (82, 93). Bertoli et al., 2017 (82) found increasing laser power for a given VED increased weld depth penetration (82).

Some studies offered alternatives particularly when detailing the limitations of these relationships, the most common of which were the specific enthalpy relationship and the normalised energy density relationships (see Equations 2.8 and 2.9)(81, 94-96).

- Specific enthalpy equation

$$\Delta H = \frac{A \cdot P}{\rho \sqrt{\pi \cdot \alpha \cdot v \cdot \phi^3}} \quad (\text{Equation 2.8})$$

Where  $\Delta H$  is Specific Enthalpy ( $\text{Jkg}^{-1}$ ),  $A$  is the laser absorptivity,  $P$  is the laser power (W),  $\rho$  is the material density ( $\text{kgm}^{-3}$ ),  $\alpha$  is the thermal diffusivity ( $\text{m}^2\text{s}^{-1}$ ),  $v$  is laser scanning speed ( $\text{ms}^{-1}$ ), and  $\phi$  is laser beam diameter (m) (81)

- NED equation

$$E_0^* = \frac{A \cdot q}{2 \cdot v \cdot l \cdot h} \cdot \frac{1}{\rho \cdot C_p \cdot (T_m - T_0)} \quad (\text{Equation 2.9})$$

Where  $E_0^*$  is Normalised Equivalent Energy Density,  $A$  is the laser absorptivity,  $q$  is the laser power (W),  $v$  is laser scan speed ( $\text{ms}^{-1}$ ),  $l$  is the layer height (m),  $h$  is the hatch spacing (m),  $\rho$  is the material density ( $\text{kgm}^{-3}$ ),  $C_p$  is the specific heat capacity ( $\text{Jkg}^{-1}\text{K}^{-1}$ ),  $T_m$  is the melting temperature (K) and  $T_0$  is the bed temperature (K) (94)

Strut thickness in Ti-6Al-4V was found to vary linearly with specific enthalpy causing an increase in specific modulus. It was also found to be effective in correlating melt pool depths in 316L. However, assuming a single material batch, the absorptivity, density, latent heat of fusion and thermal diffusivity of the powder would be consistent (see Equation 2.10). The ratio of power to the square root of scan speed was shown to correlate to the peak temperature reached in the material. However, laser beam diameters have been shown to vary with laser power (see Appendix A); the beam radius would have triple the effect of the laser scanning speed. As this varied with power, it would become the dominant input variable (81, 95).

$$\Delta H \propto \frac{P}{\sqrt{r^3 \cdot v}} \quad (\text{Equation 2.10})$$

The NED relationship would be particularly promising as it had been used to produce processing diagrams suitable for multiple materials and capable of determining the onset of different defects. However, this still assumed power, scan speed, hatch spacing and layer thickness had the same effect on process quality and therefore would suffer the same criticisms as VED relationship (94).

Despite the concerns raised, a large number of studies have still been undertaken using energy density type relationships and there is little consistency in the energy density relationships used. Additionally, all previous energy density limitation studies have been conducted on alloys which may complicate the issue due to differing melt behaviours of the various constituents. Further study should investigate the efficacy of energy density relationships for pure material systems.

### **2.5.3 – Raw materials in LPBF Processing**

Tan et al., 2017 (84) succinctly reviewed the effect of powder granulometry on build quality; the powder preparation techniques of water, gas and plasma atomisation as well as chemical reduction were summarised. Mechanical grinding could also be used however, the quality of powder produced was generally lower as the size and morphology of the material cannot be controlled. Water and gas atomisation can be used for LPBF fusion. Water atomisation was shown to give a greater impurity content and poorer morphological control (84). While gas atomisation produced generally spherical powders, they suffered from gas porosity which entered during the atomisation process (71). Due to the high melting points of the refractory metals these techniques would not be suitable and typically, chemical reduction or plasma spheroidisation was used (30). Chemical reduction produced an irregular morphology but with no internal porosity and low levels of impurity (30). Plasma spheroidised material is powder which was previously reduced in order to improve morphological control. Care must be taken in order to limit the impurity pick up during the second processing stage and the increased cost must also be considered in comparison to the improved quality. Chemically reduced powder was sourced for this study at £70/kg in comparison to £150/kg for the plasma spheroidised powder.

A number of studies have investigated powder characteristics either experimentally or via modelling, but the effects these have on final build quality is not well quantified. Wang et al., 2017 (30) showed that spheroidised powders had 18 % higher laser absorptivities than their polyhedral counterparts, with values of 0.68 and 0.5 respectively. This would promote greater densification for a given energy input (30). Through modelling Boley et al., 2016 (97) predicted that the absorptivity of spherical powders with a Gaussian size distribution would be 0.63. The measured value for tungsten powder, however, was 0.81, significantly higher than that of Wang et al., 2017 (30) and the modelled value. The authors attributed this discrepancy to a non-spherical morphology with surface roughness increasing the absorptivity. Large flat surfaces or facets in the polyhedral powder used in the study by Wang et al., 2017 (30) may more closely mimic a flat surface which Boley et al., 2016 (97) predicted would have an absorptivity of 0.4 and was found experimentally to vary between 0.25 and 0.55 by Trapp et al., 2017 (74) depending on laser powder used. This may explain some of the discrepancy found in the values but also shows that absorptivity varies significantly with morphology and literature values are unlikely to be reliable (see Table 2.9) (30, 74, 97).

The thermal conductivity in powders was significantly lower than that of the bulk material due to the ineffective conduction through the gas voids surrounding the particles. Increasing the packing density was found to increase the thermal conductivity as there are often a greater number of particles in contact for conduction (98).

The characteristics of the powder play a significant role in the occurrence of defects within a part, and good flowability and high packing density are noted to improve overall quality as high packing density increases particle contact points thereby increasing thermal conduction

through the powder bed. The packing density of powders is known to be affected by their morphology with spherical powders having the highest packing density and irregularly shaped particles having a significantly lower one for a normal powder size distribution. Increasing the quantity of fine powder particles can increase packing density but at the risk of flowability (99). Lee et al., 2015 (100) showed an increase in powder packing density increased the likelihood of a continuous melt track forming due to a more consistent powder layer preventing fluid instabilities and thus, balling. It was suggested that this was due to an increased downward fluid convection with lower packing density which further destabilised the melt pool (100). Spherical powder particles also exhibit better flowability, allowing for a more uniform layer spread during LPBF production (84). Egger et al., 1999 (101) found that typical packing densities within a powder bed vary between 40 and 60% (101). Packing densities on the lower end of the spectrum will lead to less uniform heat input, asymmetrical shrinkage and greater irregularities in recoating powder in subsequent layers due to the inherent roughness of the previous layer meaning powder particles will sit in depressions from the previous layer leaving potential gaps in powder coverage prior to melting as investigated in layer thicknesses of 30 -110  $\mu\text{m}$  (84).



Table 2.9 - Summary of Reported Laser Absorptivity Values. Taken from Field et al., 2020 (69)

Study	Powder Morphology/Preparation Method	Experimental Method	Absorptivity	Comments
Wang et al. <sup>[10]</sup>	plasma spheroidized polyhedral	temperature increase measured from insulated base plate with pre-deposited powder during laser irradiation	0.68 0.5	powder pre-deposited on plate not representative of LPBF temperature increases of < 1000 K, well below melting point of tungsten laser wavelength of 1 $\mu\text{m}$
Boley et al. <sup>[21]</sup>	spherical (Gaussian distribution) flat plate irregular	modeled-ray trace calculations of the laser through Fresnel reflections until power reaches 0.01 pct incident power a thin layer of powder in a refractory metal disk ( $\varnothing \sim 1 \text{ cm}$ ) with thermal insulation and thermocouples beneath the disk to measure temperature increase during laser irradiation	0.63 0.4 0.81	laser wavelength 970 nm layer thickness of 100 $\mu\text{m}$ Trapp et al. found increased powder thickness increase number of reflections and increase absorptivity
Trapp et al. <sup>[20]</sup>	flat plate	temperature increase during laser irradiation measured on 0.5-mm-thick disk of tungsten ( $\varnothing 10 \text{ mm}$ ) within a porous alumina holder for thermal isolation with thermocouples attached to disk base	0.25–0.55	laser scanning speed 1500 mm/s power variation 50–500 W Yb-fiber laser 65 $\mu\text{m}$ absorptivity varied dependent on conduction or keyholing mode

#### **2.5.4 – Reduction in Residual Stress through Bed Heating in LPBF Processing**

Various studies have investigated cracking properties of tungsten under thermal shock. Hirai et al., 2009 (102) showed there were two main cracking morphologies present; macro-cracks which occurred when the bulk material was below the Ductile-Brittle Transition Temperature (DBTT) due to the intrinsic brittleness of the material and a micro-cracking network occurring on grain boundaries due to high thermal gradients. Stresses were induced due to the surface of the material having expanded with the heat input in comparison to the constrained cooler material in the bulk. This resulted in tensile stresses upon cooling of the surface and resulted in cracking of the weakened grain boundaries (due to oxygen embrittlement) when those stresses exceeded its ultimate tensile strength (UTS) (102).

The intrinsic brittleness of tungsten, combined with the high cooling rates associated with LPBF, led to significant micro-cracking along grain boundaries. This is due to stresses induced in the material because of thermal expansion differential between the melting point of the material and the constrained base plate temperature. This is worsened by the effect of strain rate sensitivity for tungsten which means that the material cannot withstand the induced strain rates which occur under rapid cooling. One potential method to combat this phenomenon was through bed pre-heating which would both reduce the temperature differential within the system and reduce the cooling rate. Various studies have investigated the effect of pre-heating on the residual stresses within a component although these were conducted on more conventional materials including aluminium, titanium and steel (103-106). Studies have shown that pre-heating a steel alloy to 160 °C decreased residual stress by 40 % (104) and when producing aluminium components, pre-heating to 250 °C was found to completely remove all distortions (105). Another study, working with a steel alloy found that

while deformations in the component were only reduced by 14.3 % as a result of pre-heating via laser scanning, residual stresses were reduced to a fifth of the original value (103).

Given the high melting point (3422 °C) and thermal conductivity ( $175 \text{ Wm}^{-1}\text{K}^{-1}$ ) and high DBTT (400-600 °C) and strain rate sensitivity (6, 107), it was anticipated that significant bed heating would be required to reduce the residual stress sufficiently to reduce cracking.

### 2.5.5 – LPBF Processing of Tungsten

Limited literature exists on LPBF processing of pure tungsten. Initial studies were generally conducted on lower power systems (<200 W); as a result of the lower input power, the samples had significant incomplete consolidation (presence of lack of fusion defects) and required low scan speeds (<100  $\text{mms}^{-1}$ ) reducing the productivity of the process. Prior to 2019, the maximum densities reported were generally <85% of the theoretical density when processing tungsten or molybdenum (108, 109). To combat this, many studies used binder materials (e.g. Ni, Cu, Fe) to surround unmelted tungsten particles (see Figure 2.24) (110, 111). This both lowered the operating service temperature of the component and increased the activity of the material making it unsuitable for nuclear fusion reactors (112).

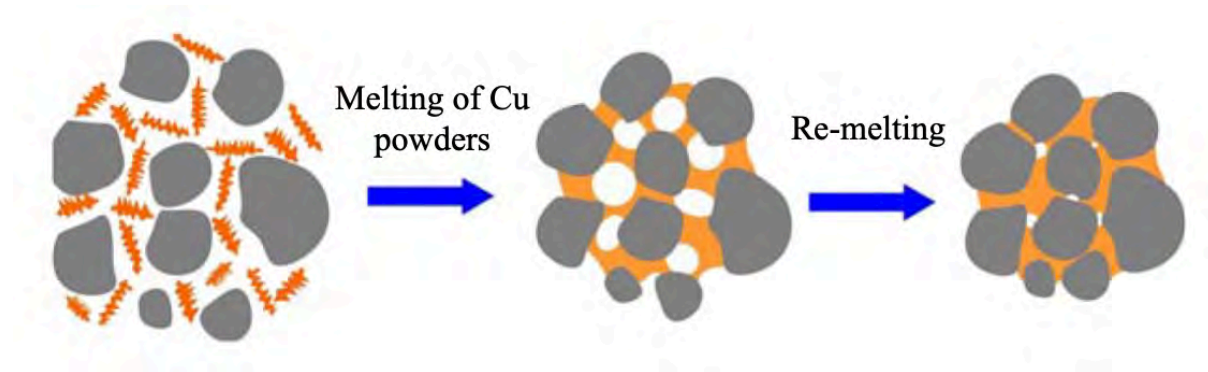


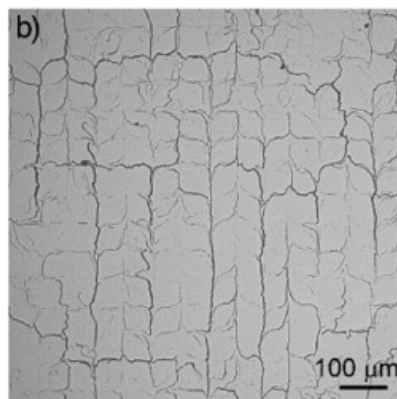
Figure 2.24 - Melting and solidification process of a W-Cu alloy during LPBF processing. Taken from Li et al., 2010 (111)

As mentioned in Section 2.5.2, Trapp et al., 2017 (74) modelled minimum power required for melting and boiling to occur using FE analysis. For tungsten, these were determined to be 286 W and 446 W respectively. However, it was found that melting could occur at lower powers due to varying absorptivities between the solid and liquid metal as well as the metal oxide. Wang et al., 2017 (30) and Faidel et al., 2015 (109) found that an input power of 200 W was insufficient to densify high melting point materials like tungsten and molybdenum. However, with a fine spot size (43  $\mu\text{m}$ ), low apparent scan speeds and good processing atmosphere, Sidambe et al., 2019 (32) yielded densities of 94-98 % using a Renishaw AM125 equipped with 200 W laser (30, 32, 74, 109).

In LPBF processing, the ease of processing materials was determined in terms of their weldability; materials with lower thermal conductivities, melting points, surface tension (resulting from their wettability and the formation of oxides) and viscosities were determined to be more readily weldable. Materials with high coefficient of thermal expansion may also crack more readily under constraint. There have been known difficulties with processing aluminium due to its conductivity and affinity to oxygen, which can vary surface tension of the weld track due to the formation of its high melting point oxide. Tungsten has high viscosity, surface tension and thermal conductivity and therefore would suffer many similar problems to aluminium despite the volatilisation of its oxide. As a result, Zhou et al., 2015 (19) showed tungsten had a predisposition toward balling due to its solidification time being much less than the spread time (46  $\mu\text{s}$  vs. 86.3  $\mu\text{s}$ ) suggesting solidification would take place before complete spreading occurred (19). Thijs et al., 2013 (113) investigated LPBF processing of tantalum, and while the microstructure was similar to those of studies in LPBF tungsten, no microcracking was present (113). Tantalum would have the high cohesive energy associated with tungsten but has a thermal conductivity less than one third of that of

tungsten which would increase the solidification time (19, 113). Tantalum and tungsten, like many refractory metals have low coefficients of thermal expansion ( $6.3 \times 10^{-6}$  and  $4.5 \times 10^{-6} \text{ K}^{-1}$ ) in comparison to iron which ( $12 \times 10^{-6} \text{ K}^{-1}$ ). It is therefore likely other mechanisms dominate given the poor weldability of tungsten despite its low coefficient of thermal expansion (8).

Increasing the density of tungsten components was found to be possible with increasing laser power (400 - 500 W systems). The machines used were a KU Leuven in-house machine, ProX DMP320 and an EOS M290 with spot sizes  $<100 \mu\text{m}$ . It was found that densities of  $\sim 98\%$  were possible under optimal processing conditions where lack of fusion defects had been eliminated. The variation from theoretical density was due to the presence of extensive cracking in the material (29, 31).



*Figure 2.25 - Optical micrograph showing ordered cracking in LPBF tungsten produced with  $400^\circ\text{C}$  bed heating ( $\text{VED } 475 \text{ Jmm}^{-3}$  built on in-house machine). Taken from Ivekovic et al., 2018 (31)*

The cracking was seen to form a pattern correlated to the laser scan path, and expected residual stress (see Figure 2.25) with cracking at the centre and edges of the scan track as well as chevron cracking against the heat flow as seen in the microstructure development in welding (31). As has been seen previously tungsten had a high likelihood of thermal shock (2). A threshold power density of  $0.3 \text{ GW/m}^2$  in 5 ms was noted to form microcracks in

tungsten (102). Above this, fine microcracks occurred between larger macrocracks (see Figure 2.26). Similarities could be seen between Figures 2.25 and 2.26 with the finer chevron cracks forming around the coarser cracks at the edge of the weld tracks.

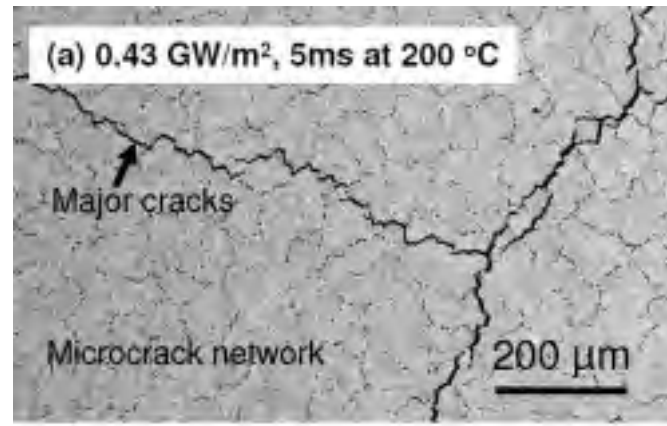


Figure 2.26 - Microstructure after a thermal shock load of  $0.43 \text{ GWm}^{-2}$  at  $200 \text{ °C}$ . Taken from Hirai et al., 2009 (102)

The main disadvantages associated with LPBF processing were the high cooling rates associated with LPBF processing ( $<10^6 \text{ Ks}^{-1}$ ) (50) and the residual oxygen in the chamber, even under argon processing. Platforms were shown to have significantly different levels of residual oxygen ( $<100 \text{ ppm}$ - $1800 \text{ ppm}$ ) although the oxygen content is likely to reduce during processing as can be seen in Appendix A (31, 32). Ivekovic et al., 2018 (31) studied tungsten and tungsten alloy samples produced with two different machine platforms with different oxygen contents (50 ppm and 150-200 ppm). The difference in densities 93 % vs. 97 % achieved was attributed to this difference in oxygen content however the two machines had different spot sizes and other potential variables were not disclosed (31).

There was some variation in texture found in tungsten produced via LPBF. Both Sidambe et al., 2017 (18) and Tan et al., 2018 (29) showed strong intensity for the (110) and (211) planes (more so than the base powders) and a weak intensity for the (200) plane (18, 29). Typical AM microstructures have a strong texture in the  $<100>$  direction with respect to the build direction as  $<100>$  is the rapid solidification direction for cubic materials. However, Ivekovic

et al., 2018 (31) and Sidambe et al., 2019 (32) showed a texture in the  $\langle 111 \rangle$  direction with respect to the build direction (31, 32). In the study by Ivekovic et al., 2018 (31) there was a stronger texture in the  $\langle 111 \rangle$  direction with the addition of tantalum (31). Sidambe et al., 2019 (32) attributed this deviation from typical AM processes to the material properties of tungsten and subsequent process requirements. It was stated that the texture in  $\langle 100 \rangle$  direction arose from a shallow elongated melt pool which formed due to high scan speeds and low thermal conductivity. With tungsten having a high melting point and therefore requiring slower scan speeds coupled with its high thermal conductivity the melt pool was expected to deepen (32).

Some of the studies utilised mechanical properties (compression strength and hardness) as a way of ranking the samples produced (29, 114). Both studies found extremely high hardness values of 450 and 475  $H_v$ , but utilised low loads (50 g and 300 g respectively). Given the few indents conducted, it was possible that such low loads were utilised as greater loads would result in cracking at the corners of the indent, invalidating the test. The hardness values were higher than those found in conventional tungsten; recrystallised tungsten had a hardness value of 300  $H_{V30}$ . Compression testing was found to give compression strength results of over 1 GPa and 902 MPa respectively. It was also shown that microcracking had no impact on the compressive strength of the material. This is unsurprising as compressive testing would close cracks whereas tensile testing would cause them to open. The brittleness of a material is less significant in compressive testing as indicated by the high compressive strengths of ceramic materials ( $Al_2O_3$  5.5 GPa) (29, 55). The results from the mechanical testing may therefore have indicated the samples produced had significant degrees of brittleness. Tensile testing would provide a greater indicator as to the level and effect of cracking within the sample.

## 2.6– Tungsten Alloys

It has been noted extensively throughout this review, that processing of tungsten was found to be difficult and prone to cracking due to its intrinsic brittleness; it has also been noted that alloying has been shown to be effective in improving its processability. Possible alloying elements have generally been limited to rhenium or other refractory metals for high temperature requirements or the addition of more ductile elements to improve fabricability.

WHA have been the most commonly used commercial tungsten alloys; they form a 2-phase structure with up to a 30 % FCC matrix comprised of Ni-Fe, Ni-Cu intended to retard crack growth. However, as has previously been mentioned elements like nickel and copper were high activation materials and therefore were not suitable for nuclear fusion. Moreover, FCC materials have been noted to have a greater degree of swelling under irradiation than BCC materials. For this reason, WHA were not considered further within this study (22, 112, 115).

Other than WHA, two distinct categories exist when considering alloying with tungsten; alloys designed to overcome impurity embrittlement and those designed to increase strength. Reactive metals have generally been used to combat the former and rhenium for the latter. Alloys of W-25Re and Mo-35Re were found to ductilise tungsten and molybdenum taking the DBTT from 425 to -200 °C. It has been found that rhenium increases the amount of twinning that occurred within the material, strengthening it and improving the elongation to failure. However, the cost is prohibitive at \$585,000/tonne and the powder supply chain for this material was not as readily available. Rhenium has also been shown to worsen the oxidation resistance of the material (9, 33). Figure 2.27 showed the W-Re phase diagram, at the levels required for ductilisation the brittle sigma phase was also formed. This could



worsen ductility under subsequent irradiation and was therefore not investigated in this this study.

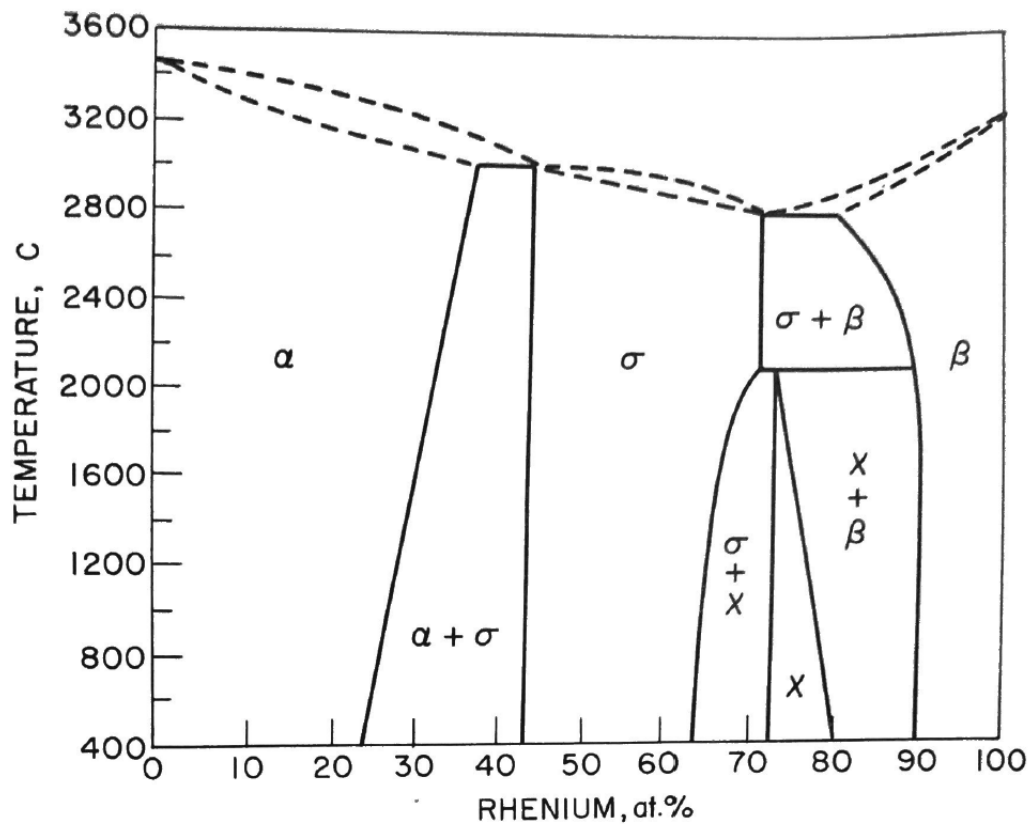


Figure 2.27 - W-Re phase diagram. Taken from Wilkinson, 1969 (2)

Various sources including Stringer and Rosenfield, 1963 and Wilkinson, 1969 (2, 116) state that the interstitial solubility level is dependent on the electron/atom (e/a) ratio. At e/a ratios greater than 5.7, oxygen is insoluble in the metal matrix, with substantial impurity solubility at e/a < 5.6. The number of valence electrons in a pure element is given by the group in which it is located in the periodic table. Thus, Ta, Nb and V have e/a ratios of 5 and W, Cr and Mo have an e/a ratio of 6 which is above the critical threshold for solubility. (4). In order to achieve an e/a ratio of 5.6 for tungsten alloying additions of a lower group metal would have to be added, with the amount required varying on the group number and atomic number of the metal selected.

Given the end use application of nuclear fusion, the effect of irradiation must also have been considered. As a result, solid solution alloys were preferred to prevent precipitate coarsening during irradiation. Figure 2.28 showed which refractory metals formed a continuous solid solution (grey square) with each metal (black square). All the refractory metals considered in this study formed continuous solid solution with a BCC structure (117).

<b>Ti</b>	V	Cr	Ti	<b>V</b>	Cr	Ti	V	<b>Cr</b>
Zr	Nb	Mo	Zr	Nb	Mo	Zr	Nb	Mo
Hf	Ta	W	Hf	Ta	W	Hf	Ta	W
<b>Ti</b>	<b>V</b>	<b>Cr</b>	Ti	V	Cr	Ti	V	Cr
<b>Zr</b>	Nb	Mo	Zr	<b>Nb</b>	Mo	Zr	Nb	<b>Mo</b>
Hf	Ta	W	Hf	Ta	W	Hf	Ta	W
<b>Ti</b>	V	Cr	Ti	V	Cr	Ti	V	Cr
Zr	Nb	Mo	Zr	Nb	Mo	<b>Zr</b>	Nb	Mo
Hf	Ta	W	Hf	Ta	W	Hf	Ta	W

Figure 2.28 - Diagram showing the formation of complete binary solid solutions between refractory metals. Taken from Mosca and Bozzolo, 2007 (117)

Tungsten-vanadium and tungsten-tantalum alloys were the most commonly investigated alloys. Tungsten-vanadium had a much larger solidus - liquidus range due to the vanadium melting point of 1926 °C and would have a lower maximum operating temperature than W-Ta alloys and were therefore deemed unsuitable for nuclear fusion applications. Tungsten-tantalum alloys have similar properties between the two elements with the added benefit of improved impurity solubility and oxidation properties from the tantalum, with a melting temperature range of only 30 °C, are therefore of interest as a method to improve the manufacturability of tungsten (see Figure 2.29) (8, 118).

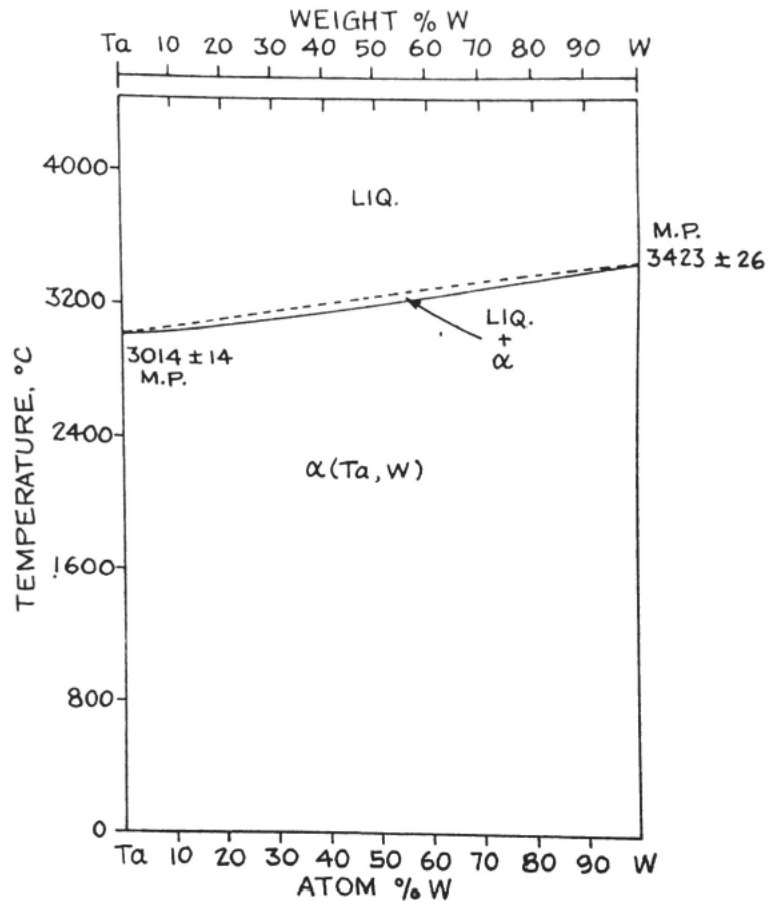


Figure 2.29 - W-Ta phase diagram. Taken from Moffatt, 1981 (118)

The conclusions have been mixed in regard to the efficacy of W-Ta alloys with regard to improved ductility. Scott and Knowlson, 1963 (26) found that tantalum was not effective as a deoxidant in tungsten and studies have shown that W-Ta alloys have higher DBTT than unalloyed tungsten (upto 1200 °C) (26, 119). Additionally, a higher hardness and the presence of cracking was also seen. However, this typically was found in W-Ta alloys with upto 5 w.t.%Ta. Low tantalum percentages have been used to maintain as high a thermal conductivity as possible, as well as to prevent tritium retention within the material. Tritium, as an isotope of hydrogen was more readily retained by tantalum than the Group VI metals and could be a problem with increasing Ta content (119, 120).

However, when the tantalum composition was increased to 15 w.t.% the properties were found to have improved; the material was found to be fully ductile by 700 °C with an

increase in ultimate flexural strength of more than 400 MPa and a more than three-fold increase in toughness (2.5 vs. 9 MPa.m<sup>0.5</sup>). Heterogeneities were found in the microstructure as a result of the elemental powder milling used for the experiments which may have worsened some of the properties (121). Ivekovic et al., 2018 (31) showed additions of 1, 5 and 10 w.t.% Ta lessened the presence of cracking within LPBF material although noted that even with preheating of up to 400 °C it was not sufficient to eliminate the cracking. It was also noted that the W-Ta alloys had a more refined grain structure in the XY direction which the Hall-Petch relationship would suggest would improve strength and toughness as well as overcoming the issues associated with grain growth in the fusion welding of unalloyed tungsten (9, 31).

Given the higher than usual oxygen content during LPBF fabrication and the somewhat promising initial results, W-Ta should be considered as a possible alloy for improving the LPBF processability of tungsten-based materials.

## **2.7– Concluding Remarks**

This literature review has summarised the factors likely to influence behaviour and properties of tungsten and relevant refractory metals, with particular regard to the intrinsic brittleness of the material and the reasons for this.

Due to the limited relevant LPBF literature on refractory metal processing, literature on welding and weld cracking was also presented. Based on this review it is clear that both impurity content and thermal history of the material (cooling rate and input process parameters) will affect the properties and cracking of tungsten. It is likely cracking cannot be avoided in the LPBF processing of pure tungsten without modifying the build set-up.

The literature review has identified the following gaps in knowledge which will be addressed by the aims and objectives of this study:

- The mechanical properties of LPBF material given the altered oxygen content, texture and grain size is unknown
- The effect of interstitial impurities at greater concentrations combined with the thermal history of LPBF is unknown
- The studies investigating powder absorptivity have been inconsistent in their results and require further investigation
- The defect mechanism in tungsten welding is well-defined but it is unclear as to how this would translate to the defect mechanism in tungsten
- The effect of bed heating is understood in conventional manufacturing but is limited to a single study in tungsten processing
- Ta additions have been shown to both improve and worsen mechanical properties depending on study; the effect of Ta additions in LPBF is not conclusive

## **2.8– Aims & Objectives**

Due to the intrinsic brittleness and associated difficulties in machining of tungsten, the current divertor designs are limited. Additive manufacturing, particularly Laser Powderbed Fusion (LPBF) offers greater flexibility both in complexity of geometry due to the netshape nature of the final component, and in potential alloy combinations with powder blending. Additionally, the low volumes required, combined with extreme environments mean using additive manufacturing to produce components of improved capability would be appealing to the fusion community. As a result, the UK Atomic Energy Authority has proposed research into the use of LPBF as a method to produce the high temperature divertor components. The

research presented within this thesis focuses on the practical challenges of producing this material via LPBF and on the materials science which can increase the understanding to overcome those challenges and acts as a feasibility study for the technique.

The overall aim of this project can be stated as:

*Investigate the feasibility of using Laser Powderbed Fusion (LPBF) as a processing method for tungsten and to explore methods to improve the processability with the aim of producing complex divertor type components.*

This aim can be broken down into a series of objectives for the research:

- To characterise the effect of these powder characteristics on build quality, in terms of density and the penetration depth of the fusion zone (Chapter 4).
- To optimise the LPBF processing parameters for pure tungsten using parametric studies to reduce defects and produce a fully dense material (Chapter 4).
- To identify the mechanism of defect production dominant in tungsten samples produced via LPBF (Chapter 4).
- To investigate the use of bed pre-heating to reduce remaining defects within the LPBF-fabricated pure tungsten (Chapter 5).
- To investigate the use of alloying with minor tantalum additions to reduce remaining defects within the LPBF-fabricated tungsten (Chapter 5).
- Finally, to investigate the use of alloying with minor tantalum additions combined with bed pre-heating to reduce remaining defects within the LPBF-fabricated tungsten (Chapter 5).

## 2.9 – References

1. Savitskii EM, Burkhanov GS. Physical Metallurgy of Refractory Metals and Alloys. New York: Consultants Bureau; 1970.
2. Wilkinson WD. Properties of Refractory Metals. New York: Gordon and Breach Science Publishers; 1969.
3. International Journal of Refractory Metals and Hard Materials: Elsevier; 2017 [Available from: <https://www.journals.elsevier.com/international-journal-of-refractory-metals-and-hard-materials>].
4. Tietz TE, Wilson JW. Behaviour and Properties of Refractory Metals. London: Edward Arnold; 1965.
5. Habashi F. Historical Introduction to Refractory Metals. Mineral Processing and Extractive Metallurgy Review. 2001;22(1):25-53.
6. Lassner E, Schubert WD. Tungsten. London, U.K.: ITIA; 2009. 134 p.
7. Lassner E, Schubert WD. Tungsten: Properties, Chemistry, Technology of the Element, Alloys, and Chemical Compounds. New York, U.S.: Plenum Publishers; 1999.
8. Wolfram Research. Element Data Source Information Illinois, U.S.2014 [Available from: <https://reference.wolfram.com/language/note/ElementDataSourceInformation.html>].
9. Lampman SR. Weld Integrity and Performance. Ohio, U.S.: ASM International; 1997.
10. Zhang P, Shen W, Zhou Y, Zhang Q. Mechanical properties of tantalum-tungsten interlayer between tungsten tile and thimble to prevent helium leak from He-cooled divertor. Journal of Physics: Conference Series. 2013;419:012025.
11. Maier V, Schunk C, Göken M, Durst K. Microstructure-dependent deformation behaviour of bcc-metals – indentation size effect and strain rate sensitivity. Philosophical Magazine. 2015;95(16-18):1766-79.
12. Yih SWH, Wang CT. Tungsten: Sources, Metallurgy, Properties, and Applications. New York: Plenum Press; 1979.
13. Beake BD, Harris AJ, Moghal J, Armstrong DEJ. Temperature dependence of strain rate sensitivity, indentation size effects and pile-up in polycrystalline tungsten from 25 to 950 °C. Materials & Design. 2018;156:278-86.
14. PLANSEE. Molybdenum. Slough, U.K.; 2017.
15. Cole NC, Gilliland RG, Slaughter GM. Weldability of tungsten and its alloys. Welding Research Supplement. 1971;50:419-26.
16. Farrell K, Schaffhauser AC, Stiegler JO. Recrystallization, grain growth and the ductile-brittle transition in tungsten sheet. Journal of the Less Common Metals. 1967;13(2):141-55.
17. Kolarikova M, Kolarik L, Vondrous P. Welding of thin Molybdenum Sheets by EBW and GTAW. Annals of DAAAM for 2012. 2012;23(1).
18. Sidambe AT, Fox P, editors. Investigation of the Selective Laser Melting process with tungsten metal powder. 19th Plansee Seminar; 2017; Reutte, Austria: University of Liverpool.
19. Zhou X, Liu X, Zhang D, Shen Z, Liu W. Balling phenomena in selective laser melted tungsten. Journal of Materials Processing Technology. 2015;222:33-42.
20. Stephens JR. Effect of Oxygen on Mechanical Properties of Tungsten. Washington, USA: NASA; 1963. Report No.: Technical Note D-1581.
21. Lancaster JF. Metallurgy of Welding. 1st ed. Cambridge, U.K.: George Allen & Unwin; 1965.
22. Danninger H, Atari A, Lux B, Kny E, Tschulik A. Embrittlement of tungsten heavy alloys by trace impurities and their analytical characterization. Fresenius' Zeitschrift für analytische Chemie. 1989;333(4):417-21.

23. Zies G, Wetzig K, Wilhartitz P, Grasserbauer M. Study of the phosphorus embrittlement in heavy metal alloys by a combination of SIMS and TEM. *Fresenius' Zeitschrift für analytische Chemie*. 1987;326(3):218-27.
24. Gludovatz B, Wurster S, Weingärtner T, Hoffmann A, Pippan R. Influence of impurities on the fracture behaviour of tungsten. *Philosophical Magazine*. 2011;91(22):3006-20.
25. Gludovatz B, Wurster S, Hoffmann A, Pippan R. Fracture toughness of polycrystalline tungsten alloys. *International Journal of Refractory Metals and Hard Materials*. 2010;28(6):674-8.
26. Scott MH, Knowlson PM. The welding and brazing of the refractory metals niobium, tantalum, molybdenum and tungsten — a review. *Journal of the Less Common Metals*. 1963;5(3):205-44.
27. Tran Huu L, Morniroli JP, Gantois M, Lahaye M. Brittle fracture of polycrystalline tungsten. *Journal of Materials Science*. 1985;20(1):199-206.
28. Braun J, Kaserer L, Stajkovic J, Leitz KH, Tabernig B, Singer P, et al. Molybdenum and tungsten manufactured by selective laser melting: Analysis of defect structure and solidification mechanisms. *International Journal of Refractory Metals and Hard Materials*. 2019;84:104999.
29. Tan C, Zhou K, Ma W, Attard B, Zhang P, Kuang T. Selective laser melting of high-performance pure tungsten: parameter design, densification behavior and mechanical properties. *Science and Technology of Advanced Materials*. 2018;19(1):370-80.
30. Wang D, Yu C, Zhou X, Ma J, Liu W, Shen Z. Dense Pure Tungsten Fabricated by Selective Laser Melting. *Applied Sciences*. 2017;7(4):430.
31. Iveković A, Omidvari N, Vrancken B, Lietaert K, Thijs L, Vanmeensel K, Vleugels J, and Kruth J-P. Selective laser melting of tungsten and tungsten alloys. *International Journal of Refractory Metals and Hard Materials*. 2018;72:27-32.
32. Sidambe AT, Tian Y, Prangnell PB, Fox P. Effect of processing parameters on the densification, microstructure and crystallographic texture during the laser powder bed fusion of pure tungsten. *International Journal of Refractory Metals and Hard Materials*. 2019;78:254-63.
33. Lessmann GG, Gold RE. Weldability of Tungsten Base Alloys. 50th American Welding Society Annual Meeting; Philadelphia, U.S.: U.S. Department of Energy, Office of Scientific and Technical Information; 1969.
34. Backman L, Opila EJ. Thermodynamic assessment of the group IV, V and VI oxides for the design of oxidation resistant multi-principal component materials. *Journal of the European Ceramic Society*. 2019;39(5):1796-802.
35. Joshi A, Strongin M. Surface segregation of oxygen in Nb□O and Ta□ alloys. *Scripta Metallurgica*. 1974;8(4):413-24.
36. Louvis E, Fox P, Sutcliffe CJ. Selective laser melting of aluminium components. *Journal of Materials Processing Technology*. 2011;211(2):275-84.
37. Tang M, Pistorius PC. Oxides, porosity and fatigue performance of AlSi10Mg parts produced by selective laser melting. *International Journal of Fatigue*. 2017;94:192-201.
38. Olakanmi EO, Cochrane RF, Dalgarno KW. A review on selective laser sintering/melting (SLS/SLM) of aluminium alloy powders: Processing, microstructure, and properties. *Progress in Materials Science*. 2015;74:401-77.
39. Gu DD, Meiners W, Wissenbach K, Poprawe R. Laser additive manufacturing of metallic components: materials, processes and mechanisms. *International Materials Reviews*. 2012;57(3):133-64.
40. Campbell J. Chapter 2 - Entrainment. In: Campbell J, editor. *Castings (Second Edition)*. Oxford: Butterworth-Heinemann; 2003. p. 17-69.



41. Reijonen J, Revuelta A, Riipinen T, Ruusuvoori K, Puukko P. On the effect of shielding gas flow on porosity and melt pool geometry in laser powder bed fusion additive manufacturing. *Additive Manufacturing*. 2020;32:101030.
42. Anwar AB, Pham Q-C. Selective laser melting of AlSi10Mg: Effects of scan direction, part placement and inert gas flow velocity on tensile strength. *Journal of Materials Processing Technology*. 2017;240:388-96.
43. Arısoy YM, Criales LE, Özel T. Modeling and simulation of thermal field and solidification in laser powder bed fusion of nickel alloy IN625. *Optics & Laser Technology*. 2019;109:278-92.
44. Hooper PA. Melt pool temperature and cooling rates in laser powder bed fusion. *Additive Manufacturing*. 2018;22:548-59.
45. Farrell K, Houston JT, Chumley JW. Hot Cracking in Fusion Welds in Tungsten. *Welding Research Supplement*. 1970;March:132-7.
46. Tabernig BR, N.; Joining of Refractory Metals and its Application. 17th Plansee Seminar; Reutte, Austria 2009.
47. Hunziker O, Dye D, Reed RC. On the formation of a centreline grain boundary during fusion welding. *Acta Materialia*. 2000;48(17):4191-201.
48. Leong KH. Laser welding of refractory metals. *Journal of Laser Applications*. 2001;13(5):199-203.
49. Savitskii EM, Tylkina MA, Ipatova SI, Pavlova EI. Properties of tungsten-rhenium alloys. *Metal Science and Heat Treatment of Metals*. 1960;2(9):483-6.
50. Wang X, Carter LN, Pang B, Attallah MM, Loretto MH. Microstructure and yield strength of SLM-fabricated CM247LC Ni-Superalloy. *Acta Materialia*. 2017;128:87-95.
51. ZEISS. Education in Microscopy and Digital Imaging Germanyn.d. [Available from: <http://zeiss-campus.magnet.fsu.edu/referencelibrary/basics/basicbooks.html>].
52. Sklenička V, Kloc L. 5 - Creep in boiler materials: mechanisms, measurement and modelling. In: Oakey JE, editor. *Power Plant Life Management and Performance Improvement*: Woodhead Publishing; 2011. p. 180-221.
53. Richardson M, Gorley M, Surrey E, Wynne B, Lowrie F. Realisation of Small Punch Testing to Accelerate Materials Qualification for Fusion Applications. In: Field A, editor. Oxford, U.K.: UKAEA; n.d.
54. Richardson M, Gorley M, Surrey E, Wynne B. An Investigation of the Mechanical Performance of Conventional and Additively Manufactured Vanadium. In: Field A, editor. Oxford, U.K.: UKAEA; n.d.
55. Guo M, Gu D, Xi L, Zhang H, Zhang J, Yang J, and Wang R. Selective laser melting additive manufacturing of pure tungsten: Role of volumetric energy density on densification, microstructure and mechanical properties. *International Journal of Refractory Metals and Hard Materials*. 2019;84:105025.
56. Cullity BD. *Elements of X-ray Diffraction*. 2nd ed. Massachusetts, U.S.: Addison-Wesley Publishing Company; 1978.
57. Renishaw. Raman Spectroscopy n.d. [Available from: <https://www.renishaw.com/en/raman-spectroscopy--6150>].
58. LSA. Secondary Ion Mass Spectroscopy Loughborough 2017 [Available from: <http://www.lsaltd.co.uk/methods/sims.php>].
59. Kohli R. Chapter 3 - Methods for Monitoring and Measuring Cleanliness of Surfaces. In: Kohli R, Mittal KL, editors. *Developments in Surface Contamination and Cleaning*. Oxford: William Andrew Publishing; 2012. p. 107-78.
60. Šćepanović M, Grujić-Brojčin M, Dohčević-Mitrović Z, Popović ZV. Effects of Confinement, Strain and Nonstoichiometry on Raman Spectra of Anatase TiO<sub>2</sub> Nanopowders. *Materials Science Forum*. 2006;518:101-6.

61. Xu L, Yin M-L, Liu SF. Ag(x)@WO<sub>3</sub> core-shell nanostructure for LSP enhanced chemical sensors. *Scientific reports*. 2014;4:6745-.
62. Ekoi EJ, Gowen A, Dorrepaal R, Dowling DP. Characterisation of titanium oxide layers using Raman spectroscopy and optical profilometry: Influence of oxide properties. *Results in Physics*. 2019;12:1574-85.
63. Guldner WG. The determination of oxygen, hydrogen, nitrogen and carbon in metals: A review. *Talanta*. 1961;8(4):191-202.
64. Mallett MW. The determination of interstitial elements in the refractory metals. *Talanta*. 1962;9(2):133-44.
65. AMGSuperalloys. Analytical Services 2017 [Available from: <https://amg-s.com/analytical-services-2/>].
66. Williamson GK, Hall WH. X-ray line broadening from filed aluminium and wolfram. *Acta Metallurgica*. 1953;1(1):22-31.
67. Vegard L. Die Konstitution der Mischkristalle und die Raumfüllung der Atome. *Zeitschrift für Physik*. 1921;5(1):17-26.
68. Al-Haj Husain N, Camilleri J, Özcan M. Effect of polishing instruments and polishing regimens on surface topography and phase transformation of monolithic zirconia: An evaluation with XPS and XRD analysis. *Journal of the Mechanical Behavior of Biomedical Materials*. 2016;64:104-12.
69. Field AC, Carter LN, Adkins NJE, Attallah MM, Gorley MJ, Strangwood M. The Effect of Powder Characteristics on Build Quality of High-Purity Tungsten Produced via Laser Powder Bed Fusion (LPBF). *Metallurgical and Materials Transactions A*. 2020.
70. Carter LN. Selective Laser Melting of Nickel Superalloys for high temperature applications. Birmingham: University of Birmingham; 2013.
71. Zhang B, Li Y, Bai Q. Defect Formation Mechanisms in Selective Laser Melting: A Review. *Chinese Journal of Mechanical Engineering*. 2017;30(3):515-27.
72. Galy C, Le Guen E, Lacoste E, Arvieu C. Main defects observed in aluminum alloy parts produced by SLM: From causes to consequences. *Additive Manufacturing*. 2018;22:165-75.
73. Weingarten C, Buchbinder D, Pirch N, Meiners W, Wissenbach K, Poprawe R. Formation and reduction of hydrogen porosity during selective laser melting of AlSi10Mg. *Journal of Materials Processing Technology*. 2015;221:112-20.
74. Trapp J, Rubenchik AM, Guss G, Matthews MJ. In situ absorptivity measurements of metallic powders during laser powder-bed fusion additive manufacturing. *Applied Materials Today*. 2017;9(Supplement C):341-9.
75. Bayat M, Thanki A, Mohanty S, Witvrouw A, Yang S, Thorborg J, Tiedje NS, and Hattel JH. Keyhole-induced porosities in Laser-based Powder Bed Fusion (L-PBF) of Ti6Al4V: High-fidelity modelling and experimental validation. *Additive Manufacturing*. 2019;30:100835.
76. Zhu G, Lin T, Cui H, Zhao W, Zhang H, Huang F. Gray Ta<sub>2</sub>O<sub>5</sub> Nanowires with Greatly Enhanced Photocatalytic Performance. *ACS Applied Materials & Interfaces*. 2016;8(1):122-7.
77. Farhoodi B, Raiszadeh R, Ghanaatian M-H. Role of Double Oxide Film Defects in the Formation of Gas Porosity in Commercial Purity and Sr-containing Al Alloys. *Journal of Materials Science & Technology*. 2014;30(2):154-62.
78. Carter LN, Martin C, Withers PJ, Attallah MM. The influence of the laser scan strategy on grain structure and cracking behaviour in SLM powder-bed fabricated nickel superalloy. *Journal of Alloys and Compounds*. 2014;615:338-47.

79. Prashanth KG, Scudino S, Maity T, Das J, Eckert J. Is the energy density a reliable parameter for materials synthesis by selective laser melting? *Materials Research Letters*. 2017;5(6):386-90.
80. Yap CY, Chua CK, Dong ZL. An effective analytical model of selective laser melting. *Virtual and Physical Prototyping*. 2016;11(1):21-6.
81. Ghose S, Babu S, Van Arkel RJ, Nai K, Hooper PA, Jeffers JRT. The influence of laser parameters and scanning strategies on the mechanical properties of a stochastic porous material. *Materials & Design*. 2017;131:498-508.
82. Bertoli US, Wolfer AJ, Matthews MJ, Delplanque J-PR, Schoenung JM. On the limitations of Volumetric Energy Density as a design parameter for Selective Laser Melting. *Materials & Design*. 2017;113:331-40.
83. Yusuf SM, Gao N. Influence of energy density on metallurgy and properties in metal additive manufacturing. *Materials Science and Technology*. 2017;33(11):1269-89.
84. Tan JH, Wong WLE, Dalgarno KW. An overview of powder granulometry on feedstock and part performance in the selective laser melting process. *Additive Manufacturing*. 2017;18:228-55.
85. Agapovichev AV, Kokareva VV, Smelov VG, Sotov AV. Selective laser melting of titanium alloy: investigation of mechanical properties and microstructure. *IOP Conference Series: Materials Science and Engineering*. 2016;156(1):012031.
86. Gu H, Gong H, Pal D, Rafi H, Starr T, Stucker B, editors. Influences of Energy Density on Porosity and Microstructure of Selective Laser Melted 17-4PH Stainless Steel. *Solid Freeform Fabrication Symposium*; 2013; Texas, U.S.
87. Wang W-H, Liu X-Y. Effect of linear energy density on pores of 316L stainless steel by selective laser melting. *IOP Conference Series: Earth and Environmental Science*. 2019;233:032008.
88. Zhang H, LeBlanc M. Processing Parameters for Selective Laser Sintering or Melting of Oxide Ceramics. In: Shishkovsky I, editor. *Additive Manufacturing of High-performance Metals and Alloys - Modeling and Optimisation*: Intech Open; 2018.
89. Bai S, Perevoschikova N, Sha Y, Wu X. The Effects of Selective Laser Melting Process Parameters on Relative Density of the AlSi10Mg Parts and Suitable Procedures of the Archimedes Method. *Applied Sciences*. 2019;9(583).
90. Carter LN, Wang X, Read N, Khan R, Aristizabal M, Essa K, and Attallah, MM. Process optimisation of selective laser melting using energy density model for nickel based superalloys. *Materials Science and Technology*. 2016;32(7):657-61.
91. Dass A, Moridi A. State of the Art in Directed Energy Deposition: From Additive Manufacturing to Materials Design. *Coatings*. 2019;9(7).
92. Garg A, Lam JSL, Savalani MM. Energy component in the density of selective laser melting fabricated prototype. *The International Journal of Advanced Manufacturing Technology*. 2016;86(1):603-11.
93. Eagar TW, Tsai NS. Temperature Fields Produced by Traveling Distributed Heat Sources. *Welding Journal*. 1983;62:346-55.
94. Thomas M, Baxter GJ, Todd I. Normalised model-based processing diagrams for additive layer manufacture of engineering alloys. *Acta Materialia*. 2016;108:26-35.
95. King WE, Barth HD, Castillo VM, Gallegos GF, Gibbs JW, Hahn DE, Kamath C and Rubenchik AM. Observation of keyhole-mode laser melting in laser powder-bed fusion additive manufacturing. *Journal of Materials Processing Technology*. 2014;214(12):2915-25.
96. Hann DB, Iammi J, Folkes J. A simple methodology for predicting laser-weld properties from material and laser parameters. *Journal of Physics D: Applied Physics*. 2011;44(44):445401.

97. Boley CD, Mitchell SC, Rubenchik AM, Wu SSQ. Metal powder absorptivity: modeling and experiment. *Appl Opt.* 2016;55(23):6496-500.
98. Gusarov AV, Kovalev EP. Model of thermal conductivity in powder beds. *Physical Review B.* 2009;80(2):024202.
99. Carr RL. Evaluating Flow Properties of Solids. *Chemical Engineering Journal.* 1965;72:163-8.
100. Lee Y, Zhang W. Mesoscopic simulation of heat transfer and fluid flow in laser Powder bed additive manufacturing. 26th Solid Freeform Fabrication Texas, U.S.: University of Texas Austin; 2015. p. 1154-65.
101. Egger G, Gygax PE, Glardon R, Karapatis NP. Optimization of powder layer density in selective laser sintering. *Solid Freeform Fabrication Symposium; Texas, U.S.: University Texas Austin; 1999.* p. 255-63--63.
102. Hirai T, Pintsuk G, Linke J, Batilliot M. Cracking failure study of ITER-reference tungsten grade under single pulse thermal shock loads at elevated temperatures. *Journal of Nuclear Materials.* 2009;390(Supplement C):751-4.
103. Furumoto TU, T.; Abdul Aziz, M.S.; Hosokawa, A.; Tanaka, R.; . Study on Reduction of Residual Stress Induced during Rapid Tooling Process: Influence of Heating Conditions on Residual Stress. *Key Engineering Materials.* 2010;447-448:785-9.
104. Shiomi M, Osakada K, Nakamura K, Yamashita T, Abe F. Residual Stress within Metallic Model Made by Selective Laser Melting Process. *CIRP Annals.* 2004;53(1):195-8.
105. Buchbinder D, Meiners W, Pirch N, Wissenbach K, Schrage J. Investigation on reducing distortion by preheating during manufacture of aluminum components using selective laser melting. *Journal of Laser Applications.* 2014;26(1):012004.
106. Yadroitsava I, and Yadroitsev I. Residual stress in metal specimens produced by Direct Metal Laser Sintering. *Solid Freeform Fabrication Symposium; 2015; Austin, Texas: University of Texas.*
107. Palacios T, Pastor JY, editors. Degradation of Tungsten Alloys at Extreme Temperatures in Vacuum and Oxidation Atmospheres. *Materials Modelling and Simulation for Nuclear Fuels; 2013; Chicago.*
108. Zhang D, Cai Q, Liu J. Formation of Nanocrystalline Tungsten by Selective Laser Melting of Tungsten Powder. *Materials and Manufacturing Processes.* 2012;27(12):1267-70.
109. Faidel D, Jonas D, Natour G, Behr W. Investigation of the selective laser melting process with molybdenum powder. *Additive Manufacturing.* 2015;8:88-94.
110. Li RD, Liu JH, Shi YS, Zhang L, Du MZ. Effects of processing parameters on rapid manufacturing 90W–7Ni–3Fe parts via selective laser melting. *Powder Metallurgy.* 2010;53(4):310-7.
111. Li R, Shi Y, Liu J, Xie Z, Wang Z. Selective laser melting W–10 wt.% Cu composite powders. *The International Journal of Advanced Manufacturing Technology.* 2010;48(5):597-605.
112. Gorley M. Activation List for Fusion Reactor Blanket. Personal Communication to Field A. Chengdu, China: SWIP; 2015.
113. Thijs L, Montero Sistiaga ML, Wauthle R, Xie Q, Kruth J-P, Van Humbeeck J. Strong morphological and crystallographic texture and resulting yield strength anisotropy in selective laser melted tantalum. *Acta Materialia.* 2013;61(12):4657-68.
114. Zhou L, Yuan T, Li R, Tang J, Wang G, Guo K. Selective laser melting of pure tantalum: Densification, microstructure and mechanical behaviors. *Materials Science and Engineering: A.* 2017;707(Supplement C):443-51.
115. Whittle K. Radiation damage. 2016. In: *Nuclear Materials Science [Internet].* IOP Publishing; [2-1-2-22]. Available from: <http://dx.doi.org/10.1088/978-0-7503-1104-5ch2>.

116. Stringer J, Rosenfield AR. Interstitial Solid Solutions In Body-Centred Cube Metals. *Nature*. 1963;199(4891):337-9.
117. Mosca HO, Bozzolo G. Surface energies of the solid solutions between Ti, V, Cr, Zr, Nb, Mo, Hf, Ta, and W. *Surface Science*. 2007;601(15):3224-32.
118. Moffatt WG. *The Handbook of Binary Phase Diagrams*. Massachusetts, U.S.: General Electric Company; 1981.
119. Rieth M, Dudarev SL, Gonzalez de Vicente SM, Aktaa J, Ahlgren T, Antusch S, Armstrong DEJ, Balden M, Baluc N, Barthe MF, Basuki WW, Battabyal M, Boldyryeva H, Brinkmann J, Celino M, Ciupinski L, Correia JB, DeBacker A, Domain C, Gagnidze E, Garcia-Rosales C, Gibson J, Gilbert MR, Giusepponi S, Gludovatz B, Greuner H, Heinola K, Hoschen T, Hoffmann A, Holstein N, Koch F, Krauss W, Li H, Lindig S, Linke J, Linsmeier C, Lopez-Ruiz P, Maier H, Matejicek J, Mishra TP, Muhammed M, Monoz A, Muzyk M, Nordlund K, Nguyen-Manh D, Opschoor J, Ordas N, Palacios T, Pintsuk G, Pippan R, Reiser J, Riesch J, Roberts SG, Romaner L, Rosinski M, Sanchez M, Schulmeyer W, Traxler H, Urena A, VanDerLaan L, Veleva L, Wahlberg S, Walter M, Weber T, Weitkamp T, Wurster S, Yar MA, You JH and Zivelonghi A. A brief summary of the progress on the EFDA tungsten materials program. *Journal of Nuclear Materials*. 2013;442(1–3, Supplement 1):S173-S80.
120. Jiang D, Wang Q, Hu W, Wei Z, Tong J, Wan H. The effect of tantalum (Ta) doping on mechanical properties of tungsten (W): A first-principles study. *Journal of Materials Research*. 2016;31(21):3401-8.
121. Tejado E, Carvalho PA, Munoz A, Dias M, Correia JB, Mardolcar UV, and Pastor JY. The effects of tantalum addition on the microtexture and mechanical behaviour of tungsten for ITER applications. *Journal of Nuclear Materials*. 2015;467(Part 2):949-55.

## CHAPTER 3 – EXPERIMENTAL METHODS

### 3.1. Introduction

This chapter will describe the techniques used during this study for the sample production and evaluation. The use of the heated bed module and powder blending methodology will also be described. In addition, mechanical testing will be detailed in order that the study can evaluate improvements made to fabricability.

### 3.2. Materials

This study investigated the feasibility of laser powder bed processing of tungsten powder as well as investigating potential methods of improving the processability. Two different high purity tungsten powders were used; a chemically reduced tungsten powder supplied from H.C. Starck GmbH and plasma spheroidised tungsten powder from LPW Technology Ltd. After initial trials with both powders, the bulk of the study investigated the LPW Technology powder. The effect of alloying with plasma spheroidised tantalum powder, in order to improve the processability, was investigated. Table 3.1 below showed details of all powders used in this study including powder production method, lot number, size distribution, and Table 3.2 detailed the impurities listed by supplier.

*Table 3.1 - Powder batch details as supplied by the manufacturer*

<b>Material</b>	<b>Manufacturer</b>	<b>Powder Production Method</b>	<b>Lot Number</b>	<b>Size Distribution (µm)</b>
Tungsten	LPW Technology	Plasma Spheroidised	UK2453	30-60
Tungsten	H.C. Starck GmbH	Chemically Reduced	W10674	<105
Tantalum	LPW Technology	Plasma Spheroidised	UK80433	15-45

To ensure adequate spreading during LPBF fabrication, it is recommended that powders used have a size distribution between 15 and 63  $\mu\text{m}$  (1). Residual unmelted powders were re-used after processing to reduce material waste. The re-used powders were sieved (mesh size 63  $\mu\text{m}$ ) to optimise the material quality and to remove partially melted material or weld spatter that may have formed during previous processing. No process to remove fine powder was used as it was expected the mean particle size would increase during powder cycling (2).

*Table 3.2 - Nominal composition of powders as supplied by the manufacturers with impurity content (ppm)*

	<b>W</b>	<b>Ta</b>	<b>Al</b>	<b>Ca</b>	<b>Cr</b>	<b>Cu</b>	<b>Fe</b>	<b>Mo</b>	<b>Ni</b>	<b>Si</b>	<b>O</b>
H.C. Starck Tungsten	bal.	-	30	20	100	10	200	100	150	50	500
LPW Technology Tungsten	bal.	30	-	-	10	-	10	30	10	-	90
LPW Tantalum	-	bal.	<1000 (all trace impurities)								<1000

In order to get sufficient bonding between the substrate and the deposit and prevent overheating of the substrate surface, a tungsten plate was adhered to a Ti-6Al-4V reducer substrate plate. Early trials using conventional steel or titanium baseplates caused build failure due to excessive melting of the build plate. The tungsten plate was a 2 mm thick hot rolled and pickled plate from PLANSEE (3). During heated bed experiments, 150x150x10 mm plates from PLANSEE were cut down to 60x45x5 mm plates via EDM. A rod with cross-section 60x30 mm also from PLANSEE was used for the conventionally manufactured tungsten material required for mechanical property testing. The composition of the material from PLANSEE could be seen in Table 3.3 below. The rod was received through UKAEA and no composition information was available.

*Table 3.3 - Nominal composition of the plate material as supplied by the manufacturer with impurity content (ppm)*

	<b>W</b>	<b>Al</b>	<b>Cr</b>	<b>Cu</b>	<b>Fe</b>	<b>K</b>	<b>Mo</b>	<b>Ni</b>	<b>Si</b>	<b>C</b>	<b>H</b>	<b>N</b>	<b>O</b>
PLANSEE Tungsten Sheet	bal.	15	20	10	30	10	100	20	20	30	5	5	20

### **3.3. Powder Characterisation**

The requirements for powder as a raw material for LPBF were higher than for other powder metallurgy techniques such as sintering due to the spreading and complete melting required (4, 5). Typically, powders selected for LPBF processing exhibit high flowability, a spherical morphology and a mean particle diameter between 15 and 63  $\mu\text{m}$  to ensure good spreading and packing in the layer thicknesses typical of LPBF (20-60  $\mu\text{m}$ ) (1, 6).

#### **3.3.1. Laser Particle Size Distribution**

Measurement of the size distribution was conducted via Laser Particle Size Diffraction (LPSD) to confirm the nominal size distributions of the as-received powder.

The testing was conducted on two machines, the first being a Sympatec GmbH HELOS system fitted with a SUCELL wet dispersing system located in Metallurgy & Materials at the University of Birmingham (M&M, UoB). Several drops of a dispersing agent ( $\text{Na}_4\text{P}_2\text{O}_7$ ) is added to distilled water to prevent powder agglomeration, and approximately 2 g of powder is added to this and mixed thoroughly to form a suspension. This is then inserted into the machine for testing. Given the expected size distribution of the powder, an R2 lens is fitted to the machine which has a detection range of 0.1 – 87.5  $\mu\text{m}$ . Due to the comparatively high density of the metal powders tested in this study, the maximum pump speed (38% maximum speed) was used to prevent settling. An average of three measurements were taken.



The second machine was a Malvern Pananalytical Mastersizer 3000 with an automated wet dispersion unit, located at Malvern Pananalytical in Malvern. This system had a higher maximum pump speed of 3500 rpm and therefore no dispersion agent was required to prevent settling. The Mastersizer 3000 had a detection range of 0.1 – 1000 µm. Five readings were taken for each measurement, and an average of three measurements was used.

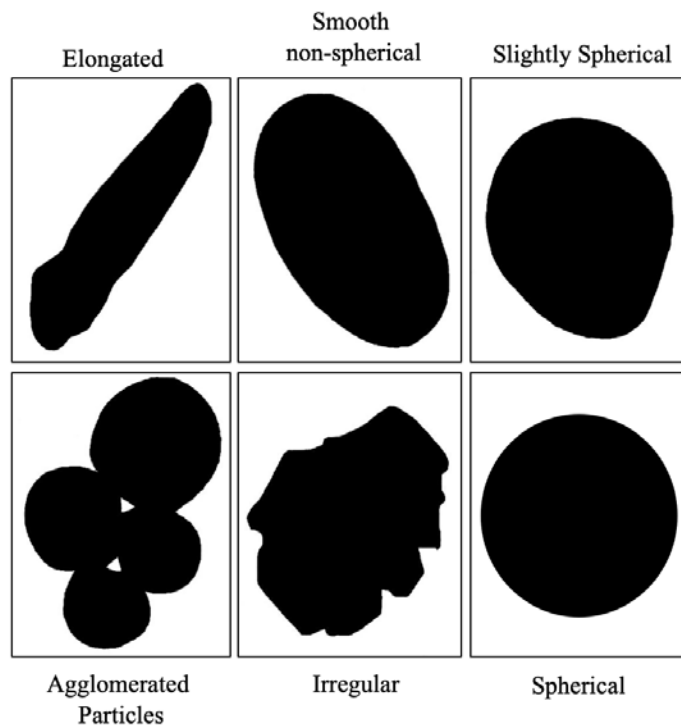
### **3.3.2. Image analysis of powder particles**

Image analysis of the powder particles was conducted using a G3 Morphologi by Malvern Instruments by the Manufacturing Technology Centre (MTC) in Coventry<sup>1</sup> which combines optical microscopy with automated image analysis software.

The powder particles were dispersed, and individual particles imaged. The morphology of the particles was assigned to a category from irregular to highly spherical. Figure 3.1 showed the categories of powder morphology and particles within the tungsten sample which were typical of the morphologies of each category (7, 8).

---

<sup>1</sup> *The author gratefully acknowledges Dr. Nick Cruchley, Mr. Shuaib Dhariwal, and Mr. Steven Smith of the Manufacturing Technology Centre for their assistance with powder characterisation*

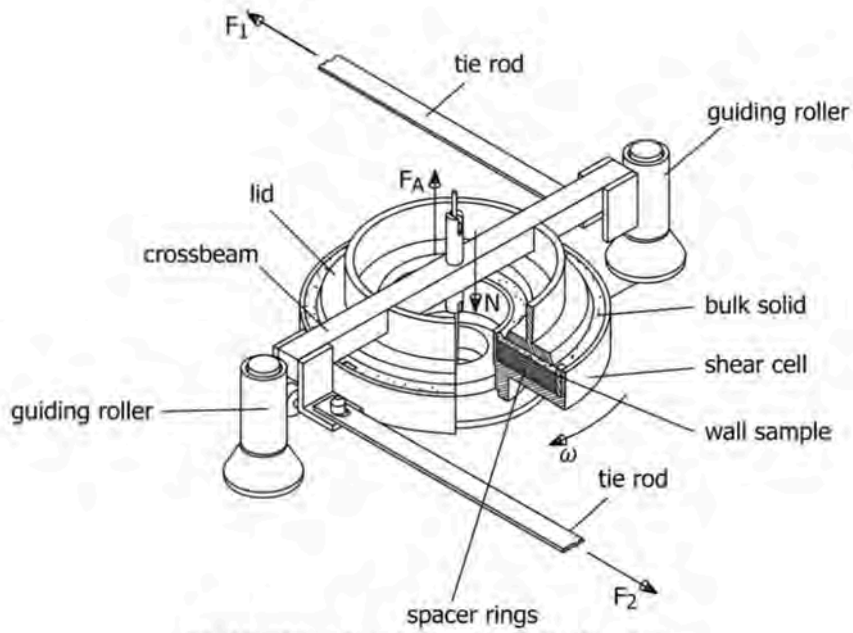


*Figure 3.1 - Powder particle morphologies typical of the categories to which they were assigned*

In addition to powder morphology characterisation the G3 Morphologi also determined the diameter of each powder particle in the size range 0.5 - 1000  $\mu\text{m}$  and produced a size distribution from the powder sample analysed.

### 3.3.3. Shear Ring Testing

Shear ring testing can be used to determine the flow characteristics of powders which is of particular interest to LPBF. Shear ring testing was conducted on a Schulze Shear Ring Tester RST-01 (located in Chemical Engineering, UoB) fitted with a small cell (Type S). The tests carried out were instantaneous tests performed in accordance with ASTM D6773 (9). A schematic of the shear cell could be seen in Figure 3.2 (10).



*Figure 3.2 - A schematic diagram showing a Schulze Shear Ring Cell. Taken from Schulze, 2006 (10)*

The mass of the unfilled shear cell (annulus) was determined. A powder sample was then loaded into the annulus such that it was slightly overfilled and subsequently levelled; its mass was then determined. The lid was then replaced, and the cell was loaded into the machine with the tie-rods attached. A vertical force was then applied to the cell, and the cell slowly rotated. The lid was constrained by the tie rods inducing the shear force in the powder which could be measured by the force exerted on the tie rods. This test could be used to determine the angle of repose and free flowing coefficient ( $ff_c$ ) as well as other flow characteristics (9, 10).

Powders with a  $ff_c$  greater than 10 could be considered to be free flowing and an angle of repose  $< 30^\circ$  indicates excellent flowability. The thresholds for flowability can be seen in Table 3.4 (4, 10).

Table 3.4 - Table showing the thresholds for flowability

Angle of repose (°)	ff <sub>c</sub>	
>65	<1	Very poor
46-64	1-2	Poor
36-45	2-4	Fair
31-35	4-10	Good
<30	>10	Excellent

### 3.3.4. Apparent and Tap Density Determination

Apparent and tap density determinations were made in accordance with ASTM standards B212 and B527 respectively (11, 12). Prior to taking measurements, the mass of a 25 cm<sup>3</sup> unfilled brass density cup was found. A Hall Flowmeter was used to slightly over-fill the cup with powder. The excess powder was removed, and the mass noted.

The 25 cm<sup>3</sup> cylinder was also used when determining tap density. The cylinder was filled with powder and compacted until no further powder could be added, levelled, and the mass of the filled cylinder was then noted. The densities were determined by taking the mass of the powder (either loosely filled for the apparent density or compacted for the tapped density) and dividing it by the volume of the container (25 cm<sup>3</sup>).

From these values, additional measures of compressibility and flowability including Hausner Ratio and Carr Index were found, with values of less than 1.25 or 15 for the Hausner ratio and Carr index respectively indicating good flowability (see Equations 3.1 and 3.2) (4, 13).

$$\text{Hausner Ratio} = \frac{\text{Tap Density (g cm}^{-3}\text{)}}{\text{Apparent Density (g cm}^{-3}\text{)}} \quad (\text{Equation 3.1})$$

$$Carr\ Index = 100 \left( 1 - \frac{Apparent\ Density\ (g\ cm^{-3})}{Tap\ Density\ (g\ cm^{-3})} \right) \quad (Equation\ 3.2)$$

### 3.3.5 Powder Blending

The required masses of the elemental tungsten and tantalum powders were determined to the nearest 0.1 g. A mix of 10 w.t.% tantalum powder and 90 w.t.% tungsten powder were produced and blended on a roller mill for a minimum of 12 hours. The powder bottles were filled in a glove box containing <1000 ppm oxygen and were sealed prior to blending. Once blending of the powder occurred, powder characterisation was conducted and EDX mapping performed to ensure uniform blending.

### 3.3. Chemical Composition Analysis

The oxygen level on a range of powders and LPBF-processed parts was analysed externally by the Manufacturing Technology Centre (MTC) in Coventry<sup>2</sup> and AMG Analytical Services in Rotherham using Inert Gas Fusion on a LECO ONH836 machine.

The external oxides of the solid parts to be tested were removed using mechanical grinding; the samples were then crushed or drilled to form a coarse powder. No preparation was necessary for the powder samples. Approximately, 1 g of the material was added to the graphite crucible, which was then heated above 3000 °C. Oxygen within the samples to be tested, reacted with the carbon in the crucible to form carbon monoxide or carbon dioxide. The gases formed were then passed through a Non-Dispersive Infrared detector. The concentration of the gas (and thus oxygen) was determined by the proportion of infrared

---

<sup>2</sup> *The author gratefully acknowledges Dr. Nick Cruchley, Mr. Shuaib Dhariwal, and Mr. Steven Smith of the Manufacturing Technology Centre for their assistance with chemical analysis of samples*

radiation absorbed by the gas and the proportion of infrared that reaches the detector unaffected. The larger the concentration of CO or CO<sub>2</sub> the greater the proportion of infrared absorbed by the molecules the less radiation can be detected (14).

### **3.4. LPBF Sample Production**

The LPBF samples were produced on an M2 Concept Laser Cusing machine at the University of Birmingham (UoB), fitted with a 400 W laser. A module to reduce the build volume was used throughout this study. Further details about machine set-up and laser profile can be found in Appendix A with an introduction to the technology presented in Section 1.3.

The work was divided into a series of stages; I-III are presented in Chapter 4 and IV-IX are presented in Chapter 5:

I: Optimisation of Build Parameters

II: Investigation into ‘Energy Density’ Relationships

III: Comparison of Powder Morphologies

IV: Effect of Minor Alloy Additions

V: Initial bed-heating trials

VI: Use of Hot Bed for Tungsten Samples

VII: Use of Hot Bed for Tungsten-Tantalum Samples

VIII: Production of Small Punch Test Pieces

IX: Production of Demonstration Parts

For each of the stages the key variables can be seen in Table 3.5.

*Table 3.5 - Summary of LPBF process variables in the different studies presented*

Stage	Powder*	Laser Power (W)	Laser Spot Radius** ( $\mu\text{m}$ )	Scan Speed ( $\text{mms}^{-1}$ )	Scan Spacing ( $\mu\text{m}$ )	Bed Temperature ( $^{\circ}\text{C}$ )
I	LPW	250-400	38-45	250-2500	22.5-112.5	RT
II	LPW	250-400	38-45	675-2500	22.5-112.5	RT
III	LPW HCS	275-400	40-45	700-1250	60-75	RT
IV	WTa	275-400	40-45	700-1250	60-75	RT
V	LPW	300	42	750	60	-
VI	LPW	300	42	750-1000	60	400-600
VII	WTa	300	42	750	60	400
VIII	LPW WTa	300	42	750	60	400
IX	WTa	300	42	750	60	400

\* LPW – LPW Technology tungsten powder; HCS – H.C. Starck tungsten powder; WTa – Blend of tungsten and tantalum powder (Powders sourced from LPW Technology)

\*\* Laser spot radius determined via laser profiling (see Appendix A)

A brief overview of the LPBF processing undertaken for each stage is covered below:

### **I: Optimisation of Build Parameters**

A parametric study was conducted varying the power, laser scanning speed and scan spacing in an attempt to maximise density. A factorial approach was used to assign the parameters of interest. Cubic samples ( $10\times 10\times 10$  mm) were produced from LPW Technology tungsten powder and density was determined via image analysis and Archimedes' density testing.

## **II: Investigation into ‘Energy Density’ Relationships**

Single laser scan tracks and cubic samples (10×10×10 mm) were produced with a range of parameters but with a fixed Volumetric Energy Density (VED) and Area Energy Density (AED) of 175 Jmm<sup>-3</sup> and 5.3 Jmm<sup>-2</sup> respectively. The width of the single scan tracks and the density of the cubic samples were measured to determine the efficacy of energy density relationships used.

## **III: Comparison of Powder Morphologies**

Each powder was used to produce fourteen 10 x 10 x 10 mm<sup>3</sup> cubes using a narrow range of build parameters (duplicate builds of seven sets of parameters, Table 3.6 (with sample codes) laser power: 275 - 400 W; scan speed: 700 -1250 mms<sup>-1</sup>; and scan spacing: 0.06 – 0.075 mm, which allowed location-specific variations to be assessed).



Table 3.6 - Table detailing parameter codes and parameters for the powder morphology study

Sample Code	Powder	Power (W)	Laser Beam radius ( $\mu\text{m}$ )	Scan Speed ( $\text{mm s}^{-1}$ )	Scan Spacing (mm)	AED ( $\text{J mm}^{-2}$ )
PS-A	PS*	300	42	950	0.06	$3.76 \times 10^{-3}$
PS-B	PS	300	42	750	0.06	$4.76 \times 10^{-3}$
PS-C	PS	400	44.5	1250	0.06	$3.60 \times 10^{-3}$
PS-D	PS	300	42	750	0.075	$4.76 \times 10^{-3}$
PS-E	PS	300	42	850	0.06	$4.20 \times 10^{-3}$
PS-F	PS	300	42	850	0.075	$4.20 \times 10^{-3}$
PS-G	PS	275	40	700	0.06	$4.91 \times 10^{-3}$
CR-A	CR*	300	42	950	0.06	$3.76 \times 10^{-3}$
CR-B	CR	300	42	750	0.06	$4.76 \times 10^{-3}$
CR-C	CR	400	44.5	1250	0.06	$3.60 \times 10^{-3}$
CR-D	CR	300	42	750	0.075	$4.76 \times 10^{-3}$
CR-E	CR	300	42	850	0.06	$4.20 \times 10^{-3}$
CR-F	CR	300	42	850	0.075	$4.20 \times 10^{-3}$
CR-G	CR	275	40	700	0.06	$4.91 \times 10^{-3}$

\* PS and CR represent the Plasma Spheroidised and Chemically Reduced powders respectively

The range of parameters used was selected to provide a range of heat inputs to the powders and had been quantified initially using a variation of area energy density (AED) (see Equation 3.3). AED is based on the laser power and the time needed to scan the entire area of the build plane, taking into account the overlap between scan tracks. In time  $\delta t$ , the laser would input an energy of  $P \delta t$ , and traverse a distance of  $v \delta t$ , see Figure 3.3. This assumed a constant absorptivity during the process and assumed the melt track width was approximately equal to laser beam diameter and will therefore be used to determine a minimum effective absorptivity for comparison only.

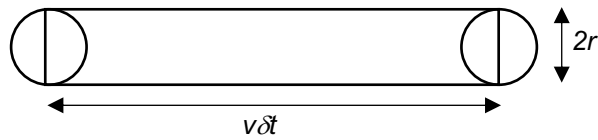


Figure 3.3 - Schematic representation of the laser scan parameters related to AED

So, in time  $\delta t$ , the area scanned by the laser corresponds to  $2r \cdot v\delta t + \pi r^2$

As  $\delta t$  increases  $2r \cdot v\delta t + \pi r^2 \rightarrow 2r \cdot v\delta t$

Therefore, the area energy density ( $\text{Jmm}^{-2}$ ) was calculated using the following equation:

$$AED = \frac{P}{2rv} \quad (\text{Equation 3.3})$$

Where P is laser power (W), v is laser scanning speed ( $\text{mms}^{-1}$ ) and r is laser spot radius (mm)

#### IV: Effect of Minor Alloy Additions

Cubic samples ( $10 \times 10 \times 10$  mm) were produced using a range of parameters from elemental powders (90 w.t.% tungsten - 10 w.t.% tantalum) blended prior to fabrication. The parameters and sample positions selected were the same as in Stage II in order to effectively compare the W-Ta blend to the results of the pure tungsten samples produced using the LPW Technology powder in order to avoid location specific variables influencing the results.

#### V: Initial bed-heating trials

(see Appendix A for more details) Initial trials to determine the efficacy and practicalities of bed pre-heating through build plate insulation and laser pre-scanning were carried out. A single deposit was produced per build to prevent thermal shielding effects from adjacent deposits, and a reduced build plate size ( $30 \times 30$  mm tungsten plate) was used to limit its heat sink capability. Six thermocouples were placed on the underside of the build plate in order to monitor the temperature across the plate throughout the build.

In the control experiments, the tungsten plate was attached to a 90x90 mm titanium substrate plate using high temperature adhesive. The thermocouples were located between the tungsten and titanium plates. In the pre-scanning experiments, a 1 mm thick  $\text{Al}_2\text{O}_3$  plate was placed between the tungsten plate and the titanium substrate plate to insulate the tungsten plate and affixed using a high temperature adhesive, PyroPutty 2400 suitable to 1300 °C. Lower temperature adhesives were trialled but caused build failure as they were exposed to higher temperatures during processing and failed. The thermocouples were located between the tungsten and alumina plates. Figure 3.4 shows a schematic of the control (left) and pre-scan (right) build set-ups with the location of the thermocouples on the tungsten plate (bottom).

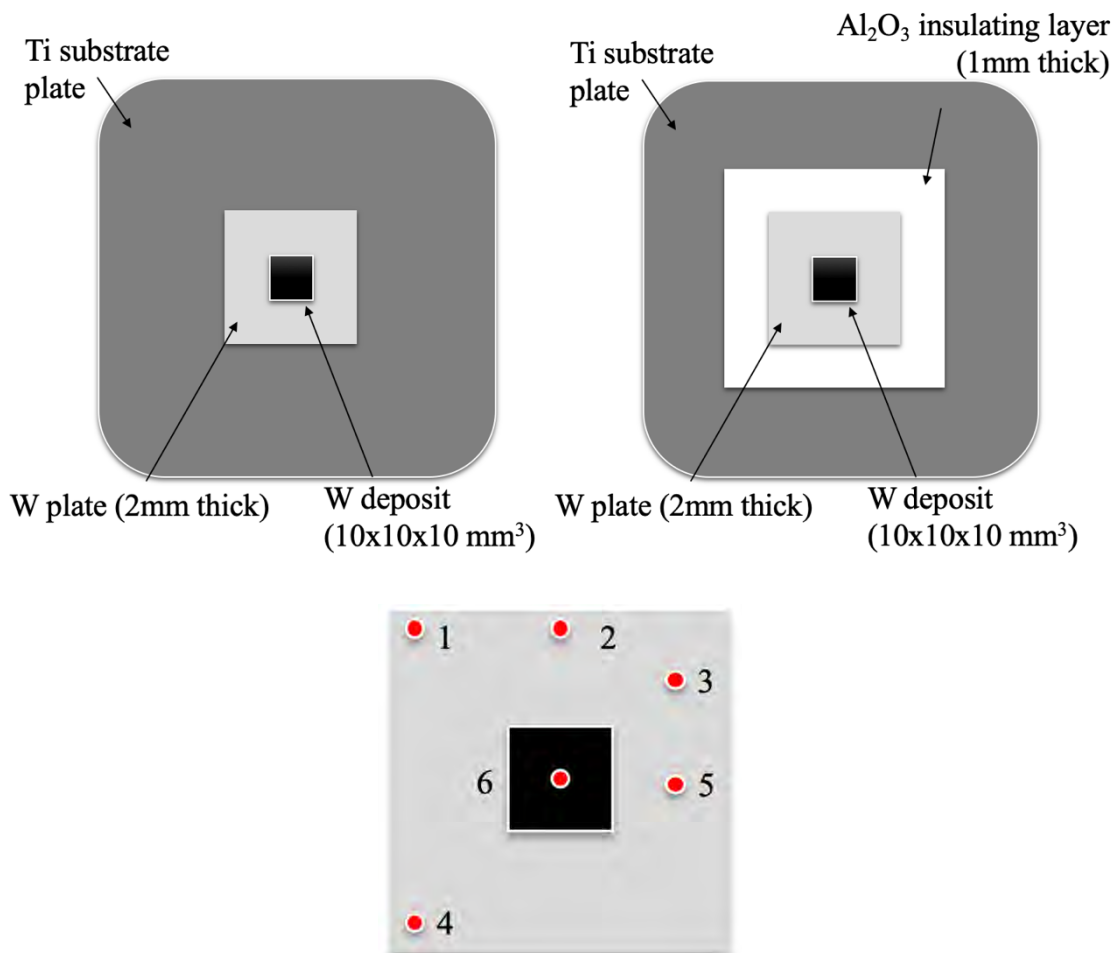
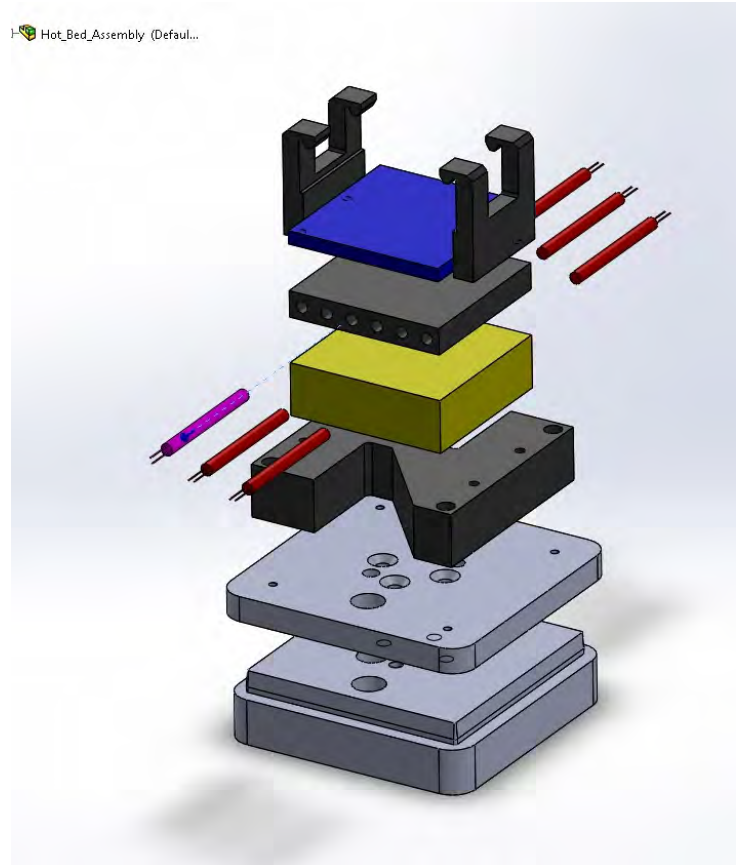


Figure 3.4 - Schematic of the build set-up for control (left) and pre-scan (right) experiments along with the location of the thermocouples on the tungsten plate (bottom)

Laser pre-scans were conducted over the plate prior to the build on the pre-scan experiment. The pre-scan consisted of 30 individual passes whereby the laser rastered across the tungsten plate, where the laser scan direction was rotated by 90° with each scan pass. The pre-scan was conducted three times prior to the start of the build.

## **VI: Use of Hot Bed for Tungsten Samples**

(see Appendix A for details) A heated bed module was designed to fit into the reduced build volume module of the Concept Laser M2 (see Figure 3.5). A 5mm tungsten plate was fixed in place using clamps at either side of the build plate. The quantity of samples produced was limited due to the reduced build volume. 10x10x10 mm<sup>3</sup> deposits and 10 mm long single scan tracks were produced with a bed pre-heating of 400 °C and 600°C. These temperatures were chosen as they are the extremes of the commonly stated temperature range of DBTT in tungsten (15).



*Figure 3.5 Schematic of the heated bed module with (from top) plate loading clips, tungsten build plate (blue), heating plate (grey) with cartridge heaters (red), ceramic insert to limit heat losses (yellow) and attachments to Concept Laser M2 reduced build volume module.*

## **VII: Use of Hot Bed for Tungsten-Tantalum Samples**

The heated bed module was utilised to produce samples from the blended tungsten-tantalum powder. A bed temperature of 400 °C was selected and to compensate for the reduced build volume the deposits were reduced in size to 8x8x8 mm<sup>3</sup>. All other set-up details were performed as in Stage VI.

## **VIII: Production of Small Punch Test Pieces**

Cylindrical blanks with a diameter of 8 mm and height of 20 mm were built, from which small punch samples could be produced. After LPBF fabrication, the cylindrical test pieces

underwent vibratory polishing for 12 hours before being prepared via EDM as necessary. Further details on sample preparation can be found in Section 3.10 discussing testing methods.

## **IX: Production of Demonstration Parts**

Three geometries were selected for both further testing, and as a final investigation into the feasibility of producing divertor-type components via additive manufacturing. The first geometry was a brazing cap designed for brazing trials to determine whether components were leak tight.

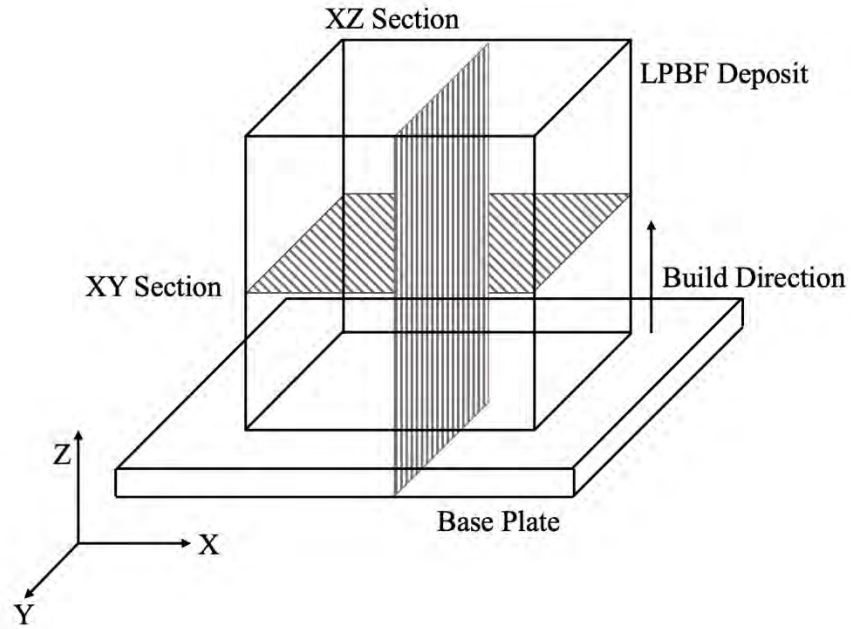
Two divertor designs were also trialled, with one being a conventional design similar to those currently being produced via powder metallurgy and machining, and the second being a rear fed divertor design optimised for additive manufacturing.

These components were produced from the blended tungsten-tantalum powder on the heated bed module with 400 °C pre-heating. After fabrication, the parts had loose powder and surface oxide removed through either grit blasting or vibro-polishing and leak tested. In addition, the two divertor designs were compared in terms of production time and material usage.

### **3.5. Metallurgical Sample Preparation**

Metallurgical samples were first removed from the substrate build plate via wire Electrical Discharge Machining (EDM) using an AgieCharmilles CUT1000 by +GF+ (M&M, UoB) and then sectioned using EDM. Samples were either sectioned parallel to the build plate to view

the XY plane or longitudinally through the sample and build plate to view the XZ plane (see Figure 3.6).



*Figure 3.6 - Schematic diagram showing the sections of the LPBF samples*

Samples were then cold mounted in acrylic resin. Grinding and polishing was conducted on a Struers Tegramin-25 fitted with a specimen plate for holding six 30mm diameter samples (M&M, UoB). Samples were coarsely ground using a P120 grit disc until the samples were planar. Further grinding down to a P4000 finish was then conducted prior to polishing with 3 and 1  $\mu\text{m}$  diamond solution, and final polishing with colloidal silica suspension (0.03  $\mu\text{m}$ ).

Submersion etching was used to reveal grain structure; a solution of  $\text{H}_2\text{O}_2$  and  $\text{NH}_4\text{OH}$  (2:1) was mixed immediately prior to etching, and the samples were submerged for a period of 15-20 s. After etching, the samples were then submerged in water, rinsed with ethanol and dried.

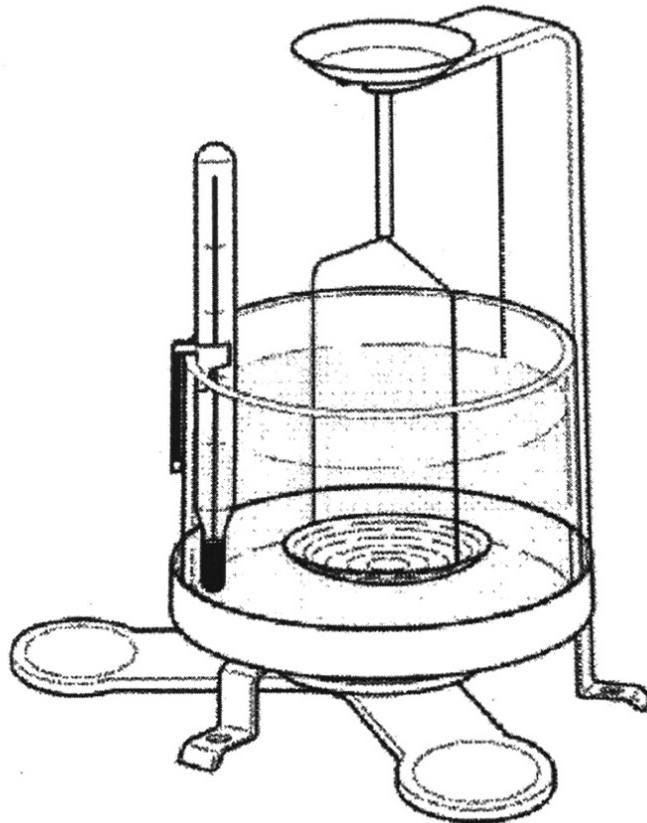
### 3.6. Archimedes' Density Testing

Archimedes' Density measurements were conducted in accordance with ASTM B962 (16).

Ethanol was used as a submersing liquid due to its lower surface tension than distilled water.

The Archimedes' testing apparatus was supplied by Ohaus and was used in conjunction with an Ohaus Adventurer Balance accurate to 0.001 g.

The temperature of the ethanol was found prior to testing to determine the density of the liquid. The mass of the sample in air was found and then the sample was submerged and placed on the cradle as can be seen in Figure 3.7. The sample was agitated under the surface of the fluid to prevent air bubbles settling on the surface, prior to taking the measurement. The mass of the submerged sample was then found.



*Figure 3.7 - A Schematic Diagram showing Archimedes' Density Testing equipment. Taken from OHAUS, 2010 (17)*



From these measurements, the density of the sample can be found in accordance with the following equation:

$$\rho = \frac{A}{A - B} \times (\rho_L - \rho_0) + \rho_0 \quad (\text{Equation 3.4})$$

$\rho$  - sample density ( $\text{g cm}^{-3}$ ),  $A$  – mass of sample in air (g),  $B$  – mass of sample submerged in ethanol (g),  $\rho_L$  – density of ethanol ( $\text{g cm}^{-3}$ ),  $\rho_0$  - air buoyancy ( $0.0012 \text{ g cm}^{-3}$ ) (17)

### **3.7. Optical Microscopy (OM)**

Optical microscopy was employed to quantify defects, including porosity and cracking, within the samples produced via LPBF as well as to investigate the grain structure in both the LPBF fabricated components and the substrate plate.

A Zeiss Axioskop 2 fitted with a monochrome charge-coupled device (CCD) camera at 50X magnification was used; this microscope was fitted with a mechanical stage and this combined with the mosaic feature of the Zeiss Axiovision software allowed for imaging across the entire surface of the section (largest section  $\sim 100 \text{ mm}^2$ ). At higher magnifications individual images or small mosaic sections were also produced.

### **3.8. Scanning Electron Microscopy (SEM)**

SEM and its associated analysis tools were used to study the microstructure, features and composition of the LPBF samples produced.

The studies within this thesis utilising SEM were:

I: Powder Characterisation

II: Analysis of single scan tracks

III: Analysis of crack morphology

IV: Microstructural Investigation

V: Analysis of oxygen distribution

VI: Fractography

SEM was employed to undertake powder characterisation, image defects within the samples and image the craters formed during Secondary Ion Mass Spectroscopy (SIMS) analysis.

Technical details of the SEMs used are listed in Table 3.7. An accelerating voltage of 20 keV was used throughout.

*Table 3.7 - Table showing details of the SEMs and the corresponding studies which utilised them*

<b>Name</b>	<b>Investigation</b>	<b>Location</b>	<b>Electron Source</b>	<b>Detectors</b>
Hitachi TM3030	I, III, IV, VI	M&M UoB	Tungsten filament	BSE, Bruker Espirit EDX
Hitachi TM3030+	II, VI	M&M UoB	Tungsten filament	SE, BSE, Oxford Aztec EDX
Tescan Mira3	IV, V	M&M UoB	FEG	SE, BSE, Oxford AZtec EDX, AZtecHKL EBSD
Tescan Vega3	V	LSA ltd. Loughborough	Tungsten filament	SE, BSE, Oxford INCA EDX

FEG – Field Emission Gun    EDX – Electron Dispersive X-ray Spectroscopy

Details of each investigation are expanded upon below:

### **I: Powder Characterisation**

Powder characterisation was performed using several means including SEM; Back-scattered Electron (BSE) SEM imaging of unmounted powder particles stuck to carbon tabs was conducted to investigate the morphologies of the different powders used and in the case of the W-Ta blended powder, the composition and homogeneity of the blend. Five images were taken at 100x magnification; each image had more than 100 particles per image meaning several hundred particles were analysed. In order to investigate morphology in more detail several images were taken at higher magnifications (up to 2000x). After blending, EDX mapping for W and Ta was also conducted on the W-Ta powder at 100x magnification.

### **II: Analysis of single scan tracks**

Single scan tracks were imaged in order to compare melt pool widths as well as cracking and general features between different laser parameters and the effect of bed heating on weld tracks. Secondary electron (SE) SEM micrographs were taken at varying magnifications (x150, x600, x1500 and x4000) in order to image both large portions of the track for melt pool measurements and get detail of crack morphology.

### **III: Analysis of crack morphology**

As in investigation II micrographs were taken at a range of magnifications (x250, x500 and x2000) to investigate cracking pattern and quantity in both LPBF W and W-Ta samples. The range of micrographs were required to contrast the cracking in the two materials as the quantity and size of cracks was noticeably different. Lower magnification images were also produced through OM.

#### **IV: Microstructural Investigation<sup>3</sup>**

Electron Backscatter Diffraction (EBSD) maps were produced on XY sections of LPBF tungsten produced with and without bed heating. The maps were taken at a magnification of 500x on the Tescan Mira3 with Oxford AZTechHKL software and subsequent analysis was conducted on Channel 5 HKL Tango software.

#### **V: Analysis of oxygen distribution**

At the sites of EBSD mapping, EDX mapping of oxygen was also conducted. However, given the interaction volume associated with the technique the results could not be conclusive. Therefore, SE imaging was also conducted on the crater bottoms produced through SIMS analysis to correlate microstructural features with the oxygen distribution found (SIMS details in Section 3.13). These were imaged such that the entire crater (~150x150  $\mu\text{m}$ ) could be viewed in a single micrograph (x900).

#### **VI: Fractography**

Fractography of the manually fractured and small punch test pieces was conducted. Ten samples produced from LPBF tungsten were manually fractured in order to analyse the fracture surface produced. The fractography of the manually fractured material was conducted on the Hitachi TM3030 which was only fitted with BSE detector. The fracture surfaces were imaged at a range of magnifications to gain a perspective of both the micro and more macro scale features present in the failures (x100 – x1500).

---

<sup>3</sup> *The author gratefully acknowledges Mr. Miles Fan for his assistance with the EBSD conducted.*

Fractography of the fractured small punch test pieces was also conducted. Each test piece was analysed at a range of magnifications. Initially, low magnification images were captured so the entire test piece was imaged (x40). Higher magnification micrographs were also captured so the fracture surfaces produced could be compared to the manual fracture specimens.

### **3.9. Image Analysis**

Image analysis was conducted using the open source software, Fiji. The three main uses for image analysis in this study were grain size measurement, defect quantification, and measurement of the penetration depth of the fusion zone.

For defect quantification, analysis was performed on the complete area of the XY section of the sample. For penetration depth measurements, the XZ section of the deposit and the substrate were analysed such that the interface between the substrate and at least 2 mm either side could be seen. The main stages of image analysis for defect quantification and penetration depth measurements are listed below:

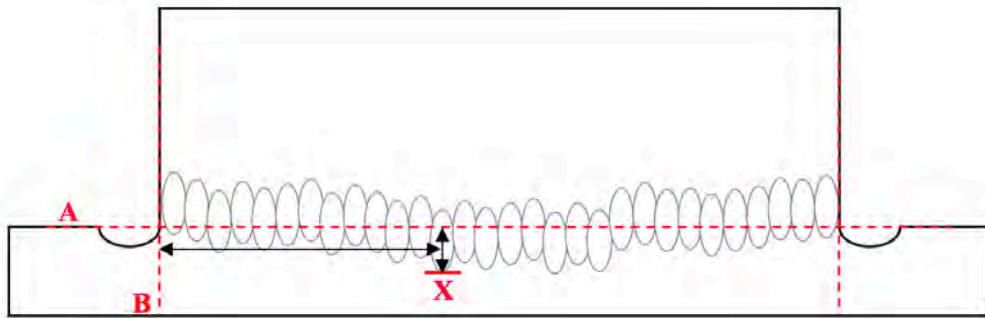
#### Defect Quantification Methodology:

- Global scale set based on the scale bar on the micrograph
- Scale bar and background areas cropped
- Background removed, 50-pixel ball radius to remove left to right gradient from inhomogeneous lighting
- Image set to 32-bit black and white image
- Threshold used to produce binary image
- Area of the relevant features measured

The cracking present was found to be extensive but fine meaning that the defects separated into individual coloured pixels. As a result, only a percentage area of cracks could be determined rather than crack length per unit area. In order to differentiate between voids and cracks the smallest pores throughout the sample sets were measured with particles  $> 1800 \mu\text{m}^2$  being defined as voids and  $< 1800 \mu\text{m}^2$  being defined as cracks.

#### Penetration Depth Measurements Methodology:

- Global scale set based on the scale bar on the micrograph
- Datum line of the substrate plate away from the deposit (A) set (see Figure 3.8)
- Zero position of the sample edge (B) set
- At, at least 0.5 mm increments, the maximum penetration depth of the fusion zone from the datum line (A→X) and the distance between the sample edge and the measurement site (B→X) was measured.



*Figure 3.8 - Schematic representation of the methodology for penetration depth measurements*

### **3.10. Small Punch Testing**

After LPBF fabrication, the cylinders were removed from the base plate via wire EDM and sectioned in discs 0.7 mm in thickness. The samples were thinned down to  $0.5 \text{ mm} \pm 0.005 \text{ mm}$  through manual grinding with a surface finish of P1200 prior to testing.

The diameter and thickness were verified with Vernier callipers and a micrometer respectively.

Small punch samples were produced from the following material sets:

- Additively manufactured tungsten (room temperature base plate)
- Conventionally manufactured tungsten
- Additively manufactured tungsten-tantalum (room temperature base plate)
- Additively manufactured tungsten-tantalum (400 °C base plate)

Samples were tested at room temperature (RT), 200 °C, 400 °C and 600 °C. Due to time and material constraints, two tests were conducted at room temperature and 600 °C and only one test was conducted at 200 °C and 400°C across all material sets. However, in order to increase confidence in the results produced, four additional repeats were produced in LPBF tungsten with no bed heating at RT and 600 °C and two at intermediate temperatures. Little difference was seen between the intermediate temperatures and less than 10 % error was seen between the repeats.

The small punch testing rig was a bespoke servo-hydraulic test rig produced by Phoenix Materials Testing Ltd., located in the Materials Technology Lab at CCFE<sup>4</sup> (see Figure 3.9). A clamping force of 10N was used to secure the disc in place, and a WC hemispherical punch placed into the die. For high temperature testing, magnesium hydroxide was applied to the die as lubricant and two thermocouples were fitted in to the die to monitor temperature.

Resistance heaters were fitted around the testing jig and a 30-minute soak time was used after

---

<sup>4</sup> *The author gratefully acknowledges Dr. Mike Gorley and Dr. Mark Richardson for their assistance with the small punch testing conducted.*

the temperature was reached to ensure uniform temperature throughout the test piece. A displacement rate of  $0.1 \text{ mm}\cdot\text{min}^{-1}$  was used and the test was discontinued at a displacement of 2 mm or when a 20 % drop from the peak load had occurred.

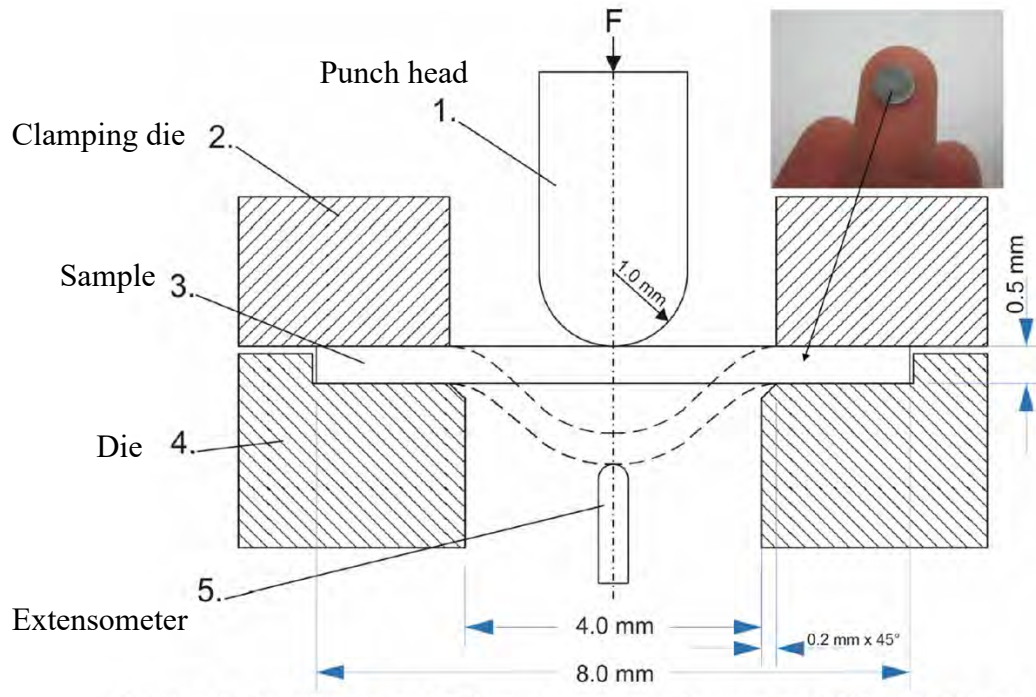


Figure 3.9 - Small Punch test set-up; (1) Punch head, (2) Clamping die, (3) Specimen, (4) Receiving die, (5) Extensometer rod. Actual specimen shown top-right. Taken from Richardson et al., n.d. (18, 19)

### 3.11. Secondary Ion Mass Spectroscopy (SIMS)

SIMS analysis was undertaken externally at Loughborough Surface Analysis Ltd. In Loughborough using an IMS 7f-Auto spectrometer from Cameca. A Cs ion beam was used for sputtering. The mass/charge ratio of the  $\text{O}^{16}$  isotope was measured in the mass spectrometer and an image produced of relative oxygen intensity across the imaging area.

Initially surface oxides generated a signal across the sample surface. The surface oxides were sputtered away to reveal the underlying oxygen distribution in both LPBF W and W-Ta produced without bed heating. Due to the cost of the technique, only one sample from each



type was analysed although multiple craters within the sample were produced and analysed. Given the average grain size of the material, it was expected that within the sample areas (150x150  $\mu\text{m}^2$ ) grain boundaries would be imaged. The ion beam rastered across the area to allow for a mapping of the oxygen distribution with the raster area being larger than the imaging area to prevent re-deposition of oxygen at the edge of the imaging area. After SIMS analysis, SEM imaging was conducted on the base of the craters produced to link microstructural features to the oxygen distribution (Section 3.8 (V)).

### 3.12. X-ray Diffraction

X-ray diffraction was conducted on a PROTO AXRD benchtop diffractometer. XRD analysis was conducted on solid samples (LPBF and conventional) and powder samples; no sample tilt was used with powder samples and the minimum rotation speed was used. The PROTO AXRD had an inclined x-ray tube which meant additional sample tilt was not required. XRD was conducted on LPW tungsten, blended W-Ta powder, LPBF W and W-Ta and conventional W material. The diffractometer (Cu  $K\alpha$  source at 15kV and 40mA) was used with a scan rate of  $3^\circ \cdot \text{min}^{-1}$  over a  $2\theta$  range of  $0 - 110^\circ$ . After pattern collection, the peaks were normalised to remove the effects of background radiation and different signal intensities. Peak identification was conducted manually using Bragg's law. Peak shift due to slight differences in sample height was corrected using the following equation:

$$\Delta 2\theta = \frac{2s \cdot \cos\theta}{R} \cdot \frac{180}{\pi} \quad (\text{Equation 3.5})$$

Where the peak position shift is  $\Delta 2\theta$  ( $^\circ$ ),  $s$  is the sample height error (mm),  $R$  is the radius of the instrument (mm) and  $\theta$  is the diffraction angle ( $^\circ$ ). The Proto AXRD benchtop diffractometer has a radius of 142 mm (20).

### **3.13. Raman Spectroscopy**

Raman scattering occurred when coherent light interacted with molecular vibrations resulting in a shift in the scattered light; the Raman effect was very weak and only occurred when the bonds could be polarised. Raman spectra were obtained for LPBF samples of tungsten and tungsten-tantalum using a Renishaw inVia Raman Microscope with 488 nm excitation laser (2 mW power). A microscope objective was used to focus the laser beam onto the as fabricated surface of the solid LPBF samples.

### 3.14. References

1. Carter LN. Selective Laser Melting of Nickel Superalloys for high temperature applications. Birmingham: University of Birmingham; 2013.
2. Zielinski J, Vervoort S, Mindt H-W, Megahed M. Influence of Powder Bed Characteristics on Material Quality in Additive Manufacturing. BHM Berg- und Hüttenmännische Monatshefte. 2017;162(5):192-8.
3. PLANSEE. Tungsten. Slough, U.K.; 2017.
4. Carr RL. Evaluating Flow Properties of Solids. Chemical Engineering Journal. 1965;72:163-8.
5. Tan JH, Wong WLE, Dalgarno KW. An overview of powder granulometry on feedstock and part performance in the selective laser melting process. Additive Manufacturing. 2017;18:228-55.
6. Han Q, Gu H, Setchi R. Discrete element simulation of powder layer thickness in laser additive manufacturing. Powder Technology. 2019;352:91-102.
7. Automated imaging - Advanced particle characterization. In: Instruments M, editor. Malvern, U.K.2008.
8. Morphologi G3 User Manual. Malvern, U.K.; 2015. Report No.: MAN0410-07-EN-00.
9. Standard Test Method for Bulk Solids Using Schulze Ring Shear Tester. West Conshohocken, PA: ASTM International; 2016.
10. Schulze D. Flow Properties of Powders and Bulk Solids Wolfenbuttel: Dietmar Schulze; 2006 [Available from: <http://www.dietmar-schulze.com/grd1.pdf>].
11. Standard Test Method for Apparent Density of Free-Flowing Metal Powders Using the Hall Flowmeter Funnel. West Conshohocken, PA: ASTM International; 2013.
12. Standard Test Method for Determination of Tap Density of Metal Powders and Compounds. West Conshohocken, PA: ASTM International; 2015.
13. Liu B, Wildman R, Tuck C, Ashcroft I, Hague R, editors. Investigation the effect of particle size distribution on processing parameters optimisation in selective laser melting process. Solid Freeform Fabrication Symposium; 2011; Texas, U.S.
14. AMGSuperalloys. Analytical Services 2017 [Available from: <https://amg-s.com/analytical-services-2/>].
15. Palacios T, Pastor JY, editors. Degradation of Tungsten Alloys at Extreme Temperatures in Vacuum and Oxidation Atmospheres. Materials Modelling and Simulation for Nuclear Fuels; 2013; Chicago.
16. Standard Test Methods for Density of Compacted or Sintered Powder Metallurgy (PM) Products Using Archimedes' Principle. West Conshohocken, PA: ASTM International; 2015.
17. OHAUS. Density Determination Kit Instruction Manual New Jersey, U.S.2010 [Available from: [https://scalenet.com/pdf/Pioneer\\_Explorer\\_Density\\_Kit.pdf](https://scalenet.com/pdf/Pioneer_Explorer_Density_Kit.pdf)].
18. Richardson M, Gorley M, Surrey E, Wynne B, Lowrie F. Realisation of Small Punch Testing to Accelerate Materials Qualification for Fusion Applications. In: Field A, editor. Oxford, U.K.: UKAEA; n.d.
19. Richardson M, Gorley M, Surrey E, Wynne B. An Investigation of the Mechanical Performance of Conventional and Additively Manufactured Vanadium. In: Field A, editor. Oxford, U.K.: UKAEA; n.d.

20. Pananalytical B.V. Basic XRD Course: Introduction to Sample Preparation Tennessee, U.S.: University of Tennessee Knoxville; 2013 [cited 2020 04/05/2020]. Available from: <http://jam.utk.edu/facilities/diffraction/Introduction%20to%20Sample%20Preparation.pdf>.

## **CHAPTER 4 : PROCESS OPTIMISATION AND IDENTIFICATION OF CRACK MECHANISM IN LPBF HIGH PURITY TUNGSTEN**

This chapter details initial optimisation studies for tungsten LPBF fabrication working towards maximising the density of the as-fabricated components and establishing a processing window for the material. Initial investigations into parameter development and the issues associated with ‘energy density’ relationships for parameter optimisation are discussed and possible mechanisms for the formation of the dominant defects present are offered. The size distribution, chemistry and flow characteristics of feedstock materials produced via two different techniques are also presented, and the defect density of the samples produced, and the relative penetration depths into the base plate with these powders compared.

### **4.1 Introduction**

Thermal properties and laser-material interaction differ from material to material and as a result, optimum process parameters must be identified as the initial stage of process development for a new material. For many typical LPBF materials these are extensively presented in the literature. For tungsten however, the process development was at a much earlier stage and many of the preliminary studies were conducted on 100 or 200 W laser systems, limiting the achievable part density to 85% (1, 2) although Sidambe et al., 2019 (3) achieved high densities using the Renishaw AM125 platform (3). Processing on 400 W systems has been more recently conducted and the review of the available literature can be found in Section 2.5.5 of the literature review. This chapter will present the results of the parametric study and identify the processing window which will subsequently be used for the remainder of the study.

Additionally, as this was a study of a pure material system, it also offered a unique opportunity to simplify the mechanisms at play. As part of the parametric study, an investigation was conducted into the validity and limitations of the commonly used 'Energy Density' relationships. The limits of the study were selected between the modelled threshold powers for melting and boiling (4). This limited the aim of the study to consolidation of the material. As such, if there were limitations to this simplified approach the issues would likely become more significant when moving to a multi-material system and attempting to optimise for opposing defect mechanisms.

Based on the literature review of welding of refractory metals and the more recent work on LPBF of tungsten (Sections 2.3 and 2.5.5), it was determined that, assuming energy input was sufficient for consolidation, the dominant defect mechanism for LPBF pure tungsten would be cracking. The high thermal gradients and associated stresses induced on cooling during LPBF combined with the intrinsic brittleness of tungsten would likely result in cracking. This may be exacerbated by oxygen embrittlement (5, 6). During this study, the cracking mechanism was investigated through analysis of deposits as well as single laser tracks.

As with all manufacturing techniques, the raw material was also an important factor to consider. As such, two high purity tungsten powders (see Table 4.1), produced with different manufacturing techniques, were characterised to determine size distribution, morphology, and flow characteristics and thus, the likely suitability for Laser Powder Bed Fusion (LPBF) production. Many of the investigations in LPBF studied the effect of process parameters on build quality but did not include the material feedstock as a variable. The present work investigated two powders with significantly different morphologies, where specimens from

duplicate builds were analysed for defect density and relative absorbed apparent power densities.

*Table 4.1 Nominal composition of powders as supplied by the manufacturers with impurity content (ppm)*

	<b>W</b>	<b>Ta</b>	<b>Al</b>	<b>Ca</b>	<b>Cr</b>	<b>Cu</b>	<b>Fe</b>	<b>Mo</b>	<b>Ni</b>	<b>Si</b>	<b>O</b>
H.C. Starck Tungsten	bal.	-	30	20	100	10	200	100	150	50	500
LPW Technology Tungsten	bal.	30	-	-	10	-	10	30	10	-	90

## **4.2 Process Optimisation**

### **4.2.1 Parameter Development**

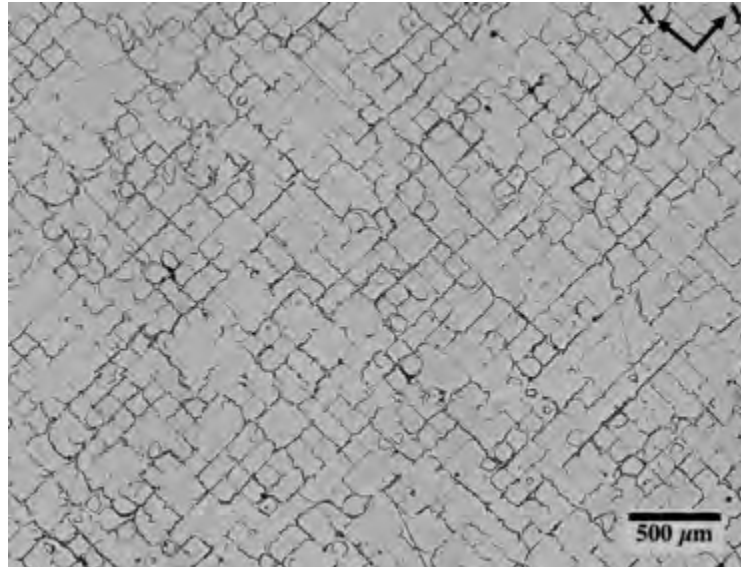
The parametric study was composed of three build stages, following the replacement of the laser in December 2016 (see Appendix A). While the results from the faulty laser were not presented due to their unreliability, they formed the basis for the subsequent parametric studies conducted. The first stage was a full factorial study of the effect of laser scanning speed on part density given the processing parameters which had been used for processing with the faulty f-theta lens. It was assumed, given the high melting point of tungsten, that the maximum machine power would be required. The scan spacing selected was the optimum found for processing with the faulty laser as a starting point as the size of study was limited due to the reduced build platform size. Table 4.2 showed the parameters selected for this initial build attempt.

Table 4.2 - Table showing the process parameters from the initial stage of parameter development

<b>Parameter</b>	<b>Laser Power (W)</b>	<b>Laser Scan Speed (mms<sup>-1</sup>)</b>	<b>Laser Scan Spacing (mm)</b>	<b>Volumetric Energy Density (Jmm<sup>-3</sup>)</b>	<b>Linear Energy Density (Jmm<sup>-1</sup>)</b>
A.1	400	250	0.1125	474	1.60
A.2	400	375	0.1125	316	1.07
A.3	400	500	0.1125	237	0.80
A.4	400	675	0.1125	176	0.59
A.5	400	750	0.1125	158	0.53
A.6	400	1000	0.1125	119	0.40
A.7	400	1500	0.1125	79	0.27
A.8	400	2250	0.1125	53	0.18

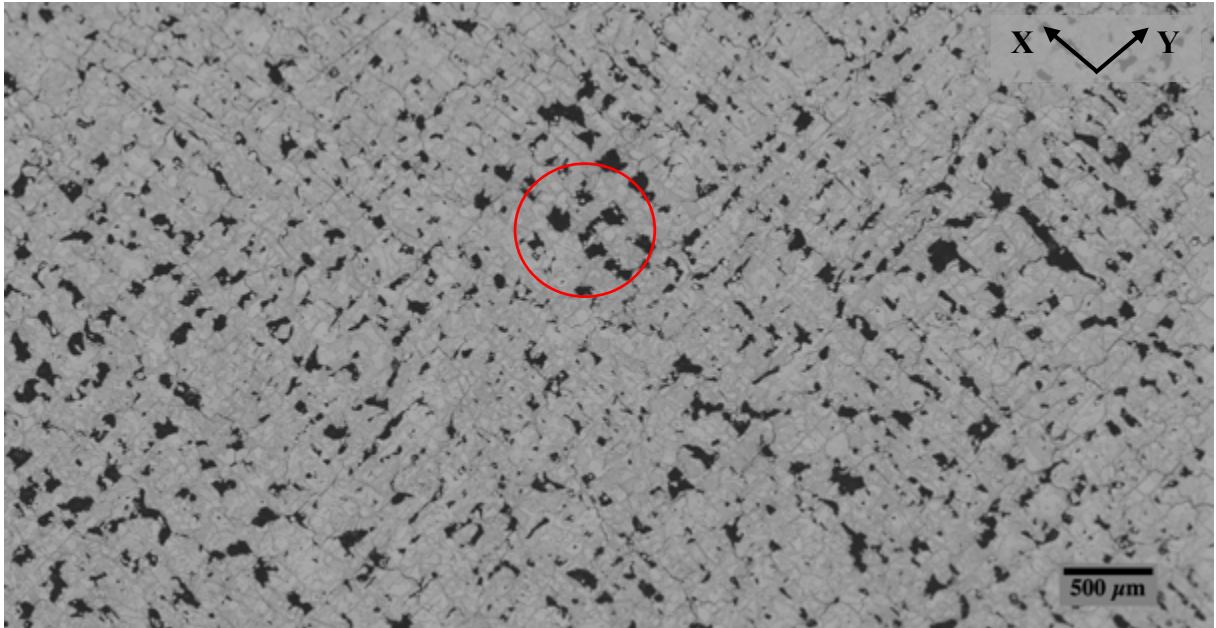
As the faulty laser beam had a larger beam diameter and was more diffuse in its power output, the scan spacing of 112.5  $\mu\text{m}$ , was too large as the new laser had a laser beam diameter of 90  $\mu\text{m}$  at focus. As a result, significant lack of fusion was found at the edges of adjacent scan tracks. Figure 4.1 showed a micrograph of a sample from the initial parametric study; X and Y denoted the laser scanning directions. A clear pattern could be seen in the lack of fusion which occurred at distances approximately equal to the scan spacing selected.





*Figure 4.1 – Optical micrograph of an XY section from parameter A.1, typical of the initial parametric study showing equally spaced lack of fusion defects*

As a result of the extensive lack of fusion at the edge of the scan tracks, the maximum density achieved was 98 %, at 400 W and 675  $\text{mms}^{-1}$ . Other parameters showed lack of fusion in areas away from the scan track overlap regions. This was seen at higher laser scan speeds, greater than 1000  $\text{mms}^{-1}$ , with Figure 4.2 showing 400 W and 1500  $\text{mms}^{-1}$  where un-sintered powder particles could be seen.



*Figure 4.2 – Optical micrograph of an XY section from parameter A.7, showing both equally spaced lack of fusion defects and defects from insufficient energy input and unmelted powder particles (circled in red)*

A second stage of the parametric study was therefore conducted around the optimised parameters with the overly large laser scan spacing. Parameters of 400 W and 675 and 1000  $\text{mms}^{-1}$  were selected with laser scan spacings of 30 – 60  $\mu\text{m}$ . Additionally, to account for the additional energy input associated with the reduced laser scan spacing, scan speeds were increased up to 2500  $\text{mms}^{-1}$  such that the ‘volumetric energy density (VED)’ (Equation 4.1) was consistent with the optimised parameter from the first stage.

$$VED = \frac{P}{v \cdot h \cdot t} \quad (\text{Equation 4.1})$$

Where P is the laser power (W), v is the laser scanning speed ( $\text{mms}^{-1}$ ), h is the laser scan spacing (mm) and t is the layer thickness (mm).

Figure 4.3 shows a photograph of the build from the second stage of the parametric study. As can be seen from the photograph, a number of parts had to be discontinued as the energy input

was excessive (red). In addition, some parts showed damage to the top surface and rounding again due to excess heat input (amber). However, a number of parameters built well (green).

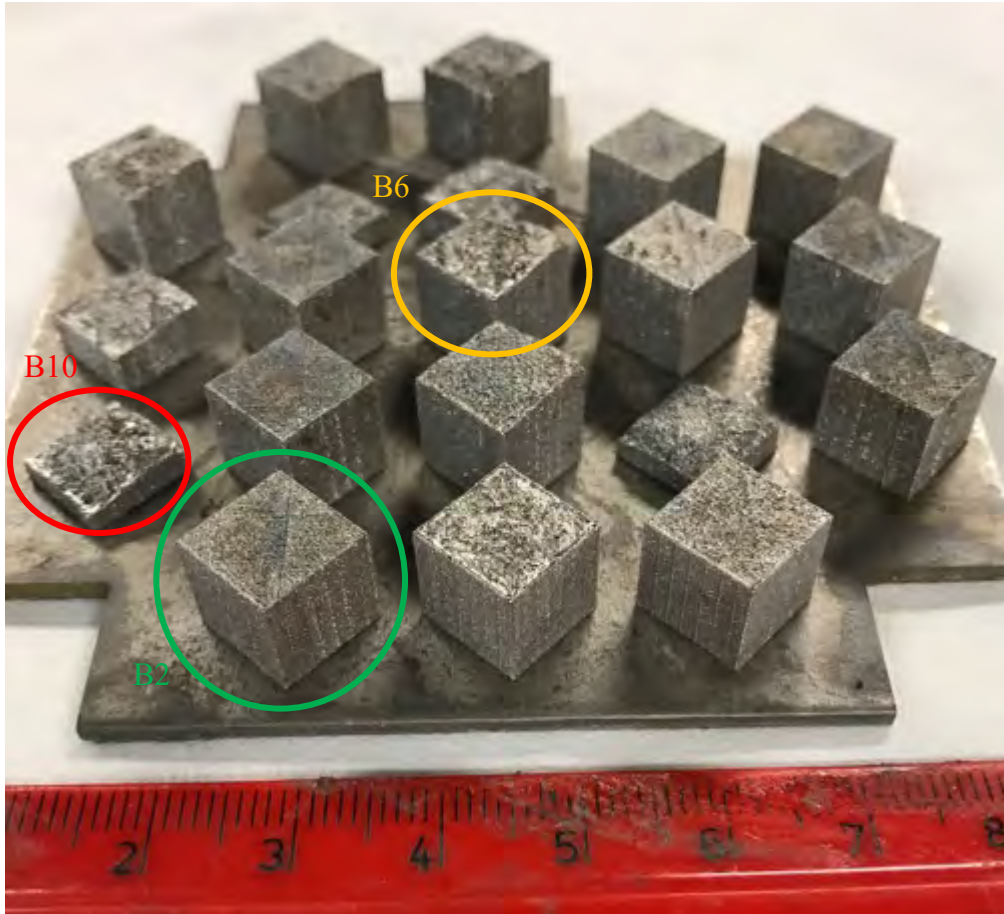


Figure 4.3 - A photograph showing the build from the second stage of the parameter development with parts showing discontinued parts (red), overmelting (yellow) and well-built parts (green)

Table 4.3 showed the parameters used for this build and are colour coded green, amber and red in accordance with how successfully the parameters built. The failed build parameters may have affected powder spreading to other components artificially lowering their density and therefore, parameters B.1-B.3 were rebuilt in the final stage of the study so density analysis could be undertaken.

Table 4.3 - Table showing the process parameters from the second stage of parameter development with discontinued part parameters (red), overmelting part parameters (yellow) and well-built part parameters (green)

Parameter	Laser Power (W)	Laser Scan Speed (mms <sup>-1</sup> )	Laser Scan Spacing (mm)	Volumetric Energy Density (Jmm <sup>-3</sup> )	Linear Energy Density (J/mm)
B.1	400	1700	0.045	174	0.24
B.2	400	1250	0.06	178	0.32
B.3	400	2500	0.03	178	0.16
B.4	400	1000	0.06	222	0.40
B.5	400	1000	0.045	296	0.40
B.6	400	675	0.06	329	0.59
B.7	400	675	0.045	439	0.59
B.8	400	1000	0.03	444	0.40
B.9	400	675	0.0375	527	0.59
B.10	400	675	0.03	658	0.59

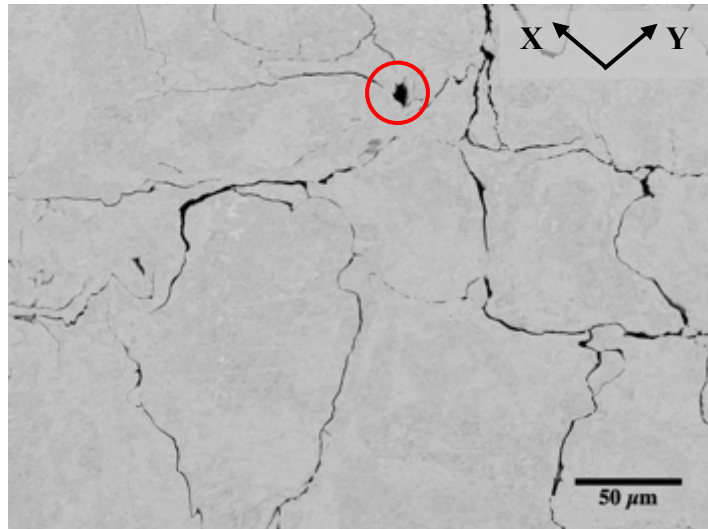
the machine capacity power of 400 W was used for the early stages of parameter development because overmelting had not been anticipated given, both the melting point and thermal conductivity of tungsten. Overmelting was likely due to the higher absorptivity of tungsten in comparison to aluminium for example, which Trapp et al., 2017 (4) found was five times higher than aluminium using a laser power of 200 W. As a result, the powers used were widened for the subsequent stages of the parametric study (250-400 W). Table 4.4 showed the parameters in the final stage of the parametric study.

Table 4.4 - Table showing the process parameters from the final stage of parameter development with optimum parameter highlighted in blue

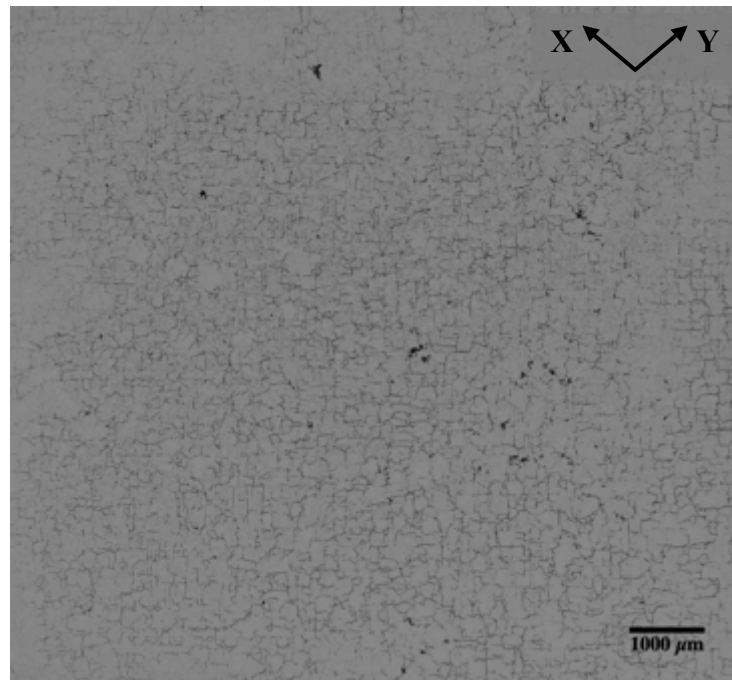
Parameter	Laser Power (W)	Laser Scan Speed (mms <sup>-1</sup> )	Laser Scan Spacing (mm)	Volumetric Energy Density (Jmm <sup>-3</sup> )	Linear Energy Density (Jmm <sup>-1</sup> )
B.1	400	1700	0.045	174	0.24
B.2	400	1250	0.06	178	0.32
B.3	400	2500	0.03	178	0.16
C.1	250	2100	0.0225	176	0.12
C.2	275	700	0.06	218	0.40
C.3	300	750	0.06	222	0.40
C.4	300	850	0.06	196	0.40
C.5	300	750	0.075	178	0.40
C.6	300	850	0.075	157	0.35
C.7	300	1900	0.03	175	0.16
C.8	300	1250	0.045	178	0.24
C.9	300	950	0.06	175	0.32
C.10	350	2200	0.03	177	0.16
C.11	350	1450	0.045	179	0.24
C.12	350	1100	0.06	177	0.32

The optimum parameter was found to be C.3 and Figures 4.4 and 4.5 showed BSE and optical micrographs respectively of this sample. These showed significant levels of cracking throughout the sample but very limited LOF defects (an example is circled in Figure 4.4).

Figure 4.5 was also provided to show the prevalence of cracking on the macroscale. While the cracking seen in Figure 4.4 was noticeably different from the narrow LOF defects previously seen in Figures 4.1 and 4.2, it still appeared to form a consistent pattern. This suggested that the scan pattern may have affected the cracking exhibition seen as had previously been shown in nickel systems (7).



*Figure 4.4 - BSE micrograph of an XY section from parameter C.3, showing extensive cracking and limited lack of fusion defects (circled in red)*



*Figure 4.5 - BSE micrograph of an XY section from parameter C.3, showing prevalence of cracking on the macroscale*

Figure 4.6 showed the Archimedes' density values of the samples against their linear energy density (Equation 4.2). Each laser scan spacing was labelled separately to show its effect in addition to the power and scan speed. As could be seen from this graph, there were two distinct regions; in the first region, density of the parts increased with increasing energy

density up to a maximum linear energy density of  $0.45 \text{ Jmm}^{-1}$  which corresponded to a sample density of between 97 and 98 %. After this, a plateau could be seen with samples having consistent densities between 97 and 98 % density up till  $1.6 \text{ Jmm}^{-1}$ . Typically, three distinct regions can be seen in parametric studies; at low energy densities, the sample density increased with increasing energy input up to a maximum density. This was due to a reduction in LOF defects with increasing energy density. The maxima at the given energy input was the second region and this was the operating window used for LPBF production. After the maxima, the densities again started to decrease as keyholing occurred (8). In this instance, however, the third region could not be seen due to it being a pure metal system and the overbuilding of the parts caused recoater issues to occur before keyhole porosity could be seen.

$$LED = \frac{P}{v} \quad (\text{Equation 4.2})$$

Where P is the laser power (W), and v is the laser scanning speed ( $\text{mms}^{-1}$ ).

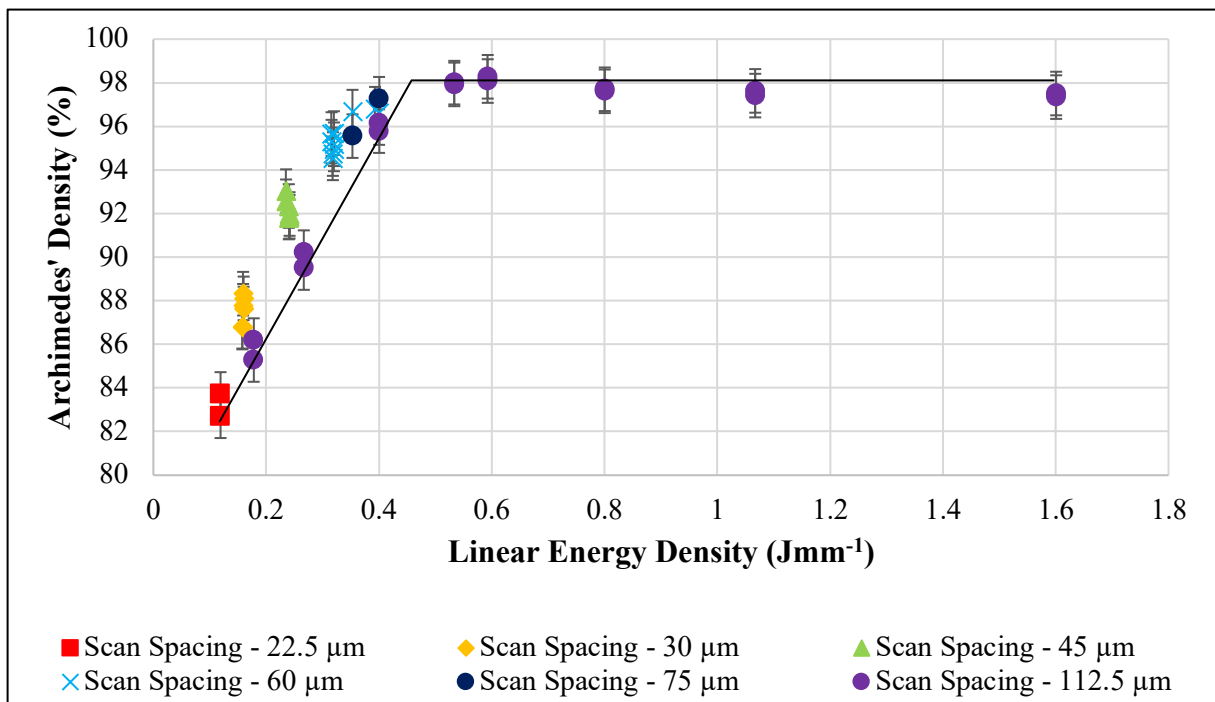


Figure 4.6 - A graph showing the effect of Linear Energy Density ( $\text{Jmm}^{-1}$ ) on the Archimedes' Density (%) of the samples with varying laser scan spacings (error 1 %)

However, it was noted that in the second trial, parts began to fail at energy densities of only  $0.6 \text{ Jmm}^{-1}$ , previously they had successfully built with linear energy densities of up to  $1.6 \text{ Jmm}^{-1}$  with larger laser scan spacings. This suggested that there were limitations to the simplest energy density relationship and possibly all energy density relationships. This will be discussed in more detail in the subsequent section.

#### **4.2.2 Validity and limitations of Volumetric Energy Density (VED) model**

The most common energy density relationship is the Volumetric Energy Density (VED) (Equation 4.1) as could be seen in the literature review, and as such was chosen as the focus of the validity study, alongside potential alternatives.

From the initial parametric study, the range of powers was widened covering 250 – 400 W, all with ‘volumetric energy density’ of  $175 \text{ Jmm}^{-3}$ . From the literature review, it was found that Trapp et al., 2017 (4) modelled a threshold power for melting to be 286 W and a threshold for keyhole porosity generation to be 446 W. However, it was noted experimentally that melting could occur at lower powers possibly due to increased laser absorptivity for the metal oxide. It was shown that melting would occur within the range identified by modelling. As a result, all parameters had a power input between 300 and 400 W. An additional parameter with a power input of 250 W was also produced to investigate the melting threshold. Eleven parameters (plus the lower power parameter) with varying power, scan speed and scan spacing but consistent Volumetric Energy Density ( $\sim 175 \text{ Jmm}^{-3}$ ) were produced. Table 4.5 detailed the parameters and the resultant densities below.



Table 4.5 - Table showing the process parameters, Volumetric Energy Density and sample density from the energy density model validation study

Parameter	Laser Power (W)	Laser Scan Speed (mms <sup>-1</sup> )	Laser Scan Spacing (mm)	Volumetric Energy Density (Jmm <sup>-3</sup> )	Archimedes' Density (%)
D.1*	250	2100	0.0225	176.4	83.0
C.5	300	750	0.075	177.8	97.3
C.7	300	1900	0.03	175.4	86.6
C.8	300	1250	0.045	177.8	91.8
C.9	300	950	0.06	175.4	95.1
C.10	350	2200	0.03	176.8	87.8
C.11	350	1450	0.045	178.8	91.7
C.12	350	1100	0.06	176.8	94.4
D.2	400	1250	0.06	177.8	94.8
D.3	400	1700	0.045	174.3	92.6
D.4	400	2500	0.03	177.8	87.6

\* low power parameter

Initially, the data was plotted as a function of the Volumetric Energy Density. From Figure 4.7, significant variation in density (>10 %) could be seen with minimal changes in energy density (<5 Jmm<sup>-3</sup>). There was also little correlation between the Archimedes' density of the samples and the given energy, with an R value of 0.017. The filled data points all lay within the modelled thresholds for melting and vaporisation, and the unfilled data point corresponded to the low power parameter samples. However, even within thresholds, significant limitations to the relationship could be seen.

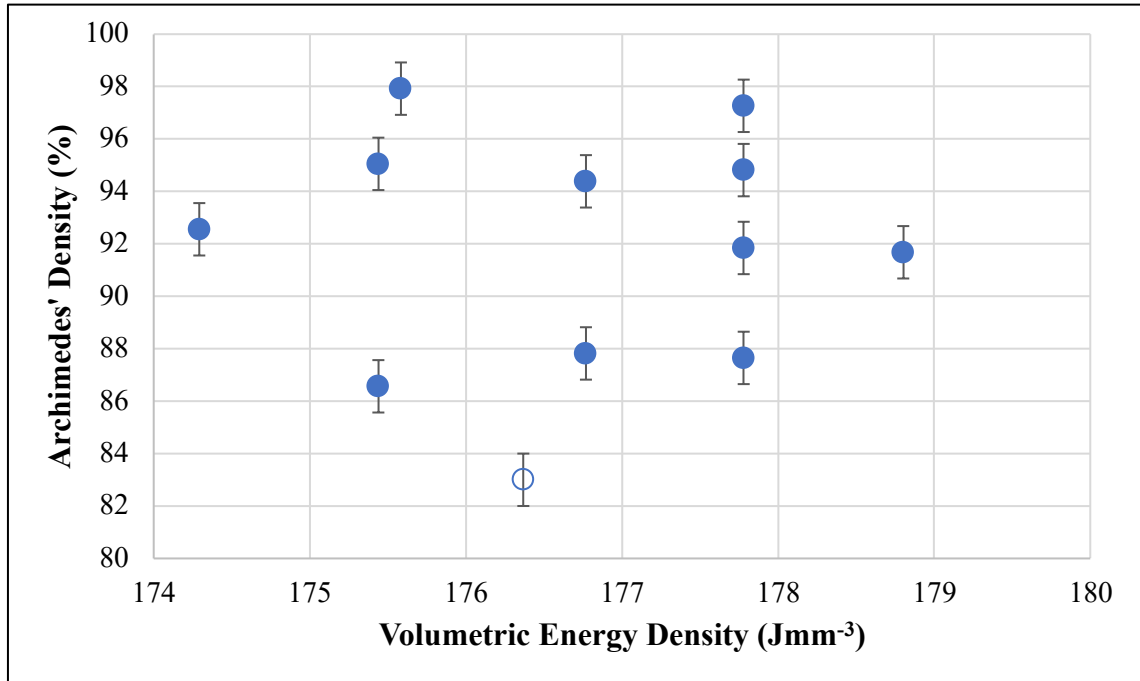


Figure 4.7 - A graph showing the effect of Volumetric Energy Density (Jmm<sup>-3</sup>) on the Archimedes' Density (%) of the samples (unfilled circle corresponded to the low power parameter; error 1 %)

Several studies have also suggested that there were limitations to the suitability of this relationship, particularly Prashanth et al., 2017 (9), which investigated the efficacy of the volumetric energy density relationship in an Al-Si alloy (9-11). This however, produced samples at extremely low laser powers (40 W) which were insufficient for melting to occur. This study showed that even in a simple pure material system, within the thresholds for melting and vaporisation, the model still had significant limitations.

The relationship did not adequately incorporate all variables which may affect build quality including scan strategy and gas flow. Even if these were controlled through the study, the melt pool size and resultant thermal conduction through the build would vary with different laser power and scan speeds; Lampman, 1997 (6) showed travel speed could elongate melt pools and Tramp et al., 2017 (4) suggested increasing power could increase melt pool penetration changing from conduction to keyhole mode. The key flaw in the volumetric energy density relationship appeared to be the equal weighting given to each of the terms

within the equation. Hatch spacing does not alter the actual heat input into the pool in a single weld pass and this energy density relationship assumes incomplete cooling between adjacent tracks. Layer thickness will vary thermal conduction in the bed because conduction through the powder is less than conduction through solid material. However, this is an over-simplification as the underlying material deposit is re-melted and the relationship does not take into account actual penetration. Moreover, increasing the layer thickness may increase weld spatter.

In the most simplified scenario, LPBF could be reduced to a number of individual weld passes, which would be analogous to the LED relationship discussed previously. However, again this is an over-simplification which assumes no temperature build up from adjacent tracks. The LED relationship used only laser power and laser scanning speed. Figure 4.8 showed a plot of Archimedes' Density against LED. As can be seen from Figure 4.8, the correlation was much stronger ( $R = 0.89$ ) than with the VED in Figure 4.7.

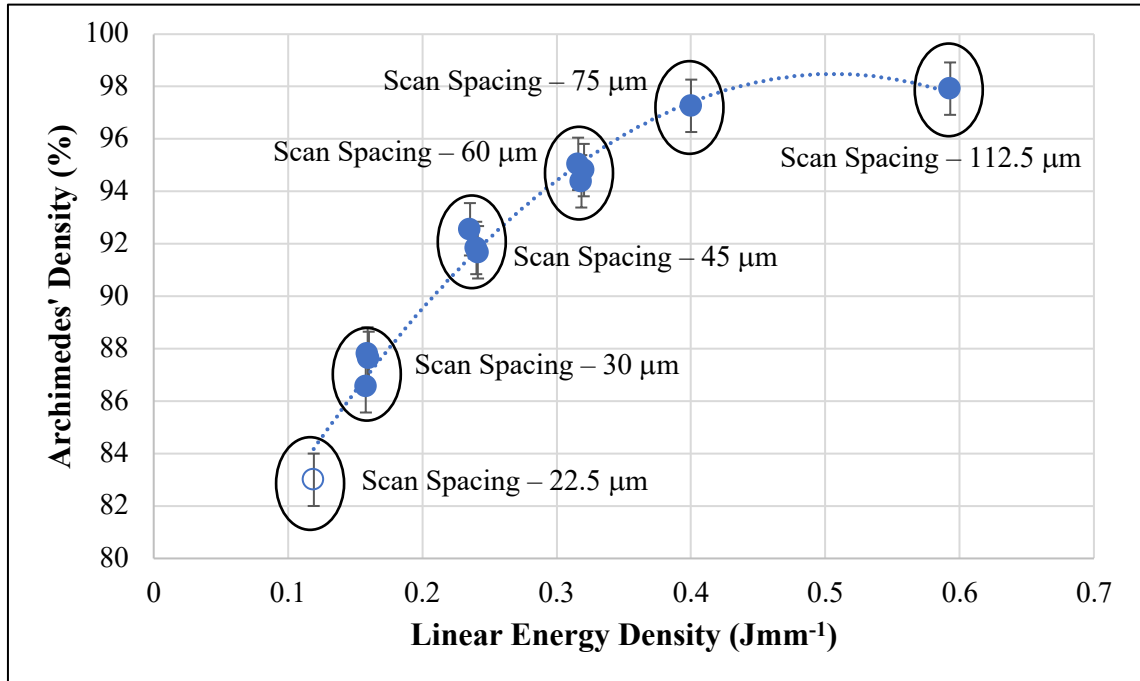


Figure 4.8 - A graph showing the effect of Linear Energy Density ( $\text{Jmm}^{-1}$ ) on the Archimedes' Density (%) of the samples

Layer thickness was not varied in this study and therefore its effects could not be considered. This suggested that laser scan spacing had a lesser effect on sample density than that of laser power and scan speed. Distinct bands, corresponding to scan spacings of the samples could also be seen in the data in Figure 4.8 (labelled in figure). The very distinct areas of data were also reapplied to the graph of sample density against VED; this can be seen in Figure 4.9. This suggested there was some build of heat from adjacent passes, and therefore some effect from hatch spacing, but that it was not as significant as energy input and would not have an effect on melt pool geometry in a single pass. Further work through thermal modelling would be required to quantify the relative effects of laser parameters.

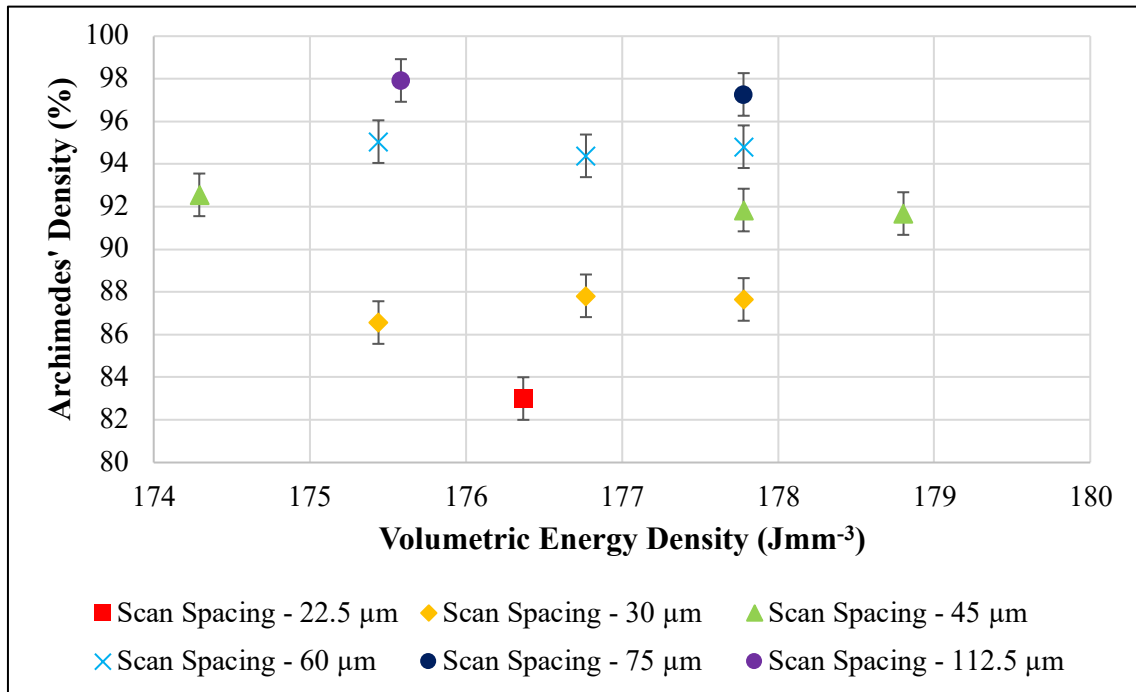


Figure 4.9 - A graph showing the effect of Volumetric Energy Density (Jmm<sup>-3</sup>) on the Archimedes' Density (%) of the samples with varying laser scan spacings

A polynomial relationship could be seen between the sample density and LED ( $P/v$ ) in Figure 4.8. This suggested that power and laser scanning speed were also not equally weighted. It has been shown that increasing laser power increased the peak temperature reached within the pool; this increased the thermal gradient and Marangoni flow within the pool. This was shown to increase the aspect ratio of the tracks and it has been shown that keyhole welds formed more readily under higher powers (10). Trapp et al., 2017 (4) also showed that the absorptivity of the material increased with increasing laser power which corresponded to an increase in melt pool depth but had limited effect on melt pool width likely due to the change from conduction to keyhole modes. This was more significant than the variation in absorptivity with a variation in scan speed; tripling the power almost doubled the absorptivity whereas a third of the scan speed only increased the absorptivity by around a quarter. Increasing scan speed has been shown to elongate the weld pool and at high laser scan speeds balling defects increased due to melt pool instability but appeared to have less of an effect on melt pool dimensions than power (4, 10). Eagar and Tsai, 1983 (12) found that when using a

Gaussian laser, as was used in this study, the maximum temperature of the material was proportional to the ratio of power over scan speed<sup>1/2</sup> and Bertoli et al., 2017 (10) found that melt-pool width was proportional to the ratio of laser power to the square root of laser scan speed. From this it could be concluded that power had a greater effect than scan speed on peak temperature, flow within the melt pool and resultant melt pool dimensions than laser scan speed (10, 12, 13).

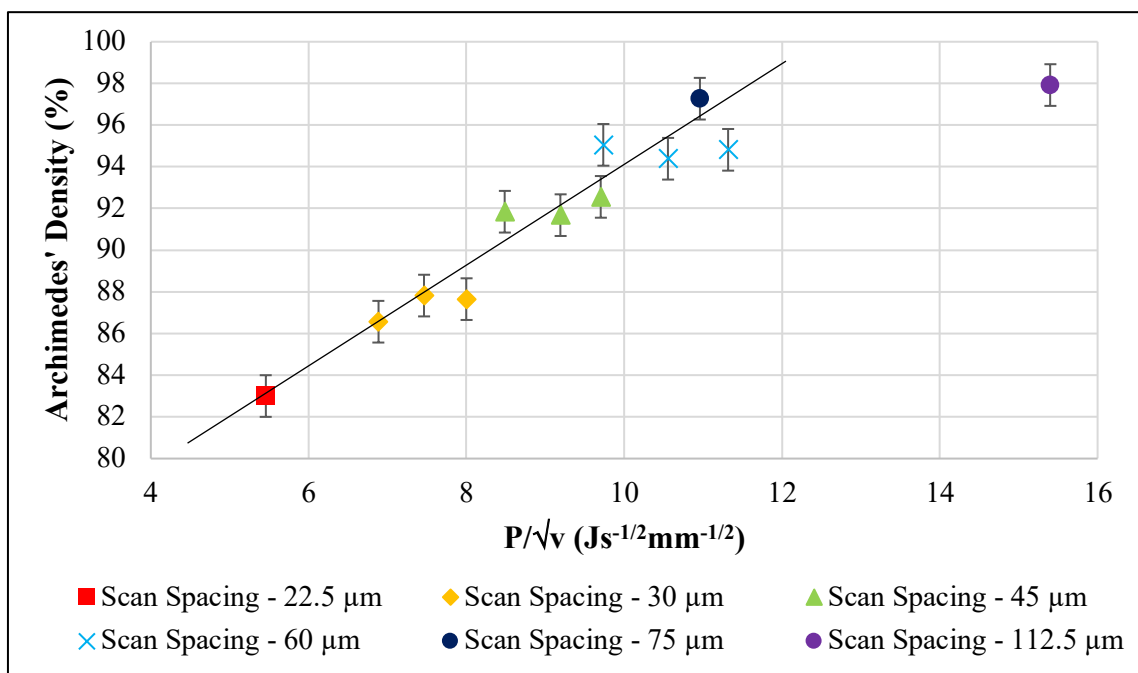


Figure 4.10 - A graph showing the effect of the ratio of laser power to the square root of laser scan speed on the Archimedes' Density (%) of the samples with varying laser scanning spacings

Figure 4.10 showed the effect of the ratio of laser power to the square root of laser scan speed against the Archimedes' density of the samples. The correlation coefficient (R) of the ratio of laser power to the square root of laser scan speed against sample density was 0.9, in comparison to an R value of 0.017 for VED against sample density.

Some studies discussing the limitations of the VED model offered alternative potential models which encompass many of the laser input parameters, the most common of which are

the specific enthalpy model (see Equation 4.4) (10, 11, 13, 14), and Normalised Energy Density (NED) (see Equation 4.5) (15).

$$\Delta H = \frac{A \cdot P}{\rho \sqrt{\pi \cdot \alpha \cdot v \cdot \phi^3}} \quad (\text{Equation 4.4})$$

Where  $\Delta H$  is Specific Enthalpy ( $\text{Jkg}^{-1}$ ),  $A$  is the laser absorptivity,  $P$  is the laser power (W),  $\rho$  is the material density ( $\text{kgm}^{-3}$ ),  $\alpha$  is the thermal diffusivity ( $\text{m}^2\text{s}^{-1}$ ),  $v$  is laser scanning speed ( $\text{ms}^{-1}$ ), and  $\phi$  is laser beam diameter (m).

$$E_0^* = \frac{A \cdot q}{2 \cdot v \cdot l \cdot h} \cdot \frac{1}{\rho \cdot C_P \cdot (T_m - T_0)} \quad (\text{Equation 4.5})$$

Where  $E_0^*$  is Normalised Equivalent Energy Density,  $A$  is the laser absorptivity,  $q$  is the laser power (W),  $v$  is laser scan speed ( $\text{ms}^{-1}$ ),  $l$  is the layer thickness (m),  $h$  is the hatch spacing (m),  $\rho$  is the material density ( $\text{kgm}^{-3}$ ),  $C_P$  is the specific heat capacity ( $\text{Jkg}^{-1}\text{K}^{-1}$ ),  $T_m$  is the melting temperature (K) and  $T_0$  is the bed temperature (K).

The specific enthalpy model was proportional to the ratio of laser power to the square root of laser scan speed as in Equation 4.4,  $A$ ,  $\rho$ ,  $\pi$ ,  $\alpha$  were all constants within a given material system so the process specific variables were power, laser scan speed and beam diameter and thus area. Latent heat of fusion is also not included in this equation but would have a significant effect on the relative energy input required for a specific material to melt. However, in reality there will be variation with temperature and between the solid and liquid state which cannot be encompassed here. The beam diameter in the Concept Laser M2 was also found to increase with increasing laser power possibly due to heating of the laser optics which would therefore have an effect on this relationship (see Table 4.6). Possible improvements to the equations might be to use melt pool dimensions rather than laser beam parameters to accurately reflect laser-metal interactions. This would require further study as

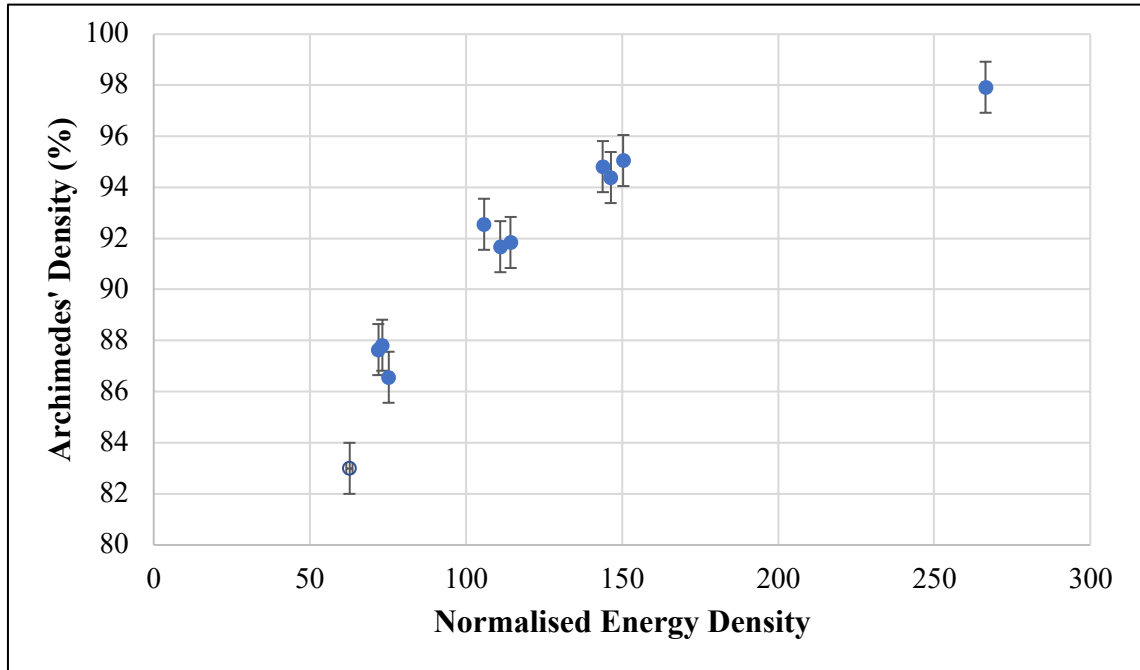
would the determination of whether these terms effectively allowed for material to material comparison.

*Table 4.6 - Table showing effect of laser power (W) on laser beam diameter ( $\mu\text{m}$ )*

<b>Laser Power (W)</b>	<b>Beam Diameter (<math>\mu\text{m}</math>)</b>
100	62
200	66
250	76
275	80
300	84
350	86
400	90

The NED term was found to be similar to VED with the addition of various material constants, as an attempt to make the term effective in comparing energy inputs from material to material, as well as making the term dimensionless. Again, further study would be required to determine if this was effective. NED was proportional to the ratio of power to laser scan speed, and the correlation coefficient was similar to that of LED (R of 0.87 vs. 0.89). Figure 4.11 showed a plot of NED against sample density; clear similarities can be seen to the LED plot (Figure 4.8).





*Figure 4.11 - A graph showing the effect of Normalised Energy Density on the Archimedes' Density (%) of the samples*

While the NED equation showed clear improvements over the VED with respect to the correlation coefficients, this equation still assumed an equal weighting between power, laser scan speed, scan spacing and layer thickness. This was a clear weakness shown in the VED model. Additionally, the use of bulk material properties could be inadequate when attempting to model laser-metal interactions.

From the different presentations of the data seen, two clear paths were taken by most energy density relationships; an equation based on the ratio of power to laser scan speed or an equation based on the ratio of power to the square root of laser scan speed. Neither showed a greater correlation to sample density, and the experimental set up may have affected this from the 'bands' of laser scan spacings used.

Both layer thickness and laser scan spacing must still be within an optimum range for processing, but this could be determined based on the powder size distribution and melt pool

width. Powder layer thickness should be on the order of magnitude of the average particle size distribution. Similarly, the scan spacing could be determined using single laser tracks to determine melt width, to which a slight overlap would be applied (16).

It has been suggested that laser scan speed had a significant effect on melt pool shape and that the melt pool shape would likely have a strong effect on microstructure due to the thermal gradients present and as a result on the elemental segregation as impurities are likely to be concentrated within the area of the melt pool which was last to solidify (6). In this study, however, a pure material was used. From literature, it has been suggested that the grain structure of tungsten can affect cracking and therefore laser power and scan speed, would be the most significant variables as these affect microstructure most strongly (6). A key take-away however should be that there were a number of material specific factors which may make certain energy density models more or less applicable.

Significant flaws were found in the VED model which incorrectly assumed all laser input parameters have equal weighting. Alternative energy density models showed improvements; however, they were based on two simplistic equations relating power and scan speed. This study suggested that laser power was the most significant input parameter and it could also be suggested that either LED or the ratio of laser power to the square root of laser scan speed offered considerable improvements over the current VED model used. However, further study would be required to establish the effect of laser beam area, as with the platform used for this study, it was strongly related to laser power utilised.

## **4.3 Determination of Cracking Mechanism**

### **4.3.1 Introduction**

It was accepted that tungsten is extremely brittle and prone to cracking; indeed, most texts focussing on tungsten and refractory metals dedicate at least one chapter to the cracking of tungsten (17-19). Welding was particularly likely to result in cracking given the high cooling rate and tungsten's susceptibility both to oxygen embrittlement and thermal shock (6, 18). As a result, cracking was expected to be an issue during the course of this study and indeed the early investigations confirmed this would be the case.

Despite cracking being a widely recognised phenomenon in tungsten, the cause of it is the subject of contention. While it is typically accepted to be as a result of interstitial embrittlement and its chemical structure resulting in a sensitivity to thermal shock, which elements are the most detrimental has not been verified (20, 21). Further details can be seen in the literature review (Section 2.2.4).

### **4.3.2 Cracking in Laser Single Scan Tracks**

Single laser scan tracks were produced as an initial step to investigate the effect of process parameters on cracking without the additional factor of reheating which may worsen cracking due to increased time spent cooling in the brittle region below the DBTT (22).

Parameters with varying energy inputs were trialled and four 10mm single scan tracks were produced to investigate weld cracking; Table 4.7 showed the parameters used.

Table 4.7 - Table showing laser process parameters for single scan tracks

<b>Parameter</b>	<b>Power (W)</b>	<b>Scan Speed (mms<sup>-1</sup>)</b>
A	400	250
B	400	675
C	300	750
D	300	250
E	300	1500
F	200	800
G	300	1000
H	200	250

The effect of various energy input parameters on the average width of the scan tracks was investigated. This furthered the work discussed in Section 4.2.2 which discussed the effect of process parameters on melt pool dimensions and the literature survey suggesting an effect based on the ratio of power to the square root of scan speed on melt pool width. Figure 4.12 and 4.13 showed the melt pool width plotted as a function of LED and the ratio of power to the square root of scan speed respectively. This data showed a consistency with the findings of Bertoli et al., 2017 (10) with a correlation coefficient of 0.94 between melt pool width and the ratio of power to the square root of scan speed (10).

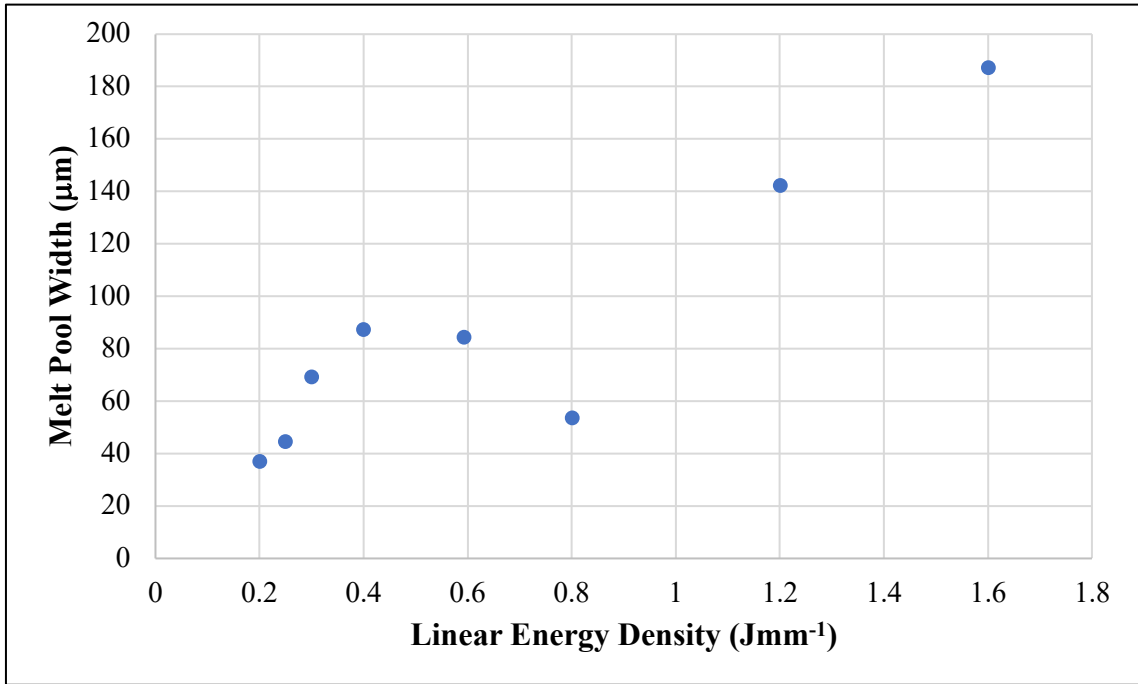


Figure 4.12 - A graph showing the effect of Linear Energy Density (Jmm<sup>-1</sup>) on the melt pool width (μm) of the single scan tracks

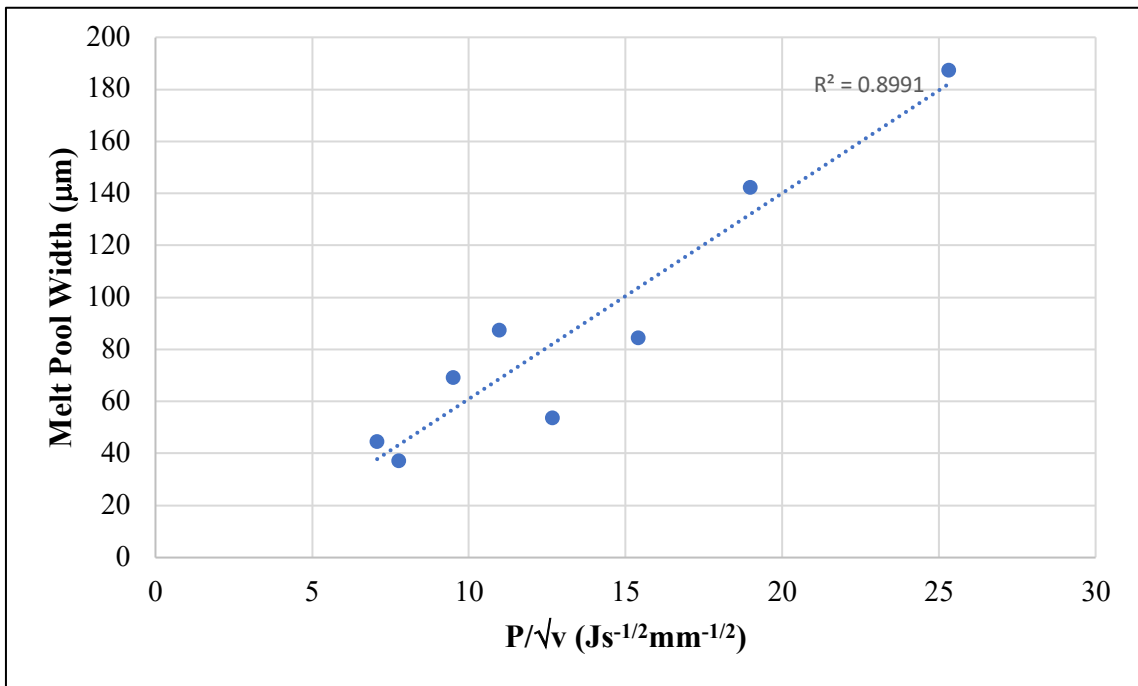
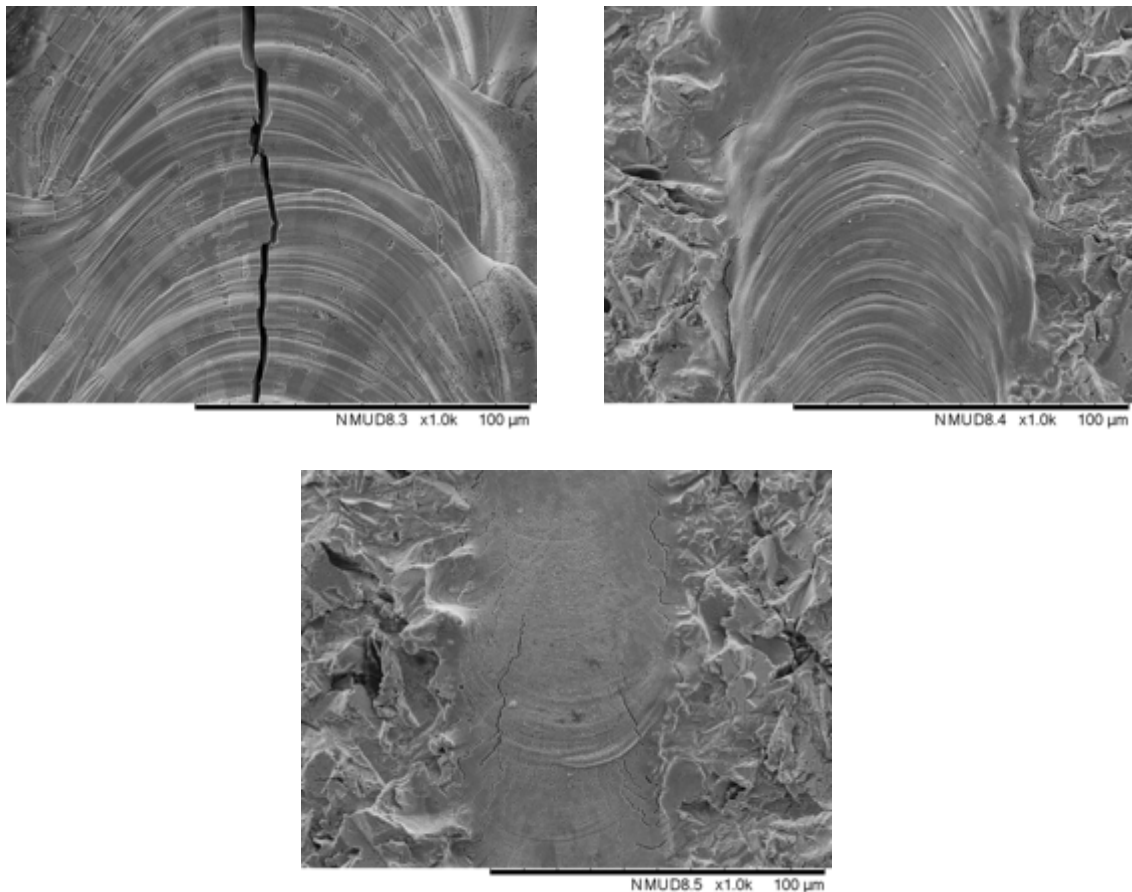


Figure 4.13 - A graph showing the effect of the ratio of laser power to the square root of laser scan speed (Js<sup>-1/2</sup>mm<sup>-1/2</sup>) on the melt pool width (μm) of the single scan tracks

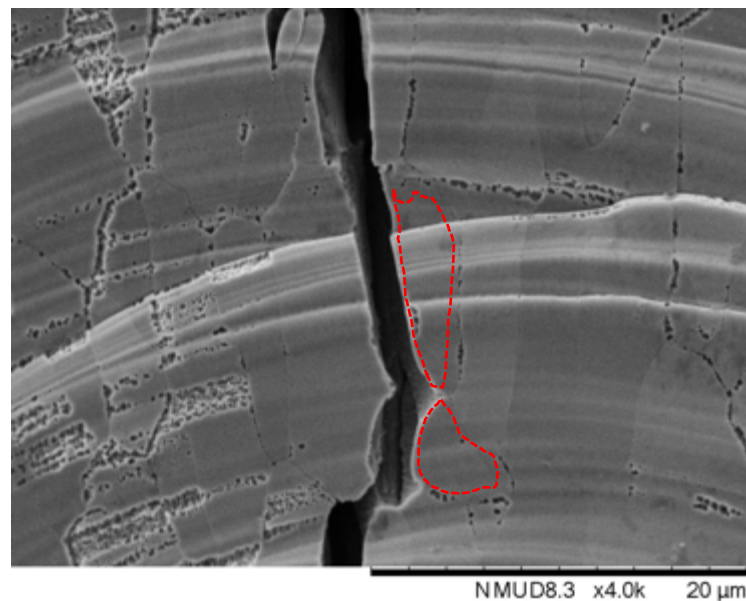
The difference in heat inputs, laser scan speeds and melt pool widths suggested a significant variation in grain structure would be seen due to the growth of the columnar grains in the direction of the thermal gradients (6). The literature review suggested a strong link between microstructure and cracking would be seen (23, 24). To review this effect the single scan tracks were reviewed under SEM. The tracks were produced on the base plate in the absence of powder and the elevation above the base plate was attributed to surface tension within the melt pool. Figure 4.14 showed SE micrographs from a higher ( $1.6 \text{ Jmm}^{-1}$ ), medium ( $0.4 \text{ Jmm}^{-1}$ ) and lower level ( $0.3 \text{ Jmm}^{-1}$ ) of energy input. The laser power and scan speed from parameter C (Table 4.7) were the optimum found from the initial parametric study (Section 4.2.1).



*Figure 4.14 - SE micrographs of single scan laser tracks at a higher, medium and lower energy input*

At higher levels of energy input cracking down the weld centreline could clearly be seen. This showed that even at the most basic level of processing, without re-melting or re-heating from adjacent laser tracks or from subsequent build layers, significant levels of cracking could be seen when operating under suboptimal process parameters.

At higher magnifications, the grain structure within the weld bead can clearly be seen (Figure 4.15). From the micrograph, the intergranular nature of the crack path could be seen. The crack could be seen to change direction around the grains and the crack morphology exhibited smooth edges throughout. To highlight the effect, the grain boundaries of two crack adjacent grains were highlighted in red.



*Figure 4.15 - SE micrograph showing centreline cracking in single scan track produced with Parameter A*

This exhibition of cracking is typically held to be solidification or hot cracking. Solidification cracking is generally understood to be affected by three main factors; excess impurities in the weld such as oxygen or sulphur, excess stress either thermal or from restraint, or improper weld parameters such as low power or high travel speeds resulting in low width to depth ratios (6, 25) (see Figure 4.16).

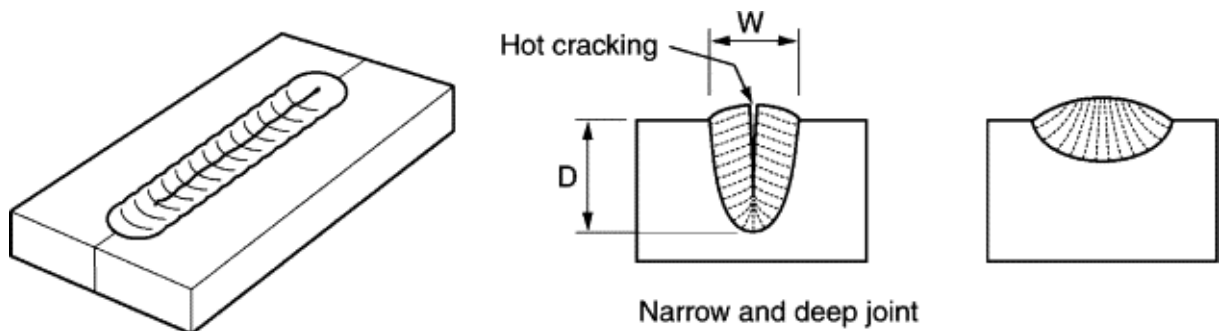


Figure 4.16 - Schematic illustrating the morphology and possible cause associated with solidification cracking. Taken from Weman, 2012 (25)

Of particular interest to this study were the effect of impurities, improper input parameters and high thermal stress. Only the input parameters will be investigated at this stage. Analysis into potential effects of interstitial impurities will be investigated in Section 4.3.3 of this chapter. Aims to reduce impurity content and thermal stress will be the basis of Chapter 5 of this thesis.



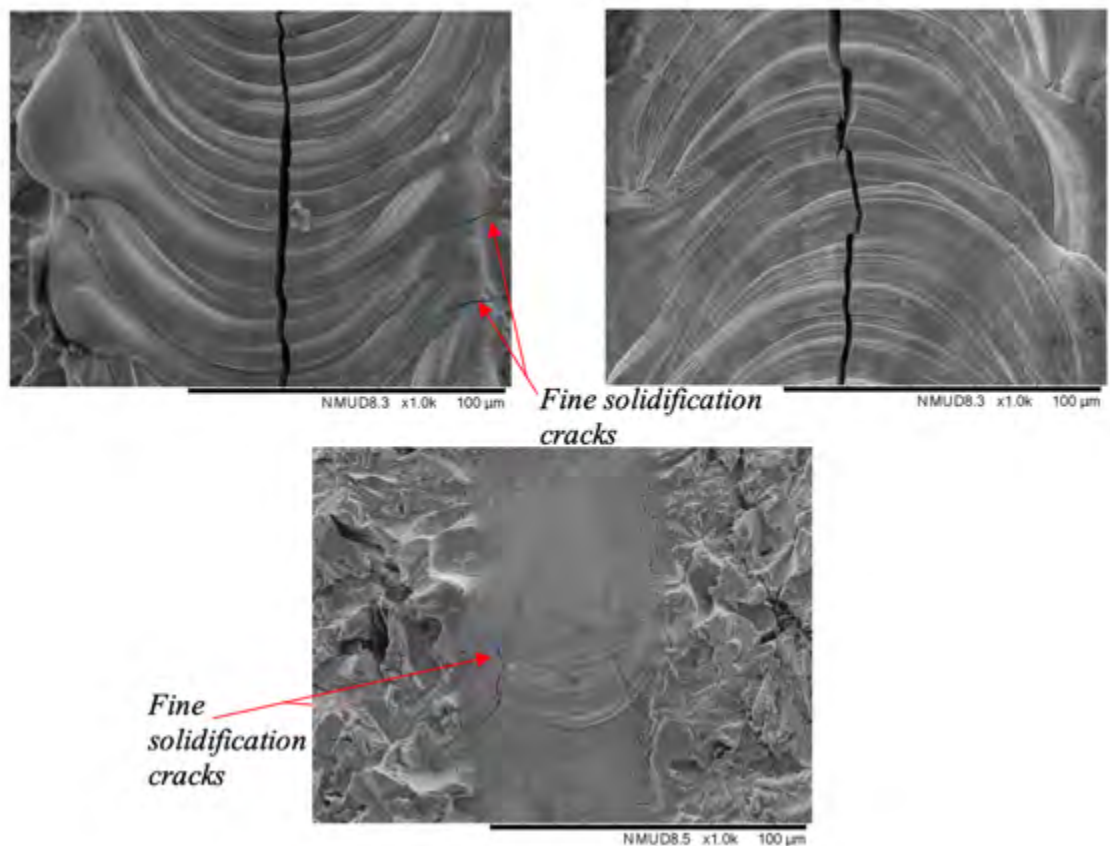


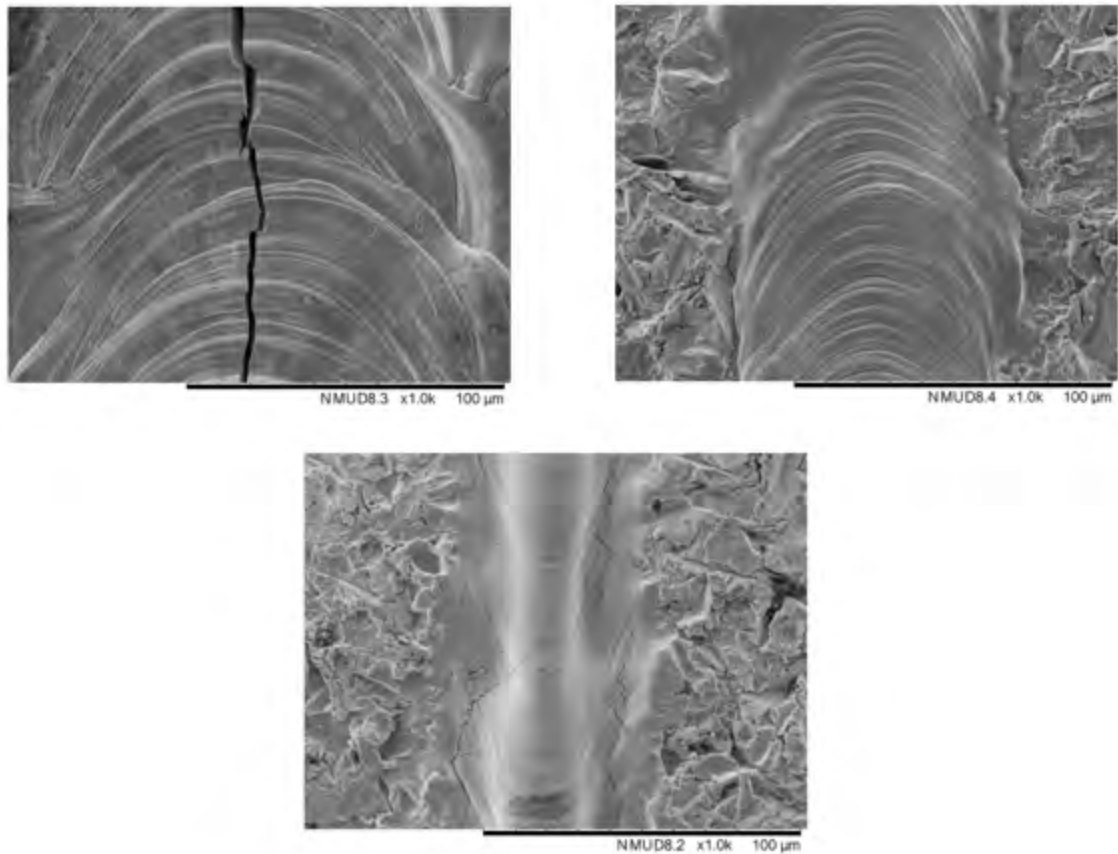
Figure 4.17 - SE micrographs of single scan laser tracks produced at varying powers (400 W (top left), 300 W (top right) and 200 W (bottom)) with a laser scan speed of 250 mms<sup>-1</sup>

The SE micrographs in Figure 4.17 showed the effect of power variation of 400, 300 and 200 W respectively with a laser scanning speed of 250 mms<sup>-1</sup>. Table 4.8 showed the average melt pool width from each of the tracks. The depth could not be measured in this study due to extensive cracking at the base of the weld pool which caused fallout during preparation. At 300 W, some areas of the track showed the typical centreline cracking seen in Figure 4.18 whereas other areas were uncracked. At 400 W however, this cracking was consistent throughout the track length. In the track produced at 200 W by contrast, no centreline cracking was seen. Instead fine solidification cracks were seen along the boundaries of the columnar grains formed behind the melt pool.

Table 4.8 - Table showing effect of laser power ( $W$ ) on melt pool width ( $\mu\text{m}$ ) of single scan tracks

Parameter	LED ( $\text{Jmm}^{-1}$ )	Power ( $W$ )	Scan Speed ( $\text{mms}^{-1}$ )	Melt Pool Width ( $\mu\text{m}$ )
A	1.6	400	250	187
D	1.2	300	250	142
H	0.8	200	250	54

In conventional fusion welding, it was generally considered that reducing laser scan speed would reduce the quantity of cracking seen, due to reduced turbulence of the melt pool reducing the likelihood of balling defects (6), however, when looking at three parameters produced with increasing scan speed at a fixed laser power of 300 W, this was not seen. Figure 4.18 showed the SE micrographs from these parameters. At the lowest level of scan speed ( $250 \text{ mms}^{-1}$ ), extensive centreline cracking could be seen. At excessively high laser scan speeds, fine solidification cracks formed at the edges of the scan tracks. The amount of shrinkage would increase with increased melt pool width and therefore the strain within the weld could also be considered to increase. The reduced cracking was seen at the intermediate speed suggesting two conflicting factors operating.



*Figure 4.18 - SE micrographs of single scan laser tracks produced at varying scan speeds ( $250 \text{ mms}^{-1}$ ,  $675 \text{ mms}^{-1}$ , and  $1500 \text{ mms}^{-1}$ ) with a laser power of  $300 \text{ W}$*

The edge of the weld track is the area which would solidify first and experience the fastest cooling rate (6, 26). The fine cracking seen at  $1500 \text{ mms}^{-1}$  was therefore likely to be a result of thermal shock at higher scan speeds.

At lower laser scanning speeds, the time at temperature would be higher resulting in greater pick-up of interstitial elements during welding. Additionally, as the centreline was the final portion of the weld to solidify, the restraint of this portion of the weld was the greatest increasing the residual stress and the interstitial embrittlement lowered the grain boundary cohesion causing the centre-line cracking seen.

Increasing the laser scan speed was also found to reduce the melt pool width of the scan track. Table 4.9 showed the average melt pool width from each of the tracks with varying laser scan speed.

*Table 4.9 - Table showing effect of laser power (W) on melt pool width ( $\mu\text{m}$ ) of single scan tracks*

<b>Parameter</b>	<b>LED (<math>\text{Jmm}^{-1}</math>)</b>	<b>Power (W)</b>	<b>Scan Speed (<math>\text{mms}^{-1}</math>)</b>	<b>Melt Pool Width (<math>\mu\text{m}</math>)</b>
D	1.2	300	250	142
C	0.4	300	750	88
E	0.2	300	1500	37

When comparing this to Table 4.8, the range of LED was  $0.8 \text{ Jmm}^{-1}$  resulting in a change on size of the melt pool width of  $134 \mu\text{m}$  for changing laser power in comparison to a range of  $1 \text{ Jmm}^{-1}$  causing a variation of  $105 \mu\text{m}$  for changing laser scan speed. This suggested laser power was the most significant input parameter determining melt pool width, furthering the conclusions of Section 4.2.2 which determined laser power was the most significant input parameter for part density. However, due to heating of the laser optics, there was a swelling of the beam by around  $20 \mu\text{m}$  over this power range. The effect of the beam swelling would need to be investigated to decouple the two effects in future works.

Much of the literature focused on the ratio of melt pool width to depth. By sectioning through the weld tracks it was attempted to investigate this phenomenon. However, extensive cracking at the base of the melt pool resulted in the melt pools breaking off during their preparation and therefore, could not be examined.

The initial single scan investigation has showed that tungsten cracks extensively under the processing conditions of LPBF. Utilising optimum process parameters, it was found that cracking could be reduced. Particularly, using the minimum acceptable power for complete melting reduced the likelihood of cracking. This was found to be around 300 W (beam

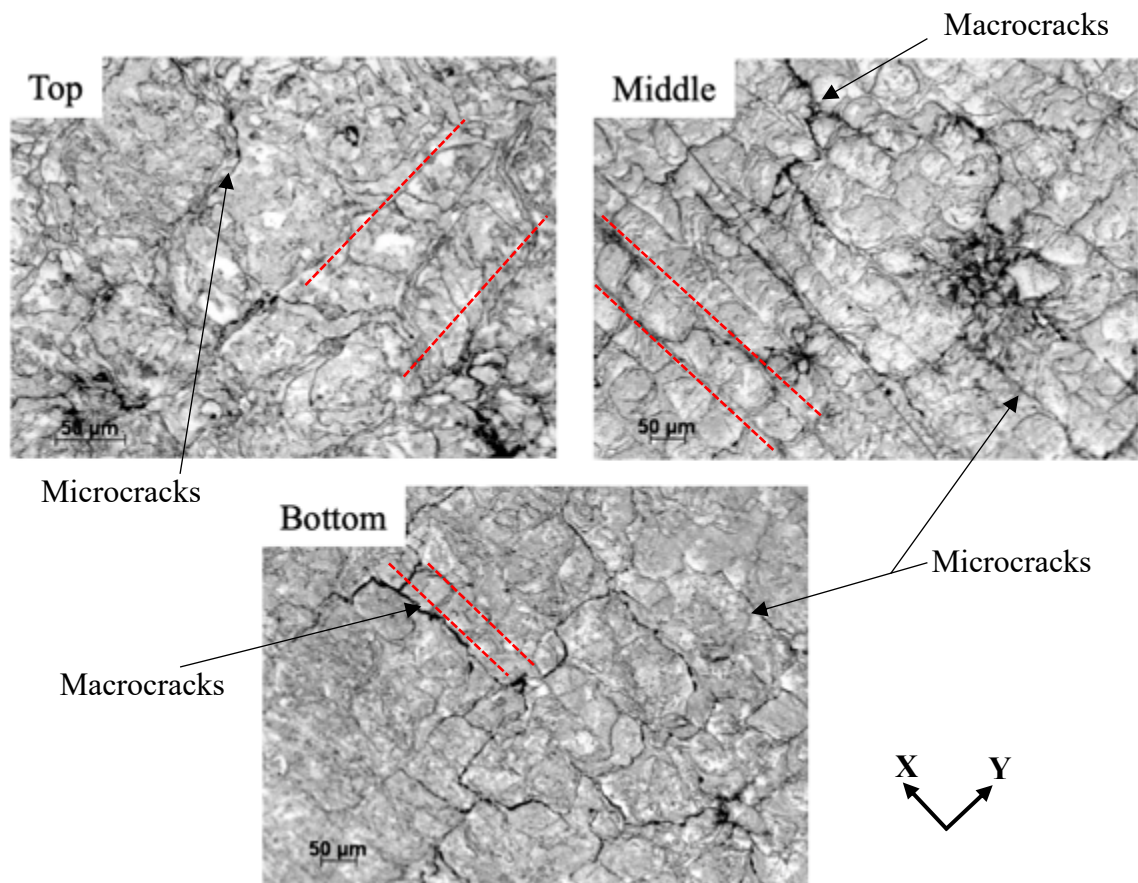
diameter 84  $\mu\text{m}$ ), in accordance with the modelling conducted by Trapp et al., 2017 (4) to determine the threshold power for melting (4).

Additionally, it was found that intergranular cracks most likely solidification cracks could be seen in the tracks and that these were likely partially resulting from the presence of impurity elements due to the non-standard response to variation in laser scan speed. These ideas will be expanded upon in the subsequent sections in this chapter as will also investigation of the effect of multiple melts as would occur in a typical LPBF sample.

### **4.3.3 Microstructure Investigation of LPBF Deposits**

While useful insights were gleaned from the analysis of laser single scan tracks, this was a significant oversimplification of the LPBF process. Much of the literature that exists investigated the welding of tungsten (6, 27, 28). However, these did not cover the key issues associated with LPBF, namely the environment being poorer despite an argon atmosphere. This was largely a machine fault and also related to the size of protective atmosphere in comparison to the local shielding possible in welding. The multiple reheating cycles of the samples through adjacent weld tracks and multiple layer build up would also alter the microstructure significantly in comparison to conventional fusion welding.

Sections were taken at the base, midsection and top of LPBF deposits and the samples were etched to reveal the grain structure such that the cracking could be related to the grain structure. Figure 4.19 showed optical micrographs of the three sections.



*Figure 4.19 - Optical micrographs showing the variation in cracking and grain structure through the build height of the deposit*

The grain structure in the three sections showed noticeable key differences; note the different magnification in the top section used as the finer cracks could not be differentiated from the grain boundaries at the lower magnifications required to see the regular pattern to the cracks in the bottom and middle sections.

A regular grain structure closely following the laser scan tracks could clearly be seen in the bottom and middle sections of the sample. Indicative laser paths were highlighted in red. As noted previously, strong similarities were seen between the bottom and middle sections with the middle section showing stronger levels of cracking. This was assumed to be as a result of the increase in residual stress due to increased thermal gradients and resultant thermal contractions with increasing build height through the sample. This was a well understood

phenomenon detailed by Furumoto et al., 2010 (29) and Yadroitsava and Yadroitsev, 2015 (29, 30). The cracking pattern was consistent with those expected from thermal shock studies conducted previously where major cracks could be seen between a network of microcracks (see Figure 4.20) (23).

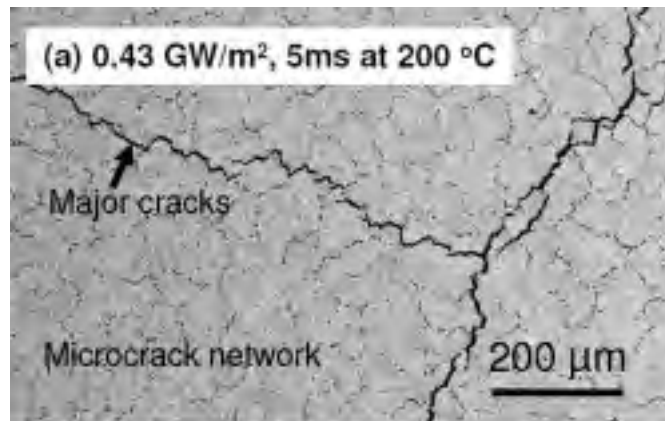
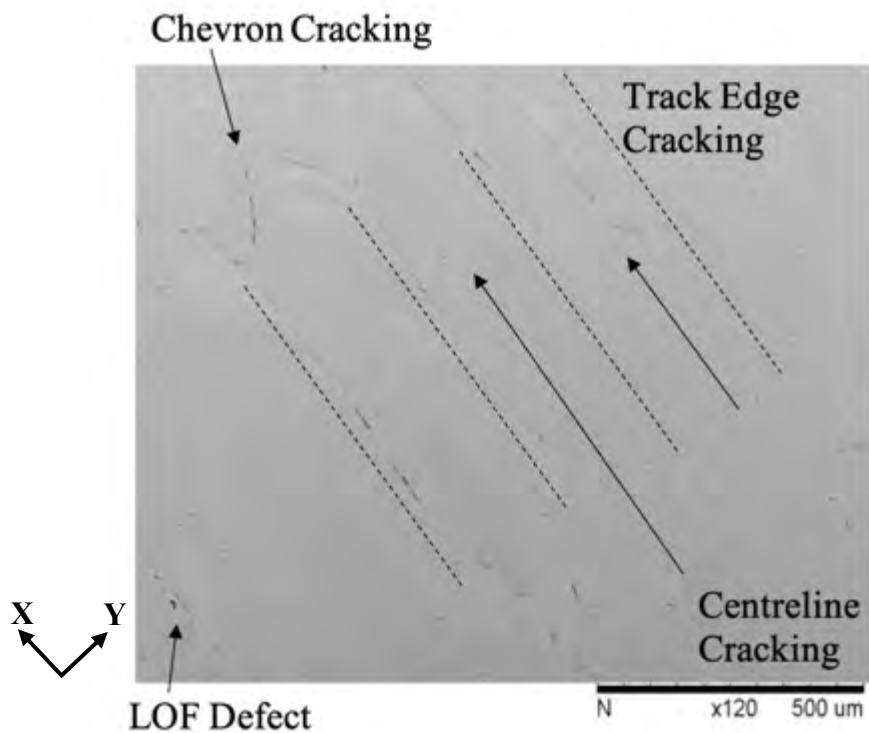


Figure 4.20 - Typical cracking in tungsten after thermal shock. Taken from Hirai et al., 2009 (23)

By contrast, the top section showed a greater degree of irregularity of the grain structure; the scan tracks could only occasionally be discerned, and the cracking was finer than the sections lower in the build height. This was considered to be as a result of this area being exposed to fewer reheat cycles and therefore less time at temperature cooling underneath the DBTT. This section appeared to only contain microcracks rather than the macro cracks seen at higher levels of thermal shock and in the bottom and middle sections (23, 31).

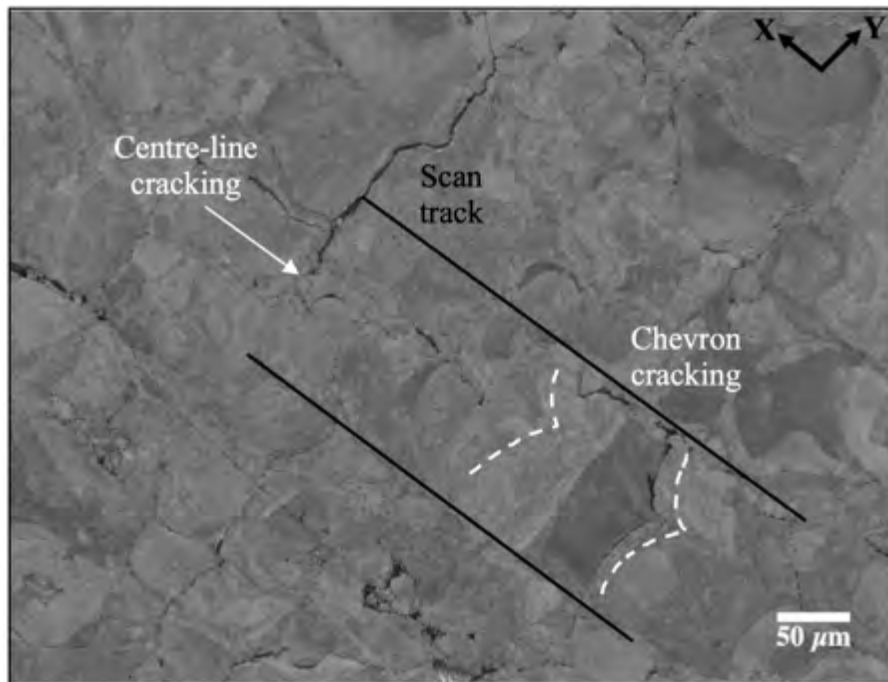
As was shown in Figure 4.19 the cracking had a close relation to the laser scan path; the BSE micrograph (Figure 4.21) showed a clear cracking pattern indicative of the microstructure of LPBF tungsten; few LOF defects could be seen but the cracking was extensive and clear patterns were seen. Cracking was seen both at the centreline and at the edges of the weld track as well as chevron shaped cracks through the weld tracks (labelled).



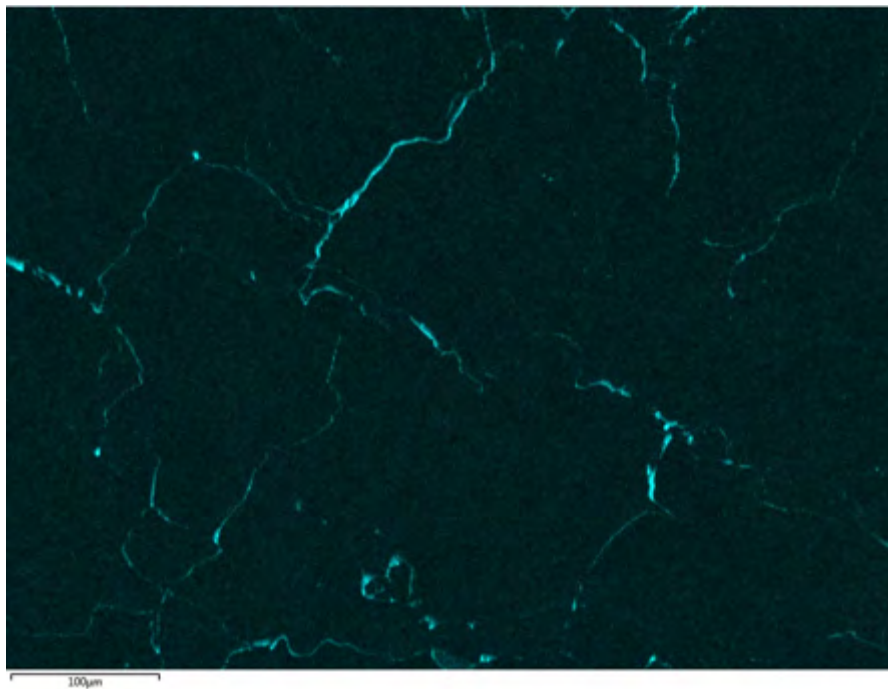
*Figure 4.21 - BSE micrograph showing cracking pattern found in LPBF tungsten samples*

This was confirmed through the use of EBSD to determine the grain structure related to the cracking seen; in Figure 4.22 a band contrast image (EBSD map where Kikuchi patterns were assigned a grey scale value) of LPBF tungsten could be seen; the scan track, centreline cracking and chevron cracking were labelled. An EDX map of oxygen from the same location (Figure 4.23) showed stronger presence of oxygen in the area of cracking. However, the EDX map could not conclusively confirm this due to issues associated with the technique; namely the interaction volume of oxygen in EDX being fairly large, combined with the issue associated with increased signal strength surrounding defects. For these reasons the level of oxygen surrounding the cracks would have to be significantly elevated to detect.





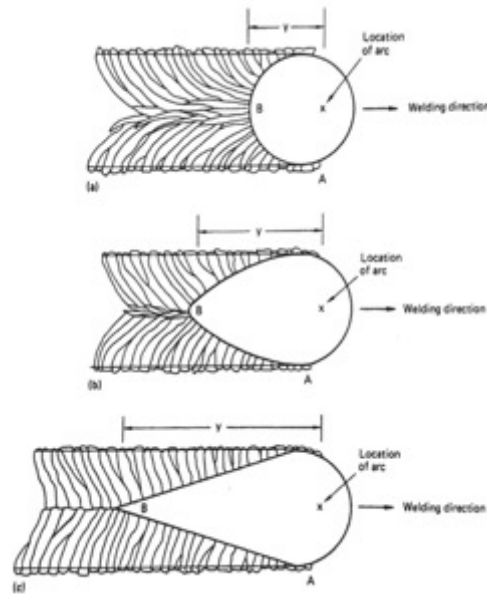
*Figure 4.22 - Band contrast image showing laser scan track and cracking in LPBF tungsten sample*



*Figure 4.23 - EDX map of oxygen distribution in LPBF tungsten sample*

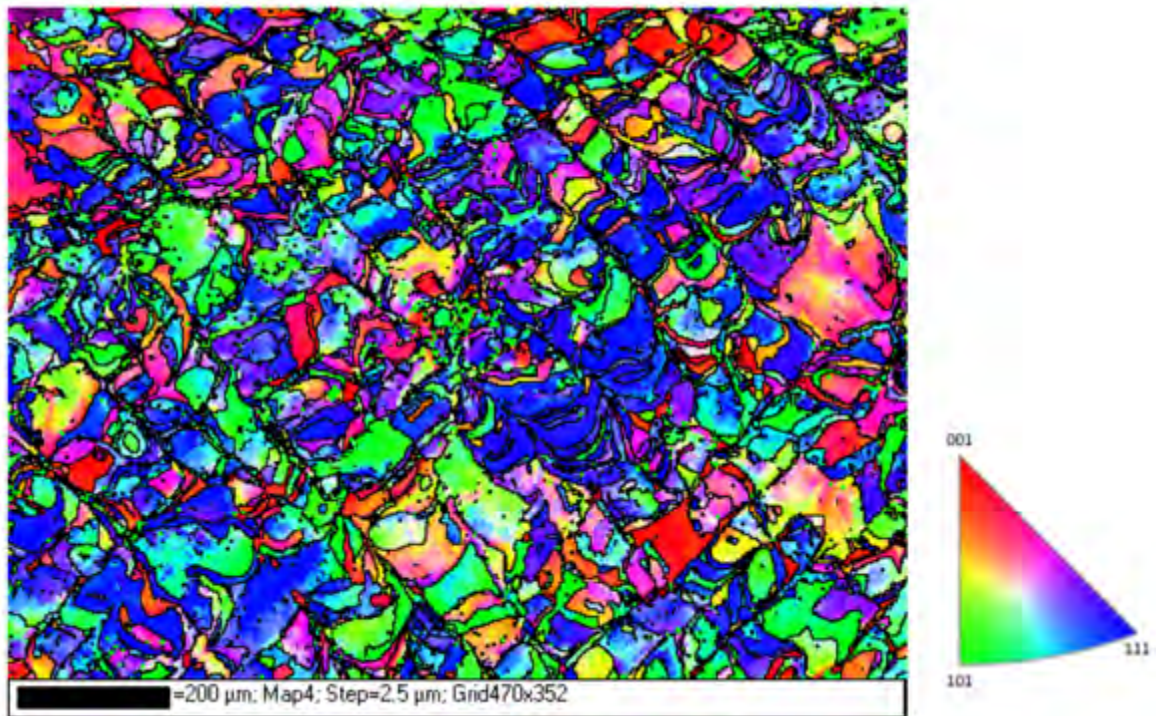
The formation of the centreline grain boundary could be seen in Figures 4.21 and 4.22; this was to be expected based on welding microstructures (see Figure 4.24). This was due to the

solidification chronology; the edges of the scan track solidified first with the melt fronts moving inwards causing the formation of a centreline grain boundary on meeting. The angled grain boundaries were formed following the direction of heat transfer away from the advancing melt pool. The chevron cracks seen were intergranular cracking which occurred along the boundaries formed against the direction of heat transfer.



*Figure 4.24 - Typical welding microstructures with varying scan speeds (low (top), intermediate (middle), high (bottom)). Taken from Lampman, 1997 (6)*

The investigations determined that cracking levels varied based on height through the build but maintained a strong link with the laser path. Cracking morphologies were seen to be similar to conventional tungsten following thermal shock showing a network of microcracks within larger macrocracks.



*Figure 4.25 - EBSD map of LPBF tungsten sample (IPF Z colouring)*

Figure 4.25 showed an EBSD map (IPF Z colouring) of the LPBF tungsten sample to analyse the texture of the material. The sample produced had a microstructure which was clearly related to the scan path of the laser and typical to the microstructures seen in the etched and band contrast images. The average grain diameter was determined to be 17 μm although there was significant variation with a small number of grains having an equivalent diameter of 85 μm. The sample also showed a noticeable texture between  $\langle 111 \rangle$  and  $\langle 110 \rangle$  directions similar to the findings of Sidambe et al., 2019 (3) and Ivekovic et al., 2019 (24); this was attributed to the variation in melt pool shape from typical AM-metals e.g. titanium due to increased thermal conductivity and high surface tension increasing the thermal gradient across the pool.

XRD was conducted to further investigate the likely texture of the material; Figure 4.26 showed the pattern of LPBF tungsten. The LPBF tungsten showed a great degree of similarity to the tungsten powder.

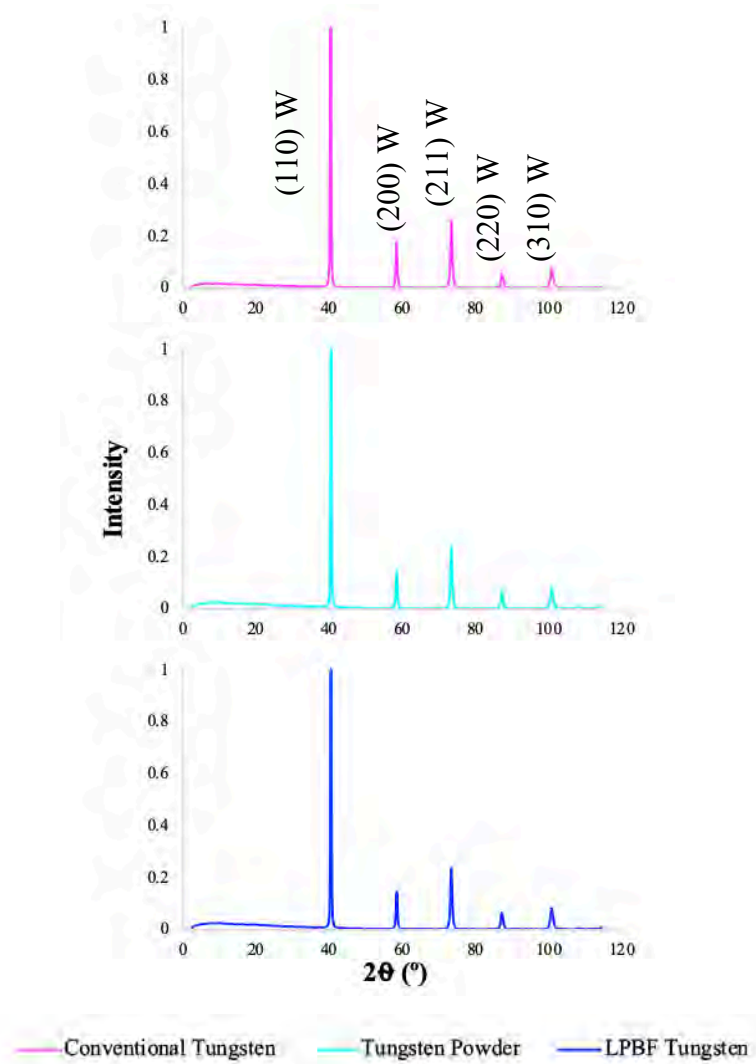


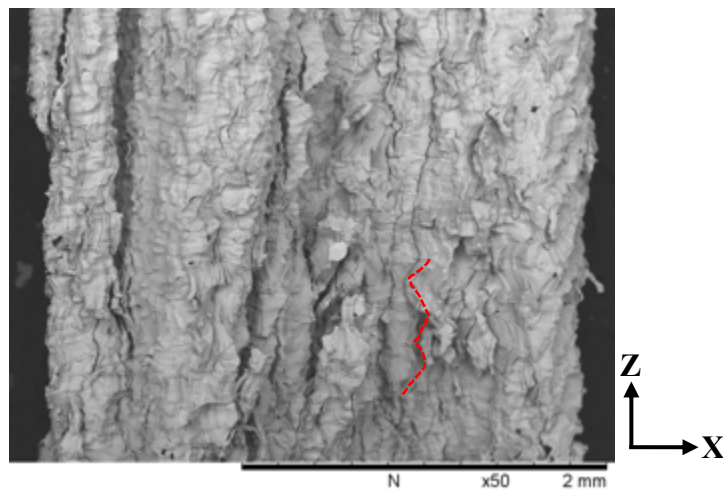
Figure 4.26 - XRD pattern of LPBF W, conventional W and W powder samples

The texture in LPBF tungsten was comparable to that found in the studies of Sidambe et al., 2017 (32) and Tan et al., 2018 (33) showed stronger intensity for the (110) and (211) planes and a weaker intensity for the (200) plane.

#### 4.3.4 Small Punch Testing and Fractography

Fracture surfaces were investigated to analyse the nature of cracking and failure within LPBF tungsten samples. Fracture surfaces were generated both through small punch fracture testing and, due to the intrinsic brittleness of tungsten samples, manual fracture.

Figure 4.27 showed a low magnification BSE micrograph of a fracture surface produced through manual fracture. Clear waving could be seen (an indicative area was shown with a red marker).



*Figure 4.27 – Low magnification BSE micrograph of LPBF tungsten fracture surface (XZ section)*

This was determined to be from the XY shift of the ‘island’ of the scan strategy used during production. A schematic of the shift could be seen in Figure 4.28, with the waving corresponding to the shift of the outer edge of the ‘island’.

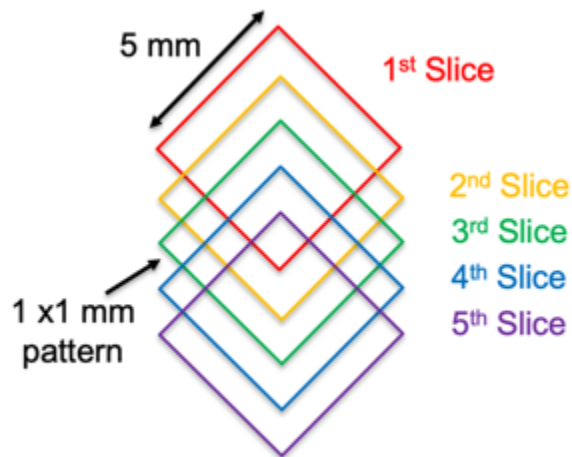


Figure 4.28 - XY shift of 'islands' in the chess scan strategy. Adapted from Carter et al., 2014 (7)

This schematic showed an interference pattern of  $1\text{mm}^2$  that may have been present from the XY shift. An optical micrograph of LPBF tungsten showed the presence of this interference pattern through a cracking network along with an indicative marker of  $1\text{mm}^2$  (see Figure 4.29).

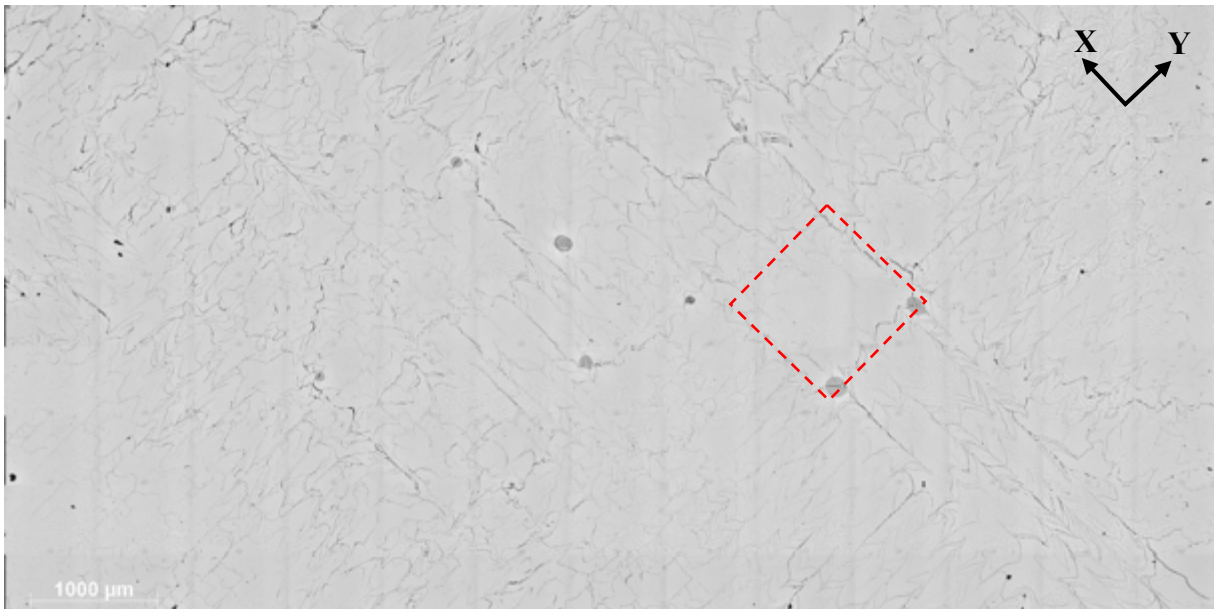
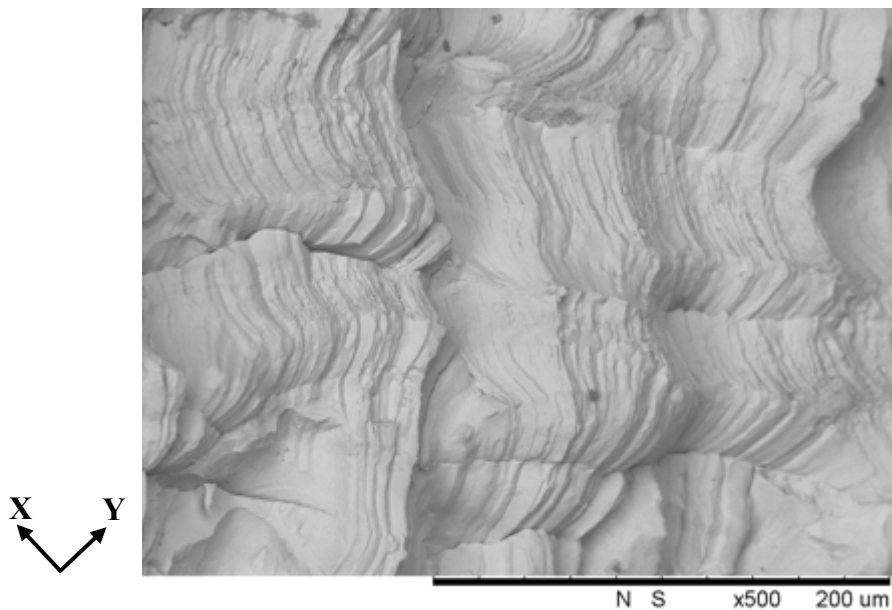


Figure 4.29 - Optical micrograph of LPBF tungsten showing the  $1\text{mm}^2$  interference pattern due to 'island' shift

Fracture surface were produced that failed both in the XZ and XY plane. The fracture surface of an XY plane was seen showing more detail (see Figure 4.30). This confirmed both the

intergranular nature of the failure but also confirmed that entire weld tracks could be pulled out during failure suggesting layer boundaries were particular points of weakness. In multi-alloy materials this would be attributed to segregation to the melt pool boundaries. As this was a nominally pure material, it could further posit the presence of impurity elements segregating to grain boundaries (18, 34). Weld track or layer boundaries could act similarly to grain boundaries with regard to impurity segregation.



*Figure 4.30 - BSE micrograph of LPBF tungsten fracture surface (XY section)*

The manual fracture specimens showed large areas of fracture which gave a clearer indication of failure mode. However, the manual fracture gave no indication of mechanical properties or comparison to conventional tungsten material; the small punch test samples provided both of these.

Figure 4.31 showed a load-displacement curve for small punch tests conducted at a variety of temperatures on LPBF tungsten. In this instance load-displacement curves were produced in the place of stress-strain curves as the stress on the sample varies during small punch testing. As expected, the room temperature test, had a higher maximum load (nearly double).

However, the instantaneous drop in load was indicative of cracking and possibly showed a lower level of ductility.

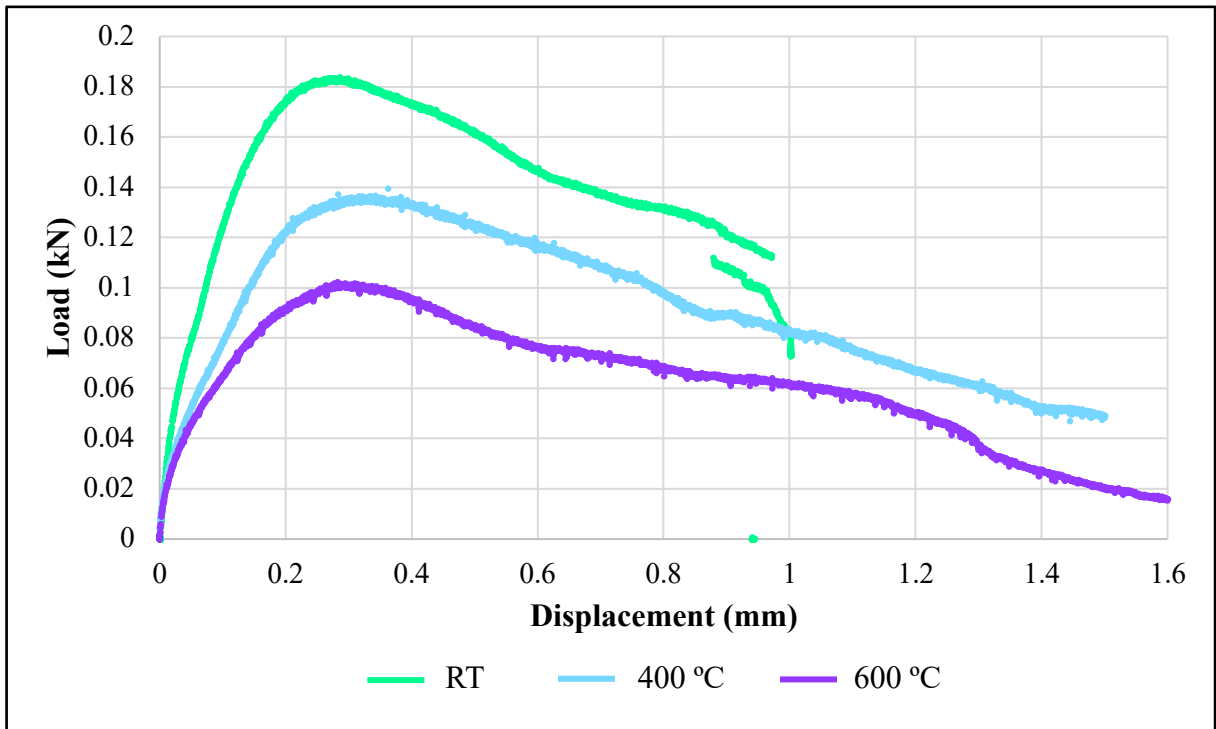


Figure 4.31 - Load/ Displacement curves for LPBF tungsten samples tested at RT, 400 °C and 600 °C

Due to time and material constraints, two tests were conducted at room temperature and 600 °C and only one test at 400°C. However, in order to increase confidence in the results produced four additional repeats were produced at RT and 600 °C, with less than 10 % error seen between the repeats.



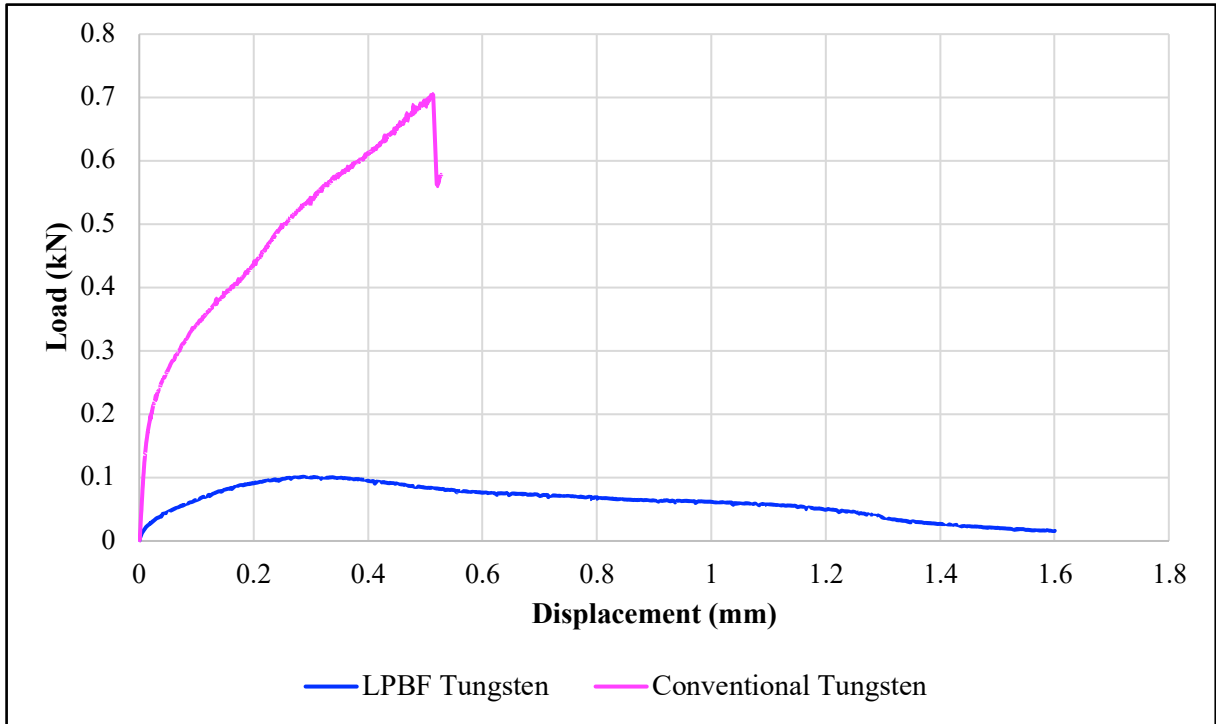
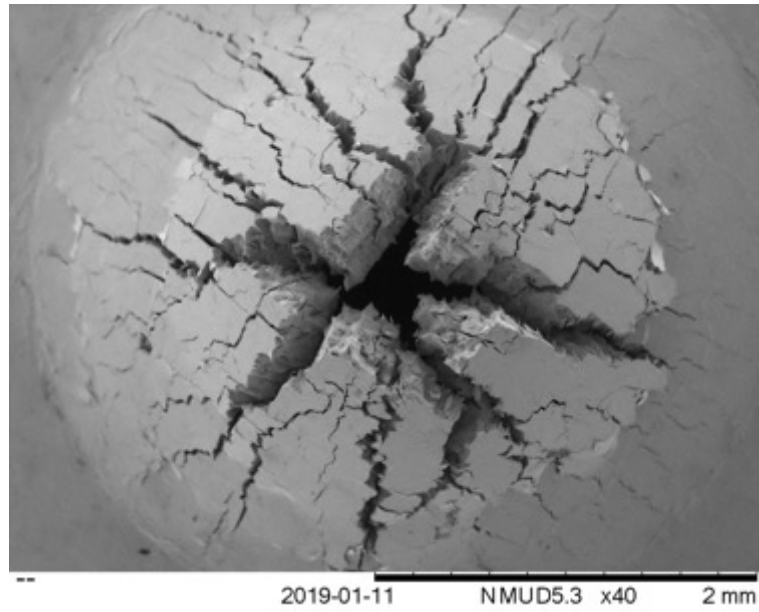
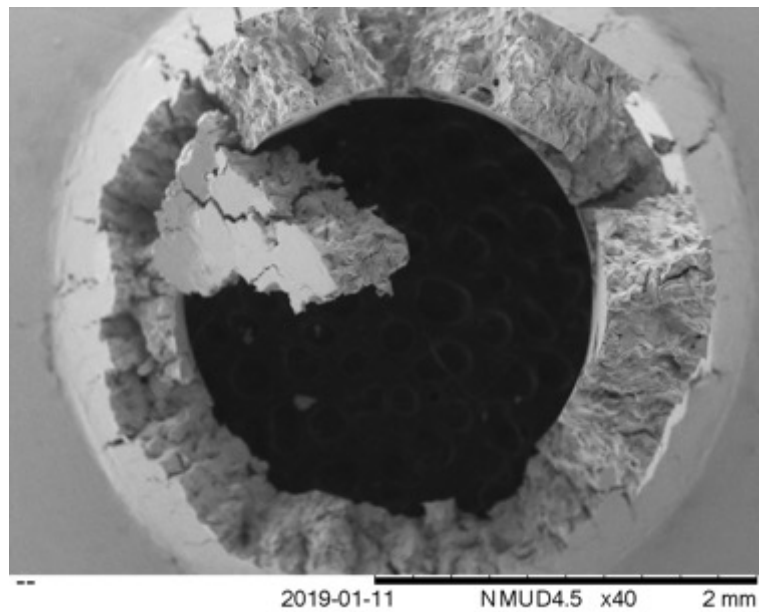


Figure 4.32 - Load/ Displacement curves for conventional tungsten and LPBF tungsten samples tested at 600 °C

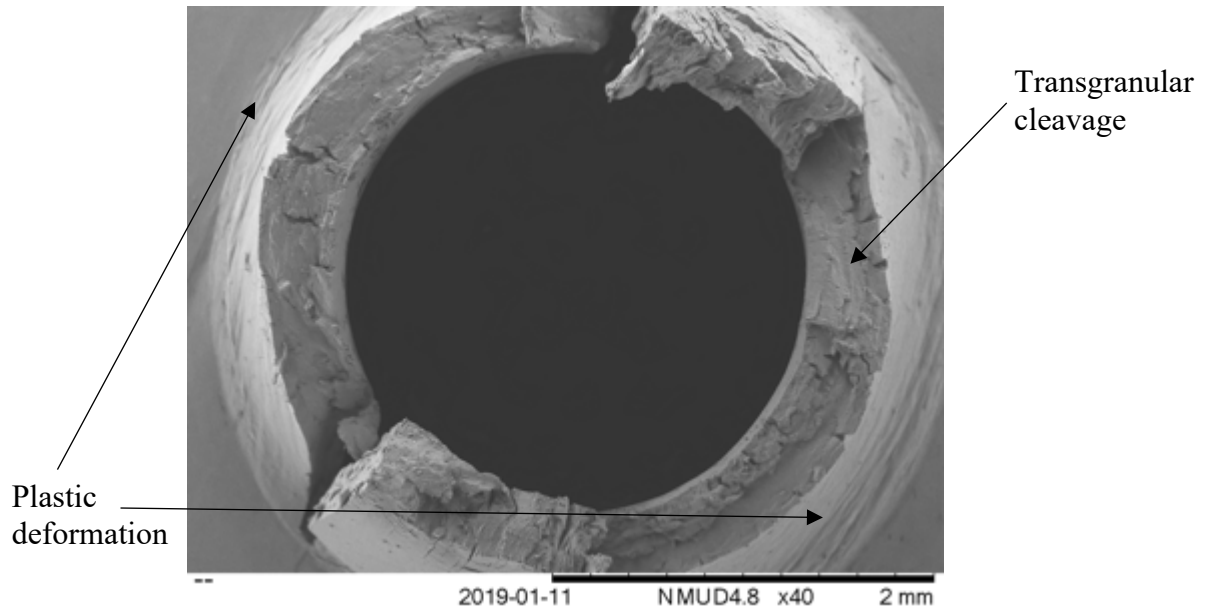
An obviously higher peak load was found for conventional tungsten versus LPBF tungsten with values of 0.7 kN and 0.1 kN respectively. It may have initially appeared that LPBF tungsten had a higher level of ductility as it reached a maximum displacement of 1.6 mm in comparison to 0.55 mm for conventional tungsten; however, when comparing displacement at maximum load, this was found to be 0.3 for LPBF tungsten and 0.5 mm for conventional tungsten (see Figure 4.32).



*Figure 4.33 - SE micrograph showing the characteristic star cracking pattern of a brittle small punch sample (LPBF tungsten tested at RT)*



*Figure 4.34 - SE micrographs showing a fractured small punch specimen from LPBF tungsten tested at 600 °C*



*Figure 4.35 - SE micrograph showing a fractured small punch specimen from conventional tungsten tested at 600 °C*

The reason for additional displacement may have been due to fracture radially and at the base of the sample forming a characteristic ‘star’ failure which allowed movement of the fractured pieces upward with the load pin (see Figure 4.33). The further movement caused the central fractured pieces to fall through (see Figure 4.34). Richardson, n.d. (35) showed similar fractographs when the materials were tested in a brittle condition i.e. below the DBTT (35).

The conventional tungsten showed areas of plastic deformation (see Figure 4.35) and the failure mechanism appeared to be transgranular in nature. This suggested the conventional material was tested at a temperature close to its DBTT. By contrast, the LPBF samples showed no plastic deformation due to the prevalence of cracking within the sample.

#### **4.3.5 Effect of Interstitial Impurities on Cracking**

As noted, there was no clear consensus on which interstitial element was the most deleterious (20, 36). However, due to the time and cost prohibitive nature of the techniques used to

investigate further, only one element could be analysed in depth. Significant initial evidence had suggested the effect may be due to oxygen and given the noticeably higher oxygen content than in conventionally manufactured or welded material, along with sources such as Yih and Wang, 1979 (36) suggesting oxygen being a greater contributor than other interstitials, this was decided as the element of focus for this stage of the study (36).

SIMS was conducted on an LPBF tungsten sample; the surface oxide of the sample was removed and then the material sputtered to liberate the secondary ions. Craters were formed during the sputtering. The isotope of interest for this study was  $O^{16}$ . The bottoms of the craters were imaged via SEM to correlate the oxygen intensity maps with the materials structure. Figure 4.36 shows SE micrographs of the crater bottoms along with SIMS maps of  $O^{16}$  from the same location.

As discussed previously, the data presented showed the possibility that oxygen was prevalent in areas where cracks had formed. However, this did not clarify if the cracking occurred due to the presence of oxygen or if the area around the cracks oxidised after the crack formed. In Figure 4.36 grain boundaries are marked with a dashed line; regions of high intensity oxygen could be seen in the SIMS map which corresponded to the boundaries seen in the crater base. Cracked areas of the boundaries were indicated in the figure; however, uncracked regions could also be seen (labelled) and still corresponded to an area of high oxygen intensity. This confirmed that the oxygen peaks arose prior to cracking rather than as a result of oxidation of cracks.

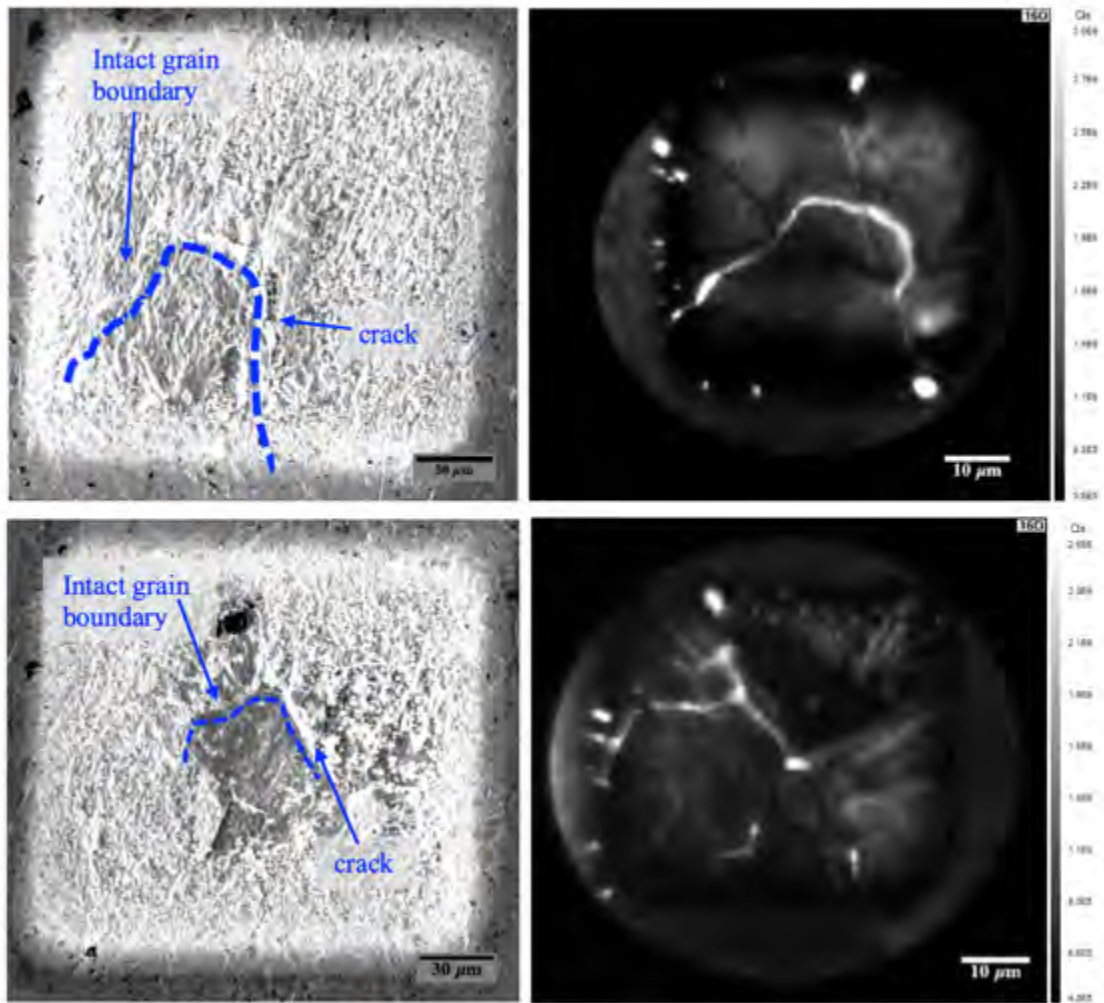


Figure 4.36 - SE micrograph of ion milled craters (left) and a SIMS maps showing  $^{16}\text{O}$  in tungsten showing grain boundary segregation

SIMS is a semi-quantitative technique if accurate reference samples of the alloy type can be used. This would require a high purity tungsten alloy with oxygen present uniformly throughout the sample in a quantity known to a good degree of accuracy. Conventionally manufactured tungsten was attempted as a reference material, but this was not of sufficient quality to quantify the results presented.

As oxide volatilisation occurred below the melting point of tungsten, it was possible that volatilisation and redeposition of the oxide could occur during processing and this was the cause of the effect seen in the SIMS maps. However, there are several reasons why this was

discounted. Much of the literature regarding oxide redeposition showed the phenomenon was often accompanied by lack of fusion defects which were not seen in the samples tested. Argon gas speed was found to be a significant factor in the quantity of redeposition found, and above speeds of  $2.5 \text{ ms}^{-1}$ (37), oxide deposits were found to be significantly reduced. Although the speed of argon flow was not monitored in the Concept Laser M2 it was considered to be above this threshold based on the work of Anwar and Pham, 2017 (38). This found that in a machine of comparable size (SLM Solutions 280HL) the argon gas speed was  $2.87 \text{ ms}^{-1}$  at 60 % of that maximum argon flow; this was found to correspond to  $42 \text{ Lmin}^{-1}$  of argon usage. In the Concept Laser M2 the gas flow was approximately  $66 \text{ Lmin}^{-1}$  and therefore gas speeds were thought to be comparable. Additionally, it is understood that LPBF is a dynamic process where material temperature can vary significantly over a small distance (39). It was therefore considered more likely that material below the oxide volatilisation temperature absorbed oxygen from residual oxygen in the chamber which was then segregated to the grain boundaries during cooling due to the reduction in solubility over this temperature range (21).

As the LPBF processing occurred in a chamber with residual oxidation this segregation and resultant cracking would therefore be extremely difficult to overcome without modifying the process set-up or the base material. This will be the subject of further investigation in Chapter 5 of this thesis.

#### **4.4 Effect of Powder Characteristics on Build Quality**

Archimedes' density testing was conducted on the samples produced via LPBF; Figure 4.37 showed the variation of sample density as a function of AED.

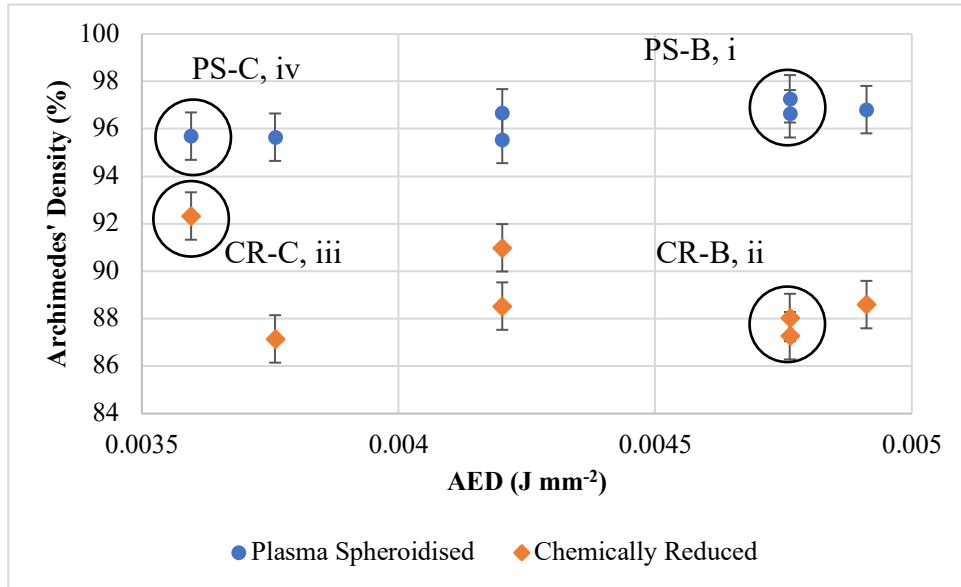


Figure 4.37 - Variation of sample density as a function of AED with points for the PS-B, CR-B and PS-C and CR-C circled

As a narrow range of build parameters close to the optimum was used for the builds, there were only slight variations in sample density indicated in Figure 4.37. Indeed, the range from highest to lowest values for density was around 5 % for the chemically reduced powder and less than 2 % for the plasma spheroidised powder. Hence, no strong trends could be seen in terms of the effect of process parameters on sample density. There appeared to be a large decrease in the density for samples prepared from chemically reduced powder from AED values of  $3.6 \times 10^{-3}$  to  $3.76 \times 10^{-3}$  J mm<sup>-2</sup>, but that appeared to be a secondary effect compared with the differences in density between the two powder types. However, while the density of the plasma spheroidised samples showed a weak increase with increasing AED, that for the compacts made from the chemically reduced powder decreased. This resulted in the difference in density between compacts increasing from 4 to 10 % (those produced from the plasma spheroidised powder having the greater density).

From the measured densities, two conditions for each powder were identified for further study. These could be seen circled and labelled (i) to (iv) (CR-B, PS-B, CR-C, and PS-C) in Figure 4.37. The conditions of interest were those which yielded the highest densities for

compacts from the plasma spheroidised and chemically reduced powders and the same parameters applied to the other powder type, *i.e.*, samples CR-B, PS-B, CR-C, and PS-C. Of note, was the fact the optimum parameter for plasma spheroidised powder utilised a power of 300 W in comparison to the 400 W (maximum machine capability) required for the chemically reduced powder. The data in Figure 4.37 included samples deposited with the same AED value, but which had different Archimedes density values due to differing scan spacings changing the heat flow and temperature profiles in the build. This weakness was highlighted in Section 4.2.2.

Archimedes' density testing did not identify the types of defect present, it merely gave an indication of overall build quality. To better understand the defect distributions in the compacts, mounted sections were imaged. Figure 4.38 showed micrographs typical for each of the samples of interest sectioned parallel to the build plate along with the densities determined by Archimedes' (AD) and Image Analysis (IA) methods. An indication of the proportion of lack of fusion (F) and cracks (C) was also determined through image analysis. Each pixel corresponded to 3  $\mu\text{m}$  in the micrograph; each manual measurement was accurate to the nearest 2 pixels, and the manual measurements had a minimum size of 1800  $\mu\text{m}^2$ , which corresponded to an error of approximately 0.5 %. The void defects were determined to be lack of fusion rather than porosity due to their irregular shape and large size. Gas or keyhole pores were typically spherical in shape. The high prevalence of large lack of fusion defects in CR-B may also lead to an increase in cracking as the defects may encourage crack initiation as their irregular shape could act as a stress concentrator. Both from the micrographs themselves and the values indicated from image analysis, it could be seen that the samples produced from the chemically reduced powder in Figure 4.38 CR-B and CR-C had higher levels of lack of fusion, whereas the plasma spheroidised samples PS-B and PS-C are



dominated by cracking, but the absolute amount of cracking, likely occurring on cooling, was consistent between 3 to 5 % throughout the samples. Under optimal conditions for this powder, the compacts produced from the plasma spheroidised powder could be considered to be nominally dense with only 0.3 % LOF voids. The quantity of cracking observed in the mid-build XY plane section results in only ~97 % theoretical density being achieved and likely occurred during the rapid cooling to which all samples were subjected rather than a parameter-specific variation.

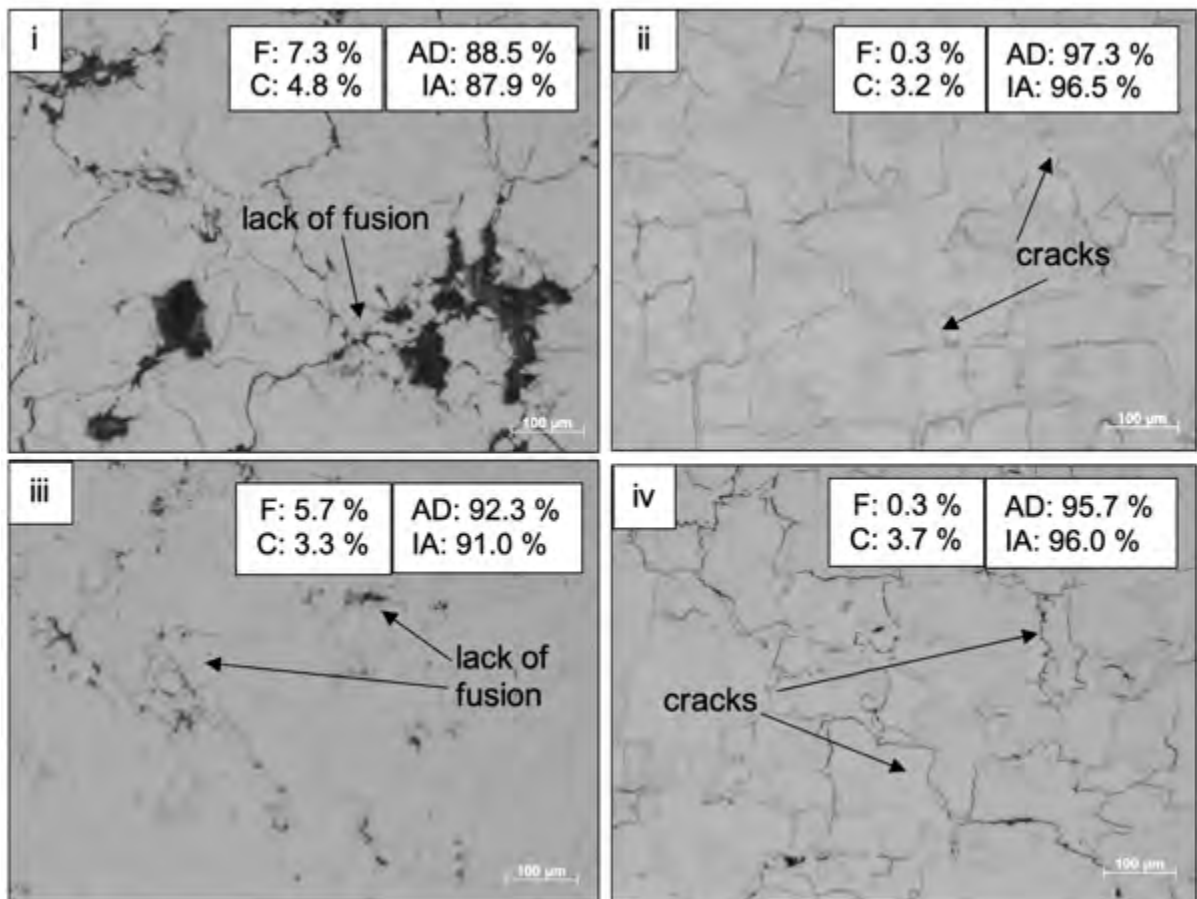


Figure 4.38 - Optical micrographs showing i) CR-B and ii) PS-B (optimised build parameters for plasma spheroidised powder) and iii) CR-C and iv) PS-C (optimised build parameters for chemically reduced powder)

The lack of fusion was attributed to short solidification time compared with the long spreading time associated with tungsten (40). Variation in packing density and powder

morphology was likely to affect the thermal diffusivity and possibly the laser absorptivity; the experimental set-up and powder layer thickness would likely have an effect on the packing density seen. In this study, the two powders were found to have noticeably different characteristics in terms of packing and flowability (see Table 4.10). The morphology of the powders can be seen in Figure 4.39. The improved flowability and higher packing of the spherical powder would be expected to result in improved build quality with higher density. From Figure 4.37, this could be confirmed, with the plasma spheroidised powder producing samples with consistently higher density. This was possibly due to the higher packing density resulting in greater contact between the particles reducing the distance for liquid spreading required to form a consistent layer (40-42). Moreover, with a higher packing density it was expected that the layer thickness would be more consistent.

Table 4.10 - Comparison of tungsten powders following characterisation

Powder	Apparent Density ( $\text{gcm}^{-3}$ )	Packing Density (%)	$\text{ff}_c$
Plasma Spheroidised	11.06	57.0	11.04
Chemically Reduced	8.64	44.5	9.59

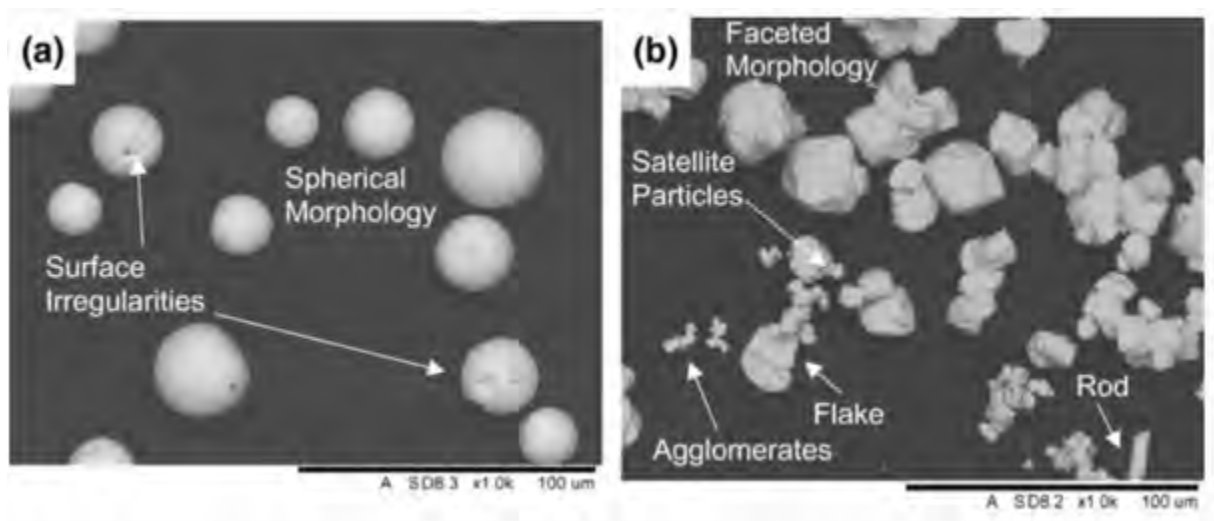


Figure 4.39 - Micrographs of (a) the plasma spheroidised powder from LPW Technology and (b) the chemically reduced powder from H.C. Starck

To confirm this, the penetration depths of the fusion zone into the substrate material were measured (see Figures 4.40 and 4.41). The samples used for this were PS-B and CR-B, respectively, and therefore the build parameters were 300 W power, 750 mms<sup>-1</sup> scanning speed, and a scan spacing of 60 μm. The average penetration depth of the fusion zone into the base plate, excluding the edge 2 mm, of the sample for the plasma spheroidised powder was 122 ± 10 μm compared with 67 ± 10 μm for the deposit produced from the chemically reduced powder, corresponding to a 1.8 times greater penetration for the plasma spheroidised deposit. Both samples showed some large defects, although, in line with the Archimedes density values and the mid-build XY sections, these were much larger and numerous for CR-B compared with PS-B. Direct correlation of different 2D sections with each other and with a 3D measure would not be exact, but the trends shown were consistent. However, if there was significant plate heating during processing the depth of the fusion zone would increase in comparison to the cold plate at the start of the process.

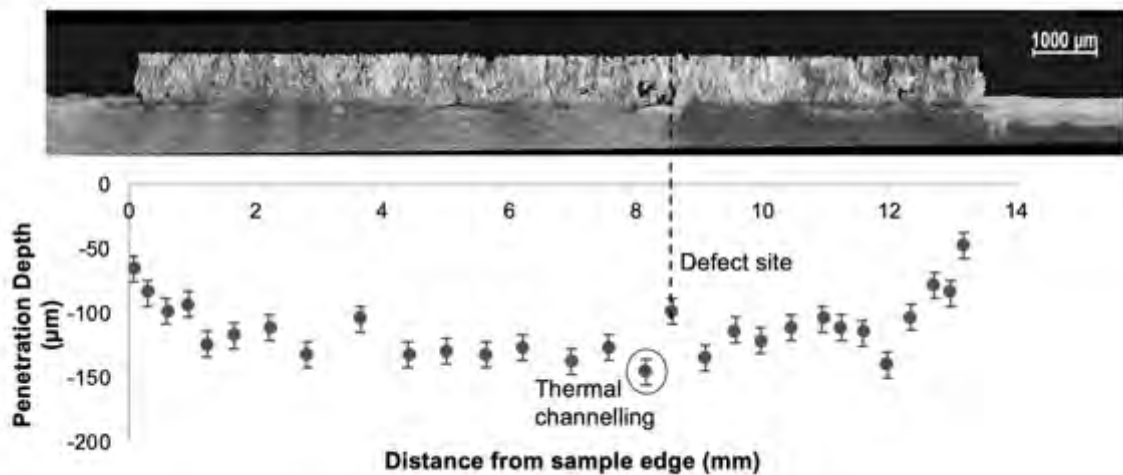


Figure 4.40 - Micrograph of section through the substrate plate and deposit produced using plasma spheroidised powder and the measured depth of the fusion zone at the corresponding position on the sample

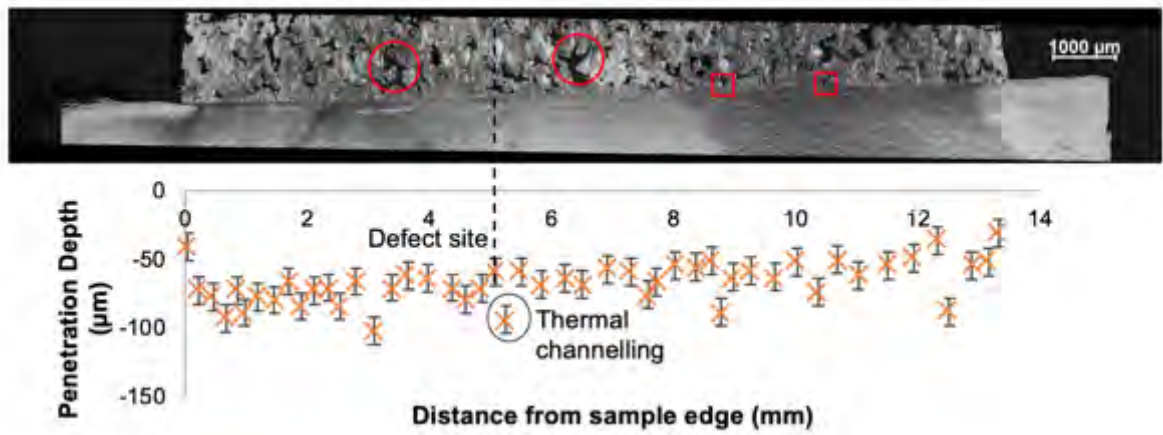


Figure 4.41 - Micrograph of section through the substrate plate and deposit produced using chemically reduced powder and the measured depth of the fusion zone at the corresponding position on the sample

Underneath the sites of defects close to the base plate, the penetration depth was smaller due to reduced thermal conduction through the void (see dashed line). There was also some evidence of deeper penetration before and after the defect (see circled points in Figures 4.40 and 4.41) consistent with channelling of the heat through the solid material around the void, deepening the fusion zone. In Figure 4.42, this could be seen more clearly with penetration deepening on increasing distance from defect sites. In order to see this effect, the defect had to form very close to the substrate plate. In the deposit produced from the chemically reduced powder (Figure 4.42), two large lack of fusion defects could be seen (circled) but were too far away from the base plate to see the effect of channelling, whereas the much smaller lack of fusion defects (indicated by a square) showed some channelling.

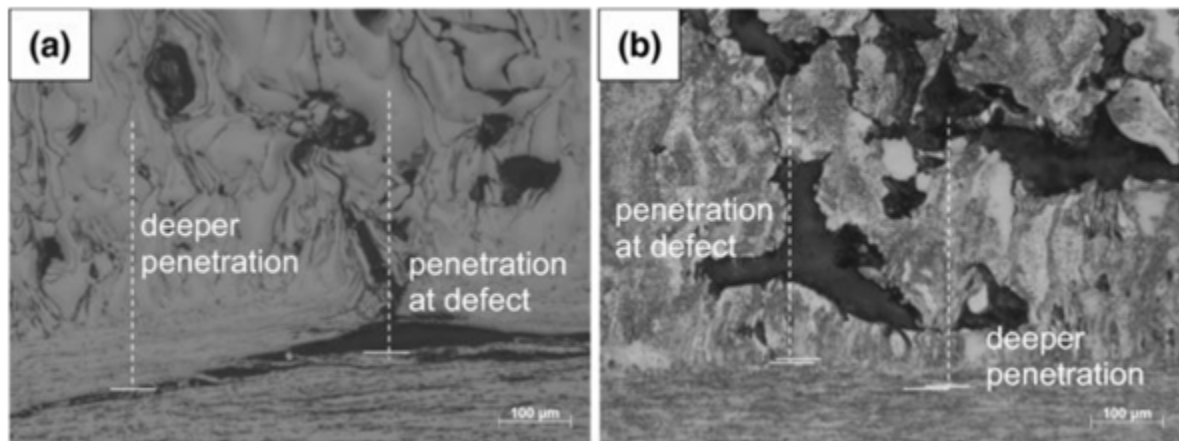


Figure 4.42 - Optical micrographs showing variation in penetration depth around areas of defects in a) plasma spheroidised powder and b) chemically reduced powder

The penetration depths were a measure of the fusion boundary for laser scanning of the first powder layer and, as such, was a measure of the heat absorbed by the powder from that layer.

Assuming that the region of average penetration is subject to one-dimensional heat flow (vertically downward in Figures 4.41 and 4.42) then the penetration depth could be used as an estimate of the minimum heat input into the powder. This would be an under-estimate of the total heat input, but as the scan rates and overlaps were the same, the amount of heat required to raise the substrate temperature for  $T < T_m$  would be the same for both powder types. The minimum heat absorption could be determined as a function of the total energy input by the laser.

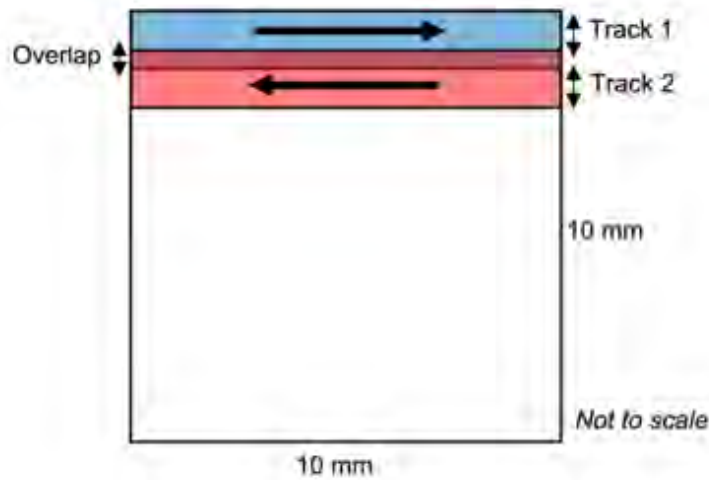


Figure 4.43 – Schematic diagram of scanning strategy and overlap

$$\begin{aligned}
 \text{Area scanned} &= \text{length of track} \times \text{no. tracks} \times 2r \\
 \text{No. tracks} &= \text{sample width} \div \text{scan spacing} \\
 \therefore \text{Area scanned} &= 10 \times \frac{10}{0.06} \times 0.084 = 140 \text{ mm}^2 \equiv 1.40 \times 10^{-4} \text{ m}^2
 \end{aligned}$$

The energy input over one layer, would be the product of the Area Energy Density ( $\text{J m}^{-2}$ ) and the area ( $\text{m}^2$ ) given by Equation 4.6

$$E = \frac{P}{2rv} \times A \quad (\text{Equation 4.6})$$

$$E = \frac{300}{2 \times (4.2 \times 10^{-5}) \times 0.06} \times (1.40 \times 10^{-4}) \approx 666 \text{ J (3 s.f.)}$$

Thus, the incident energy of the laser approximated to 666 J (to 3s.f.).

The average penetration depths,  $d$ , from the two powders, were then used along with the layer thickness,  $h$ , of the powder, the apparent,  $\rho_A$ , and theoretical densities,  $\rho_T$ , of the powders and the layer area,  $A_{\text{layer}}$ , to determine the volume of the material where the maximum temperature was greater than or equal to its melting point (Equation 4.7).

$$V = A_{\text{layer}} \times \left( d + \left( h \times \frac{\rho_A}{\rho_T} \right) \right) \quad (\text{Equation 4.7})$$

For the plasma spheroidised powder, the volume was determined to be:

$$V = 1 \times 10^{-4} \times \left( 1.22 \times 10^{-4} + \left( 3 \times 10^{-5} \times \frac{11.06}{19.3} \right) \right) \approx 1.39 \times 10^{-8} \text{ m}^3 \text{ (3 s.f.)}$$

For the chemically reduced powder, the volume was determined to be:

$$V = 1 \times 10^{-4} \times \left( 6.7 \times 10^{-5} + \left( 3 \times 10^{-5} \times \frac{8.64}{19.3} \right) \right) \approx 8.04 \times 10^{-9} \text{ m}^3 \text{ (3 s.f.)}$$

Using the molar volume of tungsten, taken to be  $9.55 \times 10^{-6} \text{ m}^3 \text{ mol}^{-1}$  (21), the number of moles,  $n$ , for the two powders were determined:

$$n_{PS} = \frac{V}{V_m} = \frac{1.39 \times 10^{-8}}{9.55 \times 10^{-6}} \approx 1.46 \times 10^{-3} \text{ mol}$$

$$n_{CR} = \frac{V}{V_m} = \frac{8.04 \times 10^{-9}}{9.55 \times 10^{-6}} \approx 8.42 \times 10^{-4} \text{ mol}$$

The change in enthalpy,  $H$  can be determined through the integration of the specific heat capacity,  $C_p$ , between the limits,  $T_m$  and  $T_o$  and the latent heat of fusion,  $L_f$  (Equation 4.8)

$$H = \int_{T_o}^{T_m} C_p \partial T + L_f \quad \text{(Equation 4.8)}$$

The specific heat capacity as a function of temperature was determined to be:

$$C_p = 0.0032426 \left( 1 - \frac{4805}{T^2} \right) + (2.1773 \times 10^{-6})T + (5.52461 \times 10^{-13})T^3 \text{ cal} \cdot \text{g}^{-1} \cdot \text{K}^{-1} \quad (36)$$

The latent heat of fusion ( $L_f$ ) was taken to be  $46000 \text{ J mol}^{-1}$  (21).

$$\int_{293}^{3695} C_p \partial T \approx 150.3 \text{ cal} \cdot \text{g}^{-1} \equiv 629.0 \text{ J} \cdot \text{g}^{-1} \equiv 115637.9 \text{ J} \cdot \text{mol}^{-1}$$

Assuming conversion factors of  $1 \text{ cal.} \equiv 4.184 \text{ J}$  (43) and the atomic mass of tungsten of  $183.84 \text{ J} \cdot \text{mol}^{-1}$  (21).

The enthalpy increases for the volumes of the two powders were found to be 236 and 136 J (3 s.f.) for the plasma spheroidised and chemically reduced powders, respectively. The

relative minimum absorbed energies could then be compared to the incident energy of the laser in the two cases, 666 J. This resulted in a minimum absorption efficiency of 0.35 and 0.20 (2 s.f.), respectively.

The value of laser absorptivity will depend on material, powder characteristics (packing density and morphology), and processing environment (44). The samples studied in this work were processed under nominally identical conditions so that differences in effective laser absorptivity could be assumed to be due to powder composition, morphology, and packing density. The powder compositions differed only in their impurity levels, so that, unless vaporisation losses caused the local environment to vary and modify its interaction with the laser beam then it was the powder geometry that was responsible for this difference. This was considered reasonable due to the similar powder size distributions between the two powders. Although easily vaporised metallic elements such as Al, Cu, and Mo were present and differed between the powders, their low levels justified this assumption that powder composition variations were not significant (Section 3.2). Oxide vaporisation may have also had this effect; however, the chemically reduced powder had less oxygen but still produced samples with poorer build quality.

Morphology and packing of particles could alter the contact area between adjacent particles and hence the path for thermal conduction. Greater powder packing density (e.g., resulting from a more spherical morphology) would result in greater thermal diffusion. It has also been suggested that absorptivity increases with increased packing density due to an increased likelihood of laser-particle interaction under the beam (45-47).



Micrographs of the two powders, Figure 4.44 indicated significant differences in the morphology and size of the two powders. The chemically reduced powder was found to have an irregular, faceted morphology with flake and rod structures in addition to small satellite particles and agglomerates. The plasma spheroidised powder had a highly spherical morphology with some small irregularities present on the particle surface. As neither powder was produced from a gas atomisation process, internal pores were not expected.

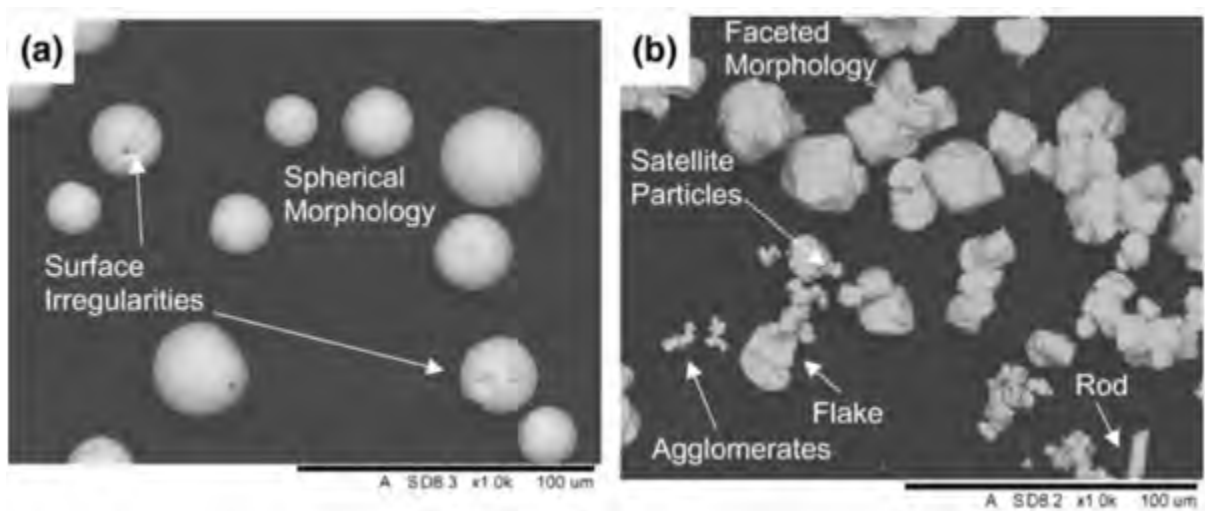


Figure 4.44 - Micrographs of (a) the plasma spheroidised powder from LPW Technology and (b) the chemically reduced powder from H.C. Starck

Through automated image analysis of the two powders it could be seen that over 85 % of the plasma spheroidised powder was highly spherical versus less than 2.5 % of the chemically reduced powder, and the most common morphology for the chemically reduced powder was irregularly shaped. Additionally, the chemically reduced powder had three times as many under and oversized particles as the plasma spheroidised powder, which was in agreement with LPSD data showing wider size distribution. The small particles may have been vaporised during processing contributing to increased lack of fusion defects. But further analysis would be required to confirm this. The chemically reduced powder also showed a significant propensity for agglomeration (see Figure 4.45).

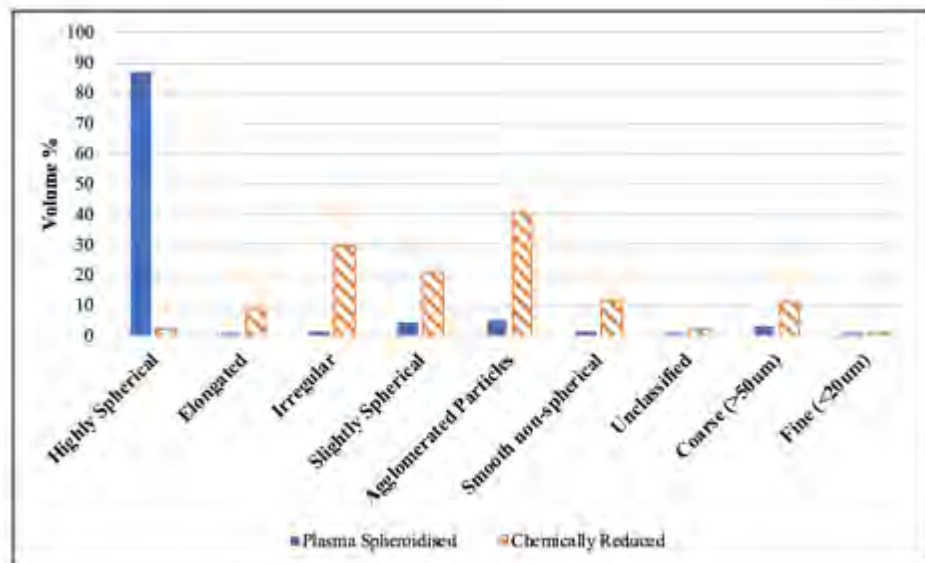


Figure 4.45 - Comparison of morphologies of the two tungsten powders

Both powders showed similar size ranges (Figure 4.46), although there was a plateau in the distribution for the plasma spheroidised powder from around 6 to 20  $\mu\text{m}$ ; over this size range the chemically reduced powder has a cumulative percentage of 44. The greater proportion of fines would give a greater tendency to agglomerate as well as having a higher proportion of surface contamination, consistent with Figure 4.45 and 4.46, along with the poorer flowability of the powder compared to the plasma spheroidised powder (Table 4.10). The poorer flowability shown by the chemically reduced powder would be expected to lead to greater variability of powder packing in the powder bed. As discussed previously, this would increase the distance required for melt spreading. A wider size distribution might be expected to result in greater packing density, but the morphology effects outweighed this tendency resulting in lower apparent density values (see Table 4.10). The single density value, however, did not represent the likely range experienced in a powder bed. Greater variation in packing may also lead to subsequent layers being thicker than nominal which could cause issues with layer-to-layer bonding.

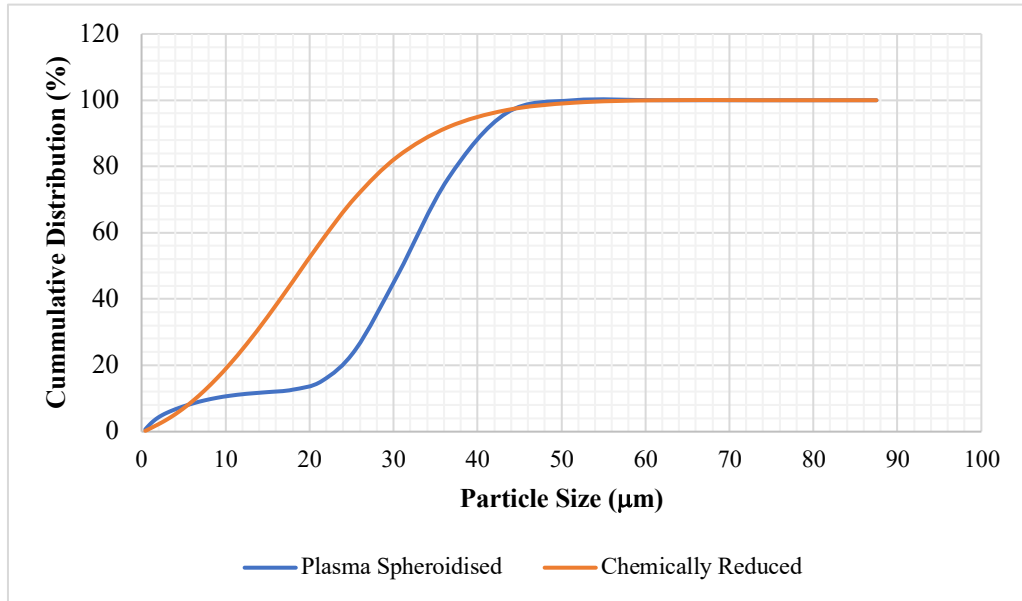


Figure 4.46 - Graph to show the size distribution of the plasma spheroidised and chemically reduced powders as determined by LPSD

Higher density values were associated with higher thermal diffusivity values and so faster thermal transport in the plasma spheroidised powder build would be expected. The more insulating nature combined with the powder facets of the chemically reduced powder creating multiple reflections, would then give higher temperatures in the powder layer and less melting of the substrate. Analysis of the structure of the builds indicated that lack of fusion defects (see Figure 4.38) were more numerous for the chemically reduced powder build than for the plasma spheroidised powder build. Thus, although thermal diffusivity effects would lead to higher local temperatures for a similar heat input, the build microstructure was indicative that local temperatures in the chemically reduced build were lower than in the plasma spheroidised build. This was consistent with reduced heat input in the chemically reduced powder build. Hence, despite the broad assumptions of the analysis above, the minimum effective laser absorptivity values determined were indicative of a much-reduced intake of energy from the laser for the chemically reduced powder bed than for the plasma spheroidised powder.

The determined minimum absorbed efficiency of 0.20 and 0.35 for the chemically reduced and plasma spheroidised powders, respectively, were significantly lower than that of previous studies (44, 46). This was likely due to the values only accounting for energy in melting rather than for all increases in substrate temperature (to less than that of the melting temperature). Additionally, the 30  $\mu\text{m}$  layer thickness used during the fabrication process would lower the absorptivity in comparison to Trapp et al., 2017 (4) where the layer thickness was three times greater allowing for multiple internal reflections.

Comparing the minimum effective absorptivity values for plasma spheroidised and chemically reduced powders, then the lower packing density of the latter would contribute to the decreased heat input (41, 42). The potential effect of vaporisation of fines and its influence has not been eliminated, although given the high argon speed this was considered less likely as has been discussed previously. The importance of packing density can be inferred from the correlation between reduced penetration depth and large lack of fusion defects, (Figure 4.41). It is likely that the poorer flowability of the chemically reduced powder leads to reduced local packing density and hence reduced heat input. This results in less particle melting and so a lack of fusion defect, while less heat is transported into the substrate, accounting for the reduced penetration.

The difference in apparent density, Table 4.10, was only 22 %, while that in the minimum laser absorptivity was 43 %, indicating that density was unlikely to fully account for the reduced heat input. Further to the modelling reported in the literature (46), the presence of facets in the chemically reduced powder would increase the amount of laser energy reflected back to the environment. The use of penetration depth to determine minimum effective absorptivity meant that a number of potential factors (e.g. scan strategy and conductivity)

were not isolated but incorporated in a single global parameter (hence the ‘apparent’ absorptivity). The use of penetration depth, particularly if single layer runs were made where powder layer thickness can be verified, is a rapid intermediate step between the simple AED values and a multi-parameter simulation.

The trends seen, in terms of increased packing density increasing laser absorptivity and increased spheroidicity increasing laser absorptivity, were consistent between studies (4, 41, 46, 48), while absolute values varied significantly depending on morphology and size distribution. This indicated the morphology of the powder was a key factor in its absorptivity but also indicated a need to identify the absorptivity of the powder used in each study as literature values are inconsistent. This was likely due to the many differences seen between powder batches including size distribution, morphology and impurity content. It also highlighted the need for further work in this area to clarify a consistent method for absorptivity measurements and thus improve comparisons of values between powders of different morphologies or different material systems.

## 4.5 References

1. Faidel D, Jonas D, Natour G, Behr W. Investigation of the selective laser melting process with molybdenum powder. *Additive Manufacturing*. 2015;8:88-94.
2. Zhang D, Cai Q, Liu J. Formation of Nanocrystalline Tungsten by Selective Laser Melting of Tungsten Powder. *Materials and Manufacturing Processes*. 2012;27(12):1267-70.
3. Sidambe AT, Tian Y, Prangnell PB, Fox P. Effect of processing parameters on the densification, microstructure and crystallographic texture during the laser powder bed fusion of pure tungsten. *International Journal of Refractory Metals and Hard Materials*. 2019;78:254-63.
4. Trapp J, Rubenchik AM, Guss G, Matthews MJ. In situ absorptivity measurements of metallic powders during laser powder-bed fusion additive manufacturing. *Applied Materials Today*. 2017;9(Supplement C):341-9.
5. Wang X, Carter LN, Pang B, Attallah MM, Loretto MH. Microstructure and yield strength of SLM-fabricated CM247LC Ni-Superalloy. *Acta Materialia*. 2017;128:87-95.
6. Lampman SR. *Weld Integrity and Performance*. Ohio, U.S.: ASM International; 1997.
7. Carter LN, Martin C, Withers PJ, Attallah MM. The influence of the laser scan strategy on grain structure and cracking behaviour in SLM powder-bed fabricated nickel superalloy. *Journal of Alloys and Compounds*. 2014;615:338-47.
8. Zhang B, Li Y, Bai Q. Defect Formation Mechanisms in Selective Laser Melting: A Review. *Chinese Journal of Mechanical Engineering*. 2017;30(3):515-27.
9. Prashanth KG, Scudino S, Maity T, Das J, Eckert J. Is the energy density a reliable parameter for materials synthesis by selective laser melting? *Materials Research Letters*. 2017;5(6):386-90.
10. Bertoli US, Wolfer AJ, Matthews MJ, Delplanque J-PR, Schoenung JM. On the limitations of Volumetric Energy Density as a design parameter for Selective Laser Melting. *Materials & Design*. 2017;113:331-40.
11. Ghouse S, Babu S, Van Arkel RJ, Nai K, Hooper PA, Jeffers JRT. The influence of laser parameters and scanning strategies on the mechanical properties of a stochastic porous material. *Materials & Design*. 2017;131:498-508.
12. Eagar TW, Tsai NS. Temperature Fields Produced by Traveling Distributed Heat Sources. *Welding Journal*. 1983;62:346-55.
13. King WE, Barth HD, Castillo VM, Gallegos GF, Gibbs JW, Hahn DE, et al. Observation of keyhole-mode laser melting in laser powder-bed fusion additive manufacturing. *Journal of Materials Processing Technology*. 2014;214(12):2915-25.
14. Hann DB, Iammi J, Folkes J. A simple methodology for predicting laser-weld properties from material and laser parameters. *Journal of Physics D: Applied Physics*. 2011;44(44):445401.
15. Thomas M, Baxter GJ, Todd I. Normalised model-based processing diagrams for additive layer manufacture of engineering alloys. *Acta Materialia*. 2016;108:26-35.
16. Han Q, Gu H, Setchi R. Discrete element simulation of powder layer thickness in laser additive manufacturing. *Powder Technology*. 2019;352:91-102.
17. Tietz TE, Wilson JW. *Behaviour and Properties of Refractory Metals*. London: Edward Arnold; 1965.
18. Wilkinson WD. *Properties of Refractory Metals*. New York: Gordon and Breach Science Publishers; 1969.
19. Savitskii EM, Burkhanov GS. *Physical Metallurgy of Refractory Metals and Alloys*. New York: Consultants Bureau; 1970.

20. Gludovatz B, Wurster S, Weingärtner T, Hoffmann A, Pippan R. Influence of impurities on the fracture behaviour of tungsten. *Philosophical Magazine*. 2011;91(22):3006-20.
21. Lassner E, Schubert WD. *Tungsten: Properties, Chemistry, Technology of the Element, Alloys, and Chemical Compounds*. New York, U.S.: Plenum Publishers; 1999.
22. Scott MH, Knowlson PM. The welding and brazing of the refractory metals niobium, tantalum, molybdenum and tungsten — a review. *Journal of the Less Common Metals*. 1963;5(3):205-44.
23. Hirai T, Pintsuk G, Linke J, Batilliot M. Cracking failure study of ITER-reference tungsten grade under single pulse thermal shock loads at elevated temperatures. *Journal of Nuclear Materials*. 2009;390(Supplement C):751-4.
24. Iveković A, Omidvari N, Vrancken B, Lietaert K, Thijs L, Vanmeensel K, Vleugels J, and Kruth J-P. Selective laser melting of tungsten and tungsten alloys. *International Journal of Refractory Metals and Hard Materials*. 2018;72:27-32.
25. Weman K. 10 - Submerged arc welding. In: Weman K, editor. *Welding Processes Handbook (Second Edition)*: Woodhead Publishing; 2012. p. 105-17.
26. Hunziker O, Dye D, Reed RC. On the formation of a centreline grain boundary during fusion welding. *Acta Materialia*. 2000;48(17):4191-201.
27. Cole NC, Gilliland RG, Slaughter GM. Weldability of tungsten and its alloys. *Welding Research Supplement*. 1971;50:419-26.
28. Farrell K, Schaffhauser AC, Stiegler JO. Recrystallization, grain growth and the ductile-brittle transition in tungsten sheet. *Journal of the Less Common Metals*. 1967;13(2):141-55.
29. Furumoto TU, T.; Abdul Aziz, M.S.; Hosokawa, A.; Tanaka, R.; . Study on Reduction of Residual Stress Induced during Rapid Tooling Process: Influence of Heating Conditions on Residual Stress. *Key Engineering Materials*. 2010;447-448:785-9.
30. Yadroitsava I, and Yadroitsev I. Residual stress in metal specimens produced by Direct Metal Laser Sintering. *Solid Freeform Fabrication Symposium*; 2015; Austin, Texas: University of Texas.
31. Suslova A, El-Atwani O, Sagapuram D, Harilal SS, Hassanein A. Recrystallization and grain growth induced by ELMs-like transient heat loads in deformed tungsten samples. *Scientific Reports*. 2014;4:6845.
32. Sidambe AT, Fox P, editors. Investigation of the Selective Laser Melting process with tungsten metal powder. 19th Plansee Seminar; 2017; Reutte, Austria: University of Liverpool.
33. Tan C, Zhou K, Ma W, Attard B, Zhang P, Kuang T. Selective laser melting of high-performance pure tungsten: parameter design, densification behavior and mechanical properties. *Science and Technology of Advanced Materials*. 2018;19(1):370-80.
34. Braun J, Kaserer L, Stajkovic J, Leitz KH, Tabernig B, Singer P, et al. Molybdenum and tungsten manufactured by selective laser melting: Analysis of defect structure and solidification mechanisms. *International Journal of Refractory Metals and Hard Materials*. 2019;84:104999.
35. Richardson M, Gorley M, Surrey E, Wynne B. An Investigation of the Mechanical Performance of Conventional and Additively Manufactured Vanadium. In: Field A, editor. *Oxford, U.K.: UKAEA*; n.d.
36. Yih SWH, Wang CT. *Tungsten: Sources, Metallurgy, Properties, and Applications*. New York: Plenum Press; 1979.

37. Reijonen J, Revuelta A, Riipinen T, Ruusuvoori K, Puukko P. On the effect of shielding gas flow on porosity and melt pool geometry in laser powder bed fusion additive manufacturing. *Additive Manufacturing*. 2020;32:101030.
38. Anwar AB, Pham Q-C. Selective laser melting of AlSi10Mg: Effects of scan direction, part placement and inert gas flow velocity on tensile strength. *Journal of Materials Processing Technology*. 2017;240:388-96.
39. Arisoy YM, Criales LE, Özel T. Modeling and simulation of thermal field and solidification in laser powder bed fusion of nickel alloy IN625. *Optics & Laser Technology*. 2019;109:278-92.
40. Zhou X, Liu X, Zhang D, Shen Z, Liu W. Balling phenomena in selective laser melted tungsten. *Journal of Materials Processing Technology*. 2015;222:33-42.
41. Carr RL. Evaluating Flow Properties of Solids. *Chemical Engineering Journal*. 1965;72:163-8.
42. Gusarov AV, Kovalev EP. Model of thermal conductivity in powder beds. *Physical Review B*. 2009;80(2):024202.
43. Thompson A, Taylor BN. Guide for the use of the International System of Units (SI). Maryland, USA; 2008. Report No.: NIST Special Publication 811.
44. Bergström D. The Absorption of Laser Light by Rough Metal Surfaces. Österund, Sweden: Luleå University of Technology; 2008.
45. Boley CD, Mitchell SC, Rubenchik AM, Wu SSQ. Metal powder absorptivity: modeling and experiment. *Appl Opt*. 2016;55(23):6496-500.
46. Boley CD, Khairallah SA, Rubenchik AM. Calculation of laser absorption by metal powders in additive manufacturing. *Appl Opt*. 2015;54(9):2477-82.
47. Rombouts M, Froyen L, Gusarov AV, Bentefour EH, Glorieux C. Photopyroelectric measurement of thermal conductivity of metallic powders. *Journal of Applied Physics*. 2004;97(2):024905.
48. Wang D, Yu C, Zhou X, Ma J, Liu W, Shen Z. Dense Pure Tungsten Fabricated by Selective Laser Melting. *Applied Sciences*. 2017;7(4):430.



## **CHAPTER 5 - INVESTIGATING METHODS OF IMPROVING THE LPBF PROCESSING OF TUNGSTEN**

This chapter presents the methods investigated to reduce cracking of LPBF processing of tungsten. As detailed previously, the two significant challenges to overcome with respect to LPBF processing of tungsten are the high cooling rates and oxygen contamination of the building environment. The combined effect of bed heating and alloy addition is also presented and possible explanations as to the efficacy of the methods detailed with respect to defect density, thermal and mechanical properties and oxide formation are discussed.

### **5.1 Introduction**

The Concept M2 Laser Cusing did not have capability for bed-heating, unlike many other commercially available machines. As discussed in Section 2.5.4 of the literature review, the purpose of bed heating was to reduce the thermal gradient and minimum temperature to which the component was exposed, thereby reducing the effect of thermal cycling and lowering the cooling rates. The desired effect was to reduce the residual stresses and defect densities within the as-fabricated component.

Alloying tungsten to improve its processability has been well researched. W-Re alloys have been the most effective, but the large quantities of rhenium required, coupled with its cost and the potential issues of irradiation damage mean that it has not been considered in this study (2). Instead tantalum was investigated as an alloying addition due to its improved oxygen tolerance and ductility, and the formation of an unlimited solid solution and a melting range of only 35 °C (3).

## **5.2 Effect of pre-scanning**

Pre-scanning was considered as an initial investigation into the potential of bed heating while requiring limited modification to the normal build set-up. Laser pre-scanning was used on a baseplate on top of thin alumina sheets to generate heating of the baseplate. Thermocouples monitored the temperature of the build plate when producing components with and without pre-scanning.

### **5.2.1 Temperature monitoring results**

Temperature monitoring was conducted in the centre of the build plate immediately below the build deposit. Figure 5.1 showed the temperature of the centre of the two build plates with respect to build time. Fig 5.2 and 5.3 showed the temperature measurements across the build plate for the control and pre-scanned samples respectively (Figure 5.4 showed the location of the thermocouples). The thermocouples were fixed in place using a high temperature adhesive which may have caused the thermocouples to shift slightly. This would explain the discrepancy between the data given for thermocouples 1 and 4 in Figure 5.3; being situated at both corners the temperature logged should have been similar however, thermocouple 4 showed a lower reading than expected.

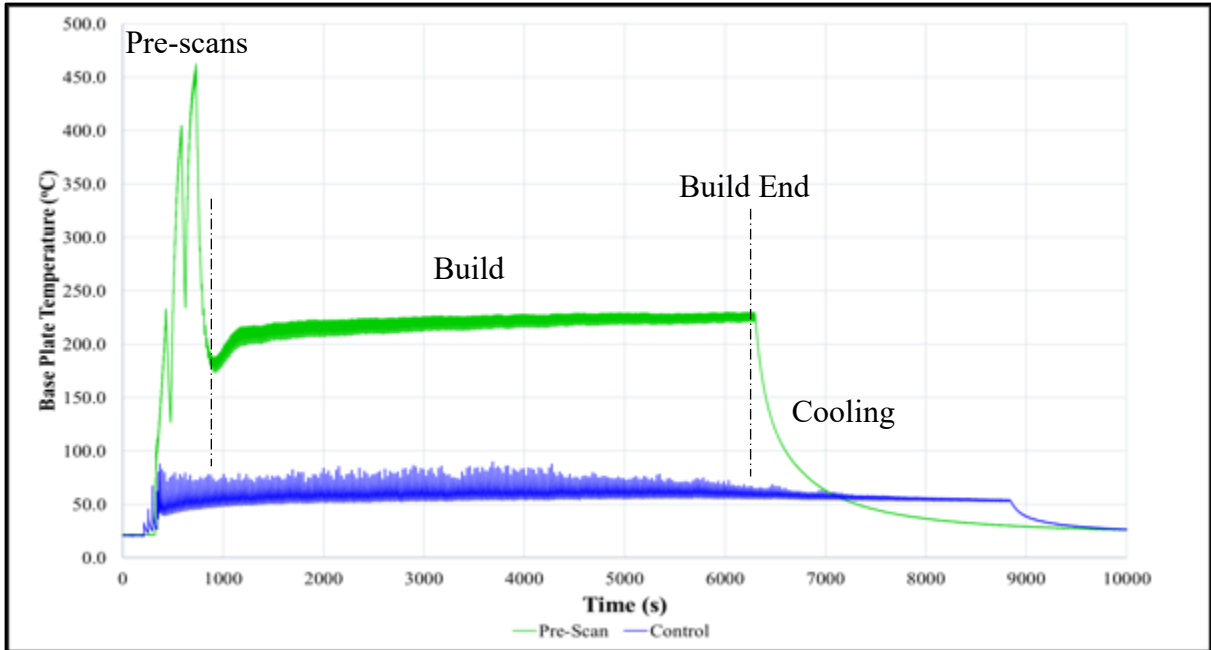


Figure 5.1 - A graph showing the base plate temperature with time for the pre-scan and control samples

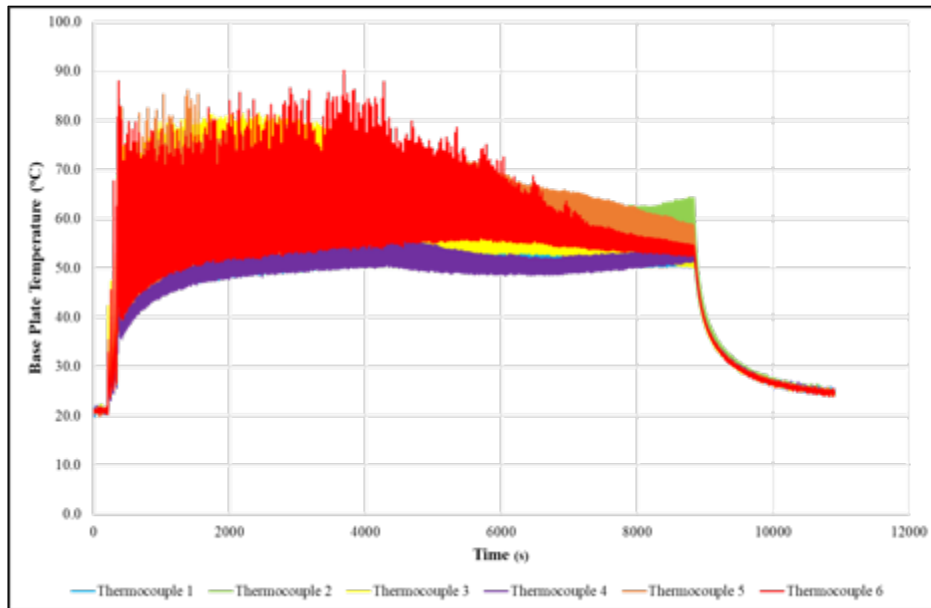


Figure 5.2 - A graph showing the temperature across the base plate for the control sample

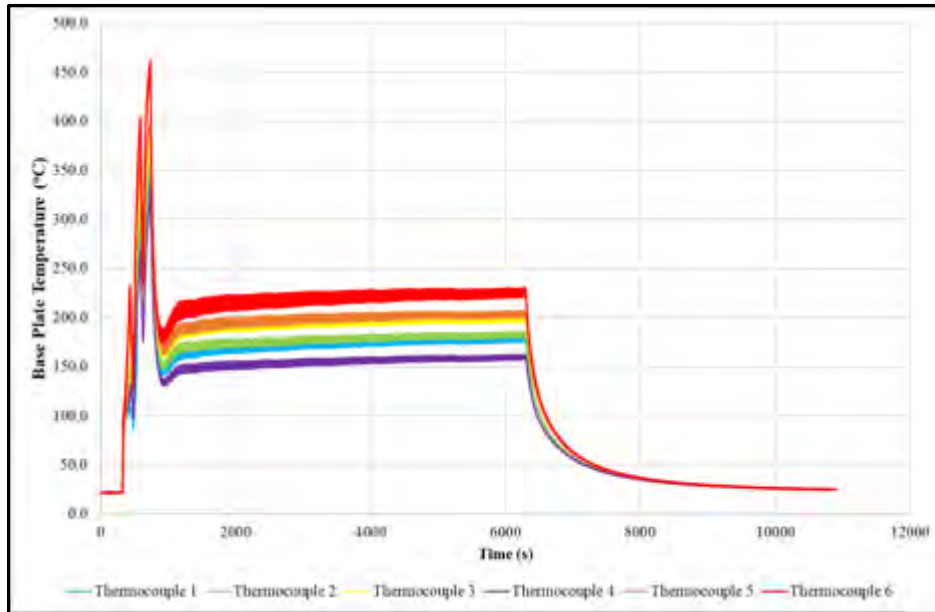


Figure 5.3 - A graph showing the temperature across the base plate for the pre-scan sample

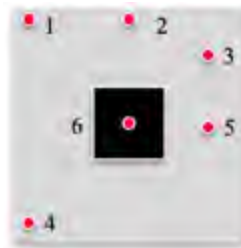


Figure 5.4 – Approximate location of thermocouples on the base plate for control and pre-scan samples (plate edge – 30 mm)

In the pre-scan sample, three distinct peaks could be seen. These were due to the pre-scanning of the base plate which was undertaken three times. Excluding these peaks, the pre-scan sample had an average base plate-temperature of approximately 225 °C in comparison to around 75 °C for the control sample. Additionally, variation in build temperature could be seen to be occurring cyclically, from the application of heat from the laser scanning of the top surface. A greater variation of this temperature cycling could be seen in the control sample versus the pre-scanned sample; the centre of the pre-scanned sample varied by around 10 °C whereas the control sample varied by over 30 °C.

This suggested that the presence of alumina sheets insulating the build plate were effective by preventing a large heat sink, reducing the amount of thermal cycling and cooling occurring between applications of the laser during the powder recoat.

Unsurprisingly, in both it could be seen that the build plate temperature was highest in the centre of the build plate. There was a greater variation in temperature across the plate for the pre-scanned sample; the temperature differences between the edge of the plate and the centre were approximately 30 °C and 75 °C for the control and pre-scanned samples respectively.

The maximum temperature reached even during the pre-scan phase was 462.5 °C suggesting that in order for pre-scanning to be sufficient a much larger insulating block would be required. It is likely supplementary heating would therefore be necessary to reach the temperatures of 400-600 °C to allow processing above the DBTT temperature of tungsten (1).

### **5.2.2 Fusion zone penetration depth measurements**

The pre-scanning could only be deemed effective if it had a meaningful effect on the heat input or defect density within the part. No significant difference in density was seen for the sectioned parts, however the penetration depths of the fusion zone into the plate as well as the quality of the interface could be seen to have improved from the control without pre-scanning and insulation. In comparison to the penetration depths shown in Chapter 4 of the LPW Technology powder there was a noticeable difference from the control sample shown here. This has been attributed to variation in experimental set-up. In this build, a single cubic sample was built on a smaller tungsten plate. This meant no thermal shielding between adjacent samples was present and a lower heat input and corresponding penetration depth would be expected and was seen.

The penetration depths for the sample produced using laser pre-scanning and plate insulation, were compared to the sample produced without. Figure 5.5 and Figure 5.6 showed etched optical micrographs of the interface with the graph beneath showing the penetration depth of the fusion zone as determined by image analysis.

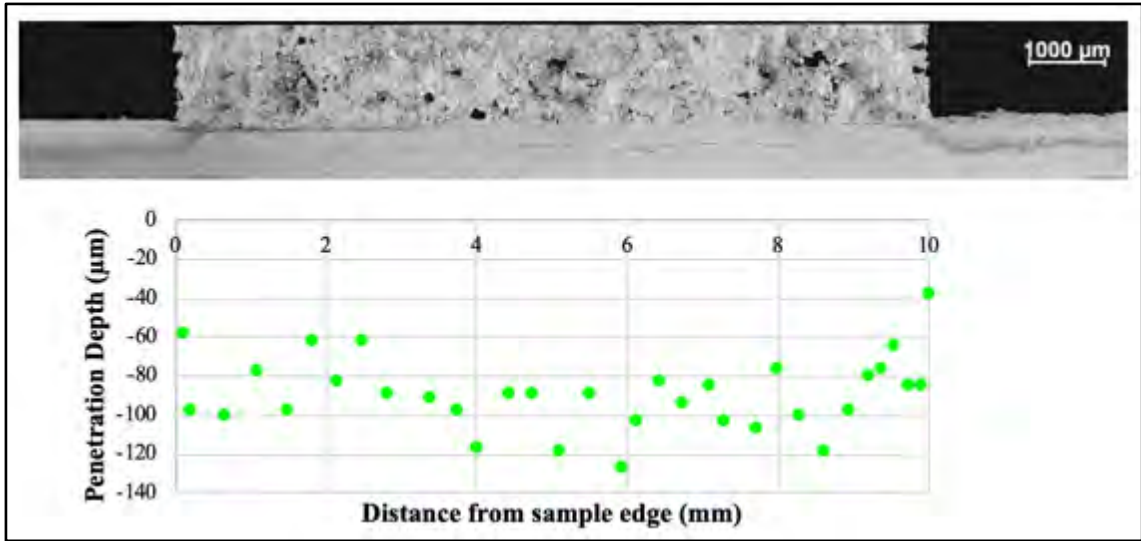


Figure 5.5 - A graph and micrograph showing the penetration depth of the fusion zone across the pre-scanned sample

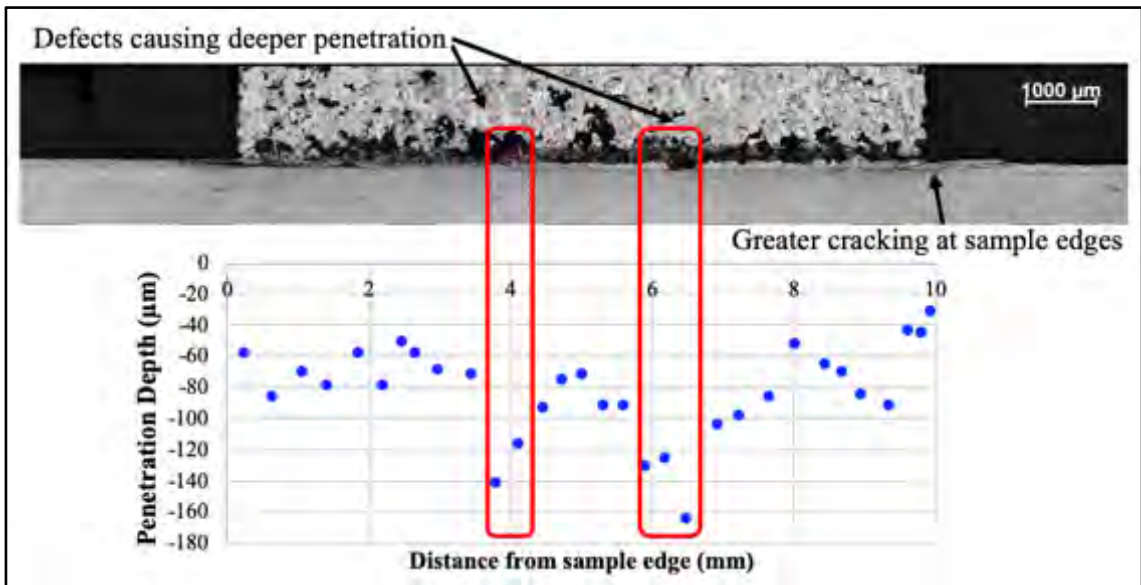


Figure 5.6 - A graph and micrograph showing the penetration depth of the fusion zone across the control sample

There were two large defects in the control sample, and at these sites the penetration depth was anomalously deep, due to thermal channelling effects. If these points were removed when calculating the mean, the average penetration depth reduced to 72  $\mu\text{m}$  which was around 20 %

smaller than with the pre-scan and insulation. The mean penetration depth for the pre-scan sample was 88  $\mu\text{m}$  ( $\pm 10 \mu\text{m}$ ).

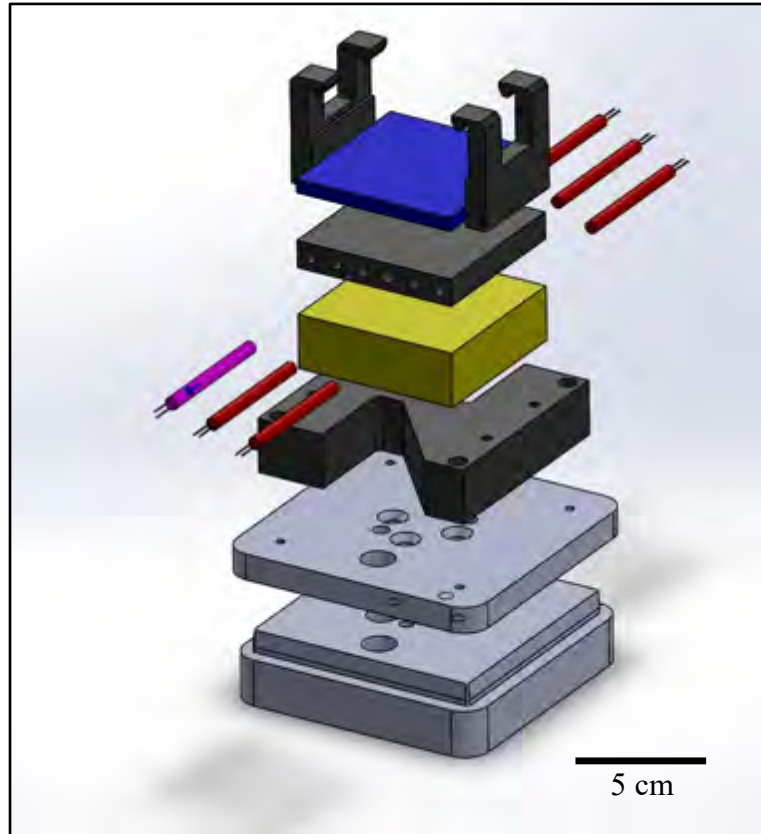
The density of the interface was significantly improved through the use of laser pre-scanning. A band of defects around 250  $\mu\text{m}$  in size could be seen across the section of the control sample; additionally, more significant cracking was seen at the edges of the build plate in the control sample than in the sample with pre-scanning.

### **5.3 Effect of heated bed module**

The results of the initial pre-scan trial suggested that build quality improvements could be made through the use of greater insulation and additional heaters to increase the bed temperature. Following the initial trials, a design for a heated bed add-in module were produced and manufactured. More information on the heated bed module could be seen in Section 3.4 and Appendix A (A.4).

A schematic of the heated bed design could be seen in Figure 5.7. Unlike the standard reducer kit module, the tungsten substrate plate was fixed in place with clamps rather than a high temperature metal adhesive.

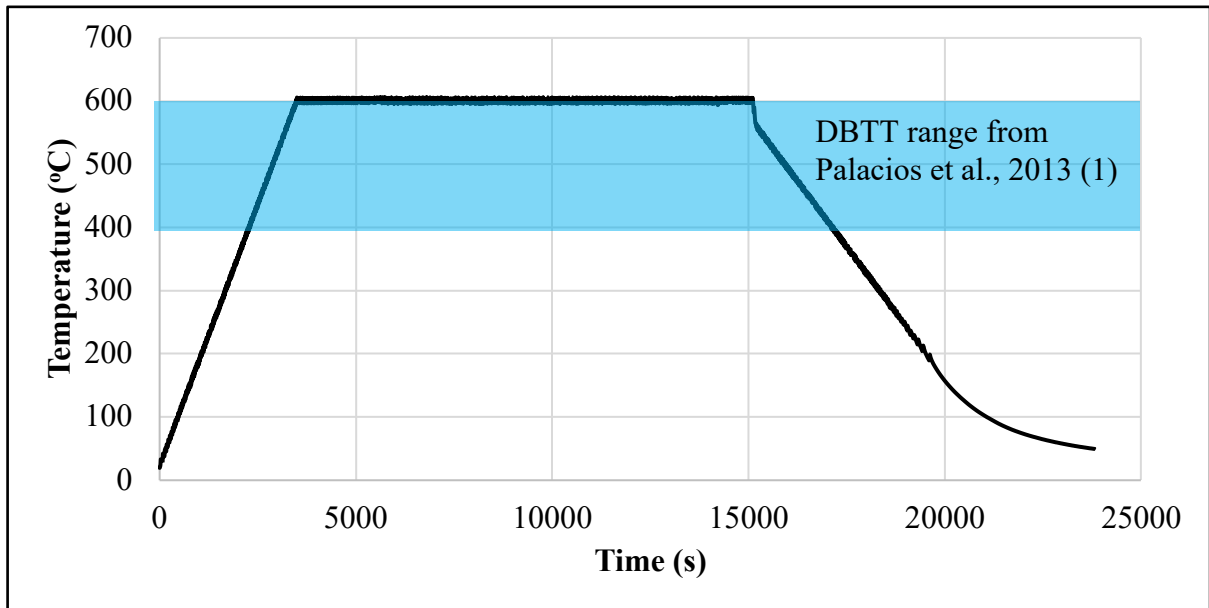




*Figure 5.7 - Schematic of the heated bed module with (from top) plate loading clips, tungsten build plate (blue), heating plate (grey) with cartridge heaters (red), ceramic insert to limit heat losses (yellow) and attachments to Concept Laser M2 reduced build volume module*

As could be seen in Figure 5.8, the temperature control on the heated bed was good, keeping the temperature within 5 °C of the target, 600 °C. The heating rate was also very close to the desired heating rate of 10 °Cmin<sup>-1</sup> with a heating rate of 9.65 °Cmin<sup>-1</sup>. The cooling rate was also largely controlled. The desired cooling was 5 °Cmin<sup>-1</sup> and the average cooling rate from 600 °C was 7.88 °Cmin<sup>-1</sup>; this was due to an initial period of rapid cooling (25 °Cmin<sup>-1</sup>) from 600 °C to 554 °C. From 554 °C to 185 °C, the rate was controlled at 5 °Cmin<sup>-1</sup> but at lower temperatures the cooling rate slowed, and the heaters were switched off. Greater insulation and an increase in bed heating designed to anticipate this initial cooling would be necessary to overcome it after the process has finished. However, given that the cooling rate was still far

lower than that of the LPBF process (around  $10^6$  °Cs<sup>-1</sup>(4)), and that the temperature was targeted to remain above the DBTT of the material, the effect was not deemed significant.



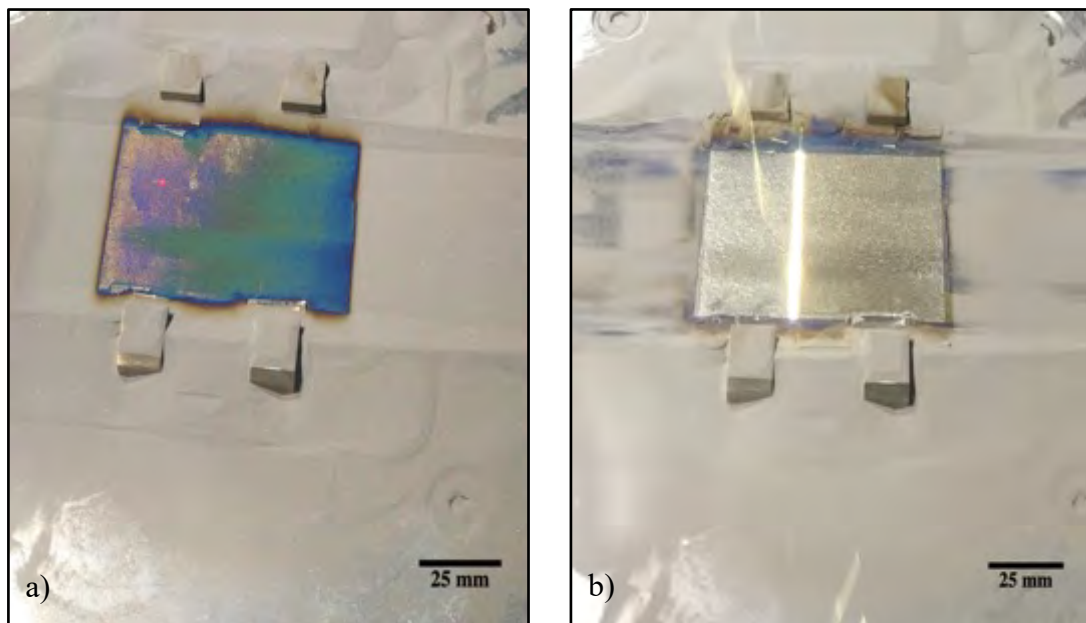
*Figure 5.8 - A graph showing the temperature of the heated bed with time for the 600 °C pre-heat*

### 5.3.1 Single Scan Results

Single laser scan tracks were conducted on the plates prior to build fabrication at 300 W power with both 750 and 1000 mms<sup>-1</sup> laser scanning speed at 400 °C and 600 °C. With the addition of the bed pre-heating, the greater heat input was expected to correspond to larger melt pools than those seen in the single scan tracks conducted with the room temperature build plate. However, scales of oxide can be seen in the 400 °C build temperature tracks and at 600 °C, the oxidation is significant. Various sources differ as to the temperature at which oxidation became significant (5, 6) however, it was empirically found in this study that visible oxide scale formation occurred at 400 °C, with rapid oxidation occurring at 600 °C of the blue oxide layer typical of WO<sub>3</sub> which corresponded to the oxidation patterns detailed by Wilkinson, 1969 (6); other sources suggested oxidation should not be significant until

temperatures of above 1000 °C (5), although this would vary with the partial pressures of oxygen in the system.

As a result of the oxidation, the surface tension of the weld pool increased leading to the formation of balling; Zhou et al., 2015 investigated this effect in LPBF of tungsten and concluded increased oxide formation could alter surface tension and worsen wettability (7). Moreover, at temperatures below that of the melting point vaporisation and re-deposition of the oxide could occur as has been discussed previously. The high gas speed during processing was likely to lessen the effects of oxide redeposition, however the quantity of oxides formed was substantially higher than in the studies available in literature (8, 9). Consequently, no accurate measurements of weld dimensions could be made to give an indication of a proportional change in heat input at 600 °C versus the room temperature tracks.



*Figure 5.9 - Photographs showing a) the oxide formed during temperature stabilisation at 600 °C and b) laser ablation of the oxide*

Figure 5.9 a) showed the quantity of oxidation during the temperature stabilisation period at 600 °C. Laser ablation was conducted using a lower power, high speed laser scan pass across

the build to remove the surface oxide (Figure 5.9 b) The surface oxide quickly reformed at 600 °C, following laser ablation such that visible tarnishing occurred during powder recoating. The residual oxygen was a disadvantage of the Concept Laser M2 which had a seal surrounding the build platform to allow the module to transfer from the handling to the processing sides and this results in poorer atmosphere control than alternative platforms.

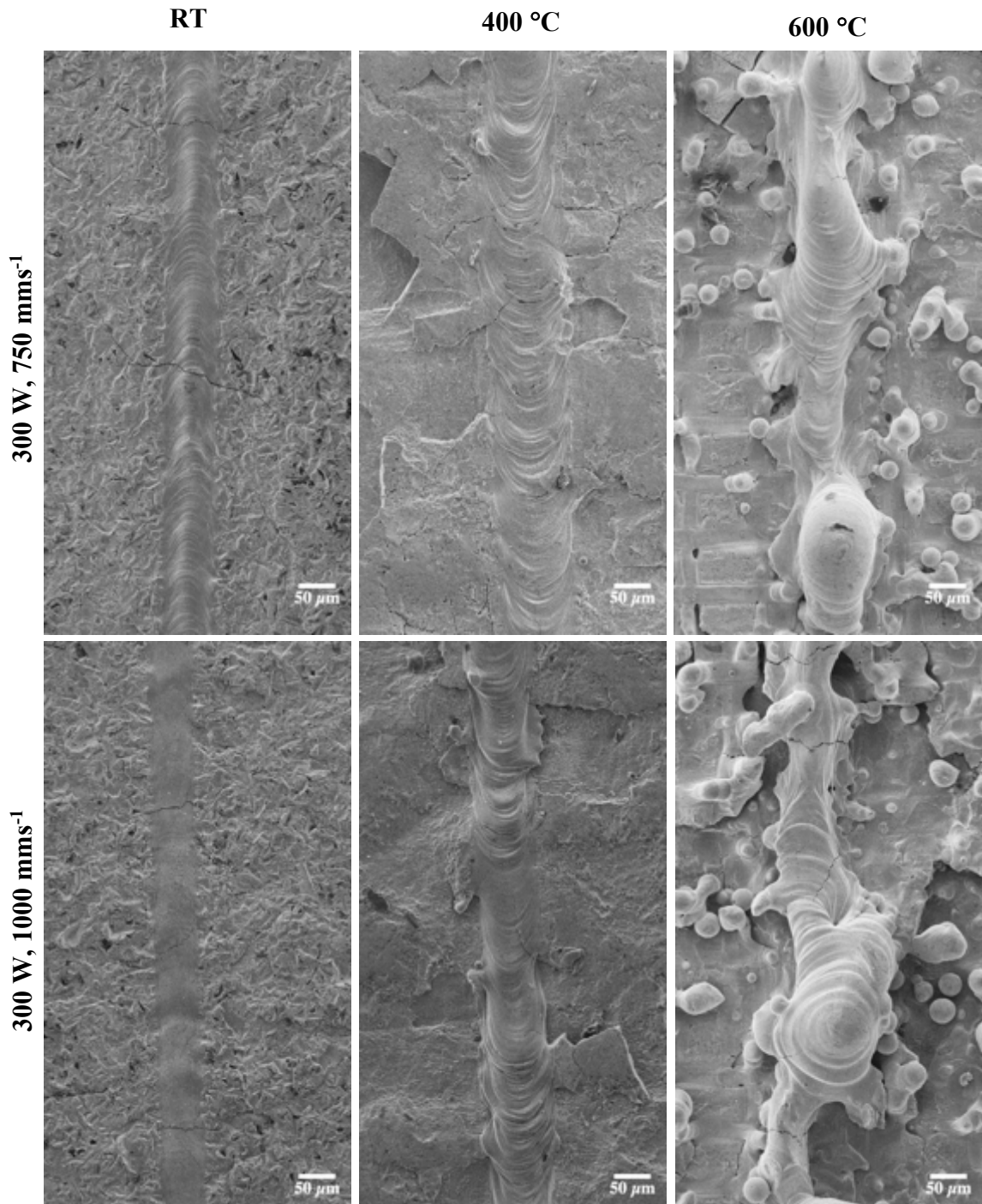


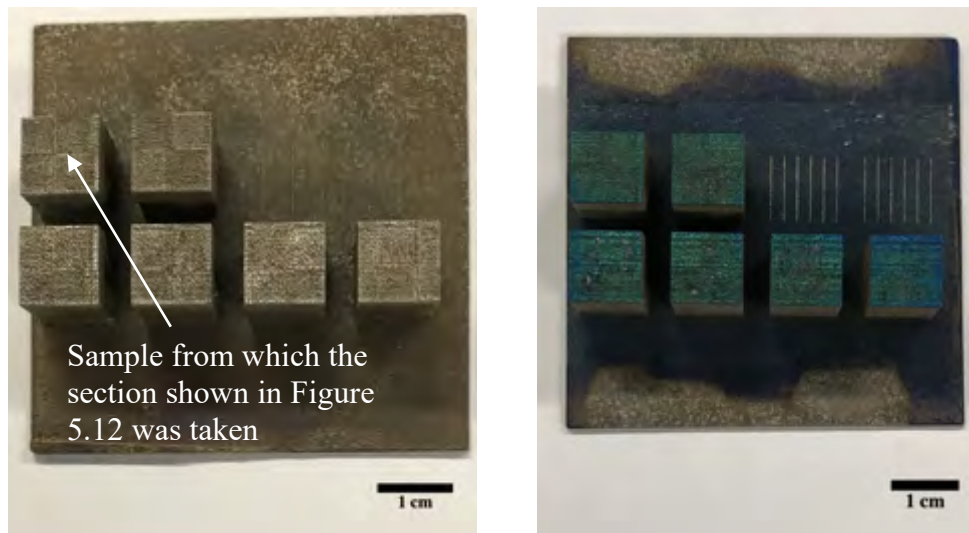
Figure 5.10 - SE Micrographs showing single scan tracks with room temperature, 400 °C and 600 °C base plates (L to R) with 300 W, 750 mm/s (top) and 300 W, 1000 mm/s (bottom)

Figure 5.10 showed scan tracks produced at different base plate temperatures and operating conditions. At 400 °C the average width of the weld beads was 117  $\mu\text{m}$  and 84  $\mu\text{m}$  ( $\pm 3 \mu\text{m}$ ) at 750 and 1000  $\text{mm s}^{-1}$  respectively, in comparison to 63  $\mu\text{m}$  and 56  $\mu\text{m}$  ( $\pm 3 \mu\text{m}$ ) for the single scan tracks conducted at room temperature. This may have indicated the 400 °C heating successfully increased the thermal input into the base plate. At 600 °C, the trends varied with widths of 67 and 138  $\mu\text{m}$  ( $\pm 10 \mu\text{m}$ ) respectively but the standard deviations of the measurements were three times larger due to the significant undulations and the balling shown in the tracks. There was also poor wetting seen likely due to the oxide on the surface of the substrate. The variation in width may also have resulted from alteration to Marangoni convection or poor wetting (7). Weld bead width measurements are not as indicative as weld pool depth measurements as there is a greater variation in depth during the transition from conduction to keyholing mode which may have occurred at higher temperatures and would mean the width to depth ratio would alter significantly (10). However, as a result of the significant oxidation, and subsequent embrittlement, no through-plate sections were successfully produced.

### **5.3.2 Build deposits with heated bed**

Due to the limited plate size, an extensive parametric study at the heated bed temperatures was not possible; additionally, it was decided that the heat inputs would not be sufficiently great to alter the build parameters substantially. The optimised parameters (300 W, 750  $\text{mm/s}$ , 0.4 a1) determined from the room temperature parametric study were therefore chosen. Additionally, a slightly lower energy input parameter of 300W, 1000  $\text{mm/s}$  and 0.4 a1 was used in order to allow for an increase in heat input from the bed heating. Three 10 mm x 10 mm x 10 mm cubic samples were produced with both parameters at 400 °C and

600 °C bed temperatures respectively; Figure 5.11 showed the completed builds. As with the single scan tracks, significant blue oxidation typical of  $\text{WO}_3$  can be seen on the 600 °C build. Given the coloured nature of the oxide, it is likely 200-300 nm thick (11).



*Figure 5.11 - Completed builds produced with bed heating of 400 °C (left) and 600 °C (right)*

The average density of the samples could be seen in Table 5.1. The density of samples built with both of the parameters did not vary greatly with bed temperature, however a slight improvement could be seen in the samples produced at 400 °C (approximately 1 %). No such improvements could be seen at 600 °C; this was likely due to the detrimental effects of oxidation at these temperatures. The increased presence of lack of fusion defects possibly suggested an increase in oxide redeposition or reduced wetting as a result of increased surface oxide (see Figure 5.12). Additionally, there were oxides present on both the substrate and on the powder. It was possible that the substrate oxides were shielded by the presence of the powder worsening the effects of wetting between the melt pool and the substrate or deposit.

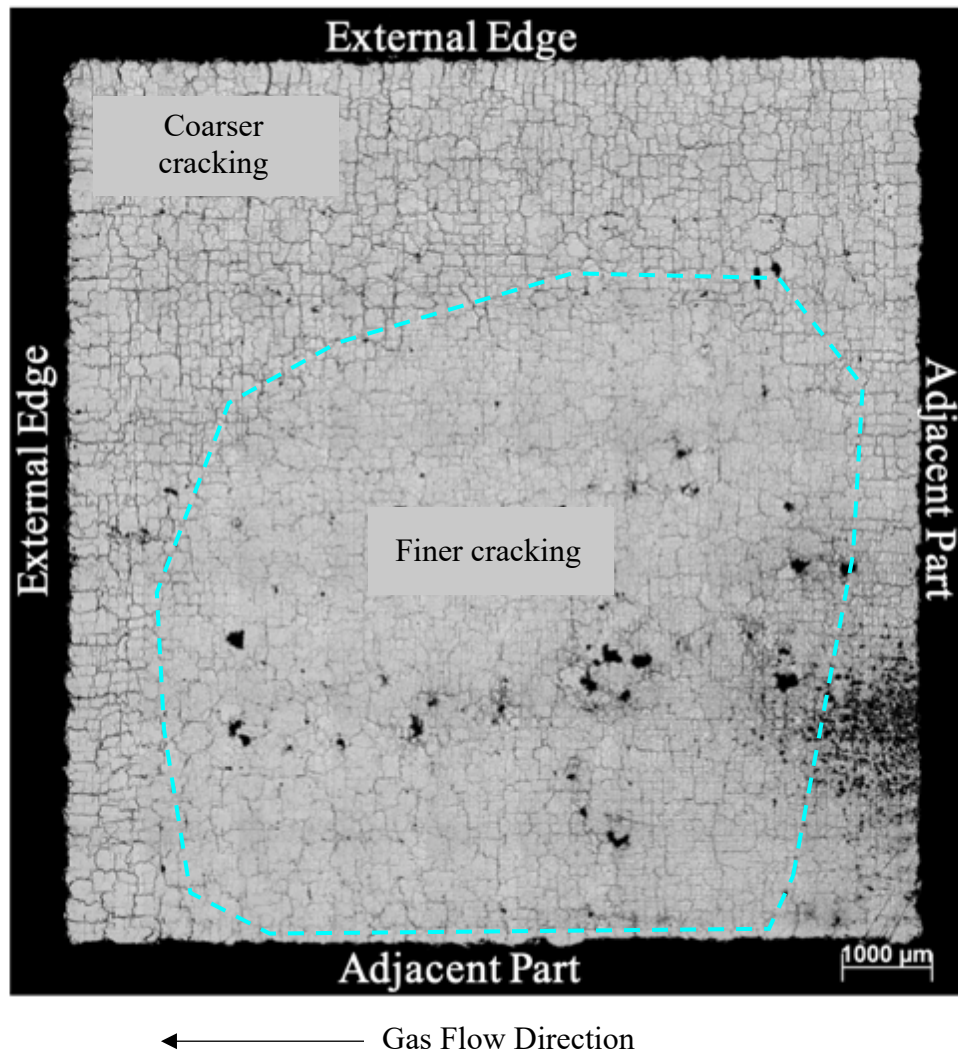
*Table 5.1 - Table showing Archimedes' density with different bed heating temperatures and processing parameters*

<b>Bed Temperature</b>	<b>Archimedes' Density (%)</b>	
	<b>300 W, 750 mm/s, a1 0.4</b>	<b>300 W, 1000 mm/s, a1 0.4</b>
RT	96.6	
400 °C	97.8	96.5
600 °C	96.5	95.1

Figure 5.12 shows an XY mid-plane section of the optimised heated bed parameters. Of note, is the inhomogeneous distribution of cracks throughout the section. At the edges of the sample, a much higher level of cracking can be seen, with the centre of the sample looking less affected. The sample was located at the edge of the baseplate (see Figure 5.11). It appeared from the offset of the uncracked area, that thermal shielding from the adjacent samples coupled with the heated bed were sufficient to lower the cooling rate of the part and prevent cracking. It could be assumed that the grain boundary would crack when the oxygen concentration reached a given critical value. A finer microstructure would result in more grain boundaries over which the oxygen present could be spread. There would therefore be more oxygen on the grain boundaries in the area of the coarser microstructure than the finer area. It could therefore be assumed that the effect of oxygen embrittlement would be greater in the area of high crack density. An alternate explanation was that weld spatter swept from right to left in the direction of the argon gas flow. However, weld spatter could have been swept from the part situated on the right-hand side of the imaged sample in the build plate.



Two possible explanations as to the cause of crack density variation over the section of the sample was the variation in oxygen concentration across the material, or the variation in thermal history across the sample.



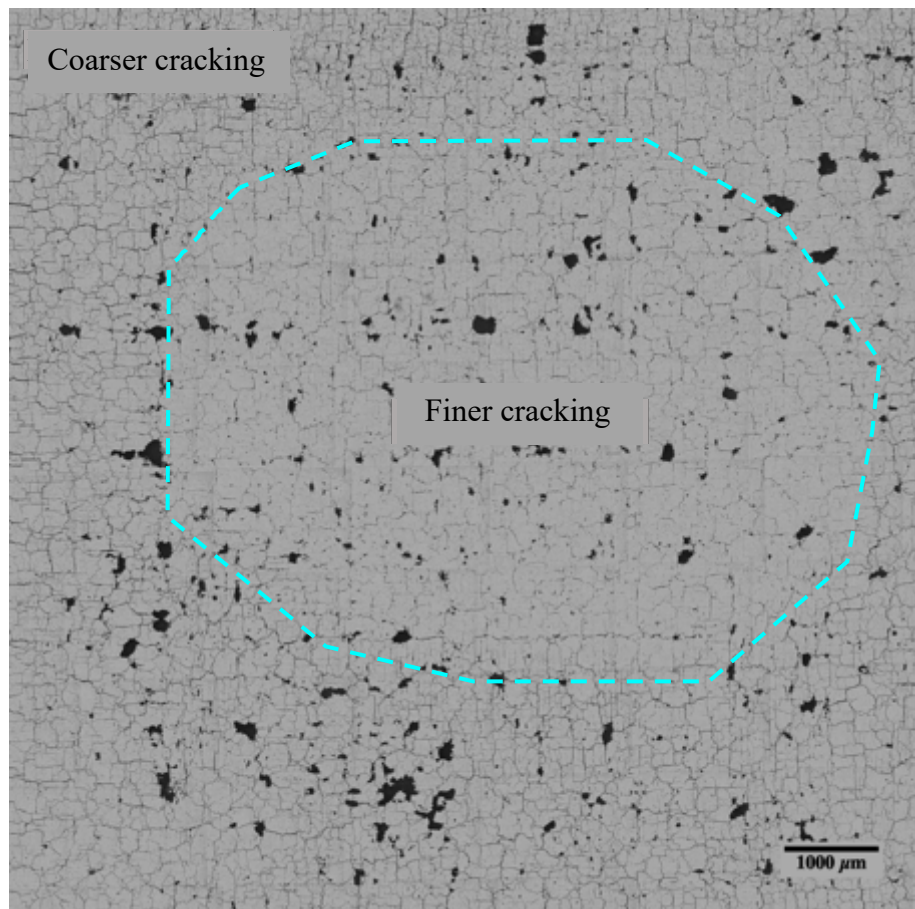
*Figure 5.12 - Optical micrograph of XY mid-plane section of sample produced with 400 °C bed heating showing inhomogeneous cracking across the surface*

As LPBF is a layer-by-layer process, all areas of the build would have been exposed to the surface at some point of the build. As a result, it was unlikely any difference in cracking or crack opening would result from variation in oxygen diffusion through the part. Further sections were taken to see if there was any variation in crack density through the build height

by taking further XY sections at the top and base of the build (see Figures 5.13 and 5.14).

Less variation could be seen across the section surface in these samples, as there was a lower and higher defect density throughout in the top and bottom of the sample respectively.

A thin band of coarser cracking could be seen at the edges of both sections. The finer cracking at the top of the build was in contrast to what was seen in many LPBF samples with residual stress increasing with increased build height (12-15). However, in tungsten the effect of oxygen embrittlement has been shown to be significant and the variation in microstructure through the build height may offset variation in residual stress. The atmosphere was likely to slowly improve throughout the build; some oxide may be volatilised and become trapped in the filters as well as the positive pressure slowly displacing residual oxygen. There would be less time at temperature for the layers deposited towards the end of the build (top section).



*Figure 5.13 - Optical micrograph of XY bottom section of sample produced with 400 °C bed heating showing inhomogeneous cracking across the surface*

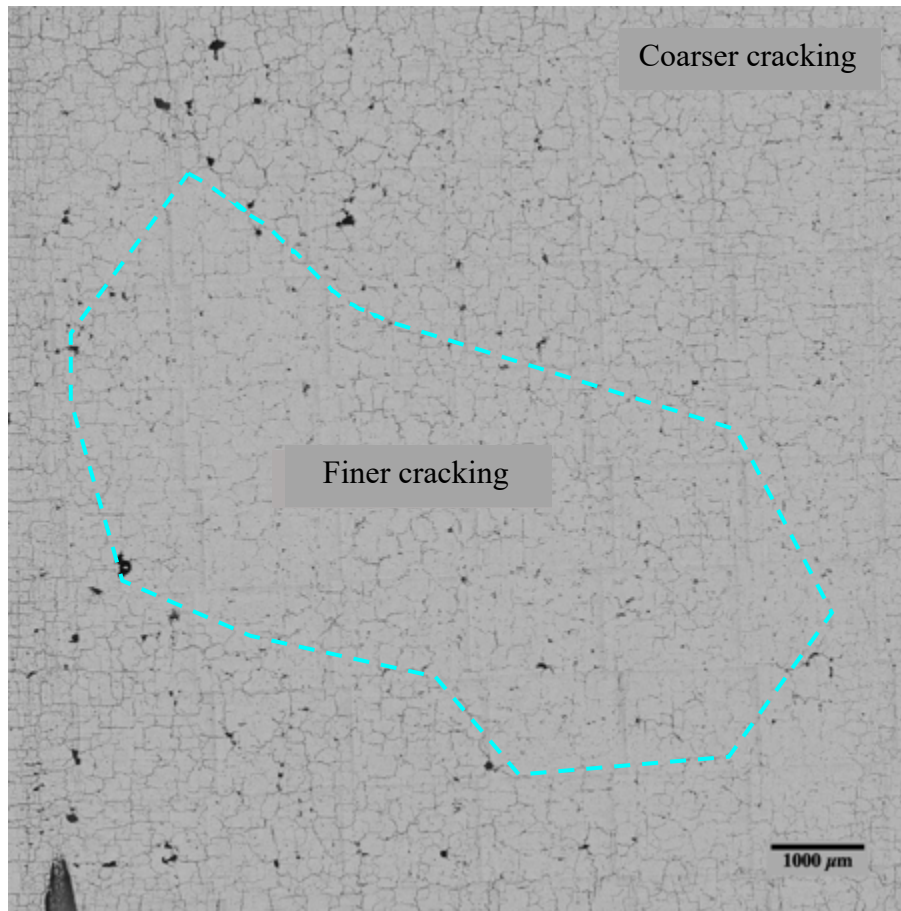


Figure 5.14 - Optical micrograph of XY top section of sample produced with 400 °C bed heating showing inhomogeneous cracking across the surface

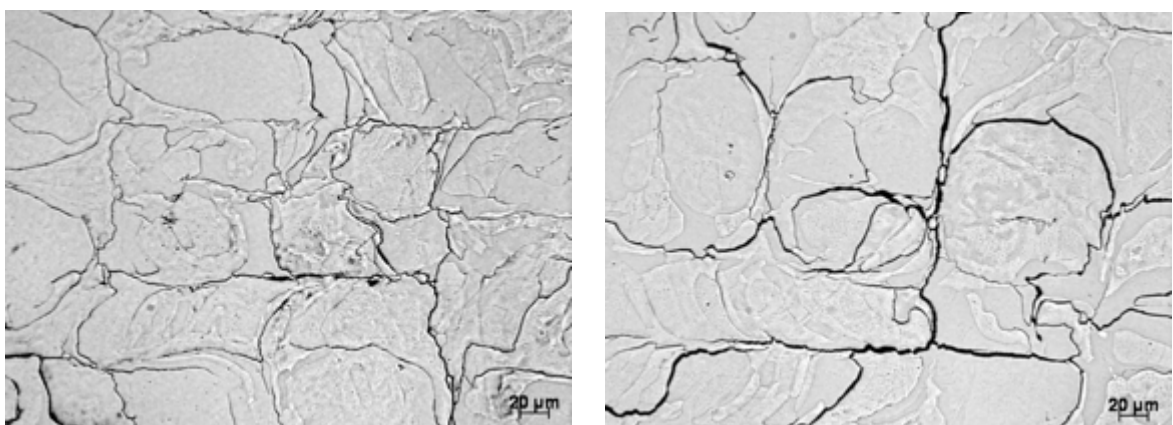
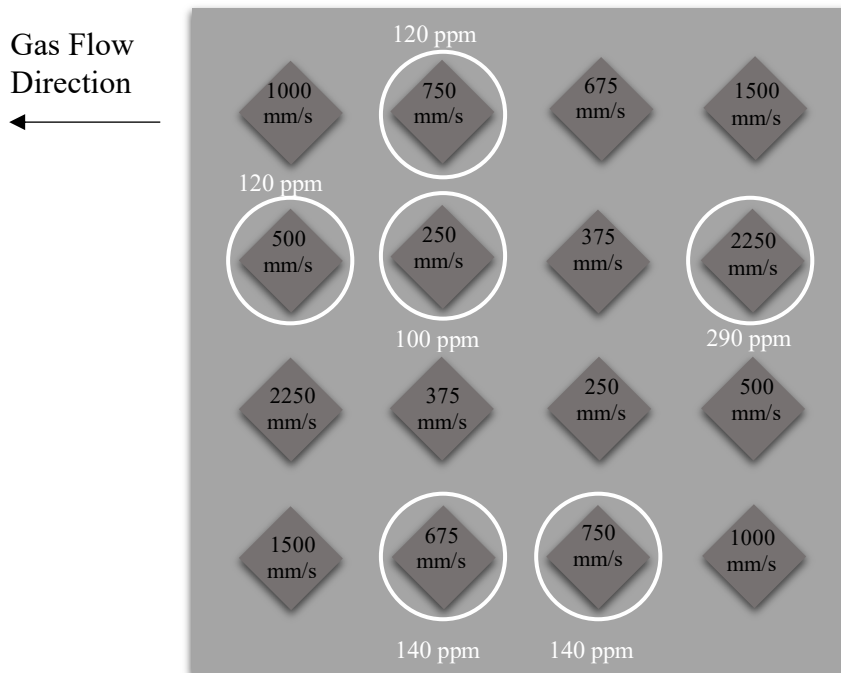


Figure 5.15 - Optical micrographs within the region of finer cracking (left) the region of coarser cracking (right)

It was important to note that while at the macroscale a noticeable difference could be seen between the regions of coarser and finer cracking, at the microscale it was clear there was still substantial cracking in both regions. Figure 5.15 showed micrographs of XY sections from the region of finer cracking and the region of coarser cracking.

It was important to note that the edge of the part (right) had a larger grain size than the interior of the part (left). An average grain size of 38  $\mu\text{m}$  (2s.f.) was found in the exterior of the part versus 24  $\mu\text{m}$  (2s.f.) for the interior of the part. These values should be taken comparatively as it was difficult to accurately separate the two areas while imaging, and a gradient of grain size was seen across the sample in accordance with the cooling rate variation across the part. As a result, a sample of approximately 500 grains was taken at the extremes of the part to generate these values. It could be assumed that the grain boundary would crack when the oxygen concentration reached a given critical value where the embrittlement lowered the grain boundary strength below the level of thermally induced stresses. A finer microstructure would result in more grain boundaries over which the oxygen present could be spread. There would therefore be more oxygen on the grain boundaries in the area of the coarser microstructure than the finer area. It could therefore be assumed that the effect of oxygen embrittlement would be greater in the area of coarser cracking.



*Figure 5.16 - Schematic showing oxygen contents of various samples across the build plate. All samples were produced with 400 W power*

It was presented that the asymmetry of the region of lower crack density corresponded to thermal shielding between parts. It was also possible that this was associated with lower oxygen content due to sample to sample gettering (see Figure 5.16). The thermal conduction and its variation through the build height should also be considered. At the base of the sample there would be little surrounding powder, with a large heat sink from the base plate and limited thermal shielding from adjacent parts, causing rapid cooling. Additionally, the oxygen content at the start of the build would be at its highest and these combined leading to a higher defect density. Towards the middle of the build, thermal shielding could become more important as the surrounding powder would limit thermal conduction laterally at the exterior of the part. The adjacent parts could also getter oxygen evidenced by the shift of the area of lower cracking density off centre. At the extreme of build height, the oxygen content at the end of the build would also be at its lowest possibly lessening the adjacent sample gettering.

Unfortunately, the use of the hot bed while reducing cooling rates and residual stresses, increased the oxidation, and therefore had only limited success in the reduction of defect concentration in LPBF of tungsten. Significant improvements to residual oxygen content would need to be made to overcome these issues; this would be most easily achieved through utilisation of a more appropriate build platform with a vacuum and purge capability.

Figure 5.17 shows an EBSD map of the heated bed tungsten sample. The sample produced without bed heating (Figure 5.18) had a microstructure which was clearly related to the scan path of the laser (Section 4.3.3) and typical to fusion welding microstructures seen. By contrast, this structure is not seen in the heated bed sample. There was greater variation in the grain size, with some grain diameters as large as 200  $\mu\text{m}$  despite the average grain size not changing significantly. The sample also showed less significant texture than the room temperature sample which had a stronger texture between  $\langle 111 \rangle$  and  $\langle 110 \rangle$  possibly due to the faster cooling rate.

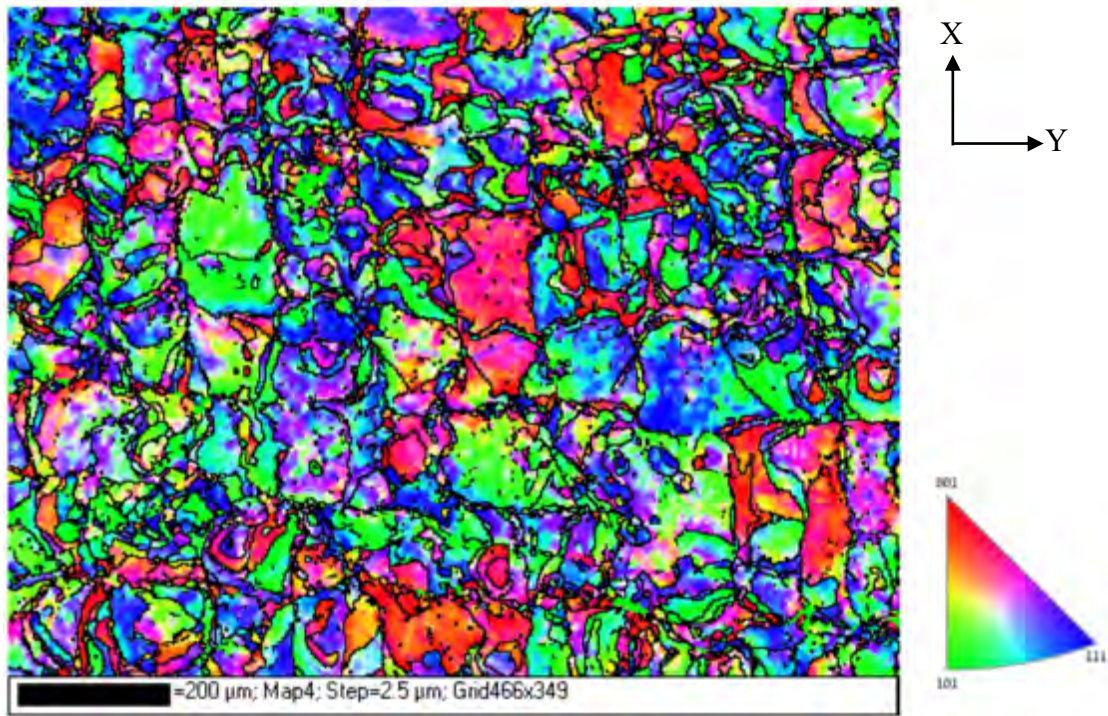


Figure 5.17 - EBSD map of LPBF tungsten sample produced with bed heating (IPF Z colouring)

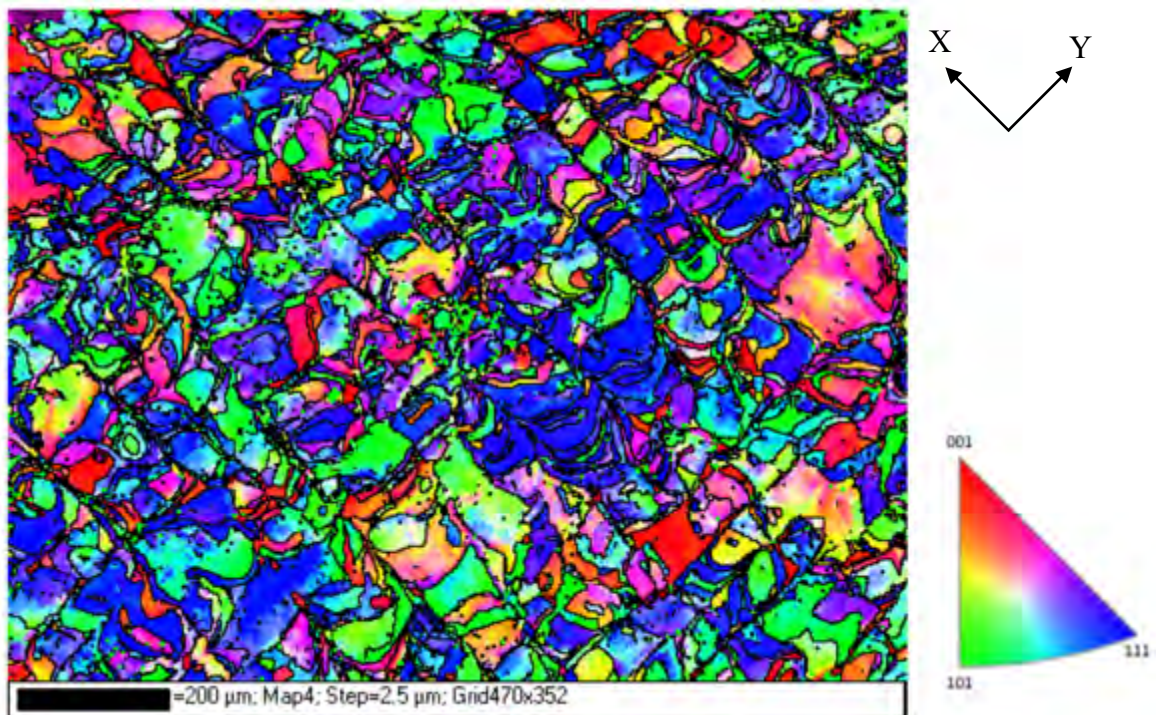
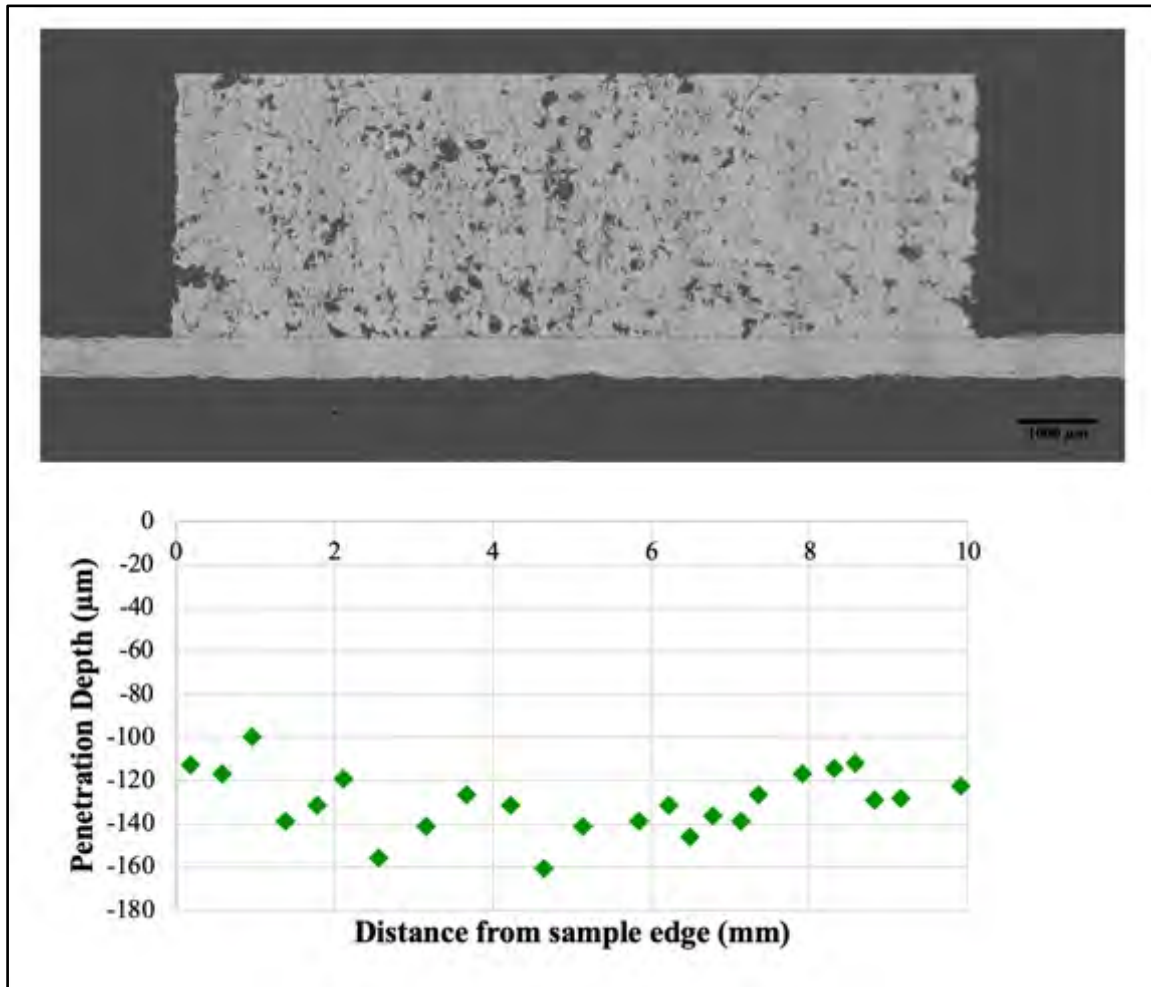


Figure 5.18 - EBSD map of LPBF tungsten sample produced without bed heating (IPF Z colouring)

### 5.3.3 Fusion zone penetration depth measurements

The penetration depths of the samples produced with the heated bed were measured and compared to the room temperature penetration depths discussed previously. At 400 °C, the average penetration depth was 130 µm in comparison to 111 µm at room temperature. This was an increase in penetration depth of 17 % (see Figure 5.19).

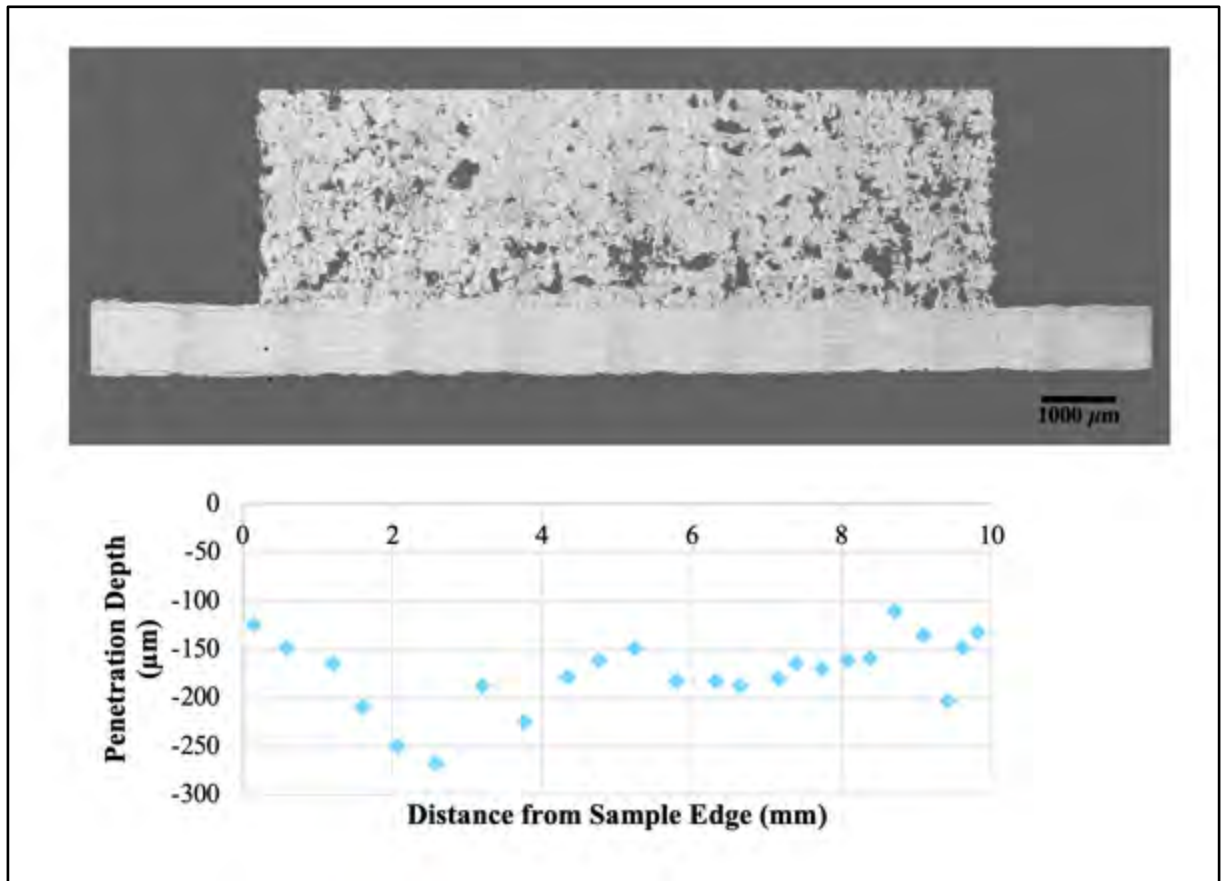


*Figure 5.19 - A graph and micrograph showing the penetration depth of the fusion zone across the 400 °C heated bed sample*

Due to the variation in experimental set-up, the hot bed samples could not be effectively compared to the pre-scan samples, as the control measurement differed from the room temperature measurement as discussed in Section 5.2.2. By scaling the average pre-scan temperature by a ratio of the room temperature to normalise for this difference in set-up, it



was found that the heated bed samples may still have had penetration depths up to 10 % larger than that of the pre-scan sample. This was unsurprising as the bed temperature was almost 200 °C higher.



*Figure 5.20 - A graph and micrograph showing the penetration depth of the fusion zone across the 600 °C heated bed sample*

The sample produced at 600 °C unsurprisingly had a greater penetration depth with an average value of 174 μm, a value 34 % and 57 % greater than the penetration depth achieved at bed temperatures of 400 °C and room temperature respectively (see Figure 5.20). There was, however, much greater variation in the penetration depths seen with a range of 158 μm seen at 600 °C compared to 61 μm at 400 °C. This was likely due to a lower build quality and less weld track uniformity at 600 °C, resulting from oxidation as seen in the single scan tracks

(Section 5.3.1) (7). Greater levels of porosity lead to less uniform heat flow, as discussed in (Section 4.4) with the comparison of powder morphologies.

#### **5.4 Effect of minor tantalum additions**

Tantalum additions were the other key method trialled to improve the manufacturability of tungsten. Tantalum was selected as the alloying addition for this study as it was the most chemically similar to tungsten; W-Ta alloys have unlimited solid solubility and a solidus - liquidus range of only 35 °C. W-V alloys also have unlimited solid solubility, however vanadium with a melting point of 1926 °C has a much larger solidus - liquidus range and will have a lower maximum operating temperature than W-Ta alloys and were therefore deemed unsuitable for nuclear fusion applications (3, 16).

Previous studies have investigated tantalum additions in tungsten however conclusions as to its efficacy have been mixed. Rieth et al., 2013 found the DBTT of the alloy would be higher than pure tungsten (17). However, Tejado et al., 2015 (18) found improved toughness (see Section 2.6).

Tejado et al., 2015 found 10 w.t.% Ta to be the optimum alloying level for improving properties. As a result, 10 w.t.% Ta was selected as the alloying level for this study.

Elemental powders of tungsten and tantalum were blended together prior to using LPBF fabrication to alloy the material.

### 5.4.1 Blended powder characterisation

Elemental tungsten and tantalum powder sourced from LPW Technology were blended. The powder size distributions for the two powders can be seen in Figure 5.21 along with the d10, d50 and d90 values.

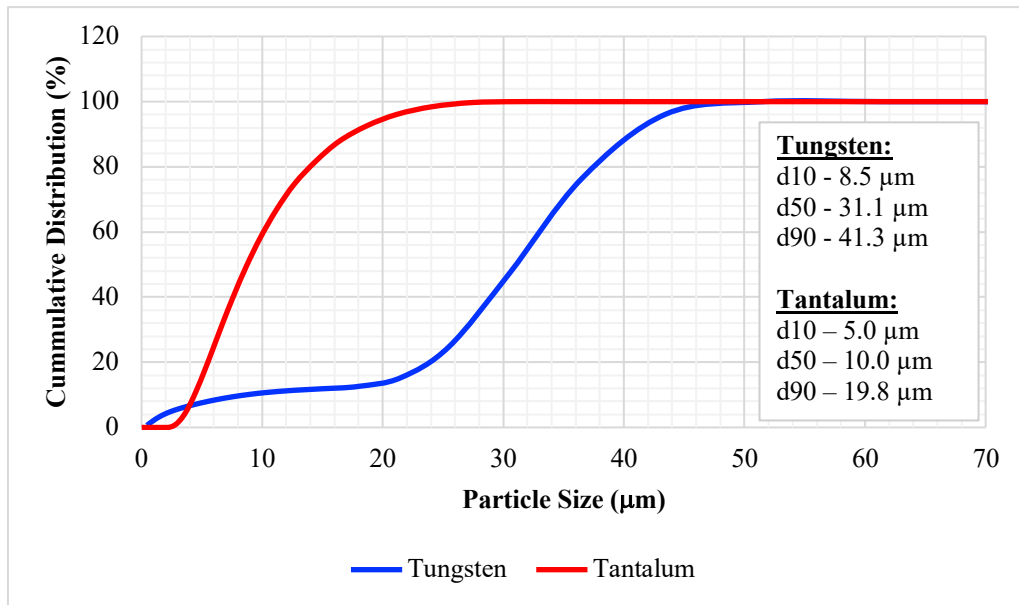
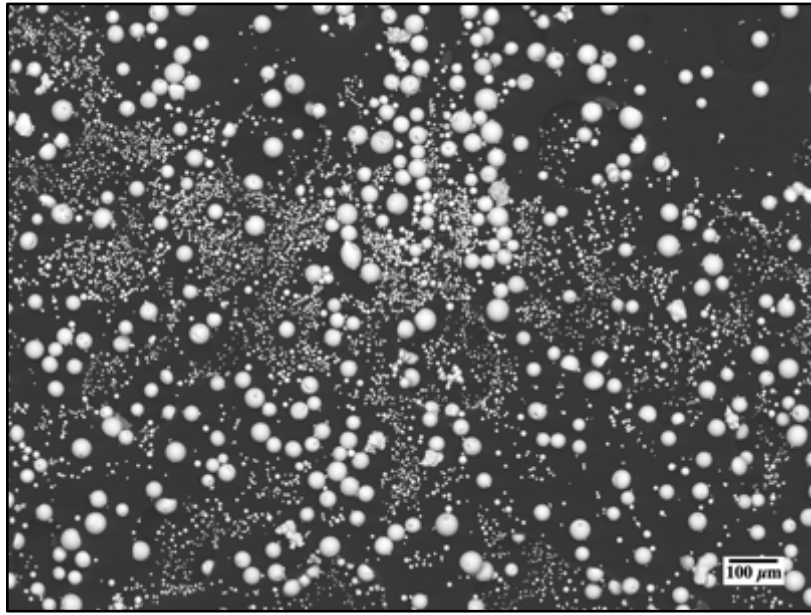
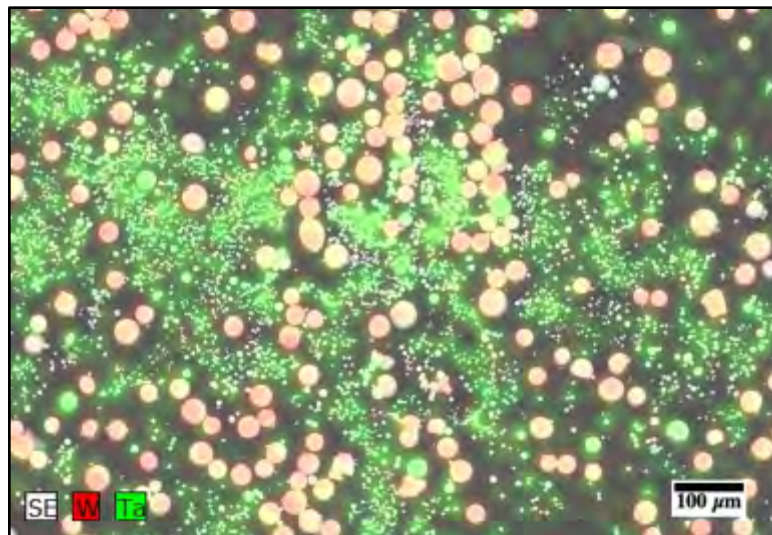


Figure 5.21 - Graph to show the size distribution of the plasma spheroidized tungsten and tantalum elemental powders as determined by LPSD

It could be seen that the size distribution of the two powders varied significantly. The mean powder particle size of the tantalum powder was 10 µm in comparison to 31 µm for the tungsten powder. This was further evidenced by the micrograph showing the blended powder (Figure 5.22). The small powder particle size may increase the risk of vaporisation of the tantalum during processing.



*Figure 5.22 – BSE Micrograph of the blended elemental tungsten and tantalum powders*  
An EDX map of the powder particles could be seen in Figure 5.23 with Table 5.2 showing the EDX results of the powder. This showed that the powder had blended and the difference in density and size distribution had not led to significant difficulties in producing a reasonably homogenous mixture.

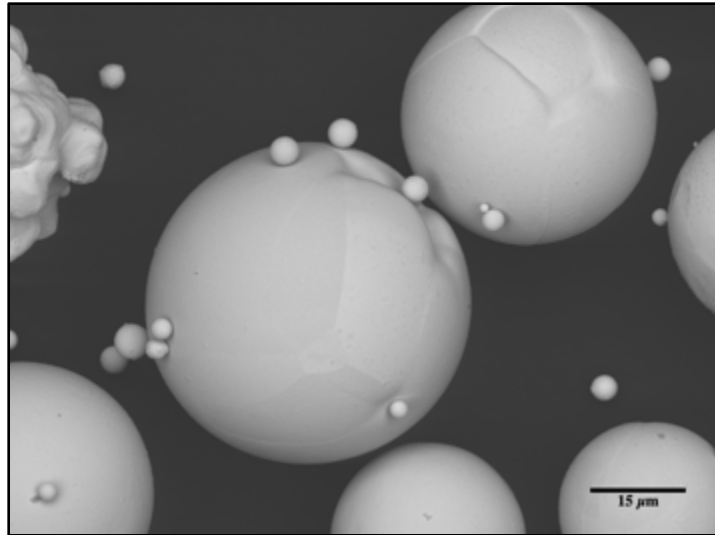


*Figure 5.23 - An EDX map of the blended powder with tungsten (red) and tantalum (green)*

*Table 5.2 - Composition of the blended powder as determined by EDX*

Element	Series	Composition (norm. wt. %)	Composition (norm. at. %)	Error in wt.% (3 Sigma)
Tungsten	L-series	90.9	90.8	14.1
Tantalum	L-series	9.1	9.2	2.2
	Sum:	100	100	

This significant variation in size may have been beneficial to the blending process, with the smaller tantalum particles surrounding a larger tungsten particle and forming pseudo satellites in surface depressions on the tungsten particles as could be seen in Figure 5.24.



*Figure 5.24 - BSE micrograph showing tantalum satellite powders in surface depressions in the tungsten powder particle*

After the blending process XRD was conducted on the powder; the patterns of both pure tungsten and the tungsten-tantalum blend can be seen in Figure 5.25.

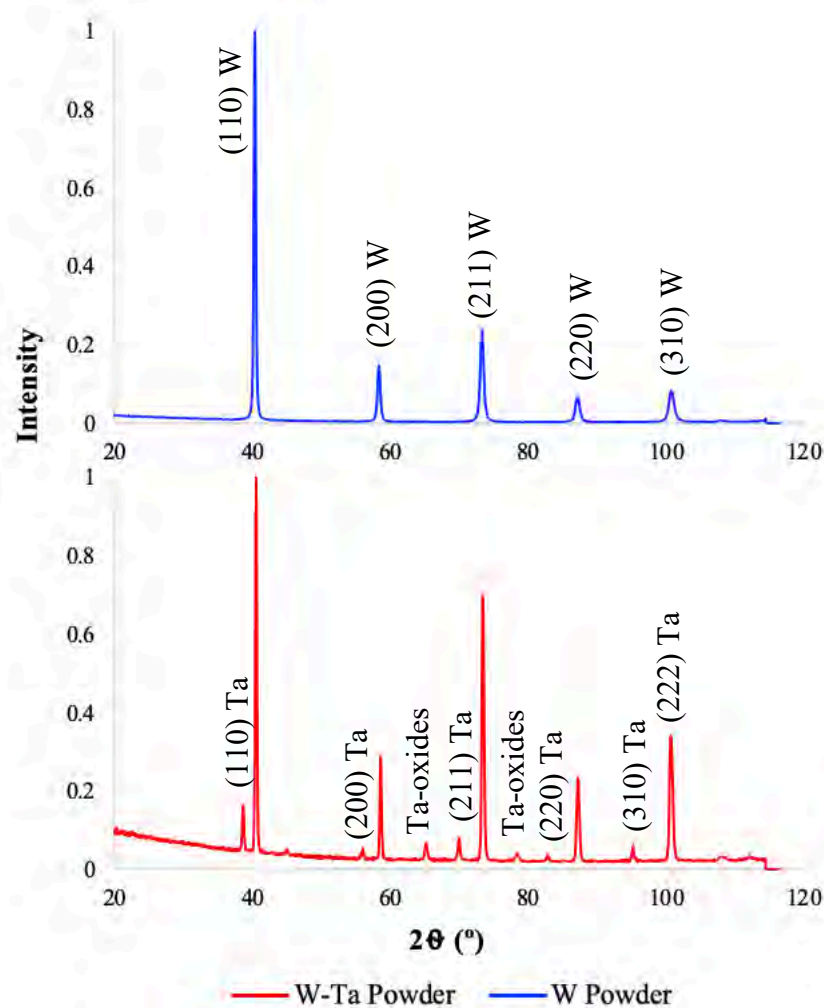


Figure 5.25 - XRD Pattern of the elemental tungsten powder and the blended tungsten-tantalum powder

Distinct tungsten and tantalum peaks could be seen in the blended powder sample. While the (110) peak was still the largest in both samples, there was an increased intensity in the (211), (220) and (310) tungsten peaks in the blended powder sample. The (310) tungsten peak coincided with the (222) tantalum peak. The remaining peaks were attributed to  $TaO_2$  occurring at the same  $2\theta$  angle as the tungsten peaks. The small peaks on the pattern were attributed to tantalum oxides. Park et al., 2008 showed oxygen deficient tantalum oxide ( $TaO_{1.7}$ ) formed a stronger XRD peak than  $Ta_2O_5$  at a  $2\theta$  of  $63^\circ$  (19-22).

#### 5.4.2 Build deposits with tantalum additions

Having confirmed that the powder had blended, an identical build to that of LPBF tungsten was conducted to mitigate any processing or locational variations between the builds.

Figure 5.26 showed the Archimedes' density of the tungsten and tungsten-tantalum samples over a range of process conditions. While both materials showed the same trends over the processing conditions, the W-Ta had slightly higher densities (about 1 %), but this was within the error associated with this technique. The W-Ta density was determined as a percentage of its theoretical density assuming a perfect 90-10 w.t.% blend.

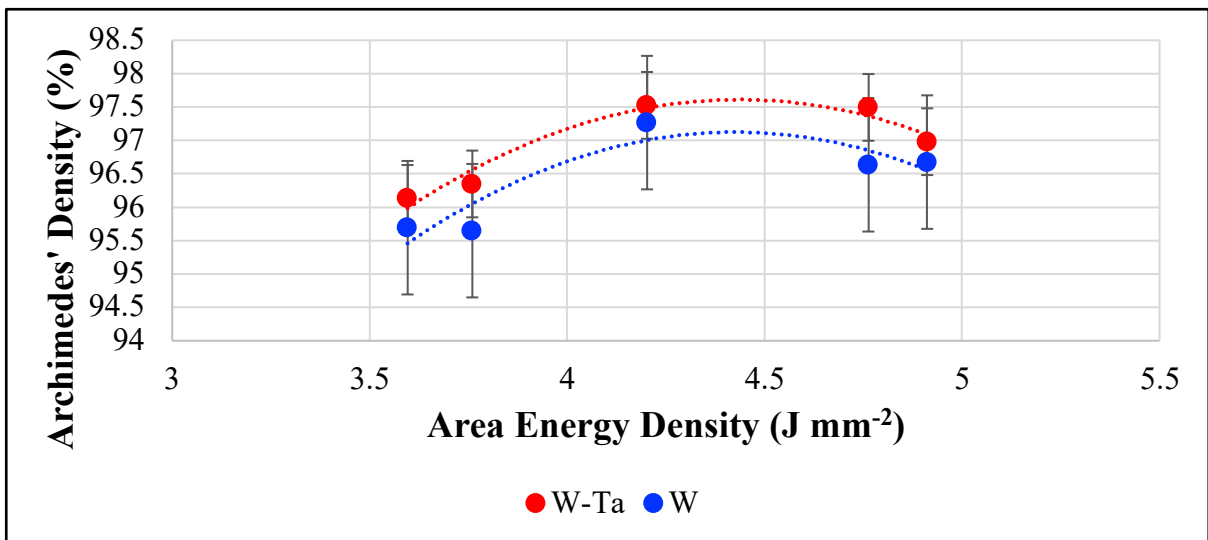
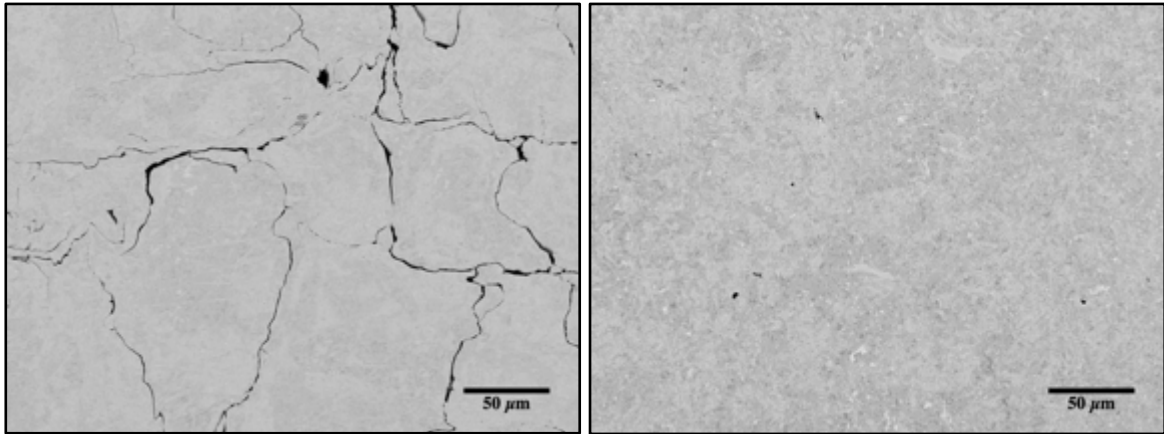


Figure 5.26 - A graph to show the variation in Archimedes' density with Area Energy Density for LPBF tungsten and tungsten-tantalum alloy samples

Inhomogeneities in the mixture, or greater vaporisation of one constituent than the other would cause inaccuracies in the Archimedes' density values. As a result, metallographic sections were prepared to investigate the defects present in the tungsten-tantalum alloy in comparison to pure tungsten. Figure 5.27 showed micrographs of the XY sections of the tungsten and tungsten-tantalum alloy.

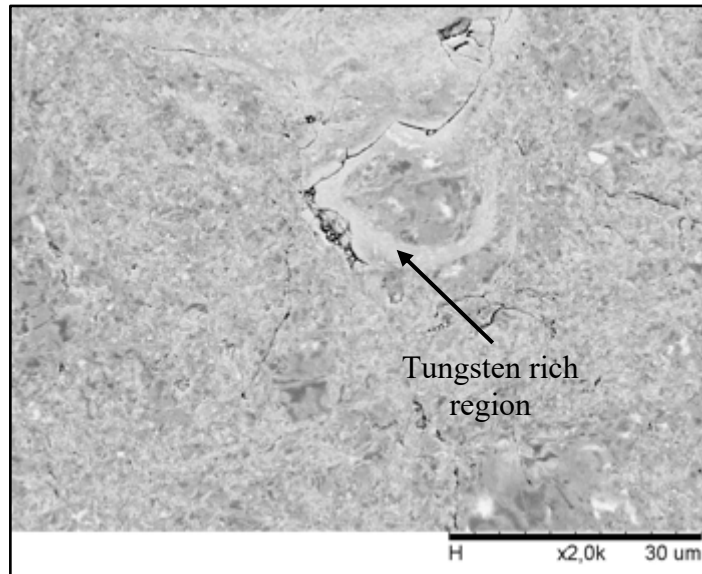


*Figure 5.27 - BSE micrographs showing cracking in tungsten (left) and tungsten-tantalum alloy (right)*

As could be seen there is a significant reduction in the cracking through the addition of tantalum. While improvements have been made, at higher magnifications fine cracks could be seen (see Figure 5.28).

A lighter band could be seen at the edge of the crack. As this is a back-scatter image, elements with higher atomic numbers scatter more electrons creating a higher signal and a brighter region of the micrograph. It is therefore possible that this was a tungsten rich region as the average atomic number of this area would be higher. An EDX map of the area was attempted to verify but due to the proportion of tungsten present throughout the sample and interaction volume associated with the technique, no differentiation between the two areas could be found. However, point scans conducted showed between 3 and 4 % tantalum present. This suggested either some vaporisation of the tantalum occurred or there were tantalum-rich regions outside of the sample analysed by EDX.





*Figure 5.28 - BSE Micrograph showing fine cracking around a tungsten-rich region of material*

There was a lack of consistency in the literature as to why the addition of tantalum would have the beneficial effect. Indeed, Ivekovic et al., 2018 showed significant levels of cracking even with tantalum additions and processed with bed heating. The authors suggested that the addition of tantalum affected average grain size which improved the mechanical properties of the alloy (23). However, the Hall-Petch effect on tungsten is limited (24, 25). It was, therefore, unlikely, that the effect of tantalum was due to grain size alone.

There were three other main hypotheses relating to tantalum and its effect on oxygen within the tungsten system; the first being that the e/a ratio increased oxygen solubility in tungsten preventing oxygen segregation to the grain boundaries. At 10 w.t.% tantalum however, the e/a ratio would be only 5.9 well above the determined interstitial solubility threshold value of 5.6 (5, 6, 26). The second was that tantalum oxide forms preferentially to tungsten oxide (27) and that the tantalum oxide does not form on the grain boundaries as has been shown in tungsten oxide (28). By contrast, tantalum oxide had been shown to segregate to the surface preventing grain boundary embrittlement (29). The final hypothesis was that as tantalum has a higher

oxygen solubility than tungsten (200 ppm vs. 1 ppm), the oxygen segregated to Ta-rich regions and the oxygen sat interstitially (5).

The only potential hypothesis not relating to the behaviour of oxygen, would be that as tantalum was more ductile it would act as a ductilising agent in the tungsten alloy and therefore reduce cracking. However, this had not been found to be the case with only a 25% W-Re alloy found to ductilise tungsten (23, 25, 30).

In order to further investigate the mechanism by which the reduction in cracking has been achieved, SIMS was conducted on the pure tungsten and the tungsten-tantalum samples.

Figure 5.29 showed the SIMS map of the pure tungsten and the SE micrograph of the crater bottom, and the map and micrograph of the W-Ta alloy.

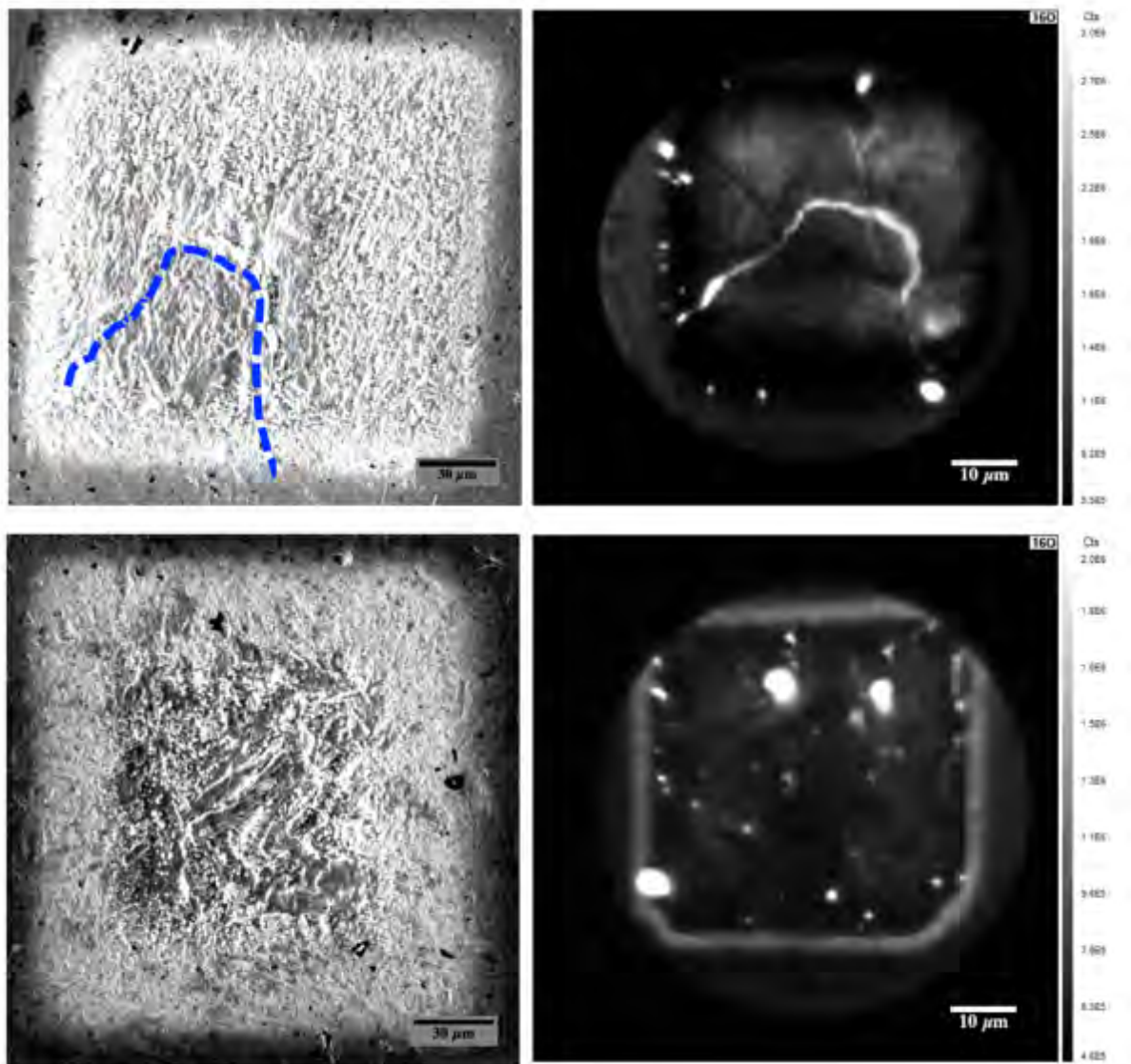


Figure 5.29 - SE micrograph of an ion milled crater and a SIMS map showing  $^{16}\text{O}$  in tungsten (top) and a SE micrograph of an ion milled crater and a SIMS map showing  $^{16}\text{O}$  in tungsten-tantalum (bottom)

Multiple craters were produced and analysed to ensure consistent results, and Figure 5.29 was indicative of the tungsten and tungsten-tantalum samples respectively. Oxygen embrittlement of the grain boundaries was found through SIMS in the pure tungsten sample. The lateral resolution of the beam meant that the oxygen signal was visible over a wider area; widths of the oxide could therefore not be determined. In the tungsten-tantalum sample, no grain boundary segregation of oxygen was seen. However, it is possible that the oxides were sitting on grain boundaries but were spheroidised, thus reducing the cracking as found by Scott and

Knowlson, 1963 (31). Further work would be required to confirm. In the SIMS map, discrete bright areas could be seen showing an increased intensity of  $^{16}\text{O}$ . This suggested that through alloying with tantalum, a fundamental change to the tungsten-oxygen interaction occurred and any improvement with tantalum was not simply due to tantalum having improved strength and ductility in comparison to tungsten. The sample chemistry was destroyed during the ionisation process in SIMS and it therefore could not be ascertained whether the oxygen was sitting interstitially in Ta-rich regions or if a tantalum oxide was forming.

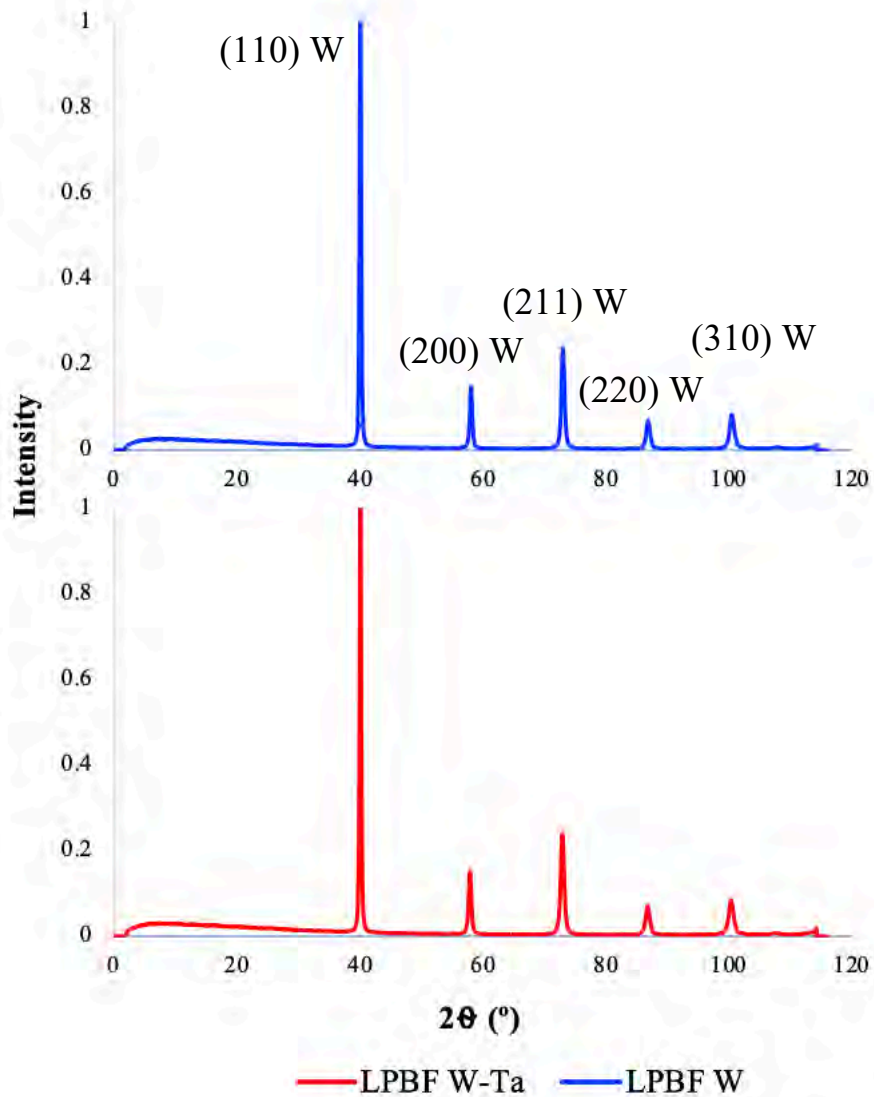


Figure 5.30 - XRD pattern of the LPBF W and LPBF W-Ta samples

XRD was conducted in attempt to analyse the sample chemistry in further detail. Figure 5.30 showed the distinct tantalum peaks present in the blended powder (Figure 5.25) were not present in the LPBF tungsten-tantalum alloy sample. Additionally, both the tungsten and tungsten alloy samples showed the same texture with dominant (110) and (211) peaks as was seen in the literature (32, 33). This suggested that the sample had formed a solid solution as expected (3).

Vegard's law was used to determine the change in lattice parameter as a result of the tantalum alloying and to determine the quantity of tantalum proportional to the peak shift (34). From this it was determined that only 4w.t. % Ta was in solid solution. This was comparable to the EDX point scans conducted. This suggested a significant amount of the tantalum powder was vaporised during processing, as the starting composition of the powder had been confirmed by EDX. Utilising a batch of tantalum with a larger mean particle size could reduce the issues of vaporisation.

Raman spectroscopy was conducted on surfaces of the tungsten and tungsten-tantalum deposits<sup>1</sup>; the spectra of which could be seen in Figure 5.31 below. Raman spectroscopy was particularly sensitive to metal-oxide bonds and could therefore indicate a variation in oxidation with the addition of tantalum (35).

---

<sup>1</sup> *The author gratefully acknowledges the assistance of Dr. Daniel Reed for his help with XRD and Raman spectroscopy.*

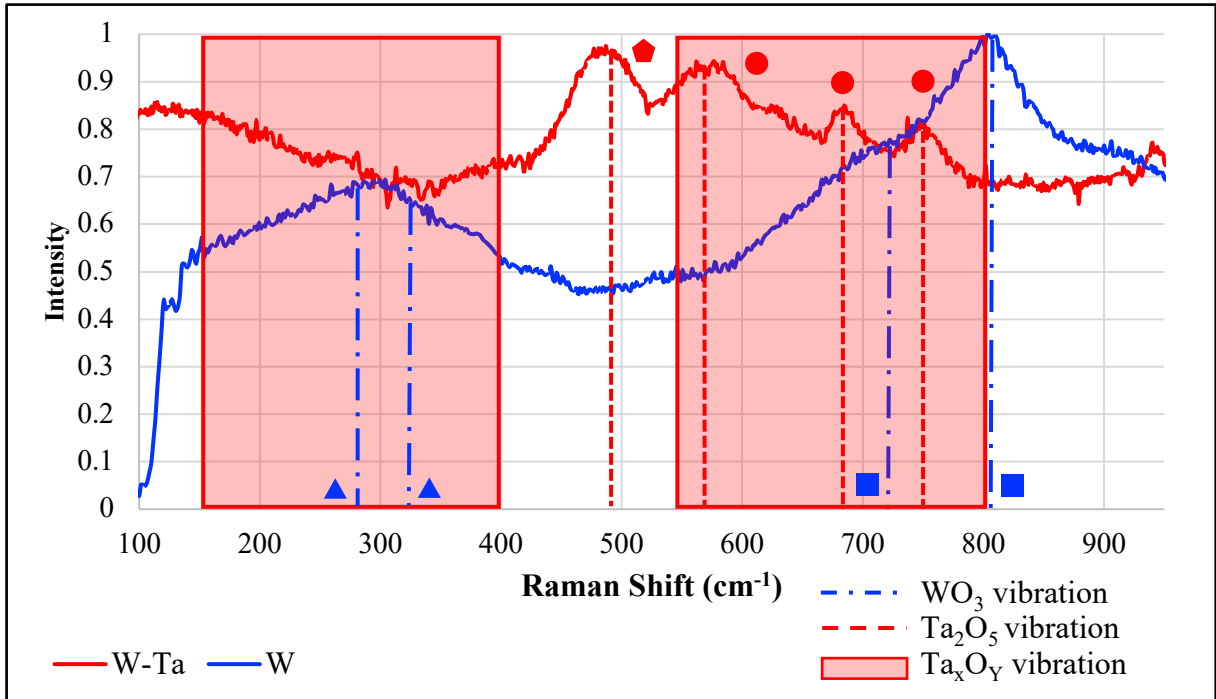


Figure 5.31 - Raman spectra of the tungsten sample (blue) and tungsten-tantalum sample (red) along with reference vibrations for tungsten and tantalum oxides (21, 36, 37)

The characteristic vibrations of  $\text{WO}_3$  occurred at 270 and 324  $\text{cm}^{-1}$  due to O-W-O bending (peaks labelled with a triangle) and at 715 and 805  $\text{cm}^{-1}$  from stretching of the O-W-O bonds (peaks labelled with a square) (36).

From literature, the amorphous  $\text{Ta}_x\text{O}_y$  oxide exhibited two broad vibrations shown as the shaded areas; the first ( $< 400 \text{ cm}^{-1}$ ) occurred from a bending of the Ta-O-Ta bond, and the second occurred between 560 and 800  $\text{cm}^{-1}$ . In  $\text{Ta}_2\text{O}_5$ , there were three peaks in this range corresponding to the geometric distortion of  $\text{TaO}_6$  (peaks labelled with a circle). Additionally, the peak labelled with a pentagon, at 495  $\text{cm}^{-1}$  resulted from the symmetric stretching of the Ta-O-Ta bond (20, 37).

As could be seen in the Figure 5.31, some defined peaks could be seen, but the peaks were broadened and much less clearly defined in both the pure tungsten, and tungsten-tantalum

samples suggesting that the oxides formed were non-stoichiometric (20), and that mixed oxides may have formed.

It could clearly be seen that the oxides formed in the tungsten and tungsten-tantalum samples were different, and this suggested that a mixed tungsten oxide formed in the pure tungsten sample, whereas a mixed tantalum oxide formed in the tungsten-tantalum sample. Moreover, tungsten oxide was shown to volatilise at temperatures below the that of the volatilisation temperature of tantalum, suggesting that the tantalum oxide could form earlier in the cooling process than the tungsten oxide (38).

It could be suggested that some tantalum formed a solid solution with tungsten, a tantalum type oxide formed in preference to the tungsten oxide, and as a result limited the oxide formation on the grain boundaries or formed spheroidised oxides. The embrittlement was lessened and consequently the cracking was reduced. Further chemical analysis would be required to confirm.

### **5.5 Combined effect of minor alloy addition and heated bed**

Partial successes had been achieved through minor alloy addition and the heated bed separately, but some level of cracking still occurred in the alloyed samples, and defects existed in the heated bed samples as a result of oxygen contamination. The two techniques were combined to investigate the effects.

### 5.5.1 Fusion Zone Penetration Depth Measurements

Figure 5.32 showed the average penetration depth across the sample of the tungsten-tantalum alloy produced with bed heating of 400 °C. The average penetration depth was 147 μm (3 s.f.) in comparison to 130 μm penetration depth of pure tungsten produced at 400 °C. Tantalum has a significantly lower thermal conductivity than tungsten ( $57.5 \text{ W}\cdot\text{m}^{-1}\cdot\text{K}^{-1}$  vs.  $170 \text{ W}\cdot\text{m}^{-1}\cdot\text{K}^{-1}$  at 20 °C) and therefore, the part remained at temperature for longer and slightly increased the penetration depth. The alloy would have a thermal conductivity of around 10 % lower than pure tungsten and the variation in penetration depths between tungsten and the tungsten-tantalum alloy was 13 % (39).

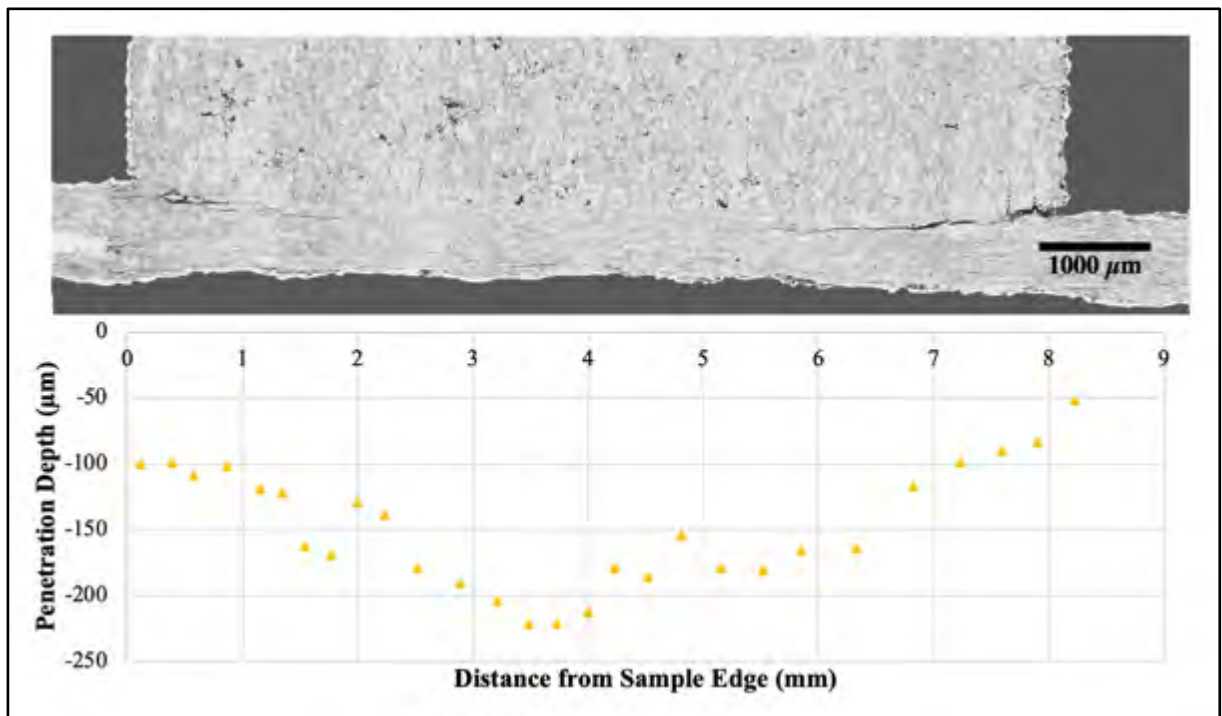


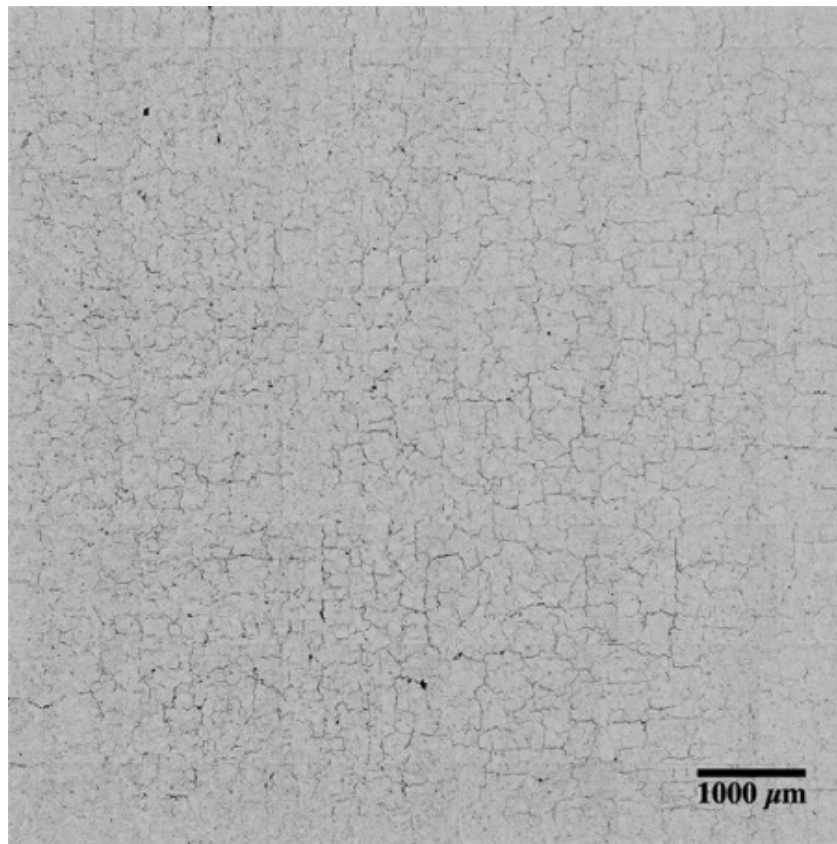
Figure 5.32 - A graph and micrograph showing the penetration depth of the fusion zone across the tungsten-tantalum sample produced with 400 °C bed heating



### 5.5.2 Build deposits produced with alloy additions and heated bed

A micrograph of an XY section of a W-Ta sample produced with a 400 °C heated bed could be seen in Figure 5.33. This showed a noticeably higher level of cracking than in the room temperature builds also produced with W-Ta.

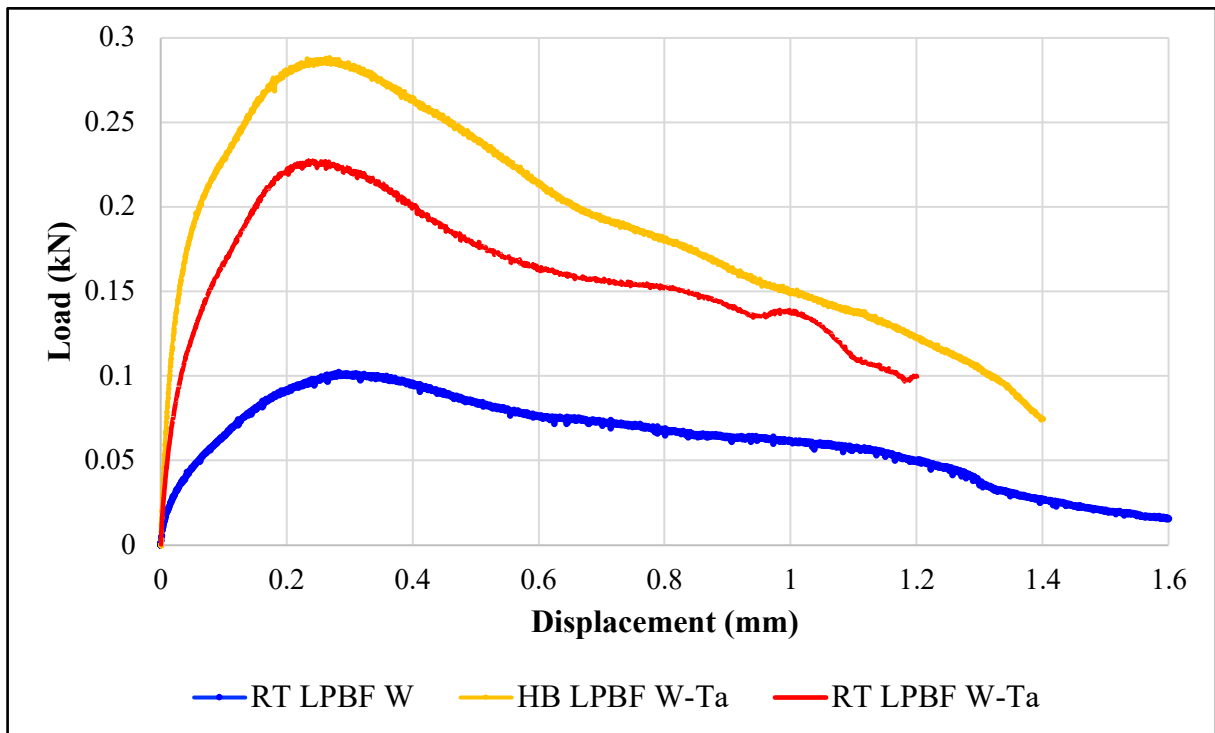
It can be assumed that the residual stress would be reduced due to the presence of bed heating due to the reduction in temperature change (12, 40). Moreover, the reduced thermal conductivity of the alloy would increase the solidification time reducing the potential for build defects (7). The increased cracking was therefore likely due to the increased oxidation weakening the grain boundaries and causing rupture as seen in the pure tungsten heated bed samples due to oxygen embrittlement.



*Figure 5.33 - Optical micrograph showing the XY section of the tungsten-tantalum alloy produced with bed heating of 400 °C*

## 5.6 Small Punch Testing

Small punch testing was conducted on a range of samples to investigate the efficacy of the methods to improve the manufacturability of tungsten and tungsten alloys. Pure tungsten samples produced with bed heating were not tested as the improvement was only seen on a localised central area of insufficient size to produce a small punch specimen.



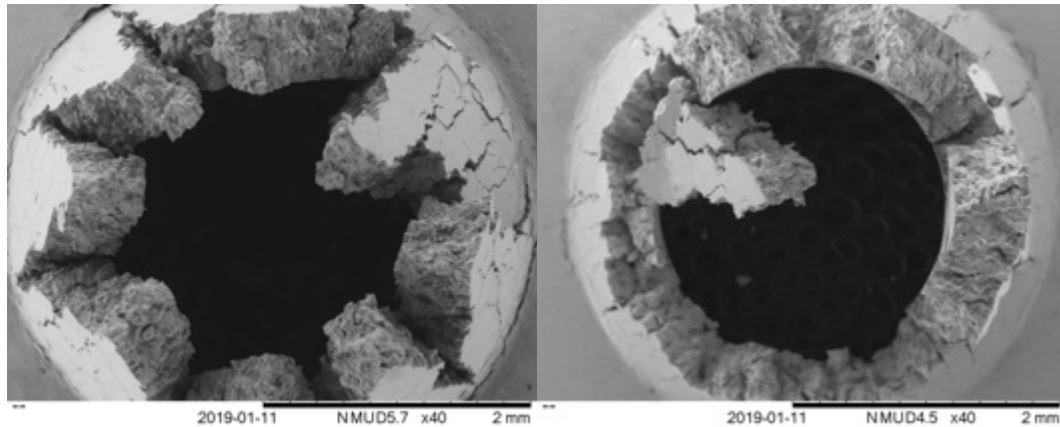
*Figure 5.34 - Load/ Displacement curves for LPBF tungsten samples produced without bed pre-heating (RT) and LPBF tungsten-tantalum samples produced with (HB) and without (RT) bed heating tested at 600 °C*

As could be seen in Figure 5.34, when tested at 600 °C, the LPBF tungsten-tantalum sample produced with bed heating had the highest maximum load of 0.29 kN (2 s.f.) compared with 0.22 kN and 0.10 kN for the room temperature LPBF tungsten-tantalum alloy and tungsten respectively.

The small punch test was considered to have failed after the load dropped back to  $0.8 F_m$ . From Figure 5.34, a displacement to failure of 0.55 mm, 0.5 mm and 0.53 mm (HB W-Ta, W-Ta, W) could be seen. A consistent displacement at maximum load of approximately 0.3 mm was seen between all samples. This suggested that while the LPBF tungsten-tantalum produced with bed heating had the highest fracture load, it did not show any additional ductility in the load-displacement curves.

The prevalence of cracking within the LPBF material meant no ductility was seen in the samples as evidenced by the low displacement to failure. Tantalum had been shown to increase the DBTT, but at the test temperature it did not show any reduced strength or ductility (17). Testing at higher temperatures would be required to fully assess the likely DBTT of the LPBF tungsten and tungsten-tantalum although it was suggested the DBTT could be in excess of  $1100\text{ }^{\circ}\text{C}$  for comparable W-V and W-Ti alloys (17, 41).

Figure 5.35 showed the fracture surfaces of the LPBF tungsten sample and LPBF tungsten-tantalum sample produced with bed heating, neither of which showed any signs of plastic deformation. The typical brittle small-punch fracture surface showed a 'star' pattern where segments of material above the punch have broken and been pushed away as the punch moves giving an appearance of greater displacement than has occurred (42, 43). In the case of LPBF tungsten, it could be seen where the broken segments had fallen through leaving just the fractured outline of the small punch.

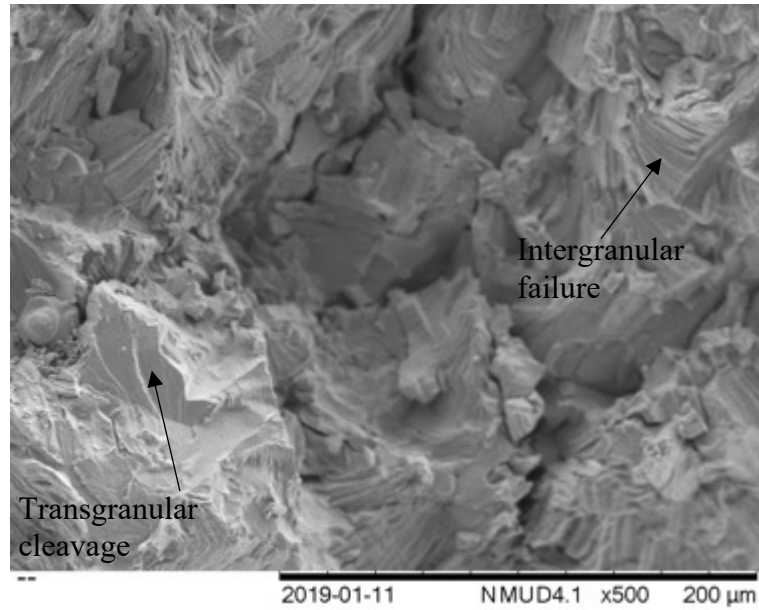


*Figure 5.35 - SE micrographs showing the fractured small punch specimens from LPBF tungsten-tantalum (left) and LPBF tungsten (right) tested at 600 °C*

Small punch testing produced load/displacement curves rather than stress/strain curves.

Unlike in tensile testing, it was challenging to convert one to the other as the stress condition varied during the test. On first contact with the punch, the stress in the disc tended to infinity although it rapidly stabilised as deformation increased. This posed particular issues for brittle materials as they had to survive this initial contact.

Figure 5.36 showed in greater detail the fracture surface of the LPBF tungsten-tantalum alloy tested at 600 °C. While similarities could be seen between the LPBF tungsten fracture surface (see Section 4.3.4) and that of the tungsten-tantalum alloy, key differences could also be noted. The key mode of failure for the LPBF tungsten sample was intergranular failure, whereas the LPBF tungsten-tantalum alloy showed some intergranular failure but transgranular cleavage could also be seen (labelled). This suggested that the grain boundaries were no longer the key point of weakness as they were in LPBF tungsten further validating the SIMS results shown earlier. However, the alloy still had DBTT in excess of 600 °C.



*Figure 5.36 - SE fractograph of LPBF tungsten-tantalum alloy tested at 600 °C*

While the initial small punch results proved promising in the improvements made through alloying and the use of the heated bed, Figure 5.37 showed the results of conventional tungsten alongside the LPBF results tested at 600 °C.

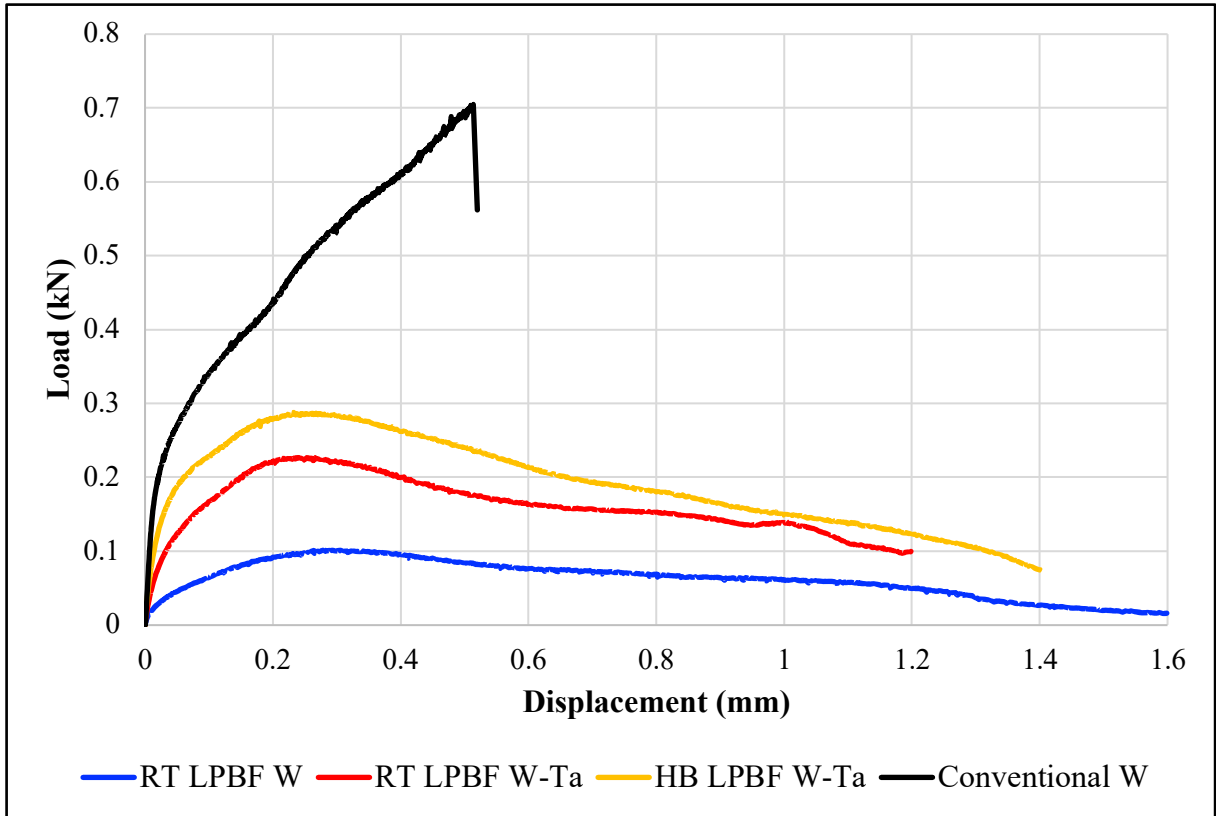
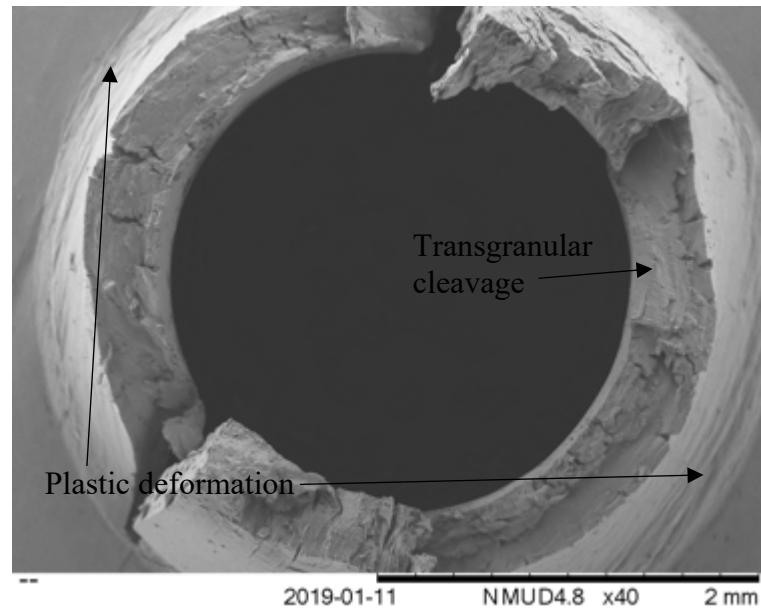


Figure 5.37 - Load/ Displacement curves for conventional tungsten, LPBF tungsten samples produced without bed pre-heating (RT) and LPBF tungsten-tantalum samples produced with (HB) and without (RT) bed heating tested at 600 °C

As could be seen the maximum load of the conventional tungsten was significantly higher (more than double) that of the LPBF tungsten-tantalum produced with the heated bed.

Additionally, the conventional material had greater levels of ductility, with a displacement at maximum load of 0.5 mm in comparison to 0.3 mm for the LPBF samples. The fractograph in Figure 5.38 still showed significant brittle failure however some ductility could be seen as the inner cone had been pushed out without the outer diameter cracking. This was likely due to the increased oxygen content in the LPBF samples increasing the DBTT (44).



*Figure 5.38 - SE micrographs showing the fractured small punch specimens from conventional tungsten tested at 600 °C*

Due to time and material constraints, two tests were conducted at 600 °C across all material sets. However, in order to increase confidence in the results, four additional repeats were produced in LPBF tungsten with no bed heating at 600 °C and the results were within 10 % error. Further testing would be required to improve confidence.

### **5.7 Demonstration Components**

As a final step to investigate the improvements made during the course of this study, demonstration components were produced. Three components were selected; brazing caps, a conventional divertor monoblock and a novel rear-fed divertor monoblock design. The brazing caps and conventional monoblock design were used for leak testing.



*Figure 5.39 - Brazing cap produced via LPBF using heated bed and the tungsten-tantalum alloy*

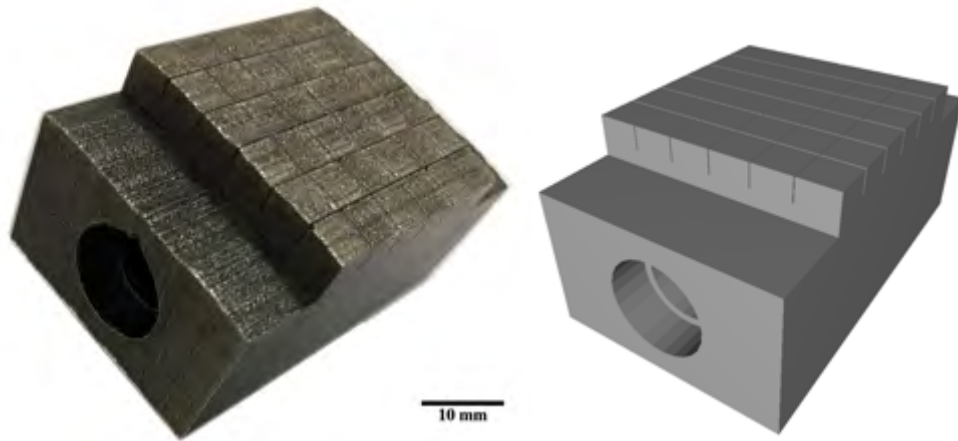
A number of brazing caps were produced (see Figure 5.39) roughly 20x20x20mm<sup>3</sup> cubes and tested along with the conventional divertor component for leak testing. This had been attempted with pure tungsten caps however, the extensive cracking meant accurate leak measurements could not be taken. Table 5.3 showed the results of the leak testing. The target leak rate was 0 mbar l/s. As could be seen, there was a consistency between the values from the two brazing caps and at double the pressure for the divertor monoblock there was a measured leak of significantly less than double. This was likely due to the larger wall thickness in the monoblock and the irregular crack pattern seen in the heated bed tungsten-tantalum sample. This suggested that the surface connected cracking seen in the LPBF room temperature tungsten parts were significantly reduced and as a result the leak rates were significantly reduced also.

*Table 5.3 – Table showing the leak testing results for the brazing caps and conventional monoblock designs produced with heated bed LPBF tungsten-tantalum*

	<b>Port Pressure (mbar)</b>	<b>Background Leak Rate (mbar l/s)</b>	<b>Measured Leak Rate (mbar l/s)</b>
Brazing Cap #1	0.2	1.0x10 <sup>-6</sup>	3.8x10 <sup>-2</sup>
Brazing Cap #2	0.2	1.1x10 <sup>-6</sup>	3.6x10 <sup>-2</sup>
Divertor Monoblock	0.4	3.0x10 <sup>-6</sup>	5.0x10 <sup>-2</sup>



The conventional divertor monoblock, (shaded CAD image of the design (right) along with the component after vibro-polishing (left)) could be seen in Figure 5.40.

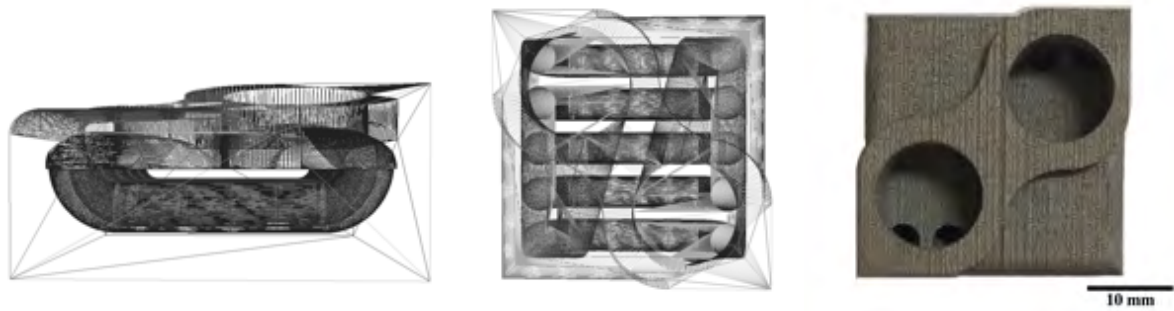


*Figure 5.40 - Conventional divertor monoblock produced with via LPBF with the tungsten-tantalum alloy and bed heating after vibro-polishing (left) and shaded CAD image of the design (right)*

The final component was a novel rear fed divertor design with an internal structure that meant it was only suitable for production via additive manufacturing.<sup>2</sup> Figure 5.41 showed wire frame CAD images of the design along with an image of the fabricated component after grit blasting. As could be seen, there were five small internal channels running through the centre of the part.

---

<sup>2</sup> The author gratefully acknowledges Dr. David Hancock and the Culham Centre for fusion Energy for the design of the rear fed divertor monoblock



*Figure 5.41 – Wireframe CAD models of the novel rear-fed divertor monoblock (left and middle) and the component produced via LPBF with the tungsten-tantalum alloy and bed heating after grit blasting<sup>3</sup> (right).*

There were several, significant advantages of the novel design over the conventional design. The first being performance and safety related – the presence of five smaller cooling channels in comparison to one larger channel increased the surface area over which heat exchange could occur, significantly improving the efficacy of the component. Moreover, multiple cooling channels offered improved safety; if there were an accident preventing coolant (loss of coolant accident (LOCA)) running through the system, the high heat flux components could undergo melting and there would be significant damage to the structural integrity of the reaction vessel which could release irradiated material from the plant (45, 46). Having multiple cooling channels would decrease the likelihood of such an incident occurring as damage to a single cooling channel would not prevent the circulation of coolant.

Additionally, there was a significant mass saving between the new and old designs; the rear-fed divertor had a mass of 158 g in comparison to 519 g for the conventional monoblock produced with the tungsten tantalum alloy. This would be a mass saving of around 70%. Given the entire divertor assembly is made up of 54 cassettes each weighing around 10 tonnes the potential weight saving would be significant (47). This would reduce the amount of plant

---

<sup>3</sup> The author would like to express their thanks to the MTC for undertaking the grit blasting of the component

material for waste storage which would be required until the activity levels reduced to allow recycling (48). There would be cost saving advantages; the powder raw material cost £150/kg, corresponding to a reduction in cost of £54 per part and with the large number of components required, transferring to the new design would give significant cost savings.

The geometric accuracy of the part was promising, and this showed potential for investigating further complex divertor designs for production via LPBF. The design had five fully internalised cooling channels which could not be machined; the channels were small (<5 mm diameter) meaning they could be produced without support structures.

## **5.8 Concluding Remarks**

Hot bed alloying was shown to be promising as it effectively increased the thermal input to the part and reduced the cooling rate. However, the uptake of oxygen was increased meaning the overall build quality was not substantially increased. This was due to the poor build atmosphere in the Concept Laser M2 machine. Tantalum additions proved more promising and successfully prevented grain boundary segregation in W-Ta alloy however inhomogeneities in the mixture still caused some cracking. Combining the two techniques showed an improved maximum load during small punch testing, however issues with oxidation persisted. The small punch samples still showed significantly poorer results than conventional tungsten suggesting significant additional work required to industrialise the process.

## 5.9 References

1. Palacios T, Pastor JY, editors. Degradation of Tungsten Alloys at Extreme Temperatures in Vacuum and Oxidation Atmospheres. *Materials Modelling and Simulation for Nuclear Fuels*; 2013; Chicago.
2. Lessmann GG, Gold RE. Weldability of Tungsten Base Alloys. 50th American Welding Society Annual Meeting; Philadelphia, U.S.: U.S. Department of Energy, Office of Scientific and Technical Information; 1969.
3. Moffatt WG. *The Handbook of Binary Phase Diagrams*. Massachusetts, U.S.: General Electric Company; 1981.
4. Wang X, Carter LN, Pang B, Attallah MM, Loretto MH. Microstructure and yield strength of SLM-fabricated CM247LC Ni-Superalloy. *Acta Materialia*. 2017;128:87-95.
5. Tietz TE, Wilson JW. *Behaviour and Properties of Refractory Metals*. London: Edward Arnold; 1965.
6. Wilkinson WD. *Properties of Refractory Metals*. New York: Gordon and Breach Science Publishers; 1969.
7. Zhou X, Liu X, Zhang D, Shen Z, Liu W. Balling phenomena in selective laser melted tungsten. *Journal of Materials Processing Technology*. 2015;222:33-42.
8. Anwar AB, Pham Q-C. Selective laser melting of AlSi10Mg: Effects of scan direction, part placement and inert gas flow velocity on tensile strength. *Journal of Materials Processing Technology*. 2017;240:388-96.
9. Reijonen J, Revuelta A, Riipinen T, Ruusuvoori K, Puukko P. On the effect of shielding gas flow on porosity and melt pool geometry in laser powder bed fusion additive manufacturing. *Additive Manufacturing*. 2020;32:101030.
10. King WE, Barth HD, Castillo VM, Gallegos GF, Gibbs JW, Hahn DE, Kamath C, and Rubenchik AM. Observation of keyhole-mode laser melting in laser powder-bed fusion additive manufacturing. *Journal of Materials Processing Technology*. 2014;214(12):2915-25.
11. Wang Z, Wang X, Cong S, Chen J, Sun H, Chen Z, Song G, Geng F, Chen Q, and Zhao Z. Towards full-colour tunability of inorganic electrochromic devices using ultracompact fabry-perot nanocavities. *Nature Communications*. 2020;11(1):302.
12. Furumoto TU, T.; Abdul Aziz, M.S.; Hosokawa, A.; Tanaka, R.; . Study on Reduction of Residual Stress Induced during Rapid Tooling Process: Influence of Heating Conditions on Residual Stress. *Key Engineering Materials*. 2010;447-448:785-9.
13. Yadroitsava IY, I, editor *Residual stress in metal specimens produced by Direct Metal Laser Sintering*. Solid Freeform Fabrication Symposium; 2015; Austin, Texas: University of Texas.
14. Wang L, Jiang X, Zhu Y, Ding Z, Zhu X, Sun J, and Biao S. Investigation of Performance and Residual Stress Generation of AlSi10Mg Processed by Selective Laser Melting. *Advances in Materials Science and Engineering*. 2018;2018:12.
15. Shiomi M, Osakada K, Nakamura K, Yamashita T, Abe F. Residual Stress within Metallic Model Made by Selective Laser Melting Process. *CIRP Annals*. 2004;53(1):195-8.
16. Research W. Element Data Source Information Illinois, U.S.2014 [Available from: <https://reference.wolfram.com/language/note/ElementDataSourceInformation.html>].
17. Rieth M, Dudarev SL, Gonzalez de Vicente SM, Aktaa J, Ahlgren T, Antusch S, Armstrong DEJ, Balden M, Baluc N, Barthe MF, Basuki WW, Battabyal M, Boldyryeva H, Brinkmann J, Celino M, Ciupinski L, Correia JB, DeBacker A, Domain C, Gagnidze E, Garcia-Rosales C, Gibson J, Gilbert MR, Giusepponi S, Gludovatz B, Greuner H, Heinola K, Hoschen T, Hoffmann A, Holstein N, Koch F, Krauss W, Li H, Lindig S, Linke J, Linsmeier

- C, Lopez-Ruiz P, Maier H, Matejicek J, Mishra TP, Muhammed M, Monoz A, Muzyk M, Nordlund K, Nguyen-Manh D, Opschoor J, Ordas N, Palacios T, Pintsuk G, Pippan R, Reiser J, Riesch J, Roberts SG, Romaner L, Rosinski M, Sanchez M, Schulmeyer W, Traxler H, Urena A, VanDerLaan L, Veleva L, Wahlberg S, Walter M, Weber T, Weitkamp T, Wurster S, Yar MA, You JH and Zivelonghi A. A brief summary of the progress on the EFDA tungsten materials program. *Journal of Nuclear Materials*. 2013;442(1–3, Supplement 1):S173-S80.
18. Tejado E, Carvalho PA, Munoz A, Dias M, Correia JB, Mardolcar UV, and Pastor JY. The effects of tantalum addition on the microtexture and mechanical behaviour of tungsten for ITER applications. *Journal of Nuclear Materials*. 2015;467(Part 2):949-55.
  19. Yu H, Zhu S, Yang X, Wang X, Sun H, Huo M. Synthesis of Coral-Like Tantalum Oxide Films via Anodization in Mixed Organic-Inorganic Electrolytes. *PLOS ONE*. 2013;8(6):e66447.
  20. Lee YJ, Lee TH, Kim DY, Nersisyan HH, Han MH, Kang KS, et al. Microstructural and corrosion characteristics of tantalum coatings prepared by molten salt electrodeposition. *Surface and Coatings Technology*. 2013;235:819-26.
  21. Zhang N, Li L, Li G. Nanosized amorphous tantalum oxide: a highly efficient photocatalyst for hydrogen evolution. *Research on Chemical Intermediates*. 2017;43(9):5011-24.
  22. Park J-C, Pee J-H, Kim Y-J, Eui-Seouck C. Synthesis of Tantalum Oxy-nitride and Nitride using Oxygen Deficiency Tantalum Oxides. *Journal of Korean Powder Metallurgy Institute*. 2008;15(6):489-95.
  23. Iveković A, Omidvari N, Vrancken B, Lietaert K, Thijs L, Vanmeensel K, Vleugels J, and Kruth J-P. Selective laser melting of tungsten and tungsten alloys. *International Journal of Refractory Metals and Hard Materials*. 2018;72:27-32.
  24. Li Y, Bushby AJ, Dunstan DJ. The Hall-Petch effect as a manifestation of the general size effect. *Proceedings of the Royal Society A: Mathematical, Physical and Engineering Sciences*. 2016;472(2190):20150890.
  25. Ren C, Fang ZZ, Koopman M, Butler B, Paramore J, Middlemas S. Methods for improving ductility of tungsten - A review. *International Journal of Refractory Metals and Hard Materials*. 2018;75:170-83.
  26. Stringer J, Rosenfield AR. Interstitial Solid Solutions In Body-Centred Cube Metals. *Nature*. 1963;199(4891):337-9.
  27. Reed TB. *Free Energy of Formation of Binary Compounds*. Cambridge, MA.: MIT Press; 1971.
  28. Xie ZM, Liu R, Miao S, Yang XD, Zhang T, Wang XP, et al. Extraordinary high ductility/strength of the interface designed bulk W-ZrC alloy plate at relatively low temperature. *Scientific Reports*. 2015;5:16014.
  29. Joshi A, Strongin M. Surface segregation of oxygen in Nb-O and Ta alloys. *Scripta Metallurgica*. 1974;8(4):413-24.
  30. Mutoh Y, Ichikawa K, Nagata K, Takeuchi M. Effect of rhenium addition on fracture toughness of tungsten at elevated temperatures. *Journal of Materials Science*. 1995;30(3):770-5.
  31. Scott MH, Knowlson PM. The welding and brazing of the refractory metals niobium, tantalum, molybdenum and tungsten — a review. *Journal of the Less Common Metals*. 1963;5(3):205-44.

32. Tan C, Zhou K, Ma W, Attard B, Zhang P, Kuang T. Selective laser melting of high-performance pure tungsten: parameter design, densification behavior and mechanical properties. *Science and Technology of Advanced Materials*. 2018;19(1):370-80.
33. Sidambe AT, Fox P, editors. Investigation of the Selective Laser Melting process with tungsten metal powder. 19th Plansee Seminar; 2017; Reutte, Austria: University of Liverpool.
34. Denton AR, Ashcroft NW. Vegard's law. *Physical Review A*. 1991;43(6):3161-4.
35. Ekoi EJ, Gowen A, Dorrepaal R, Dowling DP. Characterisation of titanium oxide layers using Raman spectroscopy and optical profilometry: Influence of oxide properties. *Results in Physics*. 2019;12:1574-85.
36. Xu L, Yin M-L, Liu SF. Ag(x)@WO<sub>3</sub> core-shell nanostructure for LSP enhanced chemical sensors. *Scientific reports*. 2014;4:6745-.
37. Perez I, Enríquez Carrejo JL, Sosa V, Perera FG, Farias Mancillas JR, Elizalde Galindo JT, et al. Evidence for structural transition in crystalline tantalum pentoxide films grown by RF magnetron sputtering. *Journal of Alloys and Compounds*. 2017;712:303-10.
38. Backman L, Opila EJ. Thermodynamic assessment of the group IV, V and VI oxides for the design of oxidation resistant multi-principal component materials. *Journal of the European Ceramic Society*. 2019;39(5):1796-802.
39. PLANSEE. Tantalum. Slough, U.K.; 2017.
40. Buchbinder D, Meiners W, Pirch N, Wissenbach K, Schrage J. Investigation on reducing distortion by preheating during manufacture of aluminum components using selective laser melting. *Journal of Laser Applications*. 2014;26(1):012004.
41. Rieth M, Dudarev SL, Gonzalez de Vicente SM, Aktaa J, Ahlgren T, Antusch S, et al. Recent progress in research on tungsten materials for nuclear fusion applications in Europe. *Journal of Nuclear Materials*. 2013;432(1–3):482-500.
42. Richardson M, Gorley M, Surrey E, Wynne B, Lowrie F. Realisation of Small Punch Testing to Accelerate Materials Qualification for Fusion Applications. In: Field A, editor. Oxford, U.K.: UKAEA; n.d.
43. Richardson M, Gorley M, Surrey E, Wynne B. An Investigation of the Mechanical Performance of Conventional and Additively Manufactured Vanadium. In: Field A, editor. Oxford, U.K.: UKAEA; n.d.
44. Yih SWH, Wang CT. Tungsten: Sources, Metallurgy, Properties, and Applications. New York: Plenum Press; 1979.
45. Andritsos F, Zucchetti M. Afterheat transient in ITER after a total loss of coolant accident. *Fusion Engineering and Design*. 1991;15(2):113-9.
46. Hino T, Hirohata Y, Yamashina T. Analysis for loss of coolant accident in a fusion reactor. *Fusion Engineering and Design*. 1996;31(3):259-63.
47. ITER. The ITER Tokamak Caderache, France2019 [Available from: <https://www.iter.org/mach>].
48. Bloom EE, Conn RW, Davis JW, Gold RE, Little R, Schultz KR, Smith DL, and Wiffen FW. Low activation materials for fusion applications. *Journal of Nuclear Materials*. 1984;122(1):17-26.

## **CHAPTER 6 - CONCLUSIONS, EVALUATION AND FUTURE WORK**

This chapter summarises the conclusions presented in Chapters 4 and 5 of this thesis and includes an evaluation of the feasibility of processing tungsten based materials via LPBF predominantly for nuclear fusion applications. The future work and developments required are also discussed.

### **6.1. Overall Conclusions**

The parametric studies conducted, found a processing range where density could be optimised. The peak density found was around 98.5 % and this occurred when lack of fusion defects were largely eliminated but extensive cracking remained. Parametric studies typically utilise energy density relationships which amalgamate key laser parameters into a single value. The validity of these relationships was investigated, and it was found the most commonly used energy density relationship (Volumetric Energy Density) has significant flaws as it inadequately assumes all parameters have equal weighting. Indeed, even within threshold powers for melting and vaporisation the density of parts varied by as much as 20 % for a given Volumetric Energy Density. Moreover, densification is the simplest metric and due to the different thermal inputs into the parts, the microstructure will vary considerably. This study has found the most simple “Linear Energy Density relationship” offered a better approximation and an alternative energy density equation was presented using data determined from an individual scan track.

The cracking mechanism was consistent between samples from the parametric study and through microscopy of polished and fracture surfaces. This mechanism was shown to be grain

boundary cracking occurring at the centre and edges of laser scan tracks. Moreover, following SIMS of LPBF tungsten components it was clear that even uncracked grain boundaries contained an enrichment of oxygen.

Small punch testing showed that the material was significantly embrittled with a fracture strength of only 15 % of the conventionally manufactured material. Fractography of the small punch samples showed that conventional material showed signs of ductility at 600 °C (the maximum operating temperature of the small punch test rig) whereas no signs of ductility could be seen in the LPBF material due to the extensive cracking within the samples.

The comparison of raw materials for LPBF showed significant variation in absorptivity depending on powder morphology (0.2 vs 0.35 for irregular and spherical morphologies); build plate analysis determined that the penetration depth of the fusion zone, and the minimum effective energy absorbed of the plasma spheroidized powder was almost double that of the chemically reduced powder. The effect on density of the final parts was also found to be significant. The effective LPBF processing window for a given material also depended significantly on the powder preparation technique and morphology of the powder and literature values may vary significantly as a result.

It was therefore concluded on the basis of the work presented in Chapter 4 that, with the machine platform available at UoB (Concept M2 Laser Cusing Machine), it was not possible to eliminate cracking when processing pure tungsten with current machine capabilities. This was due to the failure to achieve the quality of atmosphere required to prevent oxygen grain boundary embrittlement with this equipment.



As a result, work was conducted to modify the machine to include heated bed capabilities and investigate alloying additions to overcome these issues associated with oxygen embrittlement.

Initial investigations into laser pre-heating of the build plate were found to successfully increase the temperature over the control studies and these showed an improvement in interface quality and penetration depth of the fusion zone. However, the temperature increase was insufficient to move above the DBTT of the material, nor was the final cooling rate reduced. As a result, there was no noticeable effect on crack density.

As a result of these preliminary successes, a modified reduced build volume with heated bed capacity was designed, capable of achieving a bed temperature of 600 °C. Additionally, it was designed to allow controlled heating and cooling of the platform to reduce residual stresses throughout the process. This was found to have good temperature control and the cooling rate of the base plate was effectively reduced.

The deposits produced with the heated bed also showed reduced cracking in the mid-section of the part as well as showing an increase in penetration depth of the fusion zone compared to LPBF tungsten samples produced without bed-heating. As expected, there was a variation in grain size seen across the component, which may have contributed to the variation in cracking mechanism seen. Further work on modelling this process is needed to quantify the cooling rates experienced by different portions of the build throughout the process.

While some promise was shown with these samples, significant problems with oxidation were seen. The positive pressure system of the Concept M2 Laser Cusing Machine provides a

lower quality atmosphere than those machine platforms that inert through a vacuum and purge system. This residual oxygen was found to rapidly cause oxidation, particularly at 600 °C, where a visible blue oxide layer reformed between each recoat through the process. Single scan tracks which were performed on the heated build plate showed increased levels of ‘balling’ as a result of the oxidation.

The alternative methodology considered to improve the processability of the material was through alloying additions designed to decrease the material’s susceptibility to oxygen embrittlement. While a number of alloy additions have been discussed in the literature, a W-Ta alloy was selected as the most cost-effective potential solution which would also have the required thermal and mechanical properties and have the best response to irradiation damage in service.

The blended elemental powders were used to produce LPBF deposits and the resultant material showed far lower levels of cracking than had previously been seen. Moreover, the cracking seen was no longer typical grain boundary cracking and instead showed fine cracks surrounding high tungsten regions. SIMS was conducted on these parts and no segregation of oxygen could be seen, showing that the alloy addition had effectively altered this embrittlement mechanism.

Raman spectroscopy also showed that the surface of LPBF samples made with pure tungsten showed a tungsten-based oxide ( $W_XO_Y$ ) whereas the W-Ta sample surface showed a Tantalum-based oxide ( $Ta_XO_Y$ ). This was in agreement with literature which showed tantalum

oxide should be more stable and form more readily. However, little evidence of this existed in as a minor alloy addition.

The next phase of the work involved using the W-Ta alloy with a processing strategy using the heated bed module to try and eliminate the residual cracking, found in the W-Ta parts, to produce components. This had mixed success; the small punch material produced through this route had a higher fracture load, however the issues associated with oxidation had increased and in some areas of the sample higher levels of cracking could be seen than in the W-Ta samples produced without bed heating. Despite this, analysis of small punch fracture surfaces showed some transgranular cleavage in the heated bed tungsten-tantalum alloy rather than intergranular failure in the pure tungsten samples suggesting the grain boundaries have been effectively strengthened.

The demonstrator components showed improved leak testing in comparison to components previously produced with LPBF pure tungsten. Moreover, the tungsten-tantalum samples produced with bed heating had a 66% higher fracture stress than LPBF pure tungsten and 25% higher than LPBF tungsten tantalum produced without bed-heating. However, these were still significantly lower than conventional pure tungsten material; this was found to be likely due to the much higher oxygen contents in the additively manufactured material than in the conventional material (<100 ppm) versus LPBF material (360 ppm).

## **6.2. Evaluation of the LPBF Processing Route**

LPBF processing has been investigated as a potential method of producing high heat flux components for nuclear fusion from refractory metals due to the potential ability to produce

components with complex internal geometries. The current divertor monoblock design is limited due to the poor machineability of tungsten; LPBF was therefore investigated as a method of producing components which have significant potential performance, safety and cost improvements over their conventionally manufactured alternatives.

However, a review of the literature showed refractory metals are considered to have poor weldability and have a high proclivity for cracking, meaning they were likely to be difficult to process via LPBF. The results presented in this thesis have confirmed this hypothesis, and significant further work is required before these parts could be considered ready to produce in quantities required for nuclear fusion.

As could be seen from Chapter 4, the cracking in the as-fabricated condition was significant and the cracking showed strong correlations with the laser scan paths used. While some mitigation of this cracking has been trialled successfully the LPBF platform used for this study is far from the ideal platform for this material. The lack of a vacuum and purge capability in establishing the atmosphere and the requirement to move from the handling chamber to the processing chamber without protective atmosphere further worsens the difficulty associated with interstitial embrittlement of refractory metals through processing.

### **6.3. Proposed Areas of Future Work**

The topic areas listed below are the key areas of future work required in order to develop LPBF as a processing route capable of handling tungsten-based materials. The knowledge gathered would also be transferable to other materials which suffer from oxygen embrittlement.

## **I. Simulation of LPBF process**

The modelling of the LPBF processing of tungsten requires a two-fold approach. The model must accurately simulate the heat transfer and cooling rates through the part and predict the resultant microstructure and residual stresses. In addition, it must accurately predict the oxygen segregation to the grain boundaries under these conditions and offer a threshold stress and oxygen level below which cracking should not occur. The model would therefore have to predict thermal gradients on a larger scale as well the grain boundary fracture stress on a smaller scale. For this, a COMSOL based FE model could be used. A secondary stage of development would be increasing the complexity of the model to encompass the effect of other impurity elements as well as the effect of alloy additions.

This would provide a processing window, within which crack free processing of tungsten and tungsten alloys via LPBF should be possible. Moreover, the model would inform the requirements for hardware design

## **II. Improved thermal and mechanical property data**

In order to produce a model which works effectively, a greater body of thermal and mechanical property data for LPBF tungsten material at a range of temperatures and oxygen contents would be required, to establish the effect of LPBF processing on material properties. High temperature test rigs would be needed for this research as property data for temperatures of up to 2000 °C, and oxygen contents below 500 ppm would effectively cover most processing and operating conditions.

The properties likely to be of interest include:

- Thermal conductivity
- Thermal diffusivity
- Coefficient of thermal expansion
- DBTT
- Fracture stress
- Elongation to failure

### **III. Design of LPBF Hardware**

The design of LPBF hardware specifically to overcome the key challenges of producing refractory metals is required in order to consistently produce final components of adequate quality. The two key capabilities of note would be excellent atmospheric control, high gas quality (<10 ppm oxygen) and high temperature bed heating (>1000 °C). The AconityLab system currently on the market provides both of these during the processing phase but fails to adequately provide for atmosphere control during powder handling. The results shown in this thesis, and earlier welding literature suggest that producing defect free tungsten is possible under the right conditions and for the realisation of components for nuclear fusion. The volumes should be sufficient to make such an investment viable.

### **IV. Alloy Development**

Further work into variations of the W-Ta alloy particularly at establishing the minimum tantalum content required to strengthen the grain boundaries of tungsten should be

investigated. This would provide the lowest cost alloy combination and would also offer the highest service temperature, thermal conductivity and lowest coefficient of thermal expansion – key to its success within high heat flux components in nuclear fusion. Pre-alloyed powder should be investigated as a means of eliminating the heterogeneities seen during this study or another batch of tantalum with a higher mean particle size could be investigated as a lower cost alternative.

## **V. Further Crack Mechanism Investigation**

Further investigation into the cracking mechanism of LPBF tungsten should be conducted. The literature presented in Chapter 2 showed ambiguity as to the methodology of oxygen embrittlement. This work has offered some additional information particularly on the more macroscopic level, but further study would be helpful.

Particularly, it should be investigated if specific grain sizes, grain boundary angles or types, are more strongly affected by grain boundary embrittlement. Investigations into the quantity of oxygen at each grain boundary as well as confirmation of the chemistry of the grain boundaries (with regards to alternate interstitial content) should be conducted.

Transmission Electron Microscopy (TEM) would be helpful to investigate in greater detail specific grain boundaries although it would be complex to undertake. This would offer confirmation of the chemical structure (oxide or interstitial oxygen) of embrittling elements as well as investigating potential alternative interstitial elements which may have an embrittling effect.

Additionally, greater investigation into the fracture surfaces and their chemical segregation would be of interest. In-situ testing and microscopy may offer insight into the effect of chemistry and microstructure on the strength of specific grains and grain boundaries.

## **VI. Raw Material and Post Fabrication Heat Treatments**

This study has been limited to the microstructure and properties of as-fabricated material in order to better understand the underlying scientific principles behind the mechanisms of oxygen embrittlement and cracking.

If cracking occurred during release of the constraints on the sample due to the connection to the substrate i.e. during EDM cutting from the base plate, the use of post fabrication heat treatments should be investigated to reduce the defect density, lower the DBTT and improve the mechanical properties of the material. The conventional processing of tungsten relies heavily on annealing processes particularly for further deformation (1). Annealing heat treatments, as well as the investigation of stress relief heat treatments prior to removal from the base plate may reduce the defect density within the components.

Other novel ways of reducing cracking within LPBF tungsten material such as the following should be investigated:

- Reduction heat treatments to remove oxides followed by HIP to close cracking
- Encapsulation of as fabricated components prior to HIP to remove surface connected defects
- Microstructural and chemical investigations to understand the effect of the processing on oxygen and grain boundary strength which is key to the understanding of these post-fabrication heat treatment steps.



Additionally, investigations into reducing heat treatments conducted on the raw material prior to LPBF manufacture may reduce oxides on the powder surface and improve the processability of the material. However, this poses significant practical, and health and safety considerations as improper heat treatments or early removal from the furnace could not only increase oxygen uptake in the powder but also pose a flammability risk while at temperature. Correct storage of the powder under argon following removal from the furnace is also key to prevent deleterious effects.

## **VII. Effect of Irradiation on LPBF samples**

Due to the final application of these components, within a nuclear fusion reactor, understanding the effect of irradiation of the material is of key importance to the safety and performance of the components. Given the effect of microstructure and chemical composition on irradiation damage it is important to understand the effect of processing conditions and the effect of both alloying additions and impurity content at levels typical of LPBF. This would likely be done initially through ion irradiation and simulation given the time consuming and cost intensive nature of neutron irradiation which also limits the amount of damage to which the material can be subjected. However, investigations with neutron irradiation may be required prior to introduction into service.

### **6.4. Final Remarks**

This thesis was designed to act as a feasibility study taking an existing technology and a material known to be challenging and difficult to weld and study the effect of its processing. It was found that the current machine platform had insufficient atmosphere control to produce

components of adequate quality. As a result, variations to the material and processing conditions were investigated as an attempt to reduce cracking. These were found to be effective, with the strength of the modified material and processing route, almost triple the fracture strength of the initial LPBF tungsten material. However, while a substantial improvement had been found, it was still significantly weaker than the conventionally manufactured material.

The ‘future work’ suggestions have shown the need for improved material and processing control ideally within a customised machine platform designed for processing materials susceptible to oxygen embrittlement with a high temperature build platform. This combined with a greater level of process understanding is needed to produce defect free components.

While this initial work has shown some promise, significant improvements are still required. The rear-fed divertor design can only be produced with additive manufacturing, and therefore the potential rewards of overcoming this challenge would be significant. These rewards could expand beyond the nuclear fusion industry with applications in nuclear medicine, weight balancing and tooling applications.

## 6.5. References

1. Day JH. Void formation in tungsten lamp filaments. *Lighting Research & Technology*. 1973;5(1):36-40.

## **APPENDIX A: CONCEPT LASER M2 OPERATIONS, MODIFICATIONS AND LASER PROFILING**

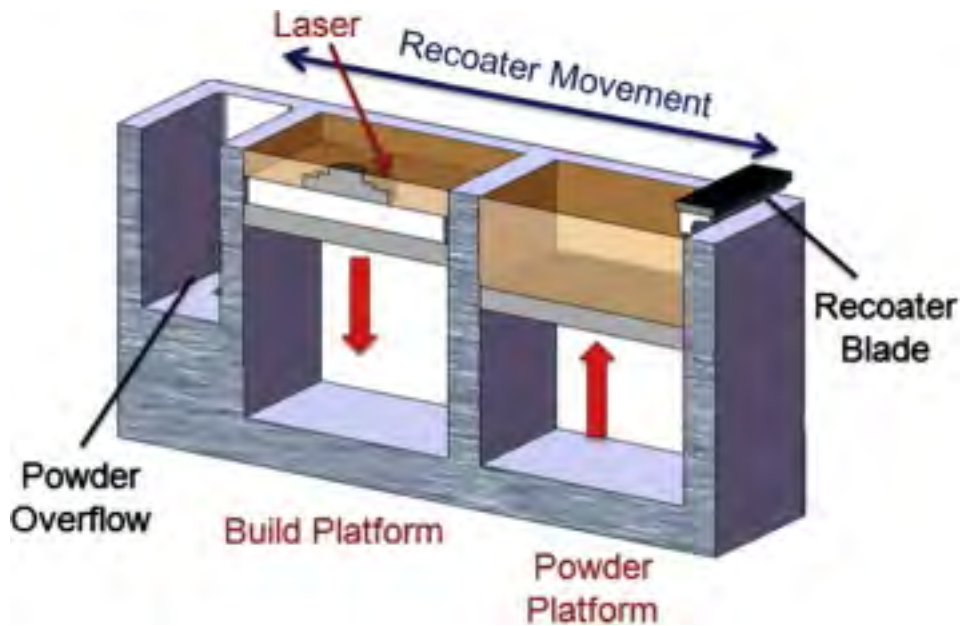
### **A.1 Standard Operation**

For the duration of this study, LPBF processing was conducted at the University of Birmingham (UoB) on an M2 Concept Laser Cusing machine (see Figure A.1). As the standard operation of the Concept Laser M2 has been previously documented (1), this appendix will only cover briefly the standard operation of the machine.



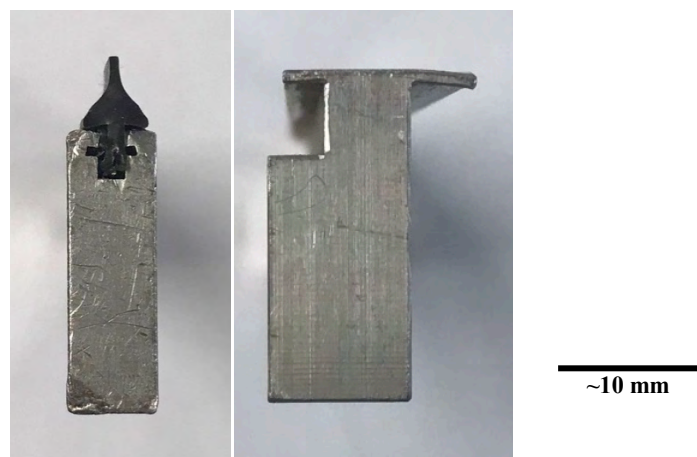
*Figure A.1 - Photograph of Concept Laser M2 with powder handling chamber (left) located in M&M UoB*

The machine has both a handling chamber and processing chamber allowing for easier cleaning, and material changeover. The technology module can be moved between these two chambers and is comprised of the powder overflow collection bin, the build and powder platforms, and recoater assembly. This can be seen in the schematic in Figure A.2.



*Figure A.2 – Schematic diagram of the Concept Laser M2 machine technology module with build and powder platforms (2)*

The recoater blade used for these studies was a flexible rubber blade which reduced the likelihood of build failure as the blade can flex over areas of distortion within the build but provides less repeatable geometric tolerances than the alternative hard aluminium recoaters provided by Concept Laser. Figure A.3 shows cross sections of the two recoater blades along with the recoater assembly (see Figure A.4).



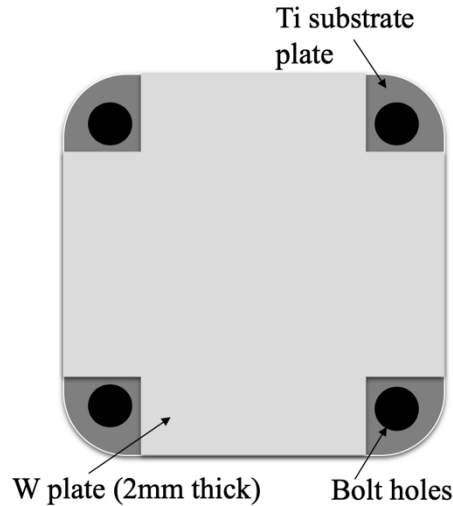
*Figure A.3 - Cross sections of the soft (left) and hard (right) recoater blades of the Concept Laser M2*



*Figure A.4 - Concept Laser M2 recoater assembly*

Both the powder and build platforms have maximum volumes of 250x250x280 mm, however a module to reduce the build volume to 90x90x110 mm was used throughout this study to minimise powder consumption. This consisted of the reduced build platform which sat on a stem which was bolted to the main build platform. A collar was placed over this to enclose the remaining build area.

Reduced size build plates (90x90 mm) were used. Due to the extreme temperatures required for melting tungsten, it was decided to use thin sheets of tungsten affixed to a titanium substrate plate with a high temperature adhesive to prevent overmelting and destruction of the main substrate plate. The tungsten plates were cut to 90x90 mm with 15x15 mm sections removed from the corners to allow access to bolt holes (see schematic in Figure A.5).



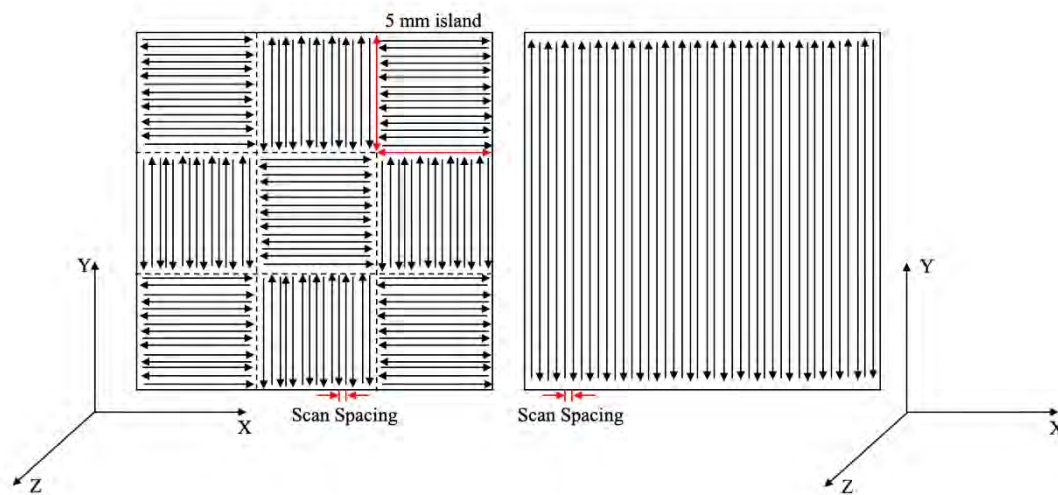
*Figure A.5 – Schematic diagram of the reduced size build plate with tungsten plate attached*

The plates and substrate plate were roughened with 120 grit paper and cleaned with ethanol to ensure a good adherence of the adhesive. A thin layer of “Pyroputty 2400” adhesive produced by Caswell was spread on to the substrate. This was air dried for 2-4 hours followed by a cure at 95 °C for 2-4 hours. After the tungsten plate was affixed and the assembly was cooled the top surface of the tungsten plate was roughened again to improve powder adhesion to the base plate and reduce the plates reflectivity to effectively melt the powder in the early stages of the build.

Prior to each build, the machine was thoroughly cleaned to reduce the risk of cross-contamination of powders by vacuuming, and wiping down with ethanol, the processing and build chambers. In addition, the laser windows were wiped down thoroughly to remove residue which may affect the both the lifetime of the laser and its profile and power reaching the build platform during the build.

All samples produced during the course of this study were produced without build support, and without contour scans and were produced either using the standard 5 mm x 5 mm chess, or the continuous scan strategy. In the chess strategy, each 5x5 mm ‘island’ is scanned

individually such that adjacent ‘islands’ have perpendicular scan directions. In the continuous scan strategy, the laser rasters back and forth across the part. Schematic diagrams of the laser scan strategies can be seen in the diagram below (see Figure A.6). Initially, the laser scan strategy was orientated at 45° to the part such that the laser was scanning into corners. However, this was changed to scan at 0° and 90° (rotating each layer) to minimise the variation in track length and prevent overheating of the component.



*Figure A.6 - Schematic diagram showing chess (left) and continuous (right) laser scan strategies*

With the exception of the mechanical test pieces and demonstrator component, all samples produced were 10 x 10 x 10 mm<sup>3</sup> cubic samples, and the processing variables altered throughout the studies were the laser power, laser scanning speed and laser scan spacing. The other machine parameters remained constant and the details of those can be found in the experimental method (Section 3.4).

## **A.2 Build Environment**

Both the handling and processing chambers are equipped with oxygen sensors accurate to 0.1 %, and the chamber is purged using a positive pressure argon flow to provide a protective atmosphere. Typically, oxygen levels in the build chamber drop to around 100 ppm of



oxygen. Figure A.7 shows the oxygen levels measured by a Systech ZR810 oxygen analyser during a typical tungsten build.

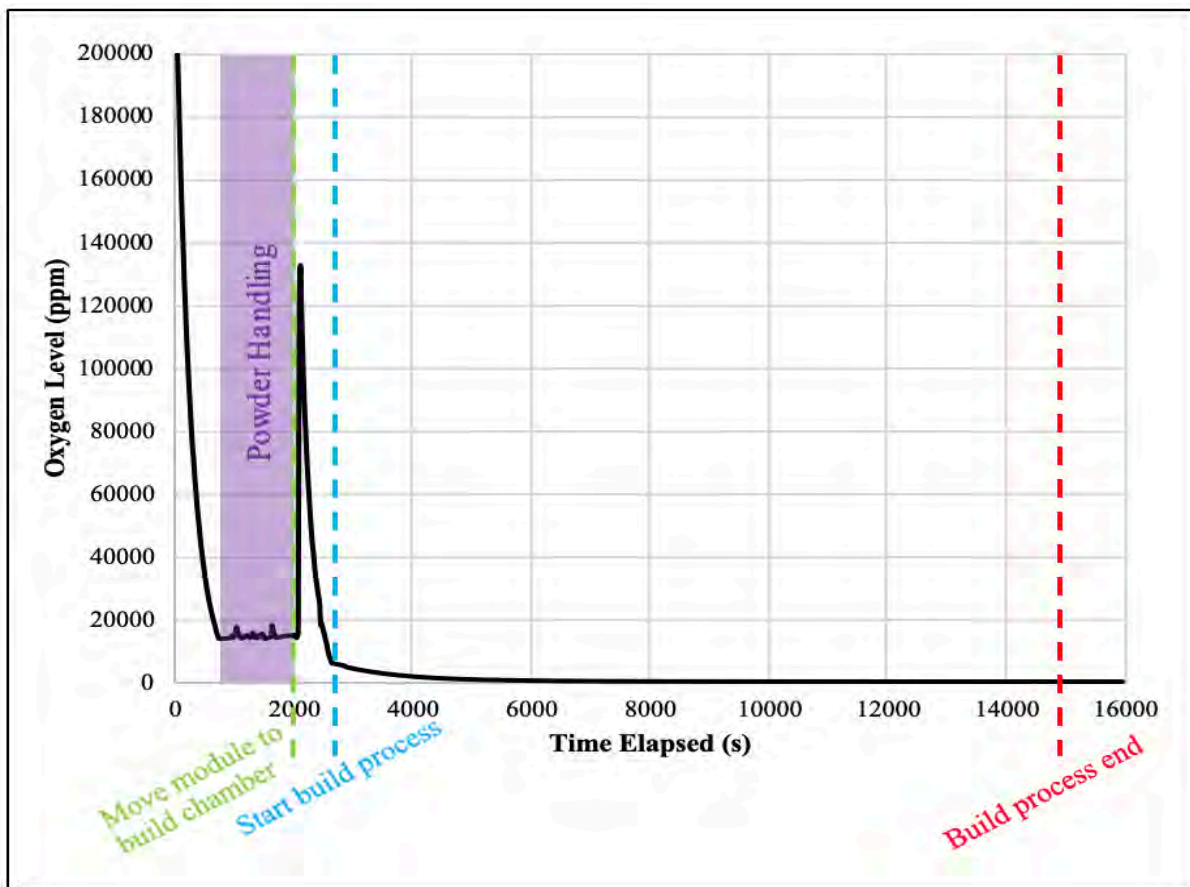


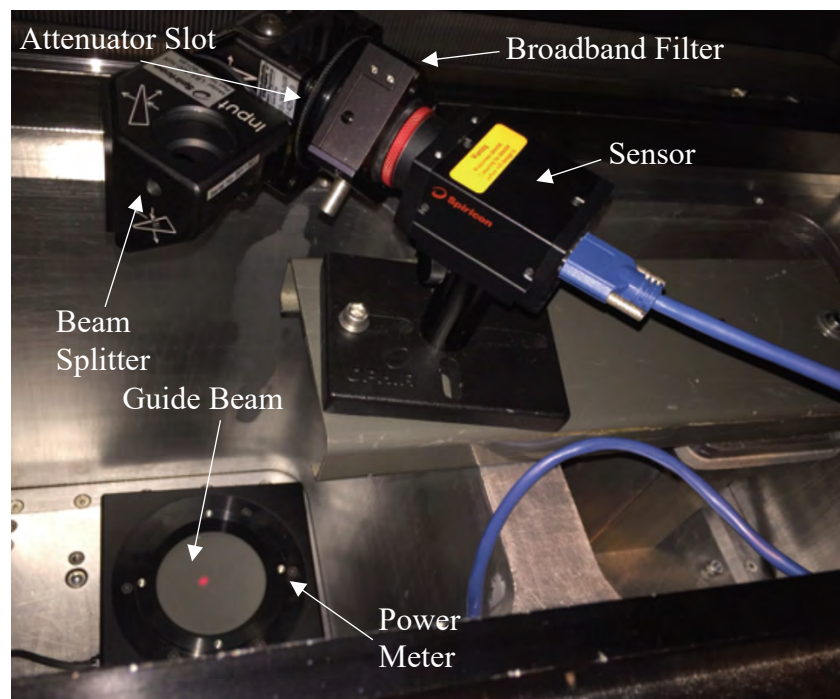
Figure A.7 – Graph showing the oxygen content of the technology module during a tungsten build

During powder handling, oxygen levels vary in the region of 1.5 %. After powder handling is completed, the technology module is transferred from the powder handling chamber to the processing chamber. Only one chamber in the machine is under argon at a time, so the oxygen levels increase during this process. The processing chamber is then purged in the same manner. The build was started when the chamber atmosphere was less than 500 ppm, and the oxygen content continued to decrease throughout the build and after about 15 minutes the oxygen content had stabilised at 50-100 ppm.

### A.3 Laser Profiling

The machine is equipped with a 400 W Yb-fibre laser with a Gaussian distribution. The nominal focal diameter stated by the manufacturer is 60  $\mu\text{m}$ .

Laser profiling was conducted to determine the beam diameter, distribution and actual power. Profiling was conducted using a focal spot analyser by Ophir with a SP300 camera and BeamGage software. The build platform was brought to the lowest point and a medium-high power fan cooled thermal sensor by Ophir (FL600A-BB-65) was placed on the build area. The guide beam was aligned such that it went through the splitter and on to the power meter below. The set-up of the laser profilometer and power meter can be seen in Figure A.8. The focal plane of the laser was found to be approximately 187 mm. Additional attenuation was needed as the power increased. The software was calibrated with every change in set up.

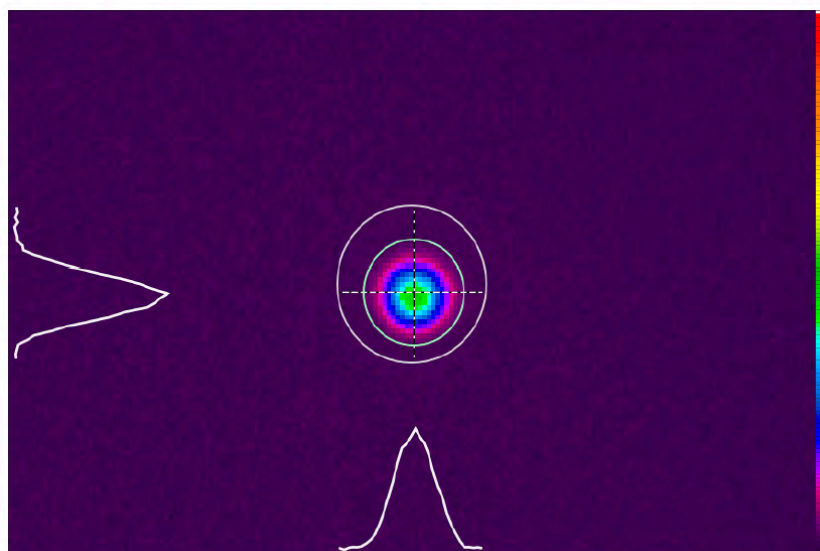


*Figure A.8 – Laser profiling set up with Spiricon camera (top) and Ophir thermal power laser sensor (bottom)*

Laser profiling found the beam diameter to vary with input power. Table A.1 below gives measured beam diameter for a range of given powers. Below 100 W, the power delivered by the laser was found to be unstable with delivered powers significantly lower than the nominal power demanded. The laser beam diameter is stable at 65  $\mu\text{m}$  up to a power of 200 W. At 200 W, the delivered laser power is consistent with the nominal value within 5 % error, and as nominal powers increase, the error band becomes tighter to  $\pm 5$  W. However, at powers greater than 200 W the laser beam diameter swells. Throughout, the laser beam remains Gaussian; Figure A.9 shows the laser profile at 300 W.

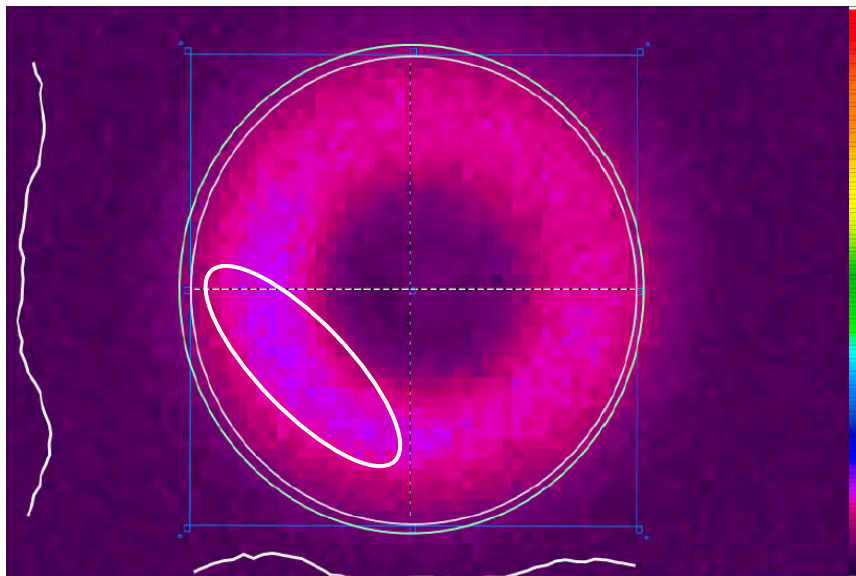
*Table A.1 – Table showing actual power and laser beam diameter for nominal powers measured on the Concept Laser M2 machine*

Nominal Power (W)	Delivered Power (W)	Laser Beam Diameter ( $\mu\text{m}$ )
50	24.5	65
80	64	65
100	85	65
200	193	68
300	294	84
400	404	89



*Figure A.9 – Laser profile of beam at nominal power of 300 W*

Profiling of the laser is key to determining laser health; insufficient maintenance and age can cause damage to the laser. Figure A.10 shows the laser beam profile at a nominal power of 300 W with a damaged F-theta lens. The beam no longer showed a Gaussian distribution and had a peak fluence a power of ten lower than a correctly functioning laser assembly ( $2.0 \times 10^6$  vs.  $1.4 \times 10^7$  Wcm<sup>-2</sup>). Additionally, when comparing Figures A.9 and A.10, a significant swelling of the beam can be seen with an approximate diameter of 175  $\mu$ m, double the diameter of the functioning laser assembly (84  $\mu$ m). The power is not evenly distributed across the beam with a concentrated area on the left-hand side (circled).



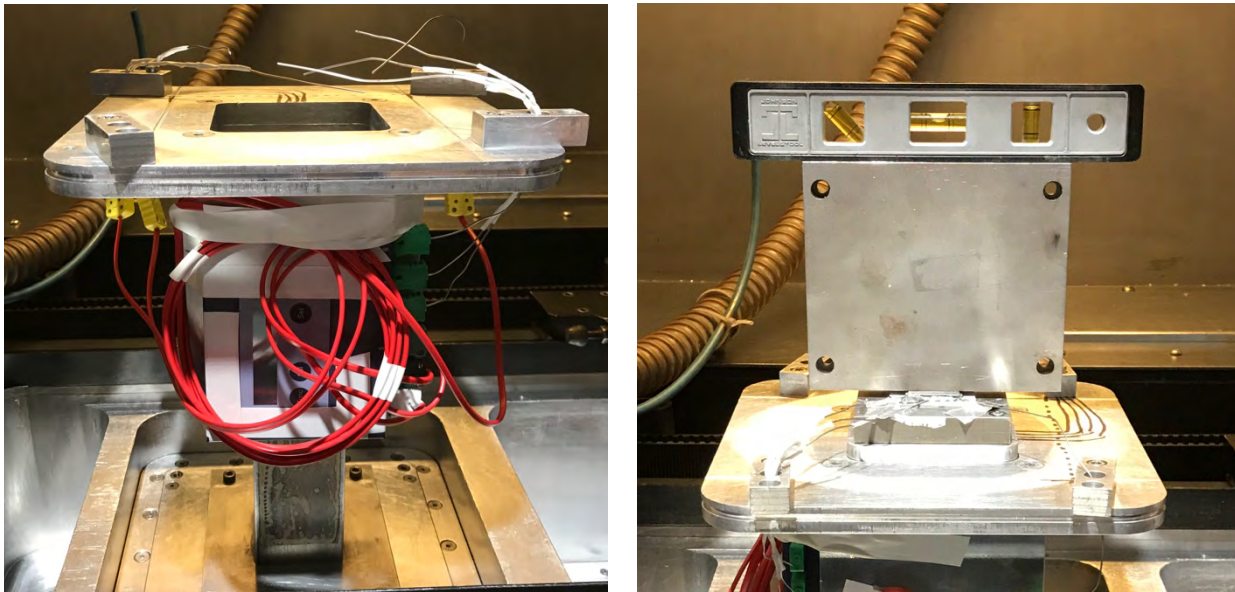
*Figure A.10 – Laser profile of beam focussed with damaged F-theta lens at nominal power of 300 W*

This shows the importance of adequate profiling when determining energy inputs and analysing defects within LPBF as the manufacturer's nominal values are inaccurate and there is significant variation with laser parameters, as well as a significant potential for laser health issues which may otherwise go undetected.

## A.4 Machine Modifications

### A.4.1 Laser Preheating

For Stage V of the LPBF processing study, modifications to the build set-up were made to allow for temperature monitoring of the base plate and initial trials into laser pre-heating were conducted.



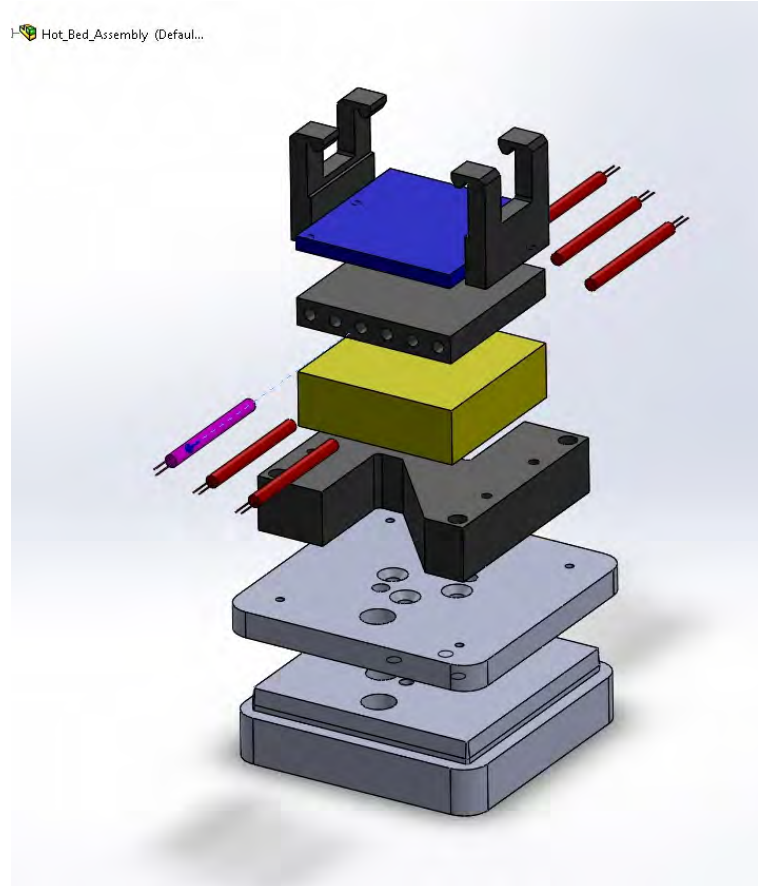
*Figure A.11 – Photograph (left) showing thermocouples connected to a data logger and a photograph (right) of thermocouples attached to a build plate with insulating plate in place.*

Figure A.11 shows photographs of the experimental set-up. The data logger used was an OQ610-S Squirrel Data Logger from Grant Instruments. Six K-type thermocouples which were fixed between the tungsten plate and the insulating plate with “Pyroputty 2400” high temperature adhesive.

Laser power and scan speed of 120 W and 1000 mms<sup>-1</sup> were chosen as this was below the threshold for melting as determined by Trapp et al., 2017 (3) and the rapid scan speed would ensure more uniform heating across the plate.

#### **A.4.2 Heated Bed Module**

A heated bed module was designed to fit into the reduced build volume module of the Concept Laser M2 (Figure A.12). The maximum build volume of the heated bed was 60x45x50 mm<sup>3</sup>, with six 100 W, 24 V cartridge heaters spaced evenly across the build area to heat to a maximum temperature of 700 °C. A 5mm tungsten plate was fixed in place using clamps at either side of the build plate. Two K-type thermocouples were located in the centre of the heating plate to monitor and control the base plate temperature during the build with temperature variations of greater than 5 °C triggering the heaters to turn on or off. A dwell time of 30 minutes was used to ensure consistency of temperature across the build plate. The argon levels were stabilized for a minimum of 4 hours prior to bed heating to avoid excess oxidation. Machine safety was a concern due to the high temperatures attempted, given the adjacent machine parts were produced from aluminium. Two additional safety thermocouples were attached to the stem and base of the heated bed module to ensure machine safety. A cut-off temperature of 100 °C was utilised above which the heaters would cut off.



*Figure A.12 - Schematic of the heated bed module with (from top) plate loading clips, tungsten build plate (blue), heating plate (grey) with cartridge heaters (red), ceramic insert to limit heat losses (yellow) and attachments to Concept Laser M2 reduced build volume module.*

## A.5 References

1. Carter LN. Selective Laser Melting of Nickel Superalloys for high temperature applications. Birmingham: University of Birmingham; 2013.
2. Carter LN, Martin C, Withers PJ, Attallah MM. The influence of the laser scan strategy on grain structure and cracking behaviour in SLM powder-bed fabricated nickel superalloy. *Journal of Alloys and Compounds*. 2014;615:338-47.
3. Trapp J, Rubenchik AM, Guss G, Matthews MJ. In situ absorptivity measurements of metallic powders during laser powder-bed fusion additive manufacturing. *Applied Materials Today*. 2017;9(Supplement C):341-9.